Moonpool in Waves

CFD Verification and Validation of Wave Elevation Inside a Moonpool

G. Marelli

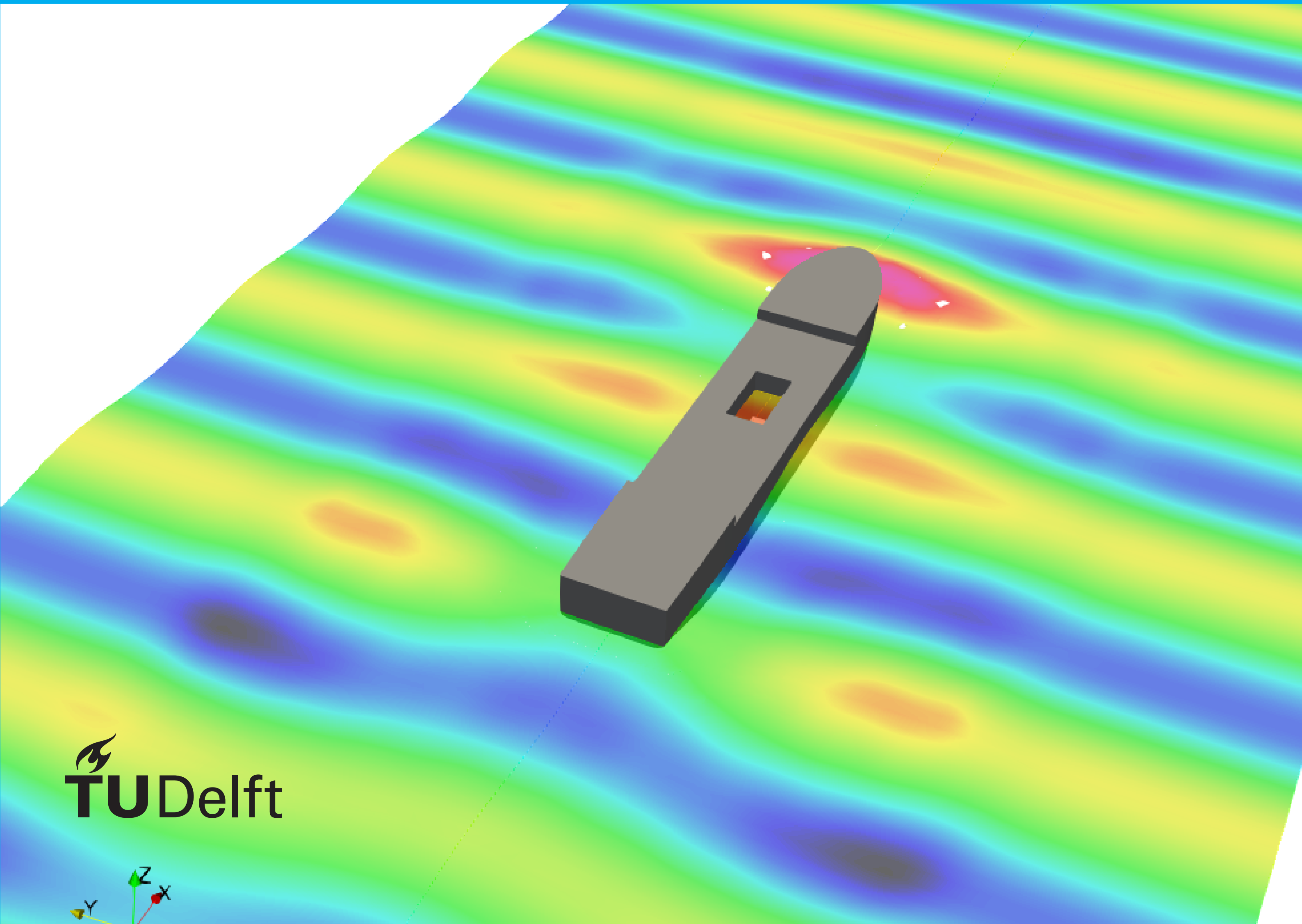

Moonpool in Waves

CFD Verification and Validation of Wave Elevation Inside a Moonpool

by

G. Marelli

to obtain the degree of Master of Science
at the Delft University of Technology,
to be defended publicly on Wednesday December 6, 2017 at 01:30 PM.

Student number:	4516109	
Project duration:	March 14, 2017 – November 8, 2017	
Thesis committee:	Prof. dr. ir. R. van 't Veer,	TU Delft, supervisor
	Dr. -Ing. S. Schreier,	TU Delft, supervisor
	MSc. F. Jaouën,	MARIN, supervisor
	Prof. dr. ir. G.H. Keetels,	TU Delft

TU Delft

Contents

List of Symbols

Γ	Sommerfeld operator
Φ	Velocity potential
α_a	Air volume fraction
α_w	Water volume fraction
α_{inc}	Air volume fraction (analytical solution)
β	Relaxation factor
ϵ	Damping factor
$\bar{\eta}_{abs}$	Non-dimensional free surface elevation, earth fixed coordinate system.
$\bar{\eta}_{rel}$	Non-dimensional relative free surface, ship fixed coordinate system.
η_{abs}	Free surface elevation, earth fixed coordinate system.
η_{rel}	Relative free surface, ship fixed coordinate system.
∇	Submerged vessel volume
ω	Angular wave frequency
ϕ	Vessel roll
ϕ_0	Estimate of the exact solution of the algebraic set of equations.
ϕ_1	Solution estimated with finest mesh, finest time step and lowest steady convergence tolerance
ρ	Water density
θ	Vessel pitch

$[A]$	6x6 Added mass matrix
$[B]$	6x6 Damping matrix
B_v	Vessel breadth
D	Experimental result
E	Comparison error
F_d	Diffraction force
F_r	Radiation force
F_{fk}	Froude-Krilov force
H	Wave height
L_{pp}	Length between perpendiculars
N	Number of oscillations

R_1	Radius of the inner ellipse
R_2	Radius of the outer ellipse
R	Reflection factor
S	Simulation result
T_a	Draught at aft perpendicular
T_f	Draught at fore perpendicular
T	Wave period
U_ϕ	Numerical uncertainty
U_{exp}	Experimental uncertainty
U_{stat}	Statistical uncertainty
U_{val}	Validation uncertainty
$\bar{a}_{abs}$	Non-dimensional absolute wave amplitude, earth fixed coordinate system.
$\bar{a}_{rel}$	Non-dimensional relative wave amplitude, ship fixed coordinate system.
a_{abs}	Absolute wave amplitude, earth fixed coordinate system.
a_{inc}	Incoming wave amplitude, earth fixed coordinate system.
a_{rel}	Relative wave amplitude, ship fixed coordinate system.
c_c	Monitored phase velocity
c	Theoretical phase velocity
h	Water depth
k	Wave number
k_{xx}	Roll radius of gyration
k_{yy}	Pitch radius of gyration
k_{zz}	Yaw radius of gyration
m	Vessel mass
n	Number of element in the data set
x_b	Longitudinal distance of b from the center of gravity
x_{CoG}	Longitudinal position of the center of gravity
y_b	Transversal distance of b from the center of gravity
y_{CoG}	Transverse position of the center of gravity
y^+	Dimensionless wall distance
z	Vessel heave motion
z_{CoG}	Vertical position of the center of gravity

Abstract

Large water motion inside the moonpool of vessels operating in waves can be excited by pressure fluctuations produced by external waves and vessel motion. Extreme consequences of this effect may include injuries for crew members, and damages to deck equipment resulting in downtime for the vessel. The accepted method to predict this non-linear phenomenon is a combination of model tests and potential solver. Nevertheless, model tests are generally conducted at the end of the design phase leading to serious problems if the moonpool performance is not sufficient. CFD solvers proved their capability of modelling complex flow phenomena and their use as a design tool for the moonpool is growing. However, a complete verification & validation is still missing.

In the present work the water motion inside a moonpool and the forces on the hull, for a vessel in head waves without forward speed, are estimated using the MARIN software ReFRESCO. In doing so, the goal is to define the accuracy of the code for a rectangular moonpool with sharp edges without additional damping devices. For a deeper comprehension of the physics involved, a stepwise approach was followed. The work starts with an empty domain in which only regular waves were generated to assess the propagation and absorption of waves in ReFRESCO. Secondly, fixed vessel simulations were performed to study the influence of grid dimension, mesh refinement and boundary conditions. Then forced heave oscillations were simulated to estimate the damping and added mass. Verification studies were carried out for all the presented to this point. Finally, results from free-floating simulations were validated against experimental results.

1

Introduction

Moonpools are defined as vertical wells running through the hull of a vessel. Their use became widespread in the offshore industry; originally used only on drillships, today they are a means of launching and retrieving bells and remotely operated vehicles. Compared to traditional vessels, those with moonpools present some advantages. They provide a sheltered area from waves, and thanks to their location, reduce the relative motion between equipment and vessel. On the other hand under the right circumstances large water motions can occur inside the moonpool of vessels operating in waves. The water motion can be excited by external waves or just by the forward speed of the vessel. Since operational conditions for this type of vessel are at zero forward speed (moored or in dynamic position), only the first case will be discussed in this project.

Large water motions in the moonpool can lead to injuries for crew members and damage to deck equipment resulting in a longer downtime for the vessel. Resonant frequency and water motion are functions of the moonpool dimensions [22], therefore moonpools are a critical aspect during the vessel design phase. Although the use of CFD (Computational Fluid Dynamics) solvers as a design tool for the moonpool is growing (Bedos [7], Cao et al. [9], Pistidda and Ottend [26]) a complete verification and validation study is still missing.

1.1. Background

The first attempt to solve this problem was done by Aalbers [5] in 1984. He derived a mathematical model based on potential theory to evaluate the natural frequency and the amplitude of the water inside a moonpool. To do that he considered only moonpools with constant cross sectional area and he simplified the water motions as a mass/spring system. Results from model tests showed good agreement with numerical results regarding the natural frequency; nevertheless the non-linear damping term was disregarded resulting in an overestimation of the water motion. To improve the accuracy of his method Aalbers added an empirical value to take into account the non-linear contribution. Thanks to model tests he also observed how friction plays a minor role in energy loss compared to vortices; similar results have been confirmed by Fredriksen et al. [15] as a result of their validation work.

Another contribution to the moonpool study are the results obtained by Molin [22]. He studied the natural frequencies associated with each mode applying a linearised potential theory to a 2D model. The vessel is simplified as a fixed barge of infinite length and width with a moonpool in the middle while waves are in deep water condition. In order to reproduce the free surface around the hull two sinks are introduced far from the moonpool. The moonpool is assumed as a vertical well with constant cross section through the entire depth. This work was later extended to non-symmetrical moonpools (Molin and Zhang [23]). With this approach he was able to observe different surface shapes for sloshing modes and establish how the water motion and the free surface shape are affected by moonpool geometrical parameters (i.e draught width ratio). The latter results have been confirmed by Zhuang et al. [30] and Haland [16].

The first attempt to use a CFD approach was done in 2008 by Sadiq and Xiongliang [28], in this case a 2D moonpool and a simplified vessel were modelled. The increase in computing performance allowed the researchers to develop numerical model capable of accurately solving complex flow problems. Despite the progress done by viscous flow solver so far, today industries rely on a combination of model test and potential flow solvers to estimate the water motion inside the moonpools. It should be noted that using a potential flow solver, the contribution of viscous damping is neglected. Due to the absence of these viscous damping effects in potential flow approaches, their results over-estimate the fluid motion in the resonant region. To fix this problem model tests are performed to evaluate the water elevation inside the moonpool. Due to the high cost and time required for a complete set of model tests to be carried out, only specific conditions are analysed. With the data obtained, a potential software is tuned to investigate a wider spectrum of cases. Although this approach allows designers to obtain results close to the full scale model, model tests are conducted at the end of the design phase. This approach leads to serious problems if the moonpool does not match the design requirements. Design errors are clearly more complex to solve during the last design phase compared to the early stage. The possibility of assessing the quality of the moonpool design at an early stage in the project can help in preventing unexpected cost during late design changes. Furthermore computational methods compared to model tests allow designers to test different configurations and study their influence on the final project leading to a safer and more efficient vessel.

1.2. Objectives

The goal of this project is to define the accuracy of ReFRESCO (the URANS code developed by MARIN) to estimate the wave elevation inside a rectangular moonpool with sharp edges and without additional damping devices. To assess the accuracy of the software a solution verification and validation is necessary. Verification and Validation are defined in Eça and Hoekstra [12] as: Verification is a purely mathematical exercise that intends to show that we are "solving the equations right", whereas Validation is a science/engineering activity that intends to show that we are "solving the right equations".

Validation requires the comparison of numerical solution with experimental results. Data from model tests were carried out in the Seakeeping and Manoeuvring Basin (SMB) at MARIN in 2016 and they were available for this project. Experiment set-up, results and conclusions are published in Abeil [6].

Solving complex flow phenomena using CFD software may require a long computational time even on a modern cluster. This drawback limits their use in commercial project in favour of faster (and sometimes less accurate) methods. In this report data obtained from forced heave simulations are used to tune a potential software and compare the results with CFD solutions. The aim in including results from a potential approach is to show whether CFD can be used to simulate simplified problems (with less computational effort and shorter time), and then use faster methods to investigate different scenarios (i.e incoming waves direction) neglecting model tests.

1.3. Thesis structure

A stepwise approach was followed in this project. This path presents two main advantages, both theoretical and practical. First of all, combining small problems in a more complex simulation is possible to evaluate the influence of every single aspect involved. Secondly, the increasing difficulty at each step is favourable to gain a good knowledge of the problem. Besides, simpler simulations require a lower number of parameters in the control file of ReFRESCO, making their settings an easier task for an inexperienced user. With this approach the same settings are used during different simulations with the aim to provide a guideline for future simulations.

Chapter 2 introduces the reader to the main theoretical aspects concerning this project. At first a description of ReFRESCO and its theory are only mentioned since a more complete approach is out of the scope of the present work. Secondly in section 2.1 an introduction to different sources of error involved in a numerical simulation is presented. Then in section 2.2 the methods used to estimate the uncertainties and perform the verification and validation are described. The chapter ends with a presentation of the two wave absorption methods available in ReFRESCO. The wave absorption capabilities of both approaches will be investigate in chapter 4.

The first case is relatively simple: wave generation and absorption in an empty domain. The aim of this chapter is to assess the numerical and statistical uncertainty of wave height and wave period in the middle of the domain; boundary conditions, settings and results are reported in chapter 3. This chapter is of great importance since for simulations involving gravity waves, the accuracy in wave generation and propagation should first be established.

Once an adequate environment is modelled the vessel is included inside the domain. Simulations involving the fixed vessel case are discussed in chapter 4. The goal of this chapter is to estimate the numerical uncertainty and statistical uncertainty for wave elevation inside the moonpool together with the forces acting on the hull. For a definition of the uncertainties refer to section 2.1. Thanks to the relatively low time required to complete a simulation compared to the free floating vessel, in this chapter an extensive investigation to reduce the influence of the error sources is presented. From section 4.4 to 4.10 domain dimensions and wave absorption techniques are discussed. Furthermore in section 4.13 simulations with different turbulence model are presented in order to highlight the differences between different methods.

In chapter 5 the forced heave case is analysed. This chapter has two main goals. The first one is to estimate the numerical and statistical uncertainty for wave elevation inside the moonpool, forces acting on the hull, added mass and damping. They are reported in section 5.4 and 5.5. The second objective is to extract the damping and the added mass from the simulation data (section 5.7). Results are used to tune the 3D linear potential flow solver DIFFRAC (software developed by MARIN). Comparison of the results with experiment and viscous flow simulations is presented in section 7.1.

Starting from the conclusions of previous cases, in chapter 6 the free floating vessel in head waves is approached. Due to the high computational time required to perform these type of simulations, the number of investigated parameter was minimized. To accurately reproduce the experiment carried out in the SMB the same set-up is used, where the latter are presented in section 6.1. Solution verification for this case was not conducted due to tight time constrains on the completion of this project.

Finally in chapter 7 results obtained by numerical methods and experiments are compared. The computational fixed vessel and forced heave cases are compared with experimental results, evaluating the possibility of using simulations of a simplified problem to model the real-world scenario while maintaining sufficient result accuracy. Validation is performed for free floating case at different wave probes to show how numerical methods give a different accuracy across the moonpool. 3D figures of the water motion inside the moonpool are reported and they are compared with observation done by Abeil [6] during experiments. Potential flow results are included to define the accuracy of the method compared to viscous flow solver of experiment.

This work terminates with a summary of the conclusions reached during the project and tips for future research topic. An extensive collection of results data per case is reported in the appendices. For sake of comprehension only the quoted data are reported in the main body of the report.

2

Theoretical formulation

The aim of this chapter is to introduce the reader to ReFRESCO software and provide a brief introduction about the most important theoretical concepts behind this work. A complete description of every subject is out of the scope of this project, so references to additional reading are included. First ReFRESCO is outlined, then in section 2.1 a description of the error sources encountered in any CFD simulation is presented. Section 2.2 introduce the reader to the concepts of verification and validation. They are important to understand the accuracy of the presented results. In section 2.3 the two absorption methods available in ReFRESCO are summarized with related pros and cons. Finally, wave properties are described in section 2.4 together with the wave notation used in this project.

ReFRESCO is a community based open-usage CFD code for Maritime World. It solves multiphase (unsteady) incompressible viscous flow using the Navier-Stokes equations, complemented with turbulence model, cavitation models and volume-fraction transport equations for different phases [29]. The equations are discretized using a finite-volume approach with cell-centered collocated variables, in strong-conservation form, and a pressure-correction equation based on the SIMPLE algorithm is used to ensure mass conservation [19]. Time integration is performed implicitly with first or second-order backwards schemes. At each implicit time step, the non-linear system for velocity is solved with a matrix-free Krylov subspace method using a SIMPLE-type preconditioner [19]. A segregated approach is adopted for the solution of all other transport equation (each equation solves one variable, they are here defined as inner-loops), then the non-linearity and the coupling of the set of equations are restored thanks to an iterative process (outer-loop). The schematic process can be represented as:

```
initialization
do (time−loop)
        increment t
        do (outer−loop)
                solve momentum eqs (inner−loop)
                solve pressure correction eqs (inner−loop)
                solve turbulence model equations (inner−loop)
                solve additional transport equations (inner−loop)
        end do (outer−loop)
end do (time−loop)
```

Both the inner and the outer loops have two exit conditions. The loops are concluded when the residuals (defined as the difference between two successive iterations) of each equation decrease to the convergence tolerance, or the maximum number of iterations is reached. In order to not confuse the reader in this report the adjective unsteady will be used to define the inner-loop (L_1 will define the unsteady residuals) while steady will refer to the outer-loop. When the steady residuals (L_2) converge to the required tolerance, or the number of outer-loops reaches the maximum number of iterations, ReFRESCO moves to the next time step. The time loop concludes when time steps reach the $maxTimesteps$ value. L_2 is of great importance for the accuracy of the final solution because the iterative error decreases refining the steady residuals convergence(for errors definition refer to 2.1). On one hand, decreasing the convergence tolerance increases the accuracy of the final solution. On the other hand it increases the computational time (more outer-loops are required). For this reason, in practical application a compromise between accuracy and time required is usually accepted. The residuals magnitude are influenced by the scale of the simulation. Their magnitude can be relatively small even if the iterative error is not. For this reason L_2 values are normalized.

Worthy of mention for this project is also the particular case of simulations involving a free surface. In this case two phases are considered, water and air with a volume of fraction (respectively α_w and α_a). Since the two quantities are related by $\alpha_a = 1-\alpha_w$ only one transport equation is necessary. In absence of source/sink, the volume fraction equation is:

$$\frac{\partial \alpha}{\partial t} + \nabla(\alpha \mathbf{V}) = 0 \tag{2.1}$$

Despite the modeling strategy (interface capturing or interface tracking technique), two boundary conditions have to be fulfilled at the free surface:

- Kinematic boundary condition: The vertical velocity of a water particle at the free surface of the fluid is identical to the vertical velocity of that free surface itself.
- Dynamic boundary condition: The pressure at the free surface is equal to the atmospheric pressure.

For additional reading about the theoretical formulation of ReFRESCO refer to its manual [2].

2.1. Error sources in CFD

Numerical solutions approximate the true solution. The true solution is defined as the solution of the real physical problem, and usually for complex flows is not known. Every approximation or simplification of the real problem introduces an error in the numerical solution. The sources of error present in any CFD simulation are below defined. Their definition is in accordance with Ferziger and Perić [14], Eça and Hoekstra [12] and they are here reported for sake of completeness.

- *Round off error*: Consequence of the finite precision of the computers, its importance increases with grid refinement.
- *Iterative error*: Defined as the difference between the iterative and the exact solution of the algebraic equations system.
- *Discretization error*: Defined as the difference between the exact solution of the conservation equations and the exact solution of the algebraic system of equations obtained by discretizing these equations.
- *Modeling error*: Defined as the difference between the true solution and the exact solution of the mathematical model.

Distinguish between different approximations is important as the verification and validation methods deal with different error sources. All simulations for this project were performed with 15 digits of accuracy, which guarantees a negligible influence of the round off error compared with the iterative error.

The set of linear algebraic equations is solved by iterative methods. An initial solution is estimated and then systematically improved. Increasing the number of iterations the solution tends to the exact solution of the algebraic equations. The iterative error in theory can be reduced to machine accuracy. However, for practical application this is too much time consuming and sometimes not even possible. Nevertheless, the iterative error should be two or three order of magnitude smaller than the discretization error in order to not disturb the estimation of the numerical uncertainty [12]. The influence of the iterative error increases with grid refinement. A large iterative error leads to qualitatively wrong solutions. Its influence will be investigated in the next chapters. Note that the iterative error cannot be neglected due to the non-linearity of the set of equations. Even if the algebraic equations are solved with a direct method a contribution of the iterative error still exists.

The influence of the discretization error decreases with mesh and time step refinement. The estimation of the discretization error is obtained with the procedure developed by Eça and Hoekstra [12]. The discretization error is estimated with power series expansions as function of the typical cell size. The error estimate is converted into an uncertainty with a safety factor that depends on the observed order of grid convergence and on the standard deviation of the fit [12]. Due to the complexity of the method an accurate description is beyond the scope of this work. The reader is referred to the mentioned paper for additional reading.

The mathematical model used to describe the real flow phenomena has inside some assumptions. The modelling error depends upon them. It includes the assumptions made in deriving the transport equations (such as the choice of the turbulence model), the influence introduced by approximate boundary conditions, by a simplification of the geometry or the fluid properties.

Additionally to the presented errors, in this work the reader will often encounter the term statistical uncertainty. As the solutions of simulations involving waves fluctuate in time, the data will be represented as the mean of certain values in a period of time (defined for each case according to the steadiness of the solution). However the mean is not sufficient to fully described the solutions. Data set with different scatters may have the same mean. For this reason, the data will be reported as the mean value ± the relative standard deviation (RSD). The relative standard deviation is defined in equation 2.2:

$$\begin{aligned} RSD &= 100 * \frac{S_{sd}}{|\overline{x}|} \\ S_{sd} &= \sqrt{\frac{\sum(x-\overline{x})^2}{n-1}} \end{aligned} \tag{2.2}$$

Where $\overline{x}$ is the mean of the data set and S_{sd} is the sample standard deviation. x is the value of one sample, n represents the total number of elements in the data set. The relative standard deviation is a measure of dispersement and define a range in which solutions are spread out. The term statistical error will refer to the relative standard deviation and it will be included in the validation process.

2.2. Verification and Validation

The following definitions are important to understand the concepts of Verification, Validation and Uncertainty. They are based on the ASME standards for Uncertainty and the Validation Panel of the 19th ITTC. They are collected in the lectures notes of professor Tom J. C. van Terwisga for the course MTM1419: Advanced Course in Resistance and Propulsion (TU Delft academic year 2015-2016).

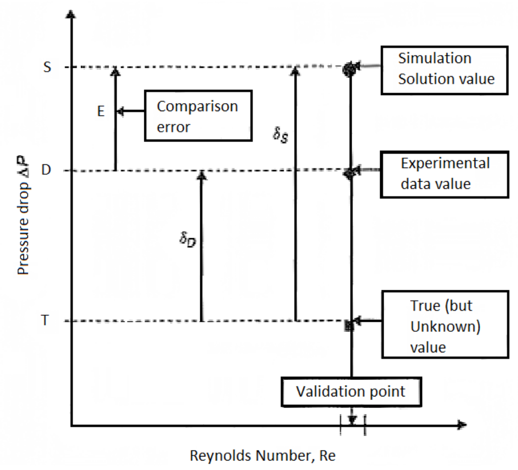

Figure 2.1: Schematic view of Validation. Picture extracted from Coleman and Steele [10]

The objective of the uncertainty analysis is to construct an uncertainty interval for any measurement, within the true value will lie with a chosen confidence (in this project equal to 95%). Verification deals with numerical accuracy and the objective is define a numerical uncertainty due to discretization and iterative error. The numerical uncertainty is estimated following the method proposed by Eça and Hoekstra [12]. Validation refers to the total process of confirming that the estimate is properly related to the true value. Validation includes all aspects, from modelling assumptions through measurement techniques and numerical methods to the production of the final estimate. In Fig. 2.1 a schematic view for validation is represented. S is the simulation result which is affected by all the error mentioned in section 2.1. The experiment result (called D in Fig. 2.1) is affected by error as well, defined as experimental error. E is the comparison error which is defined as:

$$E = S - D \tag{2.3}$$

The validation uncertainty is:

$$U_{val} = \sqrt{U_{\phi}^2 + U_{stat}^2 + U_{exp}^2} \tag{2.4}$$

The numerical uncertainty includes only the discretization error. Iterative error and round off error are neglected. U_{ϕ} is the numerical uncertainty, U_{stat} the statistical uncertainty and U_{exp} the experimental uncertainty. If the absolute value of E is larger than U_{val} then the comparison is dominated by modelling error and the numerical solution is not validate against the experimental results. On the opposite if the absolute value of E is smaller than U_{val} the modelling error is within the uncertainty bandwidth. For a more easy comprehension the statement above can be visualized in Fig. 2.2. If the numerical solution is verified the uncertainties bar overlap.

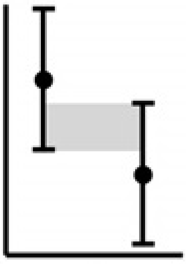

Figure 2.2: Graphical example of validation. The uncertainty bars overlap each other.

The validation process is meaningful only when the verification study is complete and the numerical uncertainty is defined. In addition, validation is possible only when experimental data are available. As already mentioned in the introduction, for this project experimental data were available only for the free floating case. Therefore a verification process is presented for every case and the validation is conducted only in chapter 7. Concluding it is important to state that this project deals with solution verification and not with code verification, i.e. the code is assumed to be free of errors.

2.3. Absorption method

ReFRESCO allows the user to chose between two different absorption methods, respectively called Sommerfeld 1 boundary condition and Relaxation zone. An introduction to both techniques with attention on pros and cons is presented in this section. Extensive studies on both the absorption methods have been carried out by Denisart [11] and Bunnik [8]. Refer to the mentioned papers for additional information. This section is included as introduction to the investigation on boundary conditions presented in chapter 4.

2.3.1. Sommerfeld 1

Sommerfeld 1 condition aims to model the absorption boundary as a non-reflecting boundary condition. Therefore waves can travel through the boundary. It is based on applying the Sommerfeld operator reported in eq. 2.6 to the first order potential theory. For sake of completeness the velocity potential of a linear wave propagating in a direction μ is below reported:

$$\begin{aligned}\Phi &= \Phi_a sin(k_x x + k_y y - \omega t)F(z)\\ \Phi_a &= \frac{ga}{\omega}\\ F(z) &= \frac{\cosh[k(z+h)]}{sinh(kh)}\\ k_x &= k\cos\mu\\ k_y &= k\sin\mu\end{aligned} \tag{2.5}$$

a is the wave amplitude, ω is the angular wave frequency, k the wave number and h the water depth. In the Sommerfeld operator c is the phase speed defined at the boundary.

$$\Gamma = \frac{\partial}{\partial t} - c\frac{\partial}{\partial n} \tag{2.6}$$

Applying the Sommerfeld operator at the absorption boundary with normal vector $\overrightarrow{n} = (n_1, n_2, 0)$ and incoming linear wave lead to:

$$\Gamma\Phi = -(\omega_0 - cn_1k_x - cn_2k_y)\Phi_a cos(k_x + k_y - \omega_0 t)F(z) \tag{2.7}$$

The equation goes to zero when:

$$c = \frac{\omega_0}{n_1k_x + n_2k_y} \tag{2.8}$$

When the equation 2.7 becomes zero the boundary does not interfere with wave propagation and it is modelled as a non-reflecting wall. Nevertheless, the equation above becomes zero if the incoming phase speed equals the phase speed defined at the boundary, and waves travel perpendicular to the boundary surface. If one of the two conditions are not satisfied, waves will be partially reflected. The reflection factor R is :

$$R = \left|\frac{c - c_c}{c + c_c}\right| \tag{2.9}$$

Where c_c is the monitored phase speed in the domain. When an object is included in the domain, waves are diffracted and they will reach the absorption boundary from different directions. Moreover, for simulations involving a wave spectrum only some waves will propagate with the phase speed defined at the boundary. In both cases only a part of waves will be fully absorbed, the majority will be partially reflected. Despite the drawbacks, Sommerfeld 1 does not require space inside the domain (it is only applied at the boundary) allowing a smaller domain compared to the relaxation zone.

2.3.2. Relaxation zone

The objective of the relaxation zone is to gradually absorb waves forcing the CFD solution toward the analytical solution calculated by potential theory. The relaxation zone is applied to velocity and volume of fraction, the pressure is adapted accordingly to the relaxed solution. To do that the domain is divided in three areas displayed in Fig. 2.3.

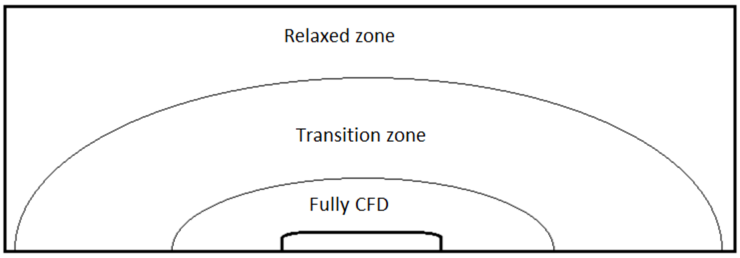

Figure 2.3: Example of relaxation zone

Inside the inner ellipse the CFD solution is computed and the relaxation factor is 0. Then from the inner ellipse to the outer ellipse the relaxation factor increases. Outside the outer ellipse the solution is completely relaxed (relaxation factor = 1). For the volume of fraction the solution becomes:

$$\alpha = (1-\beta)\alpha_a + \beta\alpha_{inc} \tag{2.10}$$

Where β is the relaxation factor, α_a is the solution computed by ReFRESCO and α_{inc} is the analytical solution. The relaxation factor inside the transition area grows from 0 to 1 following a cosine function.

$$\beta = \frac{cos(\pi\frac{R_2-r}{R_2-R_1})+1}{2} \tag{2.11}$$

R_1 and R_2 are the radius of the inner and outer ellipse and r is the point at which β is computed. R_2 is not limited to the domain dimensions, a desired β value can be applied to the boundaries simply enlarging the outer ellipse. For example, if one of the boundaries will lay at the same distance between R_1 and R_2, β at the domain edge is 0.5. The relaxation zone has been largely investigated by Denisart [11]. In his work he proposes a set of guidelines to minimize the inconveniences produced by the relaxation zone, here briefly summarized. β follows a cosine function to guarantee a smooth transition at the inner ellipse. However a too short passage leads to a too sharp transition which implies the generation of undesired numerical waves near the inner ellipse. On the opposite, a too long transition area results in a waste of space, because the area next to the inner ellipse will not influence the solution thanks to its low β value.

A second problem is related to the steady residuals convergence. In ReFRESCO the residuals are computed after the relaxation of the solution. Compute the residuals of an analytical solution is meaningless, and results in high steady residuals which are not related to the physical problem. The first consequence is the impossibility to asses the influence of the iterative error if the steady residuals do not converge. The second consequence is a drastic increase in the require computational time. ReFRESCO will spend all the outerloops trying to reach the steady convergence tolerance. Both of the problems diminish their influence decreasing β. The key for a correct application of the relaxation zone consists in finding the right values for β which maximize the absorption capability and minimize the mentioned problems.

2.4. Wave notation

Before we proceed further it is important to define the difference between wave amplitude and surface elevation and how they will be defined in this project. In a time record the surface elevation is the instantaneous elevation of the free surface, here called η. a represents the wave amplitude. In this project the wave amplitude is defined as the peak amplitude. The peak amplitude is the maximum value of η above a reference value (the reference value is zero). a_{inc} is the incoming wave amplitude generated at the inlet. $\bar{\eta}$ and $\bar{a}$ are respectively the non dimensional value of the free surface elevation and the wave amplitude. They are defined as:

$$\begin{aligned} \bar{\eta} &= \frac{\eta}{a_{inc}} \\ \bar{a} &= \frac{a}{a_{inc}} \end{aligned} \tag{2.12}$$

Therefore $\bar{a} = 1$ is equal to the incoming wave amplitude. Amplitude values are presented as the mean ± the RSD (relative standard deviation) as already discussed in section 2.1. In addition to the free surface and the wave amplitude, the reader will encounter the terms wave height, wave period and wave length. H is the wave height, defined as the vertical distance between the highest and lowest surface elevation. T is the wave period, defined as the interval between two successive downward zero crossing(refer to Fig. 2.4 for a definition of downward zero crossing). λ is the wave length defined as the horizontal distance between two consecutive downward zero crossing.

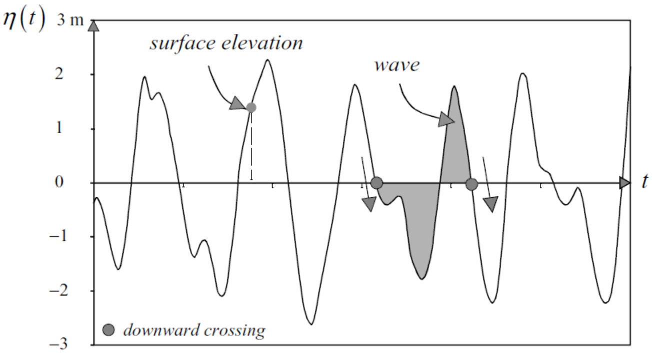

Figure 2.4: Definition of downward zero crossing. Image extracted from Holthuijsen [17]

2.4.1. Absolute and relative notation

ReFRESCO calculates the wave elevation respect to the domain fixed coordinate system, here called absolute reference system. Model test results are expressed in terms of the ship fixed coordinate system [6], here called relative reference system. To be able to compare the ReFRESCO and the experiment results, the wave elevation computed respect to the absolute reference system (η_{abs}) is converted to the relative reference system (η_{rel}):

$$\begin{aligned} \eta_{rel} &= \eta_{abs} + (-z + x_b\theta - y_b\phi) \\ \bar{\eta}_{rel} &= \frac{\eta_{rel}}{a_{inc}} \end{aligned} \tag{2.13}$$

z is the vessel heave motion, x_b and y_b are respectively the longitudinal and the transversal distance between the point b and the vessel CoG. θ is the vessel pitch and ϕ is the vessel roll. In chapter 4 the vessel motion is neglected, equation 2.14 becomes:

$$\eta_{rel} = \eta_{abs} \tag{2.14}$$

Results of chapter 4 will be reported in terms of absolute reference system. The aim is stress the difference with results obtained including the vessel motion.

3

Empty domain

The first test case is an empty domain (no vessel is modeled) in which waves are generated at the inlet, they travel across the domain and then they are absorbed at the outlet. The aim is to provide guidelines about grid density and time step to perform an accurate simulation, in addition control settings are reported. This chapter is of great importance as any simulation involving gravity waves should first ensure that propagation is correctly captured [13]. The numerical uncertainty of wave height and wave length is estimated using the method developed by Eça and Hoekstra [12].

3.1. Domain description

The domain investigated in this chapter is represented in Fig. 3.1.

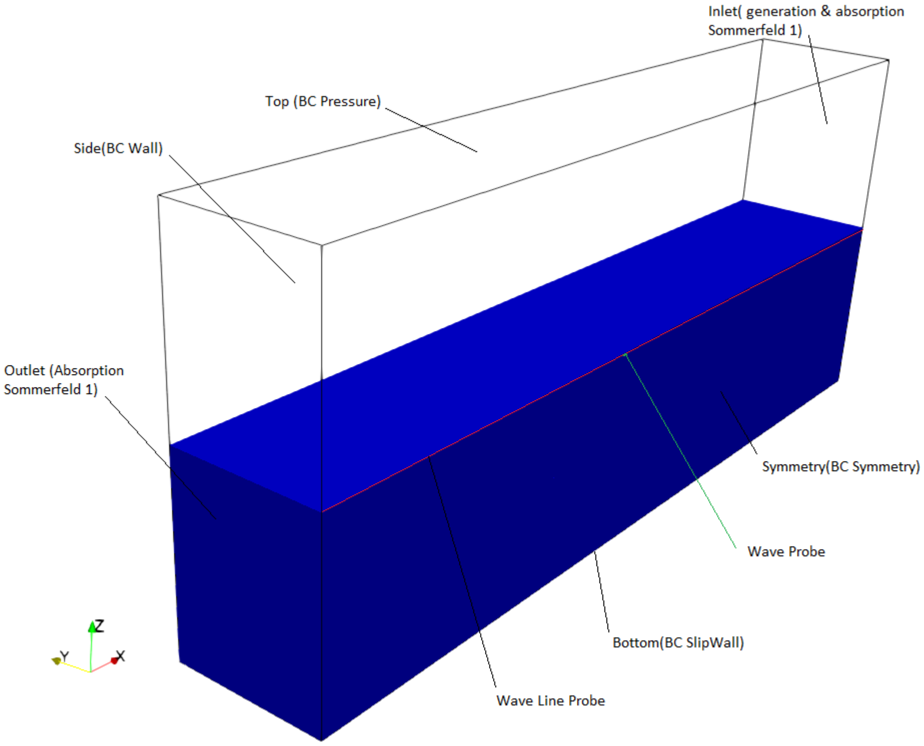

Figure 3.1: Boundary conditions and monitors

The reference system coincides with the wave probe represented by the green dot (located at equal distance between the Inlet & Outlet, at the intersection between the symmetry plane and the free surface); the same reference system will be used in the next chapters. Domain created in this chapter will be the starting point for the future test cases in which the vessel will be included. To correlate CFD results with model tests avoiding errors introduced by scale effects all the simulations were conducted at model scale, then full scale results were extrapolated. As a consequence, the domain should reproduce the SMB of MARIN (Seakeeping and Manoeuvring Basin), unfortunately the latter is too large to be completely modelled with a sufficient accuracy and a reasonable number of cells(140m x 40m x 5m in length, width and depth). Only a smaller area can be reproduced and dimensions have to satisfy the following requirement:

- Provide a domain as similar as possible to the SBM where model tests were carried out.
- Ensure boundaries do not affect the solution in the area around the vessel.
- Reproduce the same dispersion relationship.

Physical wave properties are summarized in table 3.1, refer to the mentioned table unless indicated otherwise. Domain is 7λ long, this is a compromise between cells number and space for waves to propagate before they are absorbed. The domain is 1.5λ high and 1.5λ deep (above and below the free surface) to reproduce the same dispersion relationship encountered in the SMB. For this test case the domain width is not influencing the solution as waves travel parallel to the side boundaries. To lower the cells number the width was set equal to 1.2λ as starting value, however a further investigation on it will be presented in chapter 4 where domain width plays an important role.

Table 3.1: Wave properties

Properties	Model scale	Full scale
wave type	Stokes 2	Stokes 2
H	0.10 m	2.89 m
ω	4.30 $\frac{rad}{s}$	0.80 $\frac{rad}{s}$
T	1.45 s	7.85 s
λ	3.32 m	96.21 m
c	2.27 $\frac{m}{s}$	12.25 $\frac{m}{s}$

In Fig. 3.2 the range of validity for different wave theories according to Le Méhauté [20] is reported. d is the water depth. On the x axis the dispersion relationship is reported. On the left of the axis the waves are in shallow water. Moving to the right the water depth increases. On the right of the plot the waves are in deep water condition. On the y axis the wave steepness is reported. Moving from the bottom to the top of the plot the wave steepness increases. In the present figure the simulated waves are at the intersection of the red lines. To conclude, for this project the Stokes 2nd order is sufficient.

3.1.1. Boundaries

Table 3.2 reports the boundary conditions and their related surfaces. They are reported in fig. 3.1 as well. Although the majority of the boundary conditions do not require a further explanation, few words have to be said about the domain side. For this application four reasonable possibilities are available in ReFRESCO: Pressure, SlipWall, Wall and Absorption. Pressure boundary condition applies a static pressure over the surface however, due to the presence of waves unphysical solutions are generated at the intersection between the free surface and the boundary. Waves absorption works properly only if the incoming waves are perpendicular to the surface. The difference between Wall and SlipWall is in the non slip condition. Applying a Wall condition the non slip condition is satisfied, whereas using the SlipWall the effect of shear stress is zero. The basin walls influence the flow near to them, however their influence is neglected due to the long distance from the vessel. Concluding, the best results have been obtained with a slip wall condition.

3.2. Mesh generation

The software used is Hexpress 4.2 which generates hexahedral unstructured meshes. On one hand structured meshes allow to keep the grid refinement ratio constant and grid properties remain unaffected [12]. Moreover structured meshes avoid scatters during grid refinement and they are more suited for verification purpose. On the other hand, they are more complex than unstructured grid and require more time and effort to be generated. Due to their complexity the application is limited, and they are often disregarded in favor of unstructured meshes. The aim of this project is to show how a CFD software can be applied to industry project

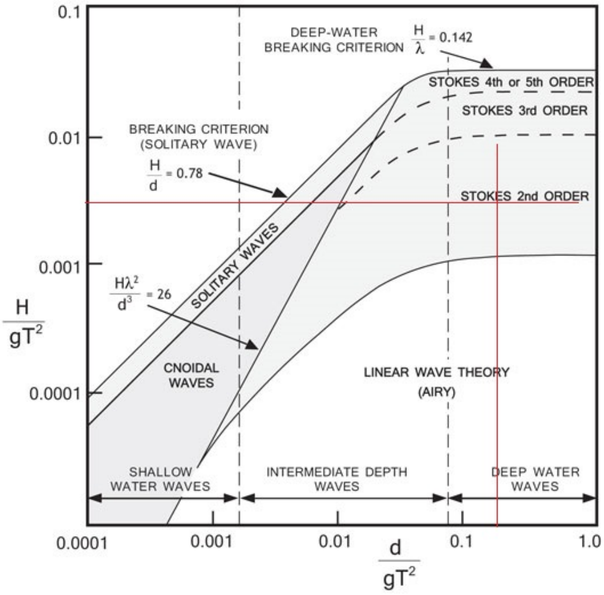

Figure 3.2: Validity of several theories for period water waves, according to Le Méhauté [20]

concerning the moonpool phenomenon, consequently an unstructured grid has been chosen. Mesh quality was established following the guidelines available at MARIN, all the meshes used in this project (not only the grids concerning this chapter) satisfy them. They are here reported, for additional reading refer to [4]:

- Negative cells, concave and twisted cells are not allowed.
- Orthogonality
  1. Range between 0° and 90°. The higher the better.
  2. Minimum $\geq 10°$
  3. Average should be $\geq 75°$
- Skewness
  1. This is indicative of how close to a perfect square the cells are. The range is between 0 and 1, the lower the better.
  2. Average should be ≤ 0.2.
  3. Maximum ≤ 0.9.

To capture the wave height and length with a certain accuracy a box refinement was located around the free surface all over the domain. The box height is equal to 2.5 H above and below the free surface. This dimension was defined investigating its effect on the final solution. With a smaller box the orbital velocities outside the refinement area were not fully captured by a too coarse mesh, resulting in a deformation of the free surface and convergence problem. A larger refinement area led to an increase of cells without any further improvement. In table 3.3 the grids used for the refinement study are described. The medium grid was generated following the settings suggested on the ReFRESCO manual. Then coarse and fine mesh were created multiplying or dividing the numbers of cells of the medium grid by a refinement factor of 1.5 in every direction. In fig A.2 grid pictures are reported.

Table 3.2: Boundary conditions

Surface	Boundary Condition
bottom	Slip wall
symmetry plane	Symmetry
Side	Slip wall
Inlet	Wave generator
Outlet	Wave absorption
Top	Pressure

Table 3.3: Grid refinement for the empty domain case

Mesh	λ	H	Cell number
Coarse	30 cells	7 cells	0.5 M
Medium	45 cells	10 cells	1.2 M
Fine	65 cells	15 cells	4.0 M

3.3. Numerical settings

In the calculations a total of 25T (wave periods) were simulated, including a ramp-up time equal to 1 wave period. The number of wave periods was defined according to results obtained by Leboulleux [21]. In his work after 15T were observed at the middle of the domain steady results. In his work Leboulleux analyzed the wave propagation trough a 2D domain, the low number of cells allowed the author to perform simulations with 40 wave periods. Due to a higher computational time required for 3D problems the simulations stopped at 25^{th} wave period. In this project a steady behaviour was noticed after 15T as explained in section 3.4. All the results are studied between 20 and 25T.

Unsteady computations are carried out solving the momentum, pressure and free surface equations. As initial conditions the free surface is completely flat, current is not included and hydrostatic pressure is initialized as zero at the free surface. A three-level time discretization scheme with fixed time step is used for every simulation. For each time step a convergence criterion was assessed for the steady residuals. Three convergence levels were investigate for this case: $L_2 = 10^{-4}$, 10^{-5} and 10^{-6} with a maximum number of outer-loops equal to 150.

The two discretization schemes used are: QUICK (Quadratic Upwind Interpolation for Convective Kinematics) and REFRICS. QUICK is integrated with a flux limiter. Sharp gradients due to drastic changes in the velocity domain may results in solution oscillations in the interested area, this often has a negative impact on the convergence of the solution [24]. To limit this problem the flux limiter can be introduced which bounds the gradient to realistic values. Discretization schemes will be subject of investigation in section 6.2. A summary of settings used is provided in tables 3.4 and 3.5, refer to the latter for the entire project if not differently stated. No turbulence model is included at this stage of the work, for additional reading about each parameter refer to [2].

Table 3.4: Numerical settings

Parameters	Momentum	Pressure	Free surface
Solver	GMRES	GMRES	GMRES
Pre-conditioner	JACOBI	BJACOBI	BJACOBI
Convergence tolerance	0.01	0.01	0.01
Maximum iterations	200	500	500
Discretization Scheme	QUICK	-	REFRICS
Imp. relaxation Max.	1	-	1
Imp. relaxation Min.	1	-	1
Imp. relaxation Factor	1	-	1
Exp. relaxation	0.3	0.10	0.25

Table 3.5: Boundaries settings

Boundary	Generation	Absorption	VelocityBCAir	absorptionType	relax	extrapolation order
Inlet	True	False	Dirichlet	Sommerfeld 1	0.1	1
Outlet	False	True	Dirichlet	Sommerfeld 1	0.1	1

3.4. Results and discussion

The study includes the effect of time step, mesh and convergence tolerance refinement. Fine mesh requires a more accurate tune of the settings to reach the desired convergence level compared to coarser grids. Moreover the influence of the iterative error compared to the discretization error decreases with coarsening the mesh. As a results a satisfactory steady convergence level for the fine mesh will be accurate enough for the medium and coarse mesh as well. Based on that the refinement study started from the fine mesh then, the number of medium and coarse simulations was optimized. Results from the refinement study are summarized in table 3.6.

Data were extracted analysing the free surface both in time and space. Fig. 3.1 shows the monitors location. A wave probe (represented by the green dot) was placed in the middle of the domain (coordinate x = 0 corresponding to the vessel mid perpendicular) on the symmetry axis to analyse the time trace of wave elevation, a wave line (highlighted by the red line) with coordinate y = 0 (oriented along the wave direction) was used to investigate the free surface shape. Wave line plots were extracted at the last time step. Waves travel from right to the left of presented plots, which is the negative x direction. Amplitude values are presented as the mean ± the RSD (relative standard deviation) as already discussed in chapter 2. The RSD of wave length was not included because λ is constant in time. In this chapter the wave length has been normalised as well. $\bar{\lambda}$ is the wave length divided by the incoming wave length (equal to the value reported in table 3.1). 3D pictures have been post-processed using Paraview 5.3, 2D plots with python scripts developed by the author. The results for the steady convergence tolerance refinement and the time step refinement are presented in Fig. 3.6 and 3.7. The summary of all the results can be found in appendix A.

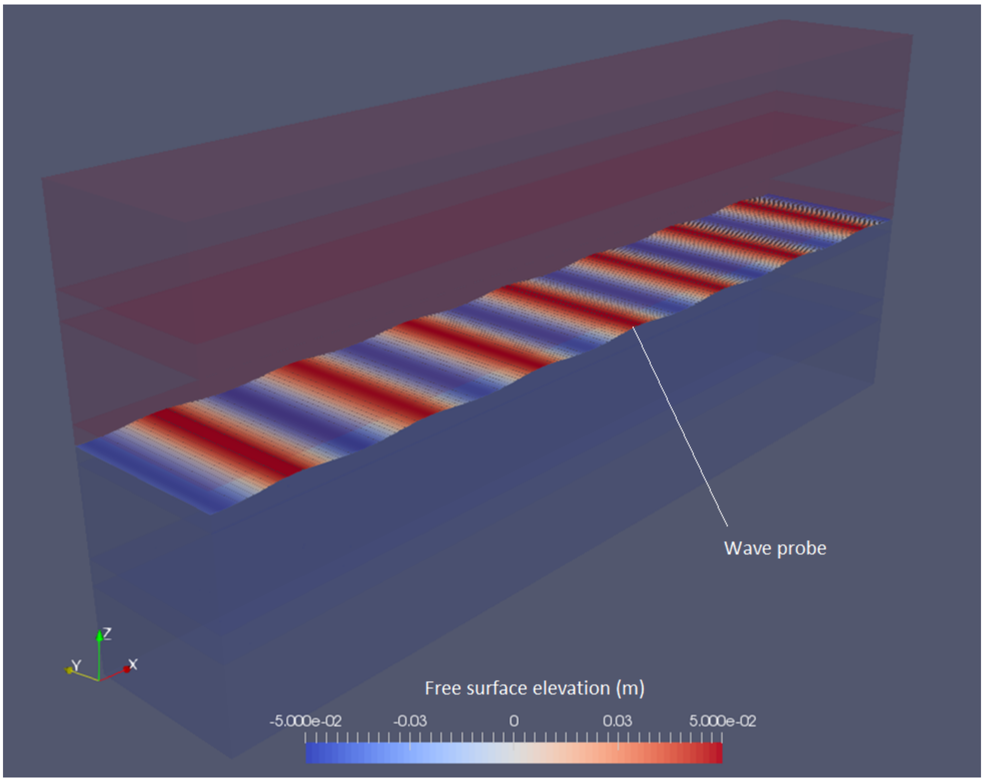

Figure 3.3: 3D wave propagation through the domain for the fine mesh $\frac{T}{800}$ and $L_2 = 10^{-5}$

Fig. 3.3 represents the wave propagation. The domain is divided in two areas. The red area is filled with air, the blue one with water. The free surface elevation is highlighted by the scale color. Waves travel perpendicular to the inlet & outlet and they do not change direction through the domain. The white line displays the wave probe location explained above and already reported in Fig. 3.1. It is here copied for sake of clarity. In Fig. 3.4a the non dimensional time trace of the free surface monitored by the wave probe is reported. The wave periods are reported on the x axis. On the y axis the free surface elevation (normalized by the incoming wave amplitude) is reported. The vertical red line is here introduced to visualize the definition of peak amplitude. In Fig. 3.4b, $\bar{a}_{abs}$ for different wave periods is displayed to show the steadiness of the solution. After a build up period the amplitude shows a steady behaviour after the 15^{th} wave period. As already explained in section 3.3 the data were extracted during the last 5 wave periods.

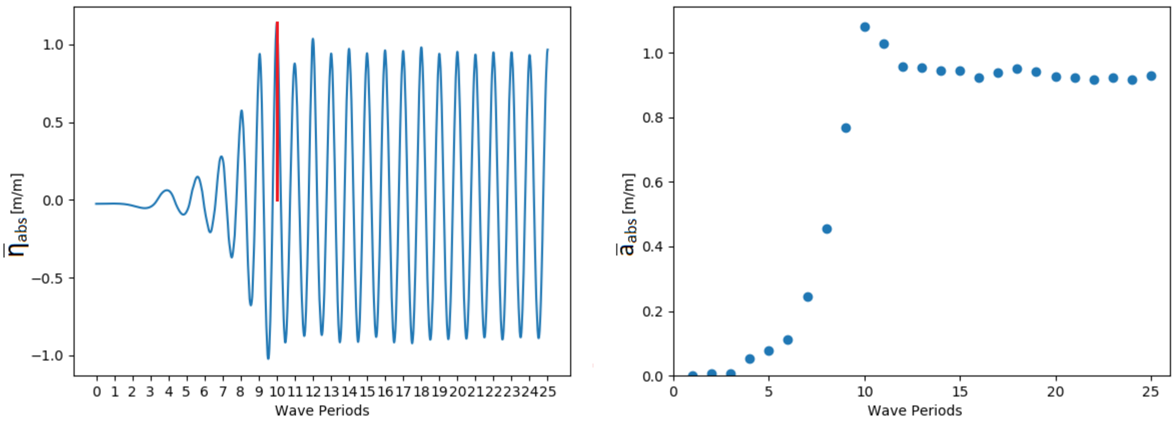

(a) Time trace of the wave elevation in the middle of the domain

(b) Scatter of the wave amplitude in the middle of the domain

Figure 3.4: Time trace of wave elevation and scatter of wave amplitude for the Fine mesh, $\frac{T}{800}$, $L_2 = 10^{-5}$

Simulations with medium and fine mesh and time step $\frac{T}{100}$ have a maximum Courant number higher than 1 (respectively 1.1 and 27.1) resulting in a poor convergence behaviour. They are included in table 3.6 for sake of completeness nevertheless, they were not used in the numerical uncertainty analysis. Fig. 3.5 shows the differences in steady residuals between simulation with a good convergence (Fig. 3.5b) and a poor convergence (Fig. 3.5a). Fig. 3.5b reports a good convergence behaviour because L_2 is for the entire simulation less or equal to the steady convergence tolerance, this is not the case of Fig. 3.5a.

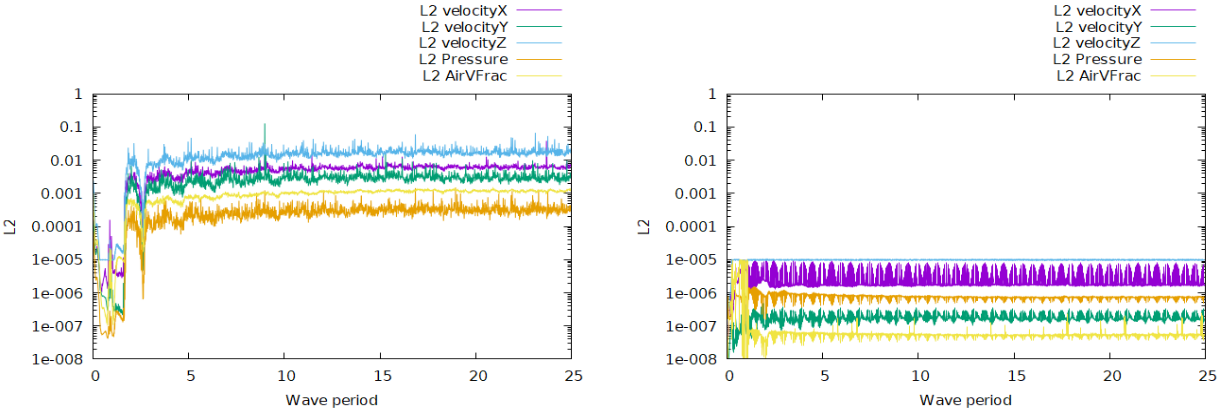

(a) Time step $\frac{T}{100}$

(b) Time step $\frac{T}{800}$

Figure 3.5: Steady Residuals for the fine mesh with steady convergence level $L_2 = 10^{-5}$

Table 3.6: Summary of the wave amplitude and wave length at the center of the domain for different mesh, time step and steady convergence tolerance.

Grid	Timestep	Steady converge tolerance	$\bar{a}_{abs}$ $\frac{m}{m}$	$\bar{\lambda}$ $\frac{m}{m}$
Coarse	$\frac{T}{100}$	10^{-4}	0.8978 ± 0.1 %	0.9878
		10^{-5}		
		10^{-6}		
	$\frac{T}{200}$	10^{-4}	0.9146 ± 0.1 %	0.9898
		10^{-5}		
		10^{-6}		
	$\frac{T}{400}$	10^{-4}	0.9159 ± 0.1 %	0.9897
		10^{-5}		
		10^{-6}		
	$\frac{T}{800}$	10^{-4}	0.9212 ± 0.1 %	0.9888
		10^{-5}		
		10^{-6}		
Medium	$\frac{T}{100}$	10^{-4}	0.9743 ± 0.1 %	1.0052
		10^{-5}		
		10^{-6}		
	$\frac{T}{200}$	10^{-4}	0.9453 ± 0.1 %	0.9951
		10^{-5}		
		10^{-6}		
	$\frac{T}{400}$	10^{-4}	0.9431 ± 0.1 %	0.9952
		10^{-5}		
		10^{-6}		
	$\frac{T}{800}$	10^{-4}	0.9479 ± 0.1 %	0.9986
		10^{-5}		
		10^{-6}		
fine	$\frac{T}{100}$	10^{-4}	0.9258 ± 0.1%	0.9911
		10^{-5}	0.9280 ± 0.2%	0.9907
		10^{-6}	0.9332 ± 0.2%	0.9881
	$\frac{T}{200}$	10^{-4}	0.9625 ± 0.1 %	1.0074
		10^{-5}	0.9670 ± 0.1 %	1.0082
		10^{-6}	0.9674 ± 0.1%	1.0082
	$\frac{T}{400}$	10^{-4}	0.9674 ± 0.1 %	1.0073
		10^{-5}	0.9700 ± 0.1 %	1.0082
		10^{-6}	0.9703 ± 0.1 %	1.0082
	$\frac{T}{800}$	10^{-4}	0.9643 ± 0.1 %	1.0016
		10^{-5}	0.9673 ± 0.1 %	1.0081
		10^{-6}	0.9674 ± 0.1 %	1.0081

3.4.1. Influence of the convergence tolerance

The steady convergence tolerance influences the iterative error, a decrease in the tolerance corresponds to a decrease in the iterative error. The L_2 tolerance has to be selected such as the iterative error is at least two orders of magnitude lower than the discretization error to satisfy the requirement of the method proposed by Eça and Hoekstra [12]. The iterative error can be estimated looking at table 3.6 between two simulations with same settings but difference convergence tolerance. For the fine mesh first simulations involved a high convergence tolerance (10^{-4}), then the latter was gradually reduced till results differences were small enough.

Fig 3.6 shows the wave propagation through the domain in space, the lines represent the free surface for different simulations. On the x axis the longitudinal coordinate is reported, on the y axis the magnitude of the free surface elevation $\bar{\eta}_{abs}$. The grid helps the reader to spot differences between waves. In every plot all the simulations reported have the same mesh and time step refinement, only the steady convergence tolerance is different. Consequently, differences between free surface shapes are due to the iterative error. In Fig. 3.6a all of the three simulations do not display a smooth free surface, this is explained by the high Courant number already discussed. In Fig. 3.6b the results show a smooth free surface for all the convergence tolerance, the low Courant number compared to the previous figure improve the final solution. In Fig. 3.6c the reader can notice how the free surface estimated with $L_2 = 10^{-4}$ and $L_2 = 10^{-6}$ for the fine mesh show larger discrepancies compared with the same convergence tolerances for the medium mesh. This occurs because a smaller time step reduces the discretization error, consequently the contribution of the iterative error increases. Solution with $L_2 = 10^{-5}$ and $L_2 = 10^{-6}$ overlap for the entire domain. To conclude, the convergence tolerance has to be decreased with time step to keep the influence of the iterative error low.

In table 3.6 $\bar{a}_{abs}$ is presented with 4 significant digits. Compare simulations with equal convergence tolerance but different time step or mesh refinement shows the order of magnitude of the discretization error. For example: the discretization error due to time step for the fine mesh affects the second significant digit of $\bar{a}_{abs}$, whereas the influence of the iterative error for a L_2 refinement between 10^{-5} and 10^{-6} affects the fourth digit. Consequently the iterative error is 2 order of magnitude smaller than the discretization error and the method of Eça and Hoekstra [12] can be applied. The same conclusions can be drawn looking at the refinement study for $\bar{\lambda}$. Concluding, to neglect the influence of the iterative error compared to the discretization error $L_2 = 10^{-5}$ is necessary. This threshold has been used to investigate the effect of mesh and time step refinement.

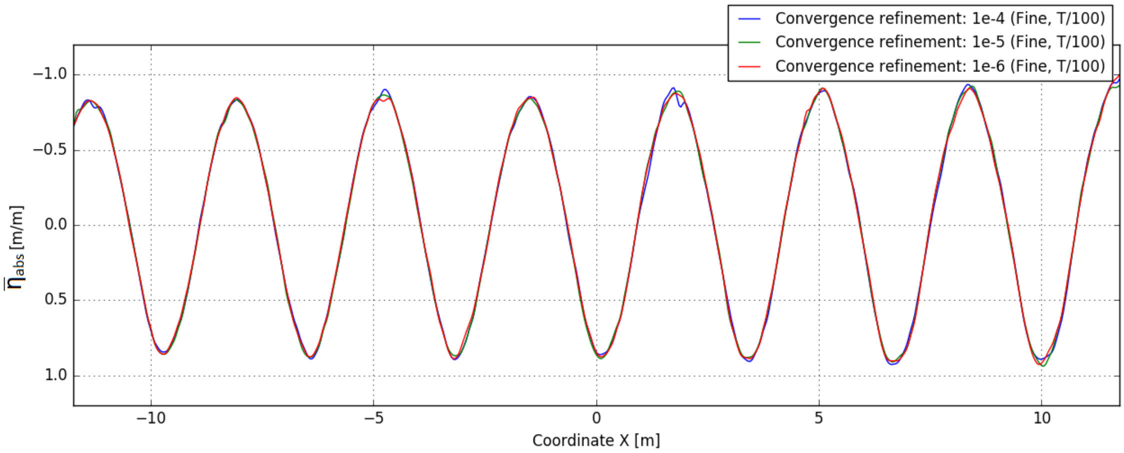

(a) Time step $\frac{T}{100}$

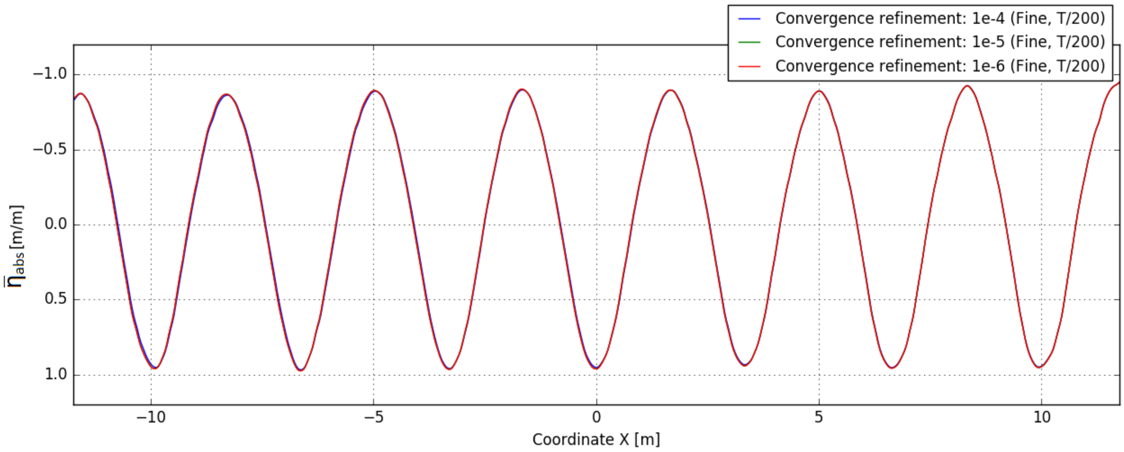

(b) Time step $\frac{T}{200}$

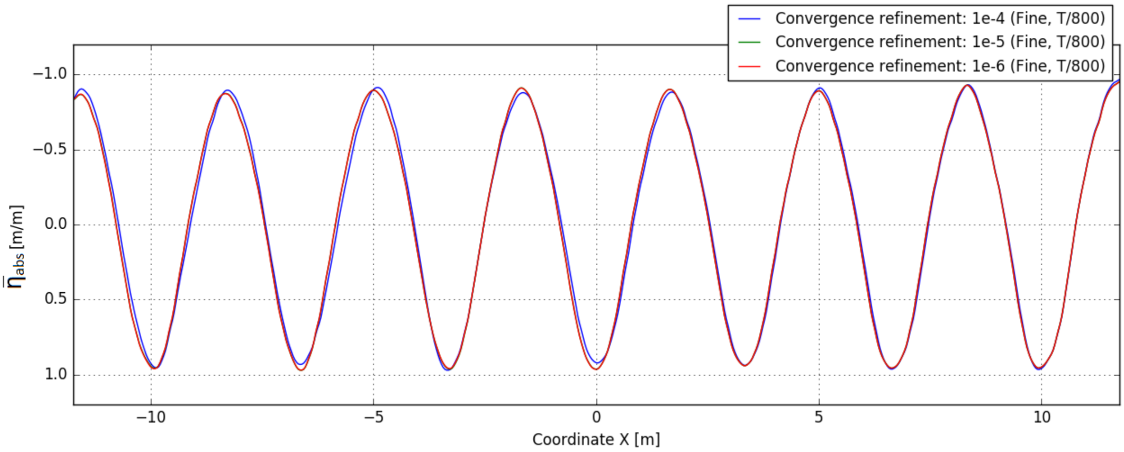

(c) Time step $\frac{T}{800}$

Figure 3.6: Steady convergence refinement for the fine mesh

3.4.2. Influence of Time step & grid refinement

With the same approach as described for Fig. 3.6, the wave propagation through the domain is represented in Fig. 3.7. In every plot results were obtained with the same mesh and L_2, only the time step varies. Consequently differences are produced by the discretization error due to time step. Fig. 3.7a displays the influence of the iterative error on the coarse mesh. Small differences are noticeable between the different time step, however it is clear how the waves decrease their height travelling across the domain. The low number of cells used to discretize the domain for the coarse mesh influences the wave propagation. In Fig. 3.7b the free surface solution estimated with the medium mesh and time step $\frac{T}{400}$ presents larger discrepancies compared to the coarse time step respect to the solution obtained with $\frac{T}{800}$. Different error sources can counteract each other, resulting in a lower error with coarser settings. However, the solution estimated with $\frac{T}{100}$ has already been mentioned for its poor convergence behaviour. As a consequence its validity should be further investigated. In Fig. 3.7c the results for the fine mesh are shown. The solutions overlap for the entire domain except for the coarsest time step. This difference is explained by the high Courant number.

The same conclusions described by Fig. 3.7 can be drawn from table 3.7 as well. Here the effect of the time step refinement is highlighted, the data are now expressed as difference in percentage compared to the finest time step. For example, a obtained with Fine mesh and time step $\frac{T}{400}$ has a difference of 0.30 % compared to a obtained with Fine mesh and time step $\frac{T}{800}$. With this table the differences spotted in the pictures are quantified. Differences in percentage are calculated using:

$$a\% = 100 * \frac{a - a_0}{\frac{a+a_0}{2}} \tag{3.1}$$

Where a is the wave amplitude result of the simulation and a_0 is the solution obtained with finest settings. The data used to create this table are collected in table 3.6. As one can notice the largest differences occur for the coarse mesh (2.57 %) and they gradually decrease reducing the cells size. Interesting to notice how the increase in accuracy obtained by refining the time step is not linear. For time step smaller than $\frac{T}{200}$ the gain in accuracy drastically decreases.

Table 3.7: Comparison between time steps for wave amplitude and length.

Grid	Timestep	a %	λ %
Coarse	$\frac{T}{100}$	2.57	0.10
	$\frac{T}{200}$	0.72	0.10
	$\frac{T}{400}$	0.58	0.09
	$\frac{T}{800}$	0.00	0.00
Medium	$\frac{T}{100}$		
	$\frac{T}{200}$	0.28	0.09
	$\frac{T}{400}$	0.51	0.08
	$\frac{T}{800}$	0.00	0.00
Fine	$\frac{T}{100}$		
	$\frac{T}{200}$	0.03	0.01
	$\frac{T}{400}$	0.30	0.01
	$\frac{T}{800}$	0.00	0.00

Table 3.8: Comparison between mesh size for wave amplitude and length.

Timestep	Grid	a %	λ %
$\frac{T}{200}$	Coarse	5.61	1.84
	Medium	2.30	1.31
	Fine	0.00	0.00
$\frac{T}{400}$	Coarse	5.76	1.85
	Medium	2.84	1.30
	Fine	0.00	0.00
$\frac{T}{800}$	Coarse	4.89	1.93
	Medium	2.03	1.30
	Fine	0.00	0.00

A similar approach is used to summarize the influence of the mesh refinement in table 3.8. Larger differences exist in the mesh refinement compared to time step. This is highlighted by table 3.8 where differences up to 5.76 % occur due to mesh refining. The results can be visualized in fig. A.6, here the different simulations are clearly noticeable and they do not overlap any more. Concluding, the empty domain case is more sensitive to mesh refinement than time step.

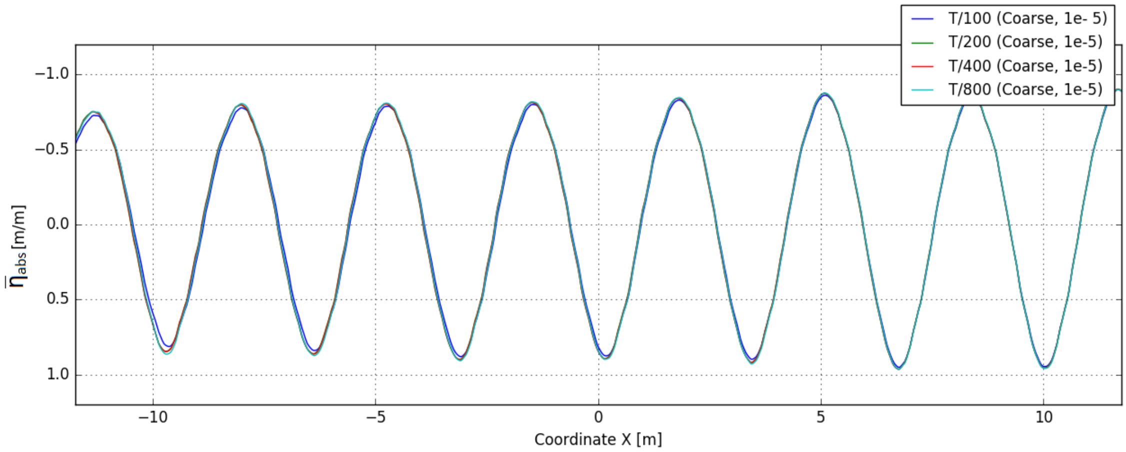

(a) Coarse mesh

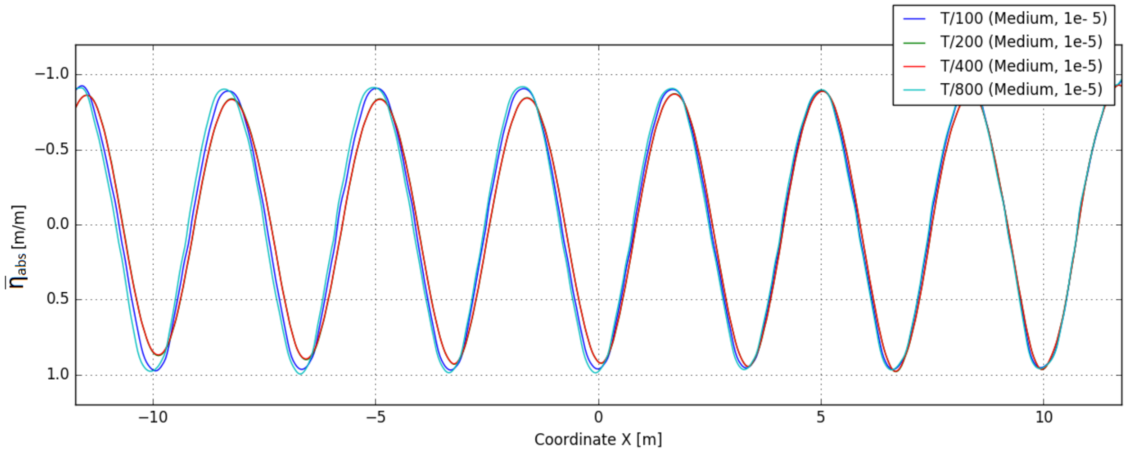

(b) Medium mesh

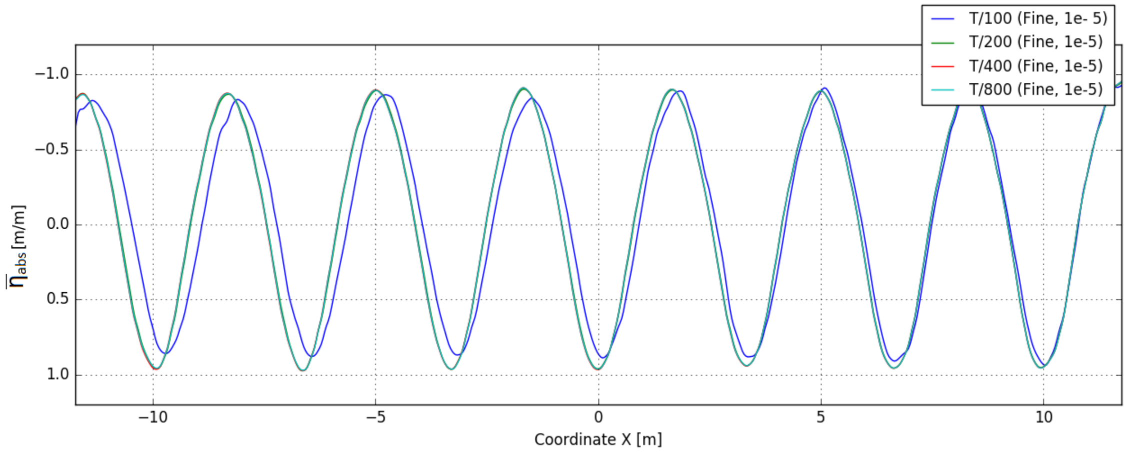

(c) Fine mesh

Figure 3.7: Time step refinement with steady convergence tolerance $L_2 = 10^{-6}$

3.5. Numerical uncertainty

At MARIN a script to evaluate the numerical uncertainty is available. The script applies the theory described by Eça and Hoekstra [12]. The code takes as input two files. One input file where the settings for the analysis are defined and a txt file where the simulation results are collected. Every line in the txt file is one simulation. the file is organized in columns: the first one represents the mesh used (expressed as number of cells), the second one the time step and then one column per data analyzed (in this case two columns, one for $\bar{\eta}_{abs}$ and one for $\bar{\lambda}$). The output are: one table where the numerical uncertainty is shown (table 3.9 for this chapter) and pictures of the surface used to fit the data. for additional reading on the script and how to use it refer to [3] (note the manual is an internal document at MARIN, its importance is limited to the practical application of the script, for the theory involved refer to the already mentioned Eça and Hoekstra [12]).

Table 3.9: Results of the uncertainty analysis for the empty domain.

Item	ϕ_0	ϕ_1	U_ϕ
$\bar{a}_{abs}$	$1.02 \times 10^{+0}$	9.67×10^{-1}	7.4%
$\bar{\lambda}$	$1.01 \times 10^{+0}$	$1.01 \times 10^{+0}$	2.1%

Results for the numerical uncertainty are collected in table 3.9. ϕ_0 is the estimation of the exact solution of the mathematical model, ϕ_1 is the solution obtained with the finest settings and U_ϕ is the numerical uncertainty. The numerical uncertainty expresses a range around ϕ_1 in which the exact solution can be found with 95% of probability. Be aware, this is not a measure of the difference between ϕ_0 and ϕ_1. The uncertainty for the wave length is lower than wave elevation.

The results are plotted in 3.8. The red dots represents the data used to fit the surface, due to the opacity of the surface some of them are not visible. The green line is the numerical uncertainty bar for the simulation with finest settings (ϕ_1). The x axis represents the mesh refinement, the y axis the time step refinement and the vertical axis the data value. The mesh and time step refinement are expressed as the ratio over the finest value, i.e $\frac{t_i}{t_1} = 2$ means the time step used is 2 times larger than the finest one ($t_1 = \frac{T}{800}$ for this case). In order to get the surface curvature at least 3 points are necessary along each axis. This is achieved using 3 meshes and 3 time step refinement ($\frac{T}{100}$ was used only for the coarse mesh). ϕ_0 is estimated by the intersection of the fitted surface with the vertical axis ($\frac{t_i}{t_1}$ and $\frac{h_i}{h_1} = 0$). Thanks to the lack of points for $\frac{t_i}{t_1} = 8$, in that area the surface curvature is not reliable, however as mentioned above the interest is focused at the intersection of the plot with the vertical axis.

Fig. 3.8a shows the fitting surface for the wave elevation. Unfortunately the results are not in the asymptotic range [12] and a fourth mesh should be investigate to decrease the numerical uncertainty. However for practical reason a very fine mesh was not tested. Same conclusions can be drawn from fig. 3.8b, however for the wave length an asymptotic trend is visible. The higher sensitivity to mesh than time step refinement is also visible in the steeper slope along the x axis (mesh refinement axis) than y axis.

The uncertainty of wave length influences the phase speed. As explained in chapter 2, a wave reaching the absorption boundary with a different phase speed respect to the theoretical phase speed defined in the control file will be partially reflected. According to the theory behind Sommerfeld 1 the reflection factor can be computed as :

$$R = \left| \frac{c - c_c}{c + c_c} \right| = 0.2\% \tag{3.2}$$

Where c is the theoretical phase speed defined in the ReFRESCO controls file, c_c is the monitored phase speed in the domain. Monitored phase velocity is extracted from λ using dispersion relationship in deep water (here λ is the ϕ_1 solution). R matches the order of magnitude of the RSD (be aware that the RSD is not a direct measure of the reflection), leading to the conclusion that the statistical uncertainty is dominated by reflected waves produced by a phase difference between the expected and the computed waves.

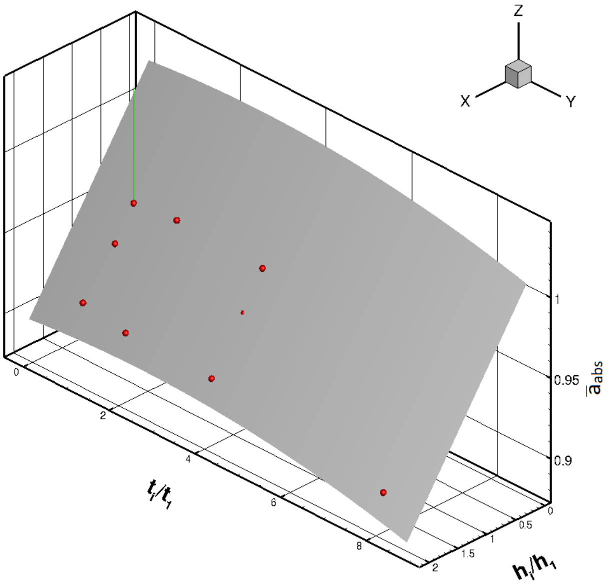

(a) Numerical uncertainty for $\bar{a}_{abs}$

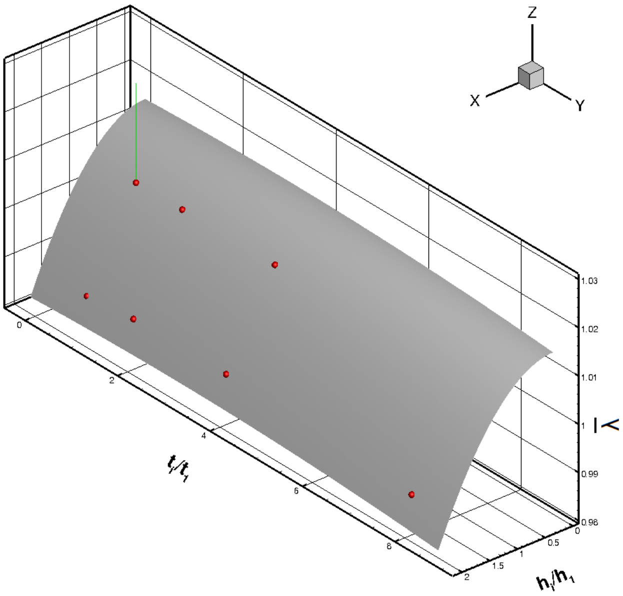

(b) Numerical uncertainty for $\bar{\lambda}$

Figure 3.8: Numerical uncertainty for the empty domain case

3.6. Conclusion

Simulations involving gravity waves should first ensure that propagation is correctly captured [13]. In this chapter the accuracy of ReFRESCO to simulate wave propagation was established. The accuracy was assessed performing a solution verification. Refinement study showed how the empty domain case is sensitive to discretization and iterative error. To assess the numerical uncertainty the iterative error should be two orders of magnitude smaller than the discretization error. This is achieved with L_2 at least = 10^{-5}. Three meshes (respectively called coarse, medium and fine) and four time steps ($\frac{T}{100}$, $\frac{T}{200}$, $\frac{T}{400}$ and $\frac{T}{800}$) have been used to define the numerical uncertainty. The uncertainty analysis shows how the empty domain case is more sensitive to mesh refinement than time step refinement. Simulations involving medium and fine mesh with time step $\frac{T}{100}$ did not reach the desired steady convergence tolerance due to the high Courant number (respectively 1.1 and 27.1). As a consequence, the choice of the mesh must be combined with an appropriate time step. To conclude, here below the suggested settings are reported. They provide results within 1 % of difference compared to the finest settings used in this project.

- 65 cells $\frac{cells}{\lambda}$
- 15 cells $\frac{cells}{H}$
- time step $\frac{T}{200}$

The numerical uncertainty with the settings suggested above is reported in table 3.10.

Table 3.10: Results of the uncertainty analysis for the recommended settings.

Item	ϕ_0	ϕ_1	U_ϕ
$\bar{a}_{abs}$	$1.02 \times 10^{+0}$	9.67×10^{-1}	7.4%
$\bar{\lambda}$	$1.01 \times 10^{+0}$	$1.01 \times 10^{+0}$	2.0%

3.7. Note on the software

In this section notes related to troubles encountered during the work on the empty domain case are reported. They are mentioned as help for the future users of ReFRESCO 2.3.0.

- In ReFRESCO 2.3.0 due to a bug in the software simulations crash if the implicit Euler solution scheme is used for unsteady calculations. ReFRESCO stops immediately, before the simulation starts. Instead of it the more accurate Implicit three time level has to be used.
- The time discretization is implicitly implemented in ReFRESCO and this makes it less sensitive to the Courant Number. Theoretically ReFRESCO is able to handle simulations with Courant Number up to 10, however good residual convergence is achieved only for a time step equal to $\frac{T}{100}$ or lower, resulting in a Courant Number lower than 1.
- For the coarse mesh the relaxation factor of pressure has to be decreased with time step to avoid divergence. For $\frac{T}{400}$ the relaxation factor is 0.1 and for $\frac{T}{800}$ is 0.05.

4

Fixed vessel

The next step of the project was to include the vessel in the domain. In this chapter the vessel motion is neglected. This chapter has 3 objectives. Define the correct settings to generate an accurate mesh. Find the best compromise between domain dimensions and absorption capacity. Assess the numerical uncertainty of wave amplitude inside the moonpool and forces acting on the hull. The chapter is organized as follow. At first a description of the domain and the physical problem involved are presented. Then mesh settings and properties are described. Section 4.3 deals with physical quantities and their related monitors are presented. Results from the simulation conducted using the settings and domain dimensions defined in chapter 3 are reported (case A). The latter were used as a starting point to study the influence of two different absorption methods. For both cases a study was conducted to find the best configuration in terms of domain size, i.e. compromise between influence of the boundaries and number of cells. The simulation time was increased from 25 wave periods to 30 to ensure the free surface inside the moonpool to be fully excited by the external wave frequency. Results for the described cases are presented in Fig. 4.8 to 4.23. The summary of all pictures and plots is collected in appendix B.

For the present project a generic drillship model was used. The moonpool has a rectangular shape with sharp edges and without damping devices. The scale of the model is 28.926. A picture of the drillship model is reported in Fig. 4.1. Main particular of the vessel are in table 4.1.

Figure 4.1: Drillship model. Picture extracted from Abeil [6]

Table 4.1: Main particulars

	Model scale	Full scale
L_{pp}	6.91 m	200.00 m
B_w	1.24 m	35.87 m
T_a	8.97 m	0.31 m
T_f	8.97 m	0.31 m
∇	2.16 m^3	52216.2 m^3

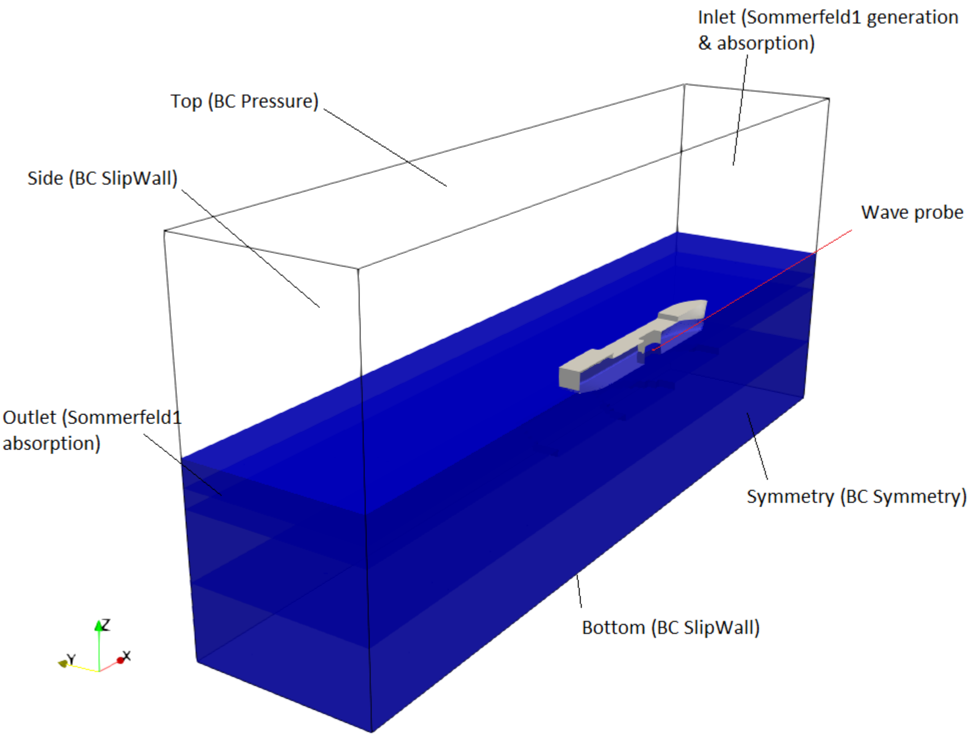

Figure 4.2: Fixed vessel domain and boundary conditions

4.1. Domain description

The domain investigated in this chapter is represented in Fig. 4.2. The depth and the height are 1.5 λ each, they have already been discussed in section 3.1 and they were not changed; the length and the width will be subject to investigation to reduce the influence of boundaries on the solution. The reference system and incoming wave directions did not change compare to the previous case. Model test used as reference for this project are reported in Abeil [6]. The wave properties are summarized in table 3.1, at this frequency according to the results of Abeil [6] the water columns inside the moonpool is expected to be dominated by the piston mode. The total exciting force experienced by the vessel is:

$$F_{tot} = \rho g \nabla + F_{fk} + F_d + F_r \tag{4.1}$$

$\rho g \nabla$ is the hydrostatic force, F_{fk} the Froude-Krilov force, F_d the diffraction force and F_r the radiation force. In this chapter the ship motion is neglected and the response of the water motion is function only of the incoming and diffracted wave. Due to the negligence of the vessel motions the radiation force is not included in the total force. The total force experienced by the vessel will be:

$$F_{tot} = \rho g \nabla + F_w + F_d \tag{4.2}$$

4.2. Mesh generation

The medium mesh of chapter 3 was used as starting point for the mesh generation in the fixed vessel case. Two box refinements were added, represented in Fig. 4.3a and 4.3b. The vessel box refinement was intended to define the ship surface with an higher accuracy, while a volume refinement inside the moonpool was used to better capture the water motion. All the simulation from Case A to Case G used this box combination, the mesh settings are reported in table 4.2. Once the numerical settings were established, a mesh refinement study was conducted refining by a factor of 1.5 the mesh in all directions, results are discussed in section 4.12. Unexpected results arose from the refinement study which led to a redefinition of the mesh settings. The new settings, defined in table 4.3 were used for the estimation of the numerical uncertainty, the reason why the new settings were investigated and why they provide better results are explained in section 4.12.

The new settings used for the refinement study were generated using the method proposed by Rapuc [27]. In his work he provides guidelines about box refinement dimensions and number of cells to accurately model simulations involving waves. The vessel box refinement was enlarged to include the whole inner ellipse and the depth was increase to $\frac{1}{2}\lambda$. The aim of this new box refinement is to correctly capture the diffracted waves around the ship. The vessel box is 2.5 H above the water to match the free surface refinement and reduce the hanging nodes. The hanging nodes occur when a cell is split in half but its neighbour is not (this occur for example at the boundaries of a refinement box), the result is a grid node which sit in the middle of a cell face. High residuals are usually produced by hanging nodes. Outside the inner ellipse the free surface is forced to an analytical solution by the relaxation zone, therefore less cells are necessary. Free surface and vessel boxes have the same refinement over the z direction; hanging nodes at the free surface produce undesired numerical waves. In Fig. 4.3c the new box refinement is displayed. A surface refinement of the vessel was added to have a proper definition of the hull form.

Table 4.2: Cells distribution for Case A to Case G

Box refinement	cells number x/y direction	z direction
Free surface	$45\ \frac{cells}{\lambda}$	$10\frac{cells}{H}$
Vessel box	$60\ \frac{cells}{B_v}$	$60\ \frac{cells}{B_v}$
Moonpool box	$60\ \frac{cells}{B_v}$	$60\ \frac{cells}{B_v}$

Table 4.3: Cells distribution for the uncertainty analysis

	Coarse	Medium	Fine
Free surface	$20\ \frac{cells}{\lambda}$	$30\ \frac{cells}{\lambda}$	$45\ \frac{cells}{\lambda}$
	$5\ \frac{cells}{H}$	$8\ \frac{cells}{H}$	$12\ \frac{cells}{H}$
Vessel surface	$40\ \frac{cells}{B_v}$	$60\ \frac{cells}{B_v}$	$90\ \frac{cells}{B_v}$
Vessel & moonpool box	$20\ \frac{cells}{\lambda}$	$30\ \frac{cells}{\lambda}$	$45\ \frac{cells}{\lambda}$
	$5\ \frac{cells}{H}$	$8\ \frac{cells}{H}$	$12\ \frac{cells}{H}$

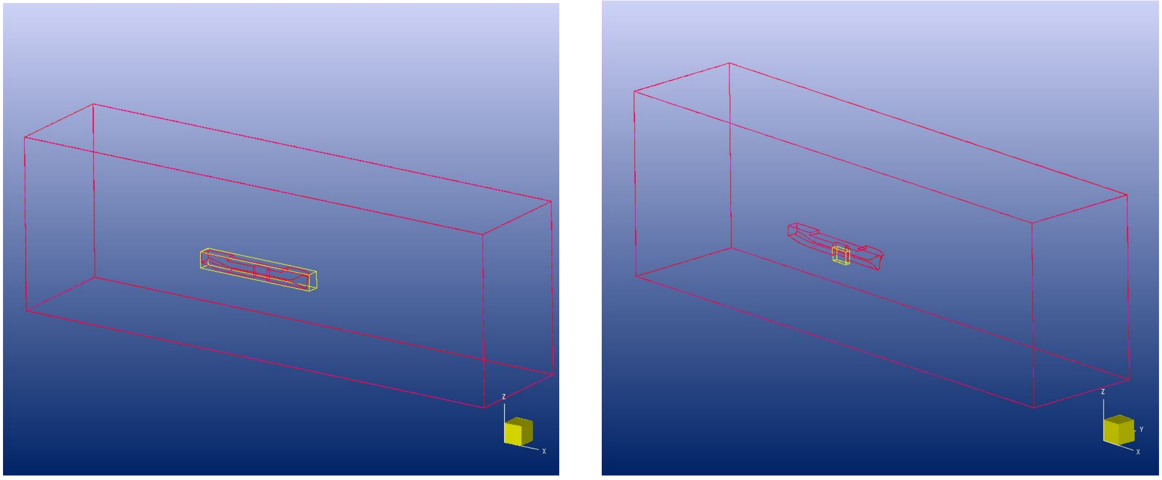

(a) First vessel box refinement

(b) Moonpool refinement

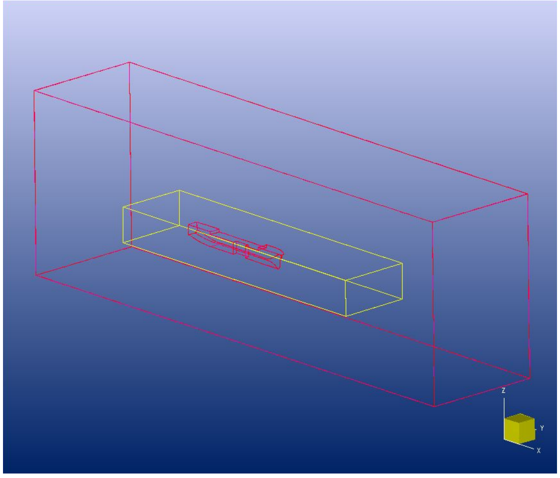

(c) Final box refinement

Figure 4.3: Box refinements

4.3. Monitors

Inside the moonpool 6 waves probes were located in accordance with settings used by Abeil [6]. In Fig. 4.4 probes distribution and distances in the moonpool are represented both for model and full scale, each probe is characterized by a name. In the following simulations only half of the vessel is modelled reducing the number of wave probes from 9 to 6. In this chapter $\bar{a}_{abs}$ and $\bar{\eta}_{abs}$ are computed. They are respectively the absolute wave amplitude and the absolute free surface elevation. For additional explanation on the notation refer to section 2.4.

In each calculation forces acting on the hull were monitored. It is noted that the effect of the hydrostatic pressure is included in the monitor. This is the reason why vertical force acting on the hull is not zero when the simulation is initialized, it includes the buoyancy force. Time trace of the forces are reported together with scatter plots. The scatter plots display the height of the force over one period. In Fig. 4.5a an example of the time trace for the force is reported. The horizontal axis represents the wave periods, the vertical axis reports the force expressed in Newton. The vertical red line is introduced to visualize the height of the force over one period. The height of the force per wave period is reported in Fig. 4.5b. In this project the attention is more focused on the steadiness of the forces than their physical meaning. The mentioned representation of the data was chosen to highlight differences between wave periods.

Data extracted from monitors were post-processed using python script developed by the author. The script results are: time trace and scatter diagram of wave elevation and forces. Attention is focused over the last 10 wave periods were the differences in amplitude were assessed to determine the steadiness of the

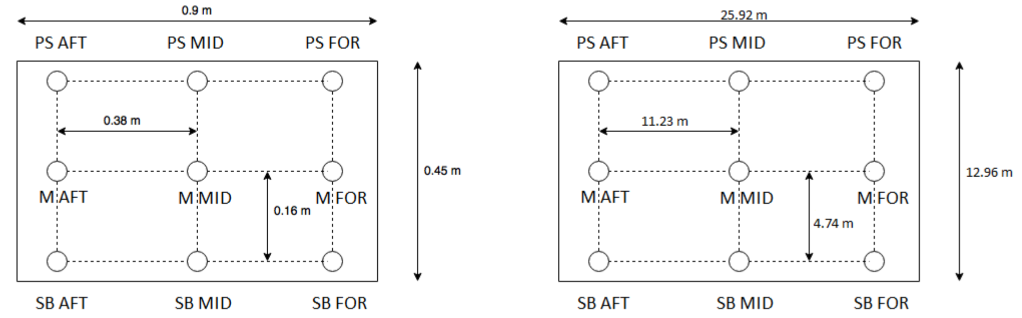

(a) Model scale (b) Full scale

Figure 4.4: Wave probes location

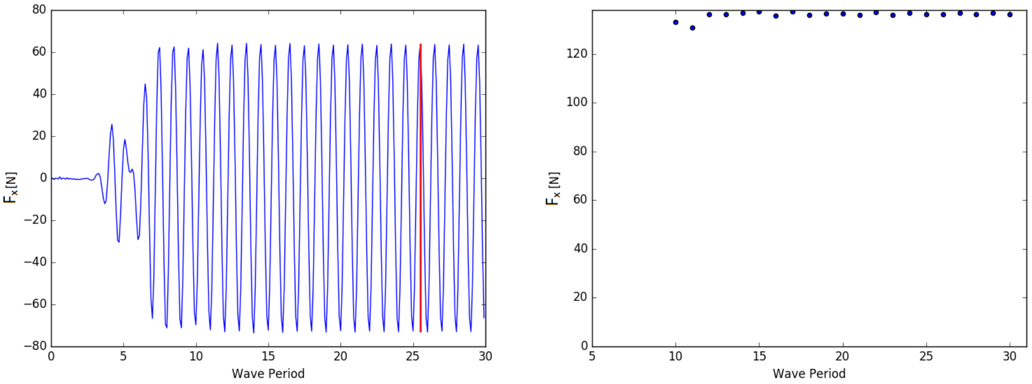

(a) Force time trace (b) Force scatter plot

Figure 4.5: Example of time trace and scatter plot of force

solution. The first 10 wave periods are disregarded from the scatter diagrams. All the monitored quantities are expressed as the mean value for the last 10 wave periods ± the relative standard deviation. During model tests accuracy in the order of 2% is usually accepted, the same value will be used for this project. If not different specified $\bar{\eta}_{abs}$ and $\bar{a}_{abs}$ refer to the wave amplitude monitored at M MID.

4.4. Case A

In case A the same settings as applied to the empty domain were used, simulation details are available in appendix B.1. In Fig. 4.6 the domain dimensions for the present case are reported for sake of clarity.

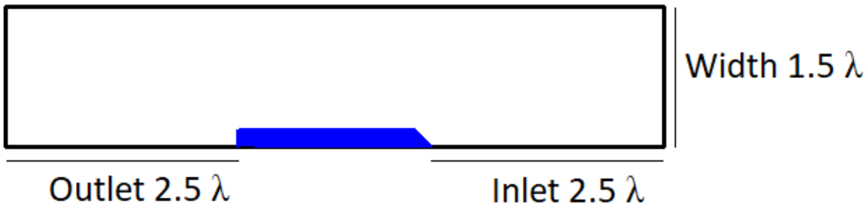

Figure 4.6: Domain case A

In Fig. 4.7a $\bar{\eta}_{abs}$ is reported. From 0 to 4 wave periods waves travel from the inlet to the central probe, the water inside the moonpool remains calm. Between 5 and 15 wave periods the water motion inside the moonpool builds up. In Fig 4.7b $\bar{a}_{abs}$ for the last 20 wave periods is displayed. The result is $\bar{a}_{abs} = 1.91\ \frac{m}{m} \pm 1.9\%$.

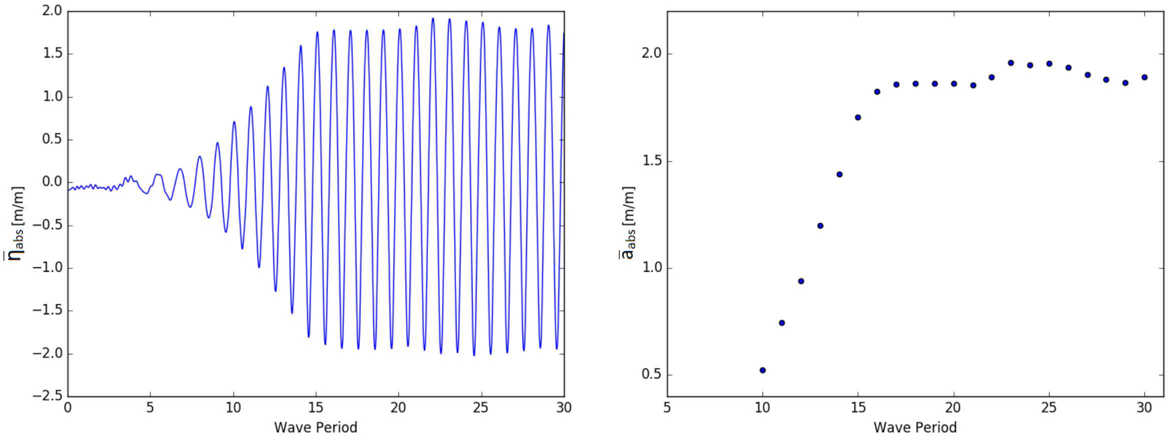

(a) Time trace wave elevation (b) Wave amplitude

Figure 4.7: Absolute free surface and wave amplitude at the middle of the domain for case A.

F_x and F_z are the forces acting on the hull along the x and z axis (respectively the longitudinal and the vertical axis). Force monitors record the waves influence on the hull from the 3^{rd} wave period. F_x is equal to 139 N ± 7.4%. Larger oscillations are noticeable for F_z which oscillates between 463 and 323 N, which correspond F_z = 378 N ± 13.9%, they are highlighted by Fig. 4.8.

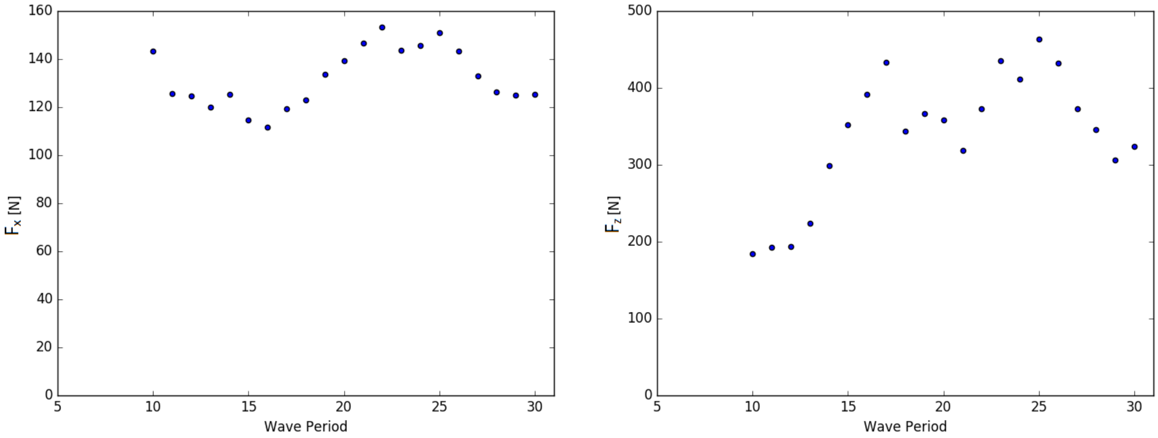

(a) Scatter plot of F_x

(b) Scatter plot of F_z

Figure 4.8: Case A

Although monitors provide an overview of results they do not display what physically happens inside the domain and why oscillations between wave periods occur. Additional informations come from the wave pattern and pressure distribution. For sake of brevity in Fig. 4.9a and 4.9b η_{abs} for the 27^{th} and 30^{th} wave period are displayed. In fig. B.5 wave patterns for the last 4 wave periods are shown. Colors and isolines report the free surface elevation in the domain. White areas display values out of range. Data refer to model scale results. In a perfectly steady solution there would be no differences between pictures since they represent the same moment at each wave period. Therefore differences help to visualize where discrepancies are. In Fig. 4.9b and 4.9d differences are highlighted by red circles to help the reader to visualize them. Discrepancies are noticeable at different areas of the domain: along the the side, at the wave crest reaching the bow, and at the first wave through from the inlet. Variations near the domain edges suggest a poor capacity to absorb waves by boundaries. A further aid in analyze the physics involved comes from the pressure distribution over the hull. In fig. 4.9c and 4.9d the pressure distribution over the bottom is shown. In these pictures the largest differences are noticeable at the high pressure areas at the ship stern and at the isobars around the moonpool.

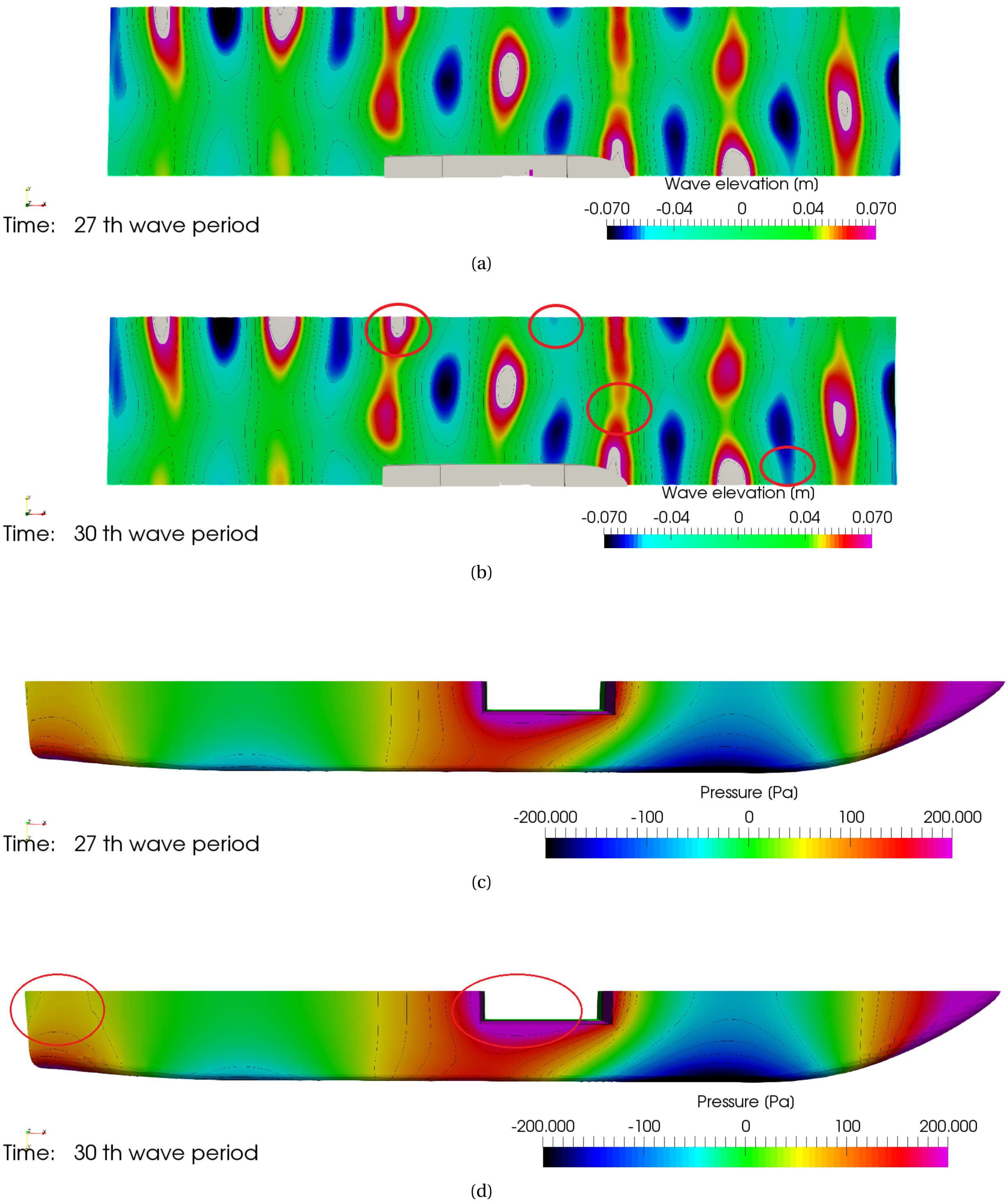

Figure 4.9: Free surface elevation and pressure distribution along the bottom for case A

4.5. Case B

Case A showed a non steady behaviour. Nevertheless the statistical uncertainty can have two different sources. It can be physical or numerical. Results of Abeil [6] showed the presence of a second harmonic in the wave elevation inside the moonpool for the tested frequency. The non harmonic free surface motion could also explain the pressure fluctuations around the moonpool observed in Fig. D.3. Moreover the influence of the discretization error is still unknown and it could also influence the final results. In order to better understand the causes the following cases aim evaluate the influence of boundaries on the statistical uncertainty.

To investigate the boundaries influence the domain was enlarged to move them farther from the vessel. The consequence is a domain two times longer and larger compared to case A. With a larger domain the reflected waves take longer to hit the vessel, in addition a less disturbed wave pattern reaches the outlet increasing the percentage of absorption. Any discrepancy between case A and B will be produced by boundaries. Domain B is reported in Fig. 4.10.

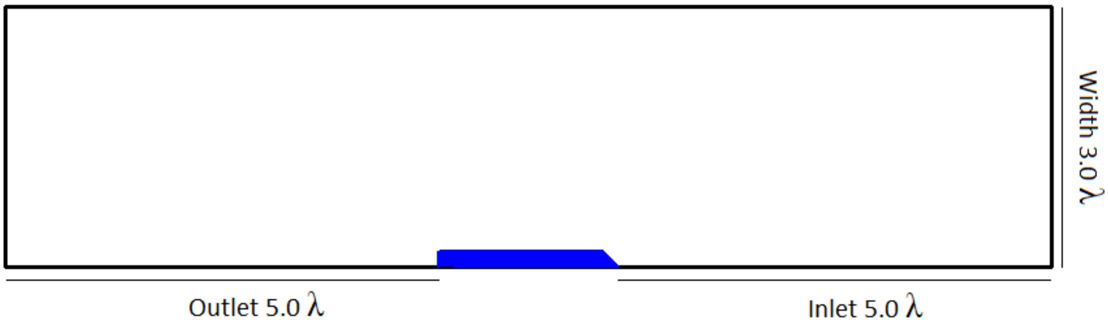

Figure 4.10: Domain case B

Noticeable differences between case A and case B are visible. After the 20^{th} wave period $\bar{a}_{abs}$ starts oscillating around 1.44 $\frac{m}{m}$ ± 1.2%. The domain extension influence forces as well: F_x = 156 N ± 4.8%, F_z still shows the largest oscillations, varying between 500 and 380 N, which correspond F_z = 454 N ± 7.3%.

Comparing Fig. 4.11a with Fig. 4.11b one can notice how the wave elevation around the vessel decreases increasing the domain size. The shadow area behind the vessel is better defined and the wave propagation is more clear. The iso-lines near the Inlet & outlet tend to be parallel to the boundary which means an improved absorption capacity. However in Fig. 4.11a η_{abs} increases behind the vessel and near the domain side (represented by the white areas), this phenomenon suggests the presence of a reflected waves travelling back in the domain. In Fig. 4.11c and 4.11d the new pressure distribution is represented, be aware: both figures represent the pressure distribution for case B, the only difference is the wave period. The reduction in wave elevation around the vessel and inside the moonpool influence the pressure distribution which decreases the magnitude. Differences between wave periods are not as clear as in case A, however they are visible looking at the isobars of the low pressure region at the vessel stern.

Concluding case B displays lower variations between wave periods compared to case A. This means boundaries decreases their influence on the results increasing the domain size, which is reflected by a lower RSD. Despite the lower statistical uncertainty the higher waves behind the vessel suggest a reflected wave and consequently still a poor absorption capacity of the boundaries. Although case B displays a more steady solution, the high number of cells led to a long computation making infeasible a future refinement study necessary to assess the numerical uncertainty. Moreover larger domains should be simulated to prove that the boundaries influence is now a minor component of the solution. Instead of further increase the domain a different absorption method was investigated. First results are presented in section 4.6. Case C and D reports results from intermediate domains between case A and B.

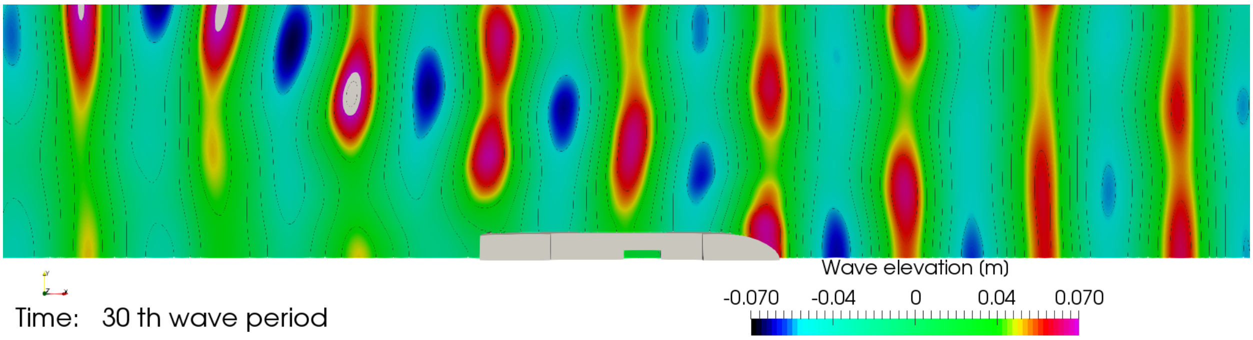

(a) Free surface elevation for Case B

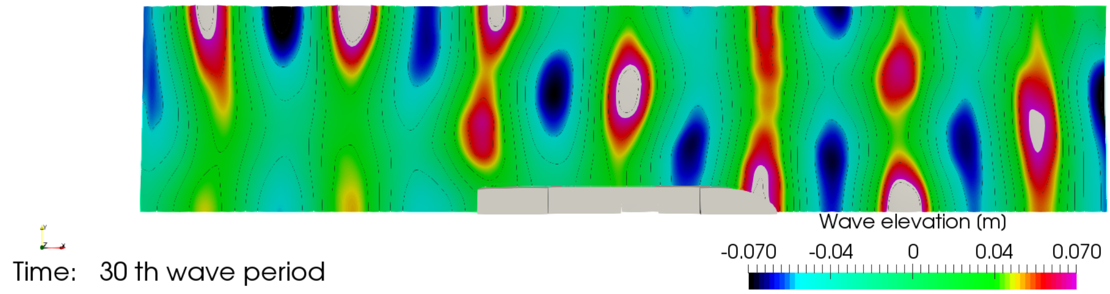

(b) Free surface elevation for Case A

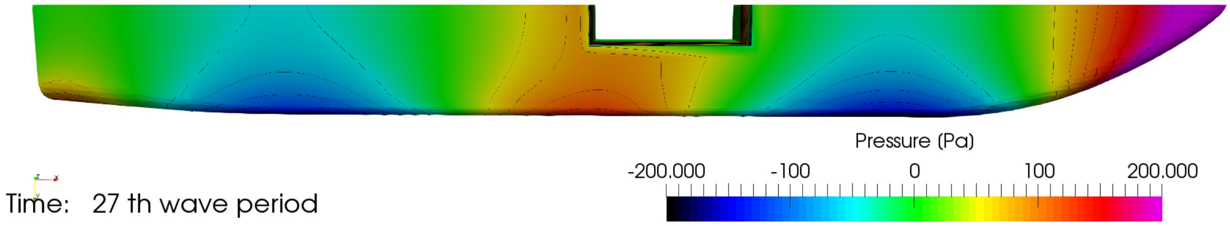

(c)

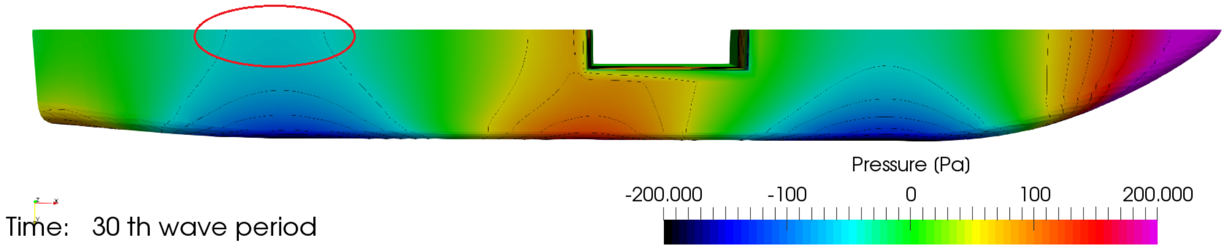

(d)

Figure 4.11: Comparison of free surface elevation between case A and B. Pressure distribution along the bottom for case B.

4.6. Case E

In case E a relaxation zone is included to improve the absorption capacity. The domain has the same dimensions of case D (summarized in appendix B.4), the only difference is the presence of the relaxation zone. Domain is displayed in Fig. 4.12.

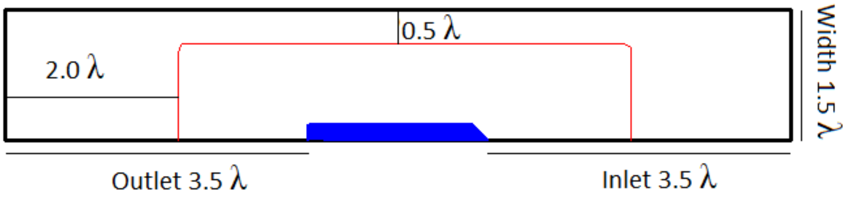

Figure 4.12: Domain case E

With this method waves reaching the domain edges should be fully absorbed irrespective of their frequency or direction, however as explained in chapter 2 a poor setting of relaxation zone could result in converge problems or numerical waves. As starting point guidelines suggested by Denisart [11] were used.

In fig. 4.13 one can observe how the relaxation zone provides interesting results (for a definition of the quantities plot in Fig. 4.13 refer to subsection 2.4 and section 4.3):

- $\bar{a}_{abs} = 1.44\ \frac{m}{m} \pm 0.5\%$
- $F_x = 136$ N ± 0.3%
- $F_z = 312$ N ± 0.3%

Despite the smaller domain, wave amplitude has the same value to case B but with even smaller RSD. Even the forces which showed the largest statistical uncertainty in the previous cases now display a steady behaviour. The relaxation zone has a better capacity to absorb waves, despite the smaller statistical uncertainty the influence of each parameter in the relaxation setting is not clear yet. The following cases have the aim to find the best compromise between domain size, convergence and solution steadiness. Only one parameter per simulation is changed till differences between solutions become negligible. This study was carried out looking at relaxation factor and relaxation length for every boundary. For sake of brevity only two limit cases are discussed below: relaxation zone applied only at Inlet & Outlet and only applied along the side. All the other simulations are then summarized.

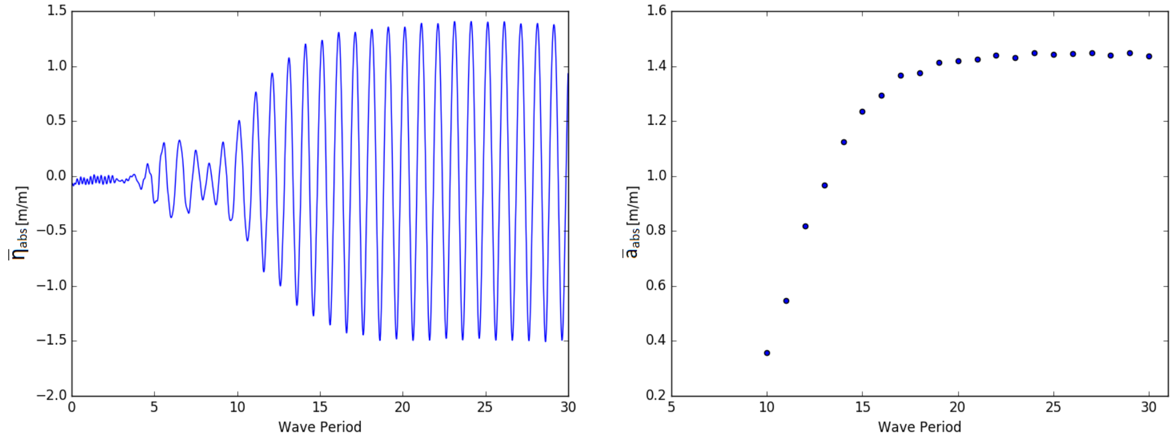

(a) Time trace free surface elevation

(b) Scatter plot of the wave amplitude

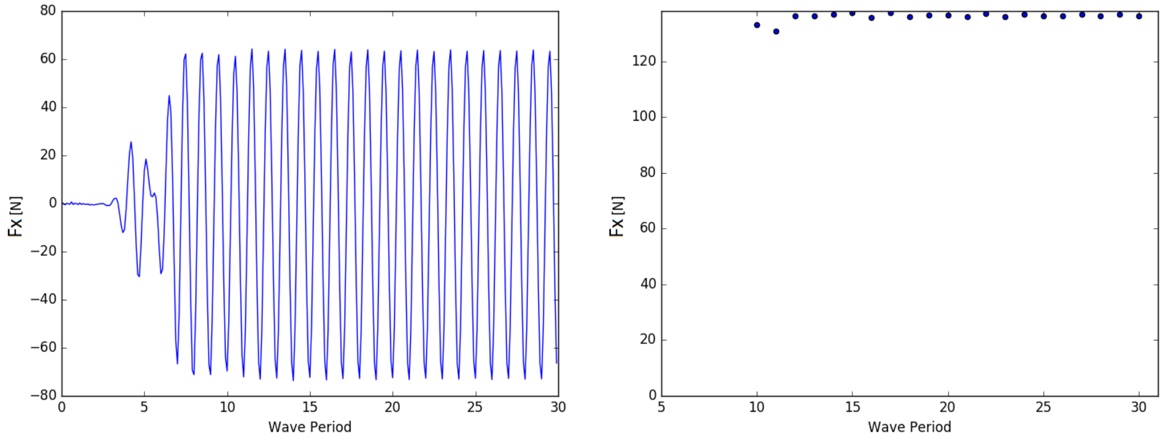

(c) Time trace F_x

(d) Scatter plot of F_x

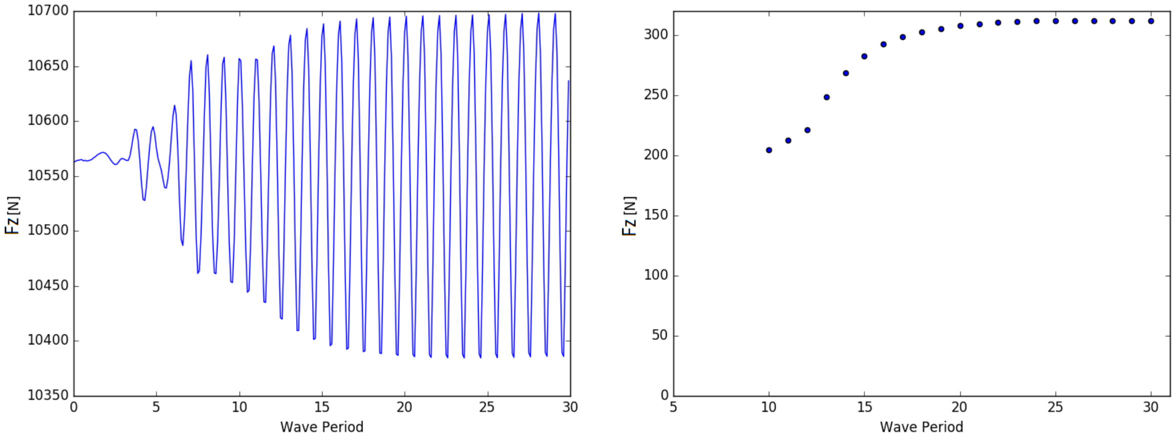

(e) Time trace F_z

(f) Scatter plot of F_z

Figure 4.13: Free surface elevation, amplitude and forces for case E

4.7. Case F & G

The intention of these two simulations is to investigate the influence of each boundary on the final solution. In case F the relaxation zone is applied only at Inlet & outlet, in case G only along the domain side. As observed for case E the relaxation zone reduces the statistical uncertainty. Differences between case F or G and case E are due to the poor absorption capacity of the non-relaxed boundary.

case F

- $\bar{a}_{abs} = 1.95 \; \frac{m}{m} \pm 2.3\%$
- $F_x = 144$ N ± 4.2%
- $F_z = 362$ N ± 11.6%

case G

- $\bar{a}_{abs} = 1.52 \; \frac{m}{m} \pm 1.8\%$
- $F_x = 137$ N ± 0.3%
- $F_z = 328$ N ± 1.0%

In Fig. 4.15 the result comparison for the case investigated so far is reported. Plots on the left column display the variation of absolute wave amplitude or force height per wave period, dots are connected with lines to help the reader follow the trend. Each color represent one case. On the right column the bar charts reports the average of the last 10 wave periods of the left column plots. The uncertainty bars display the statistical uncertainty. To recap case A, B and D use Sommerfeld 1 as absorption method, whereas case E, F and G both Sommerfeld 1 and the relaxation zone. $\bar{a}_{abs}$ (Fig. 4.15a and 4.15b) is mainly affected by the domain side. Enlarging the latter (case B) or applying the relaxation zone (case E and G) modifies both the mean and the RSD. F_x does not displays differences as large as $\bar{a}_{abs}$. From Fig. 4.15c one can notice how Case E and G have a steady behaviour during the last 10 wave periods (respectively yellow and purple line), suggesting a major influence of the side boundary on the F_x solution. Case D and F differ only for the presence of the relaxation zone at Inlet & outlet, differences show an influence of this area on F_x.

In Fig 4.15e and 4.15f the force acting along the vertical axis for different cases is compared. F_z seems to be the most sensitive data analysed and the results show large variations between different cases. Absorbing waves only with the Sommerfeld 1 boundary condition results in large variations between the wave periods and consequently a large statistical uncertainty. Applying the relaxation zone the solution shows drastic changes. Both the mean and the RSD drastically decrease. However the relaxation zone has a difference influence on F_z according to the relaxed area. Relaxing the solution along the domain side has a larger influence compared with the Inlet & Outlet, consequently F_z has the highest sensitivity to the domain side. Both case E and G show an asymptotic behaviour for the last 10 wave periods. Finally, it is interesting to notice how the relaxation zone has a larger influence on the F_z than $\bar{a}_{abs}$. For $\bar{a}_{abs}$ simply enlarging the domain would lead to a similar solution than using the relaxation zone, this is not the case for forces.

To conclude, oscillations noticed in case A were produced by the poor absorption capacity of the boundaries and their short distance from the vessel. The relaxation zone provides better results compared to Sommerfeld 1. On one hand $\bar{a}_{abs}$ is less sensitive to the the absorption method, providing similar results between case B and Case E and G. On the other hand forces presents larger variations between different configurations. The following simulations aim to define the correct settings for the relaxation zone.

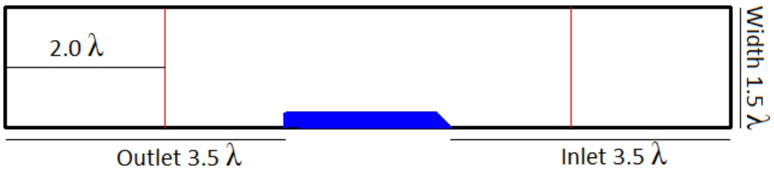

(a) Domain case F

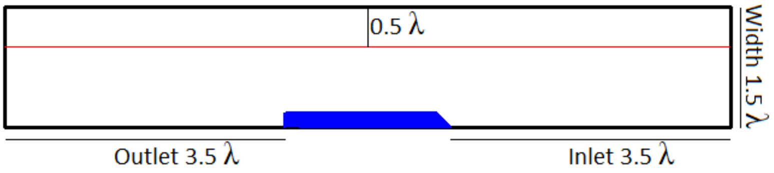

(b) Domain case G

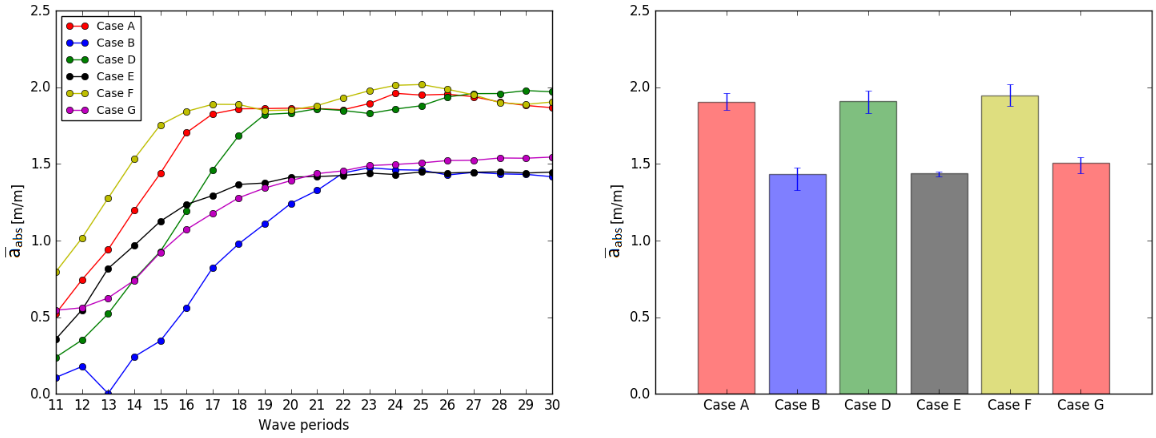

(a) Absolute wave amplitude (b) Absolute wave amplitude

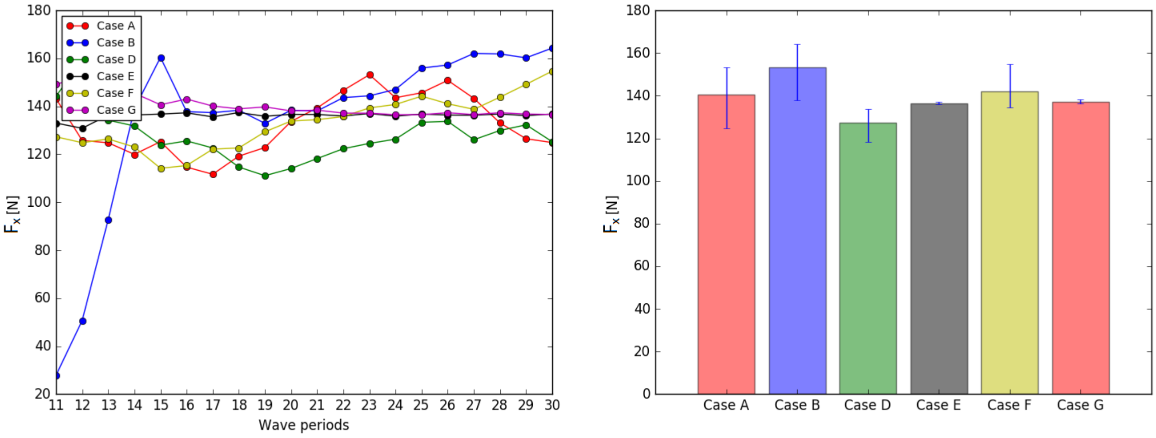

(c) F_x (d) F_x

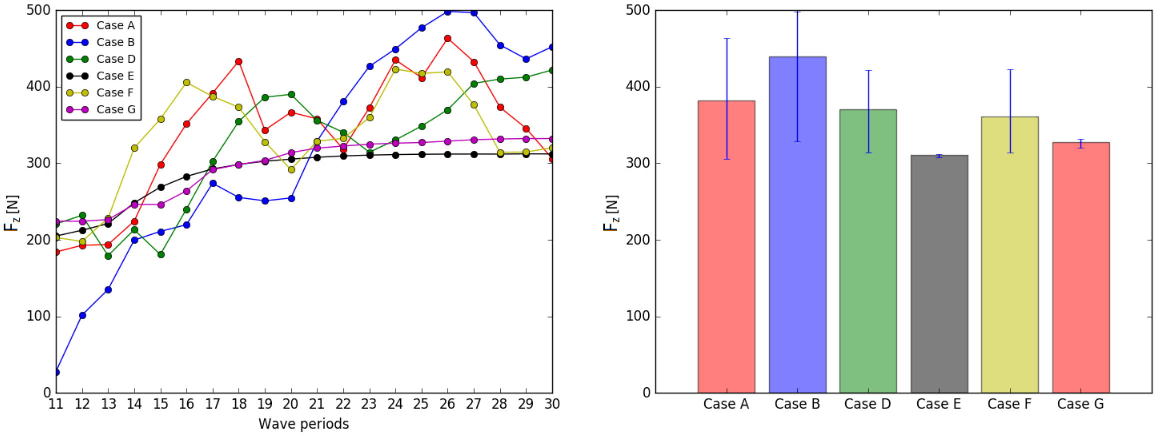

(e) F_z (f) F_z

Figure 4.15: Results comparison for case A,D,E,F and G

4.8. Influence of relaxation factor

The influence of the relaxation factor was investigated in a range between 0.05 and 0.15. The lower limit was chosen in accordance with results obtained by Denisart [11], in his work he showed how β lower than 0.05 was not sufficient to properly absorb waves. The upper limit was defined by the steady residuals convergence, with a relaxation factor higher than 0.15 (both for Inlet & Outlet and domain side) the convergence tolerance was not reachable any more.

In Fig. 4.16 the influence of the relaxation factor both for the inlet & Outlet (plots on the left column of the page) and and for the domain side (plots on the right column of the page) are displayed. The only difference between simulations in each plot is the relaxation factor, domain and ellipse dimensions do not vary. Results are displayed with the mean (the blue dot) and the statistical uncertainty (the blue error bar). The green error bar represents the numerical uncertainty. Since the numerical uncertainty is influenced by mesh and time step it was evaluate only for the final settings. Only simulations outside the numerical uncertainty are clearly influenced by the relaxation factor; The numerical uncertainty is defined as the range in which the exact solution can be found with a probability of 95%. Simulations within it are considered acceptable. In Fig. 4.16 (left column) the influence of β at the Inlet & Outlet is displayed. Common settings for the plotted simulations are:

- Domain length: 3.5 λ in front and aft the vessel
- Domain width: 1.5 λ
- β at domain side: 0.05

The $\bar{a}_{abs}$ results are almost constant and all the solutions lay within the statistical uncertainty of the other simulations. Although F_z shows larger variation between solutions, as already noticed for $\bar{a}_{abs}$ all the solution lay within the numerical uncertainty and its is difficult to assess whether the differences are produced by the relaxation factor or by the discretization error. F_z is largely influenced by the numerical uncertainty (the statistical uncertainty is too small to be noticed) and all the simulations do not show significant differences. To conclude all the data do not seems to be significantly affected by the β at the Inlet & Outlet and to improve the convergence behaviour a relaxation factor equal to 0.05 was chosen. Data are collected in table 4.4.

Table 4.4: Influence of relaxation factor at Inlet & Outlet

Relaxation factor	$\bar{a}_{abs}$ $\frac{m}{m}$	F_x N	F_z N
0.05	1.473 ± 1.0 %	136.7 ± 0.3%	322.8 ± 0.4%
0.07	1.476 ± 1.0 %	137.2 ± 0.3%	322.5 ± 0.4%
0.10	1.471 ± 1.0 %	135.7 ± 0.3%	322.5 ± 0.2%
0.12	1.471 ± 0.9 %	135.4 ± 0.4%	322.5 ± 0.2%
0.15	1.471 ± 0.9 %	135.1 ± 0.4%	322.7 ± 0.2%

In Fig. 4.16 (right column) the influence of β at side is displayed. Common settings for the plotted simulations are:

- Domain length: 3.5 λ in front and aft the vessel
- Domain width: 2.0 λ
- β at Inlet & Outlet: 0.10

$\bar{a}_{abs}$ displays a constant increasing trend through the entire displayed range. All the data are within the numerical uncertainty making difficult to define a correct relaxation factor. The same conclusions are observed for F_x and F_z. Despite the absence of an asymptotic trend, for F_z with β larger than 0.10 simulations oscillates within 2% of difference. Therefore a relaxation factor of 0.10 was chosen for the domain side to provide a compromise between absorption capacity and simulation convergence. Data are collected in table 4.5.

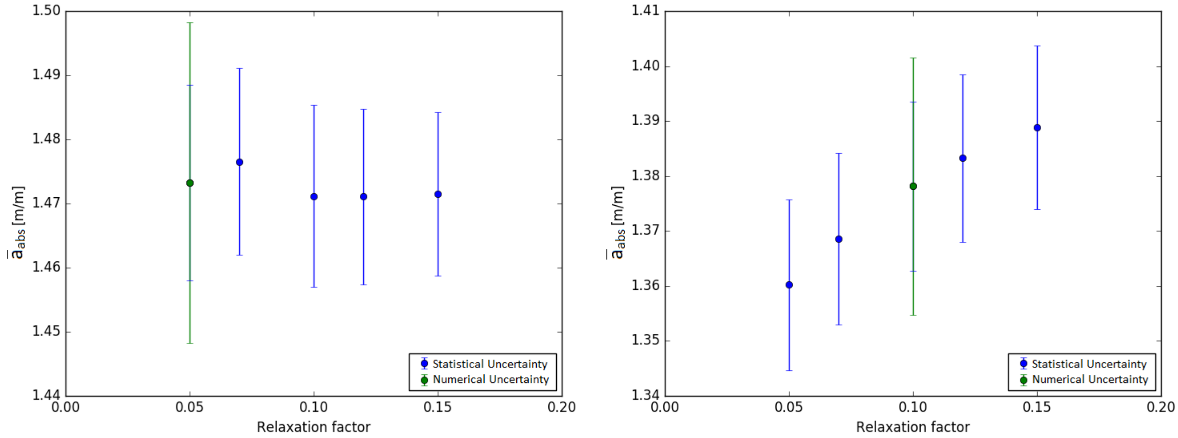

(a) η_{abs} (b) η_{abs}

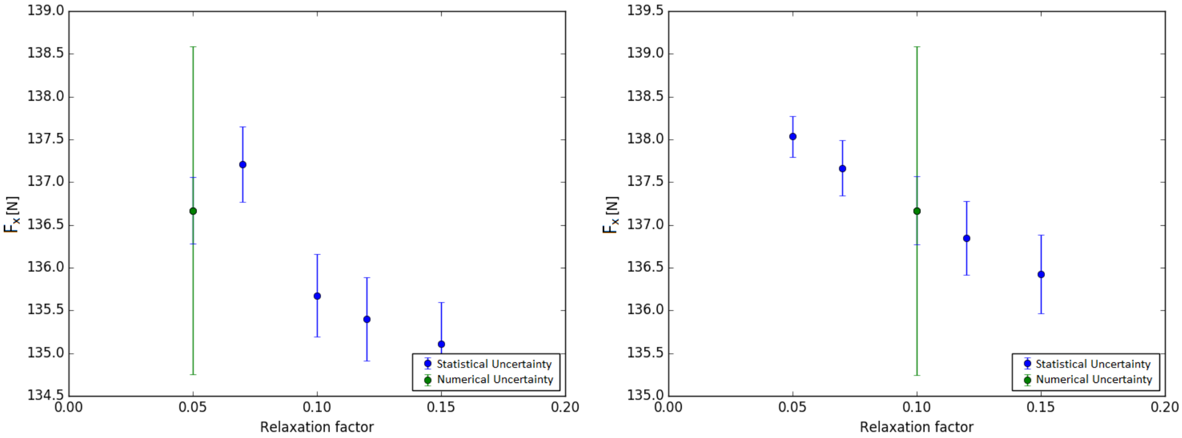

(c) F_x (d) F_x

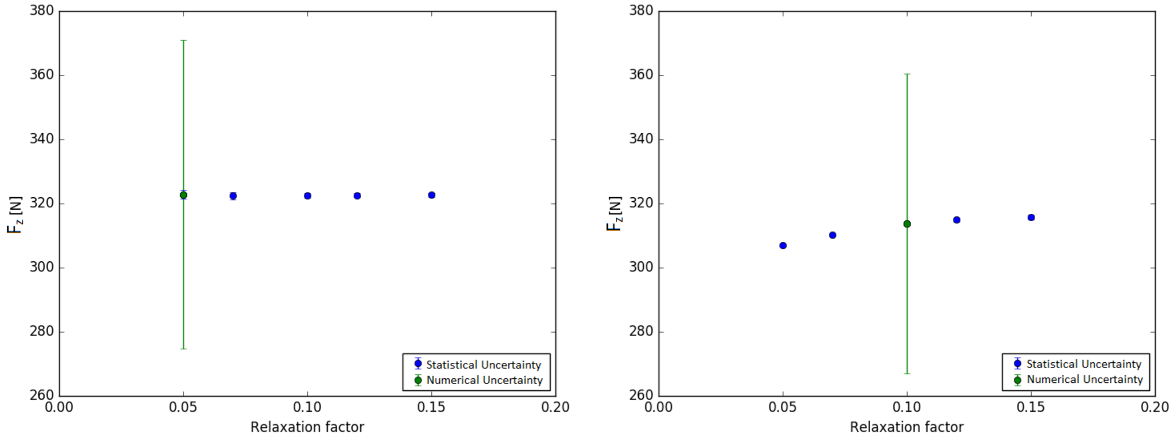

(e) F_z (f) F_z

Figure 4.16: On the left column the influence of β at the Inlet and outlet, on the right column the influence of β at domain side

Table 4.5: Influence of relaxation factor at Side

Relaxation factor	$\bar{a}_{abs}$ $\frac{m}{m}$	F_x N	F_z N
0.05	1.360 ± 1.1 %	138.0 ± 0.2%	307.0 ± 0.1%
0.07	1.368 ± 1.1 %	137.7 ± 0.2%	310.2 ± 0.1%
0.10	1.378 ± 1.1 %	137.1 ± 0.3%	313.7 ± 0.2%
0.12	1.383 ± 1.1 %	136.8 ± 0.3%	315.0 ± 0.2%
0.15	1.388 ± 1.1 %	136.4 ± 0.3%	315.7 ± 0.2%

4.9. Influence of relaxation length

The relaxation length is defined as the distance between the inner ellipse (inside the inner ellipse the CFD solution is computed) and the outer ellipse (outside of that only the analytical solution is computed). The domain width was gradually increased up to 3λ (1λ the inner ellipse radius plus 2λ of relaxation zone), larger domains were not tested as they would require a computational time too high (the largest domain was discretized in 6.0 M of cells with coarse settings). For sake of clarity, in Fig. 4.17 the domains used for the investigation are reported. The dash lines display the gradually domain enlargement. All the simulations involved in this section share the same settings, only the domain width and consequently the relaxation length differ. Here below the common settings are reported:

- Domain length: 3.5 λ in front and aft the vessel
- β at Inlet & Outlet: 0.10
- β at domain side: 0.05

Solutions from different meshes are now compared, differences are affected by discretization error and statistical uncertainty at the same time which makes it difficult to assess their magnitude. The numerical uncertainty is now excluded from the plots because it varies for every mesh, the estimation of the numerical uncertainty was computed only for the final settings due to limit in the project time.

In Fig. 4.18a the influence of the relaxation length along the side on $\bar{a}_{abs}$ is presented. Although solutions do not follow a monotonic behaviour, for relaxation length of 1.0 λ or longer $\bar{a}_{abs}$ discrepancies are within 2%. Furthermore results obtained with relaxation length longer than 1.0 λ lay within the statistical uncertainty of $\bar{a}_{abs}$ with relaxation length of 1.0 λ. Similar conclusions are noticeable for forces as well. In the end a relaxation length equal to 1.0 λ was chosen as the results shown a good compromise between solution accuracy and domain dimensions.

Table 4.6: Influence of relaxation length along the domain width

Relaxation length λ	$\bar{a}_{abs}$ $\frac{m}{m}$	F_x N	F_z N
0.5	1.438 ± 0.5 %	135.5 ± 0.3%	310.2 ± 0.3%
1.0	1.406 ± 0.3 %	138.0 ± 0.2%	307.0 ± 0.1%
1.5	1.399 ± 0.2 %	138.2 ± 0.1%	303.6 ± 0.1%
2.0	1.417 ± 0.2 %	138.1 ± 0.2%	305.1 ± 0.1%

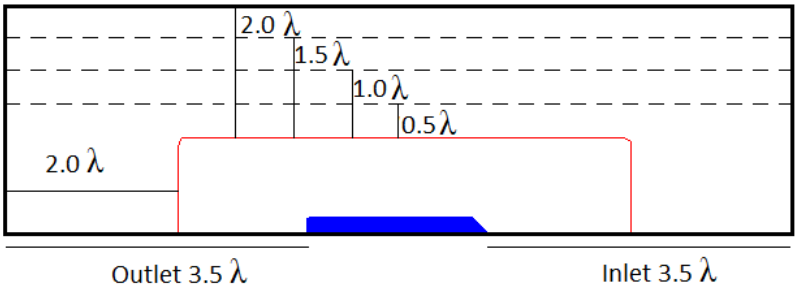

Figure 4.17: Influence of relaxation length. Domain dimensions

4.10. Influence of absorption method

Once the correct settings for the relaxation zone are defined it is interesting to look at the contribution that Sommerfeld 1 still has. If waves are fully absorbed by the relaxation zone the contribution of boundaries become negligible and can be substitute by a BC SlipWall condition. This simplify the controls file in ReFRESCO. In Fig. 4.19 the two simulations differ only for the boundary condition at the inlet and outlet, both of them have the relaxation zone. Plots show a good agreement between simulations with and without Sommerfeld 1: wave amplitude differs for 0.13 %, F_x for 0.13 % and F_z for 0.31%. The contribution of BC Waves is now negligible and in the final settings it is substituted by BC SlipWall. From here, if not different stated the boundaries condition are the one reported in table 4.7.

Table 4.7: Boundary conditions for fixed vessel case

Surface	Boundary Condition
bottom	Slip wall
symmetry plane	Symmetry
Side	Slip wall
Inlet	Slip wall
Outlet	Slip wall
Top	Pressure
Vessel	Wall

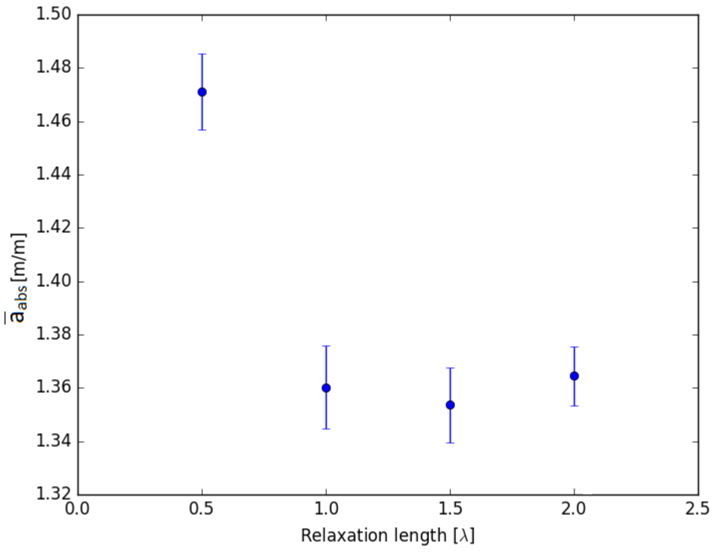

(a) a_{abs}

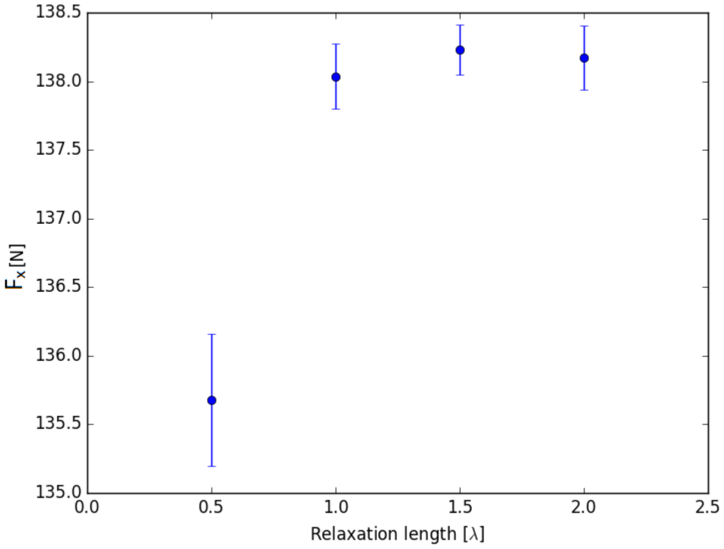

(b) F_x

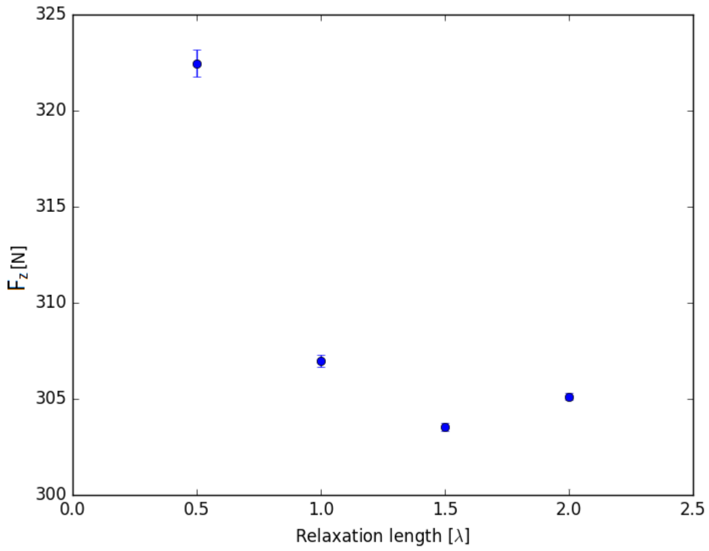

(c) F_z

Figure 4.18: Influence of relaxation length along the domain width

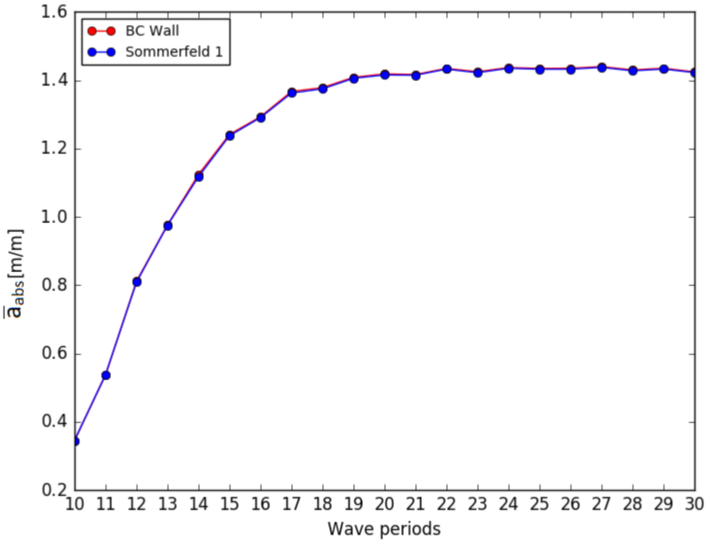

(a) $\bar{a}_{abs}$

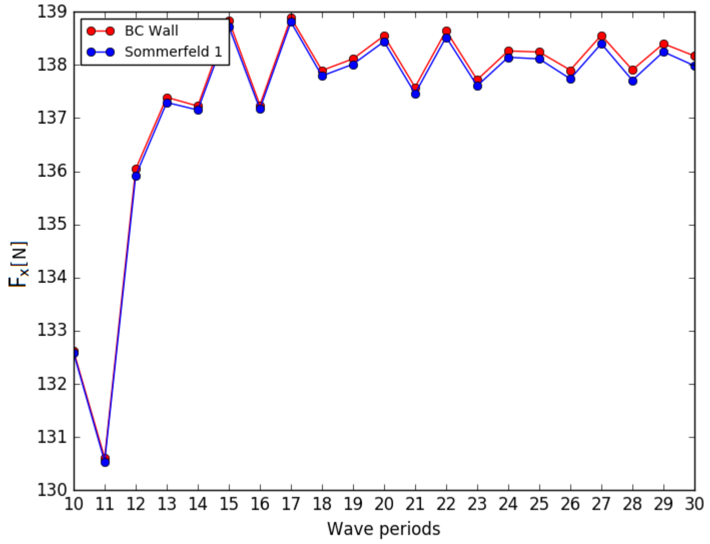

(b) F_x

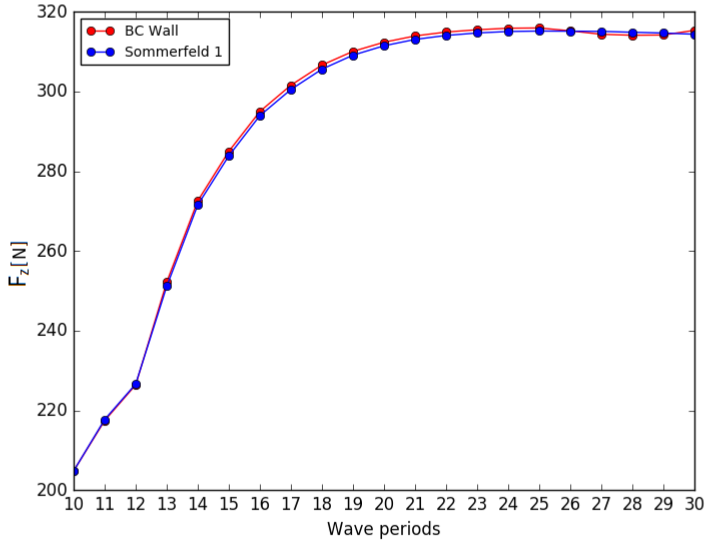

(c) F_z

Figure 4.19: Results comparison for simulations with and without Sommerfeld 1 boundary condition

4.11. Final settings

Outcome of the previous sections are the final settings used for the refinement study. These are considered the best settings found by the author in term of steadiness, number of cells and convergence behavior. Results are summarized in appendix B.8. Final settings and results are:

- Grid: Coarse (4.2M cells)
- Timestep: T/100
- Convergence level : 10^{-4}
- Domain length: 3.5 λ in front and aft the vessel
- Domain width : 2.0 λ
- Boundary conditions:
    1. Inlet: BC Wall
    2. Side: BC Wall
    3. Outlet: BC Wall
- Relaxation zone:
    1. Inner radius along x direction: 1.5 λ
    2. Relaxation factor at Inlet & Outlet: 0.05
    3. Relaxation length: 2.0 λ
    4. Inner radius along y direction: 1.0 λ
    5. Relaxation factor at Side: 0.10
    6. Relaxation length: 1.0 λ
- Results
    1. $\bar{a}_{abs}$ 1.43 $\frac{m}{m}$ ± 0.48 %.
    2. F_x 138.00 N ± 0.24 %.
    3. F_z 314.62 N ± 0.20 %.

Waves are absorbed by the relaxation zone. The contribution of Sommerfeld 1 boundary condition at Inlet & Outlet is now insignificant. This has been shown in the previous section. Finally, boundary conditions at Inlet & Outlet have been changed to BC Wall.

4.12. Influence of mesh refinement

One of the goal of this chapter was to investigate the influence of boundaries on the final solution and provide a good compromise between absorption capacity and domain dimensions. The next step involves the refinement study. Mesh settings were already described in section 4.2. Results obtained with medium mesh are reported in appendix B.9. For sake of brevity here only the pressure distribution over the bottom is reported in Fig. 4.20b (the same observation could be done for the pressure distribution along the side). With medium mesh the pressure areas are not clearly defined any more, the most confuse pressure distribution is noticeable at the bow. To investigate whether these results are physical (the coarse mesh does not capture the water motion around the hull with enough accuracy) or they are driven by discretization error (low mesh quality) it has been decided to generate new meshes following new mesh settings.

Guidelines presented in the work of Rapuc [27] were used to generate a new grid. As already mentioned in section 4.2 his work had the objective to define guidelines to generate mesh for the study of ships in waves, taking into account the presence of a relaxation zone. The most important ideas are: Include a surface refinement on the vessel to define the hull with a higher accuracy. Include a box refinement around the inner ellipse to capture the diffracted (and radiated waves if the vessel is moving) waves and their orbital velocities

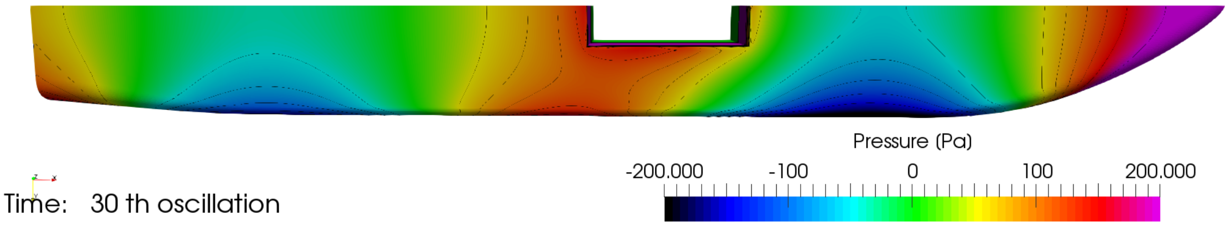

(a) Medium mesh generated with guidelines of Rapuc [27]

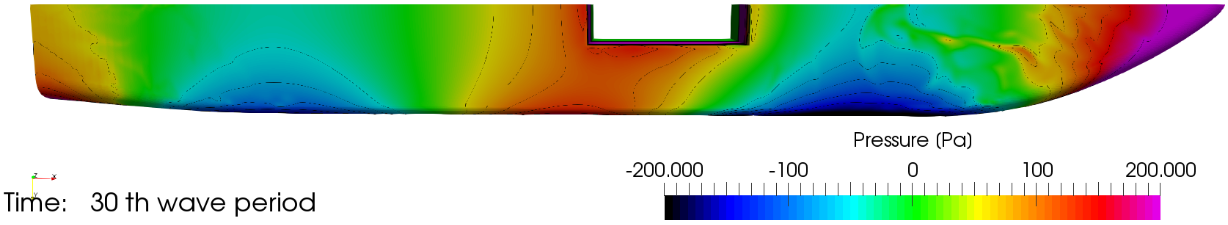

(b) Medium mesh generated with first mesh settings

Figure 4.20: Comparison of the pressure distribution for the medium meshes generated with and without Rapuc [27] guidelines

(the box refinement should be at least 0.5 λ in depth). Outside the inner ellipse the free surface solution is forced by the relaxation zone to the analytical solution; only the interface between the two fluids is refined to capture the free surface shape. These guidelines have already been used with success in others MARIN projects. Results for the medium mesh are summarized in appendix B.10 for comparison, here only the pressure distribution along the bottom is reported in Fig. 4.20a.

Using the mentioned guidelines the pressure distribution between coarse and medium mesh are similar, the latter does not show a confused pattern any more. The explanation can be found in the box refinement dimensions around the vessel. The first mesh was generated using a box refinement too tight to the vessel placing the hanging nodes in an area still interested by the water motion, with the new mesh they were moved farther. Refining the mesh the ratio between cells inside and outside the vessel box increases and with it the number of hanging nodes; this could explain why this problem was not noticed in the coarse mesh. Concluding the new meshes showed better results and they were used for the next simulations.

4.13. Turbulence model

Once the settings were defined and the right meshes were generated the turbulence model was included. Four different turbulence models were used: SKL and MENTER as one equation model, $k-\omega$ standard and $k-\epsilon$ as two equations models. The introduction of the turbulence model requires the modelling of the viscous layer.

4.13.1. Mesh

The generation of the viscous layer starts defining the thickness of the first cells next to the wall, the latter is defined by y^+ value. y^+ is a dimensionless quantity which measures the distance from the wall in terms of viscous length. The viscous sublayer is within $y^+ = 5$, in this area the viscous shear dominates the flow. For the outer layer where the large scale turbulent shear dominates y^+ is larger than 30. This value is chosen accordingly to the physical problem represented. For an attached flow usually a large y^+ value (above 30) is used and the viscous sublayer is modeled with a wall function. This approach is often used because it is robust and requires less cells. However the wall functions are inadequate in simulations involving flow separation in which the sub-layer needs to be solved, for these application a $y^+ = 1$ or 5 are usually accepted.

For this application a $y^+ = 1$ was chosen. The y^+ value is predictable only for simple geometries (such as flow over a flat plate), for complex geometries like a vessel a trial and error approach is used. At first the thickness suggested for a flat plate geometry is used and then with an iterative approach the desired $y+$ is reached. For the following simulations involving a turbulence model y^+_{max} (the maximum y^+ in the entire domain) is 0.4.

After first cell thickness is defined, the number of layers is chosen to guarantee a smooth transition between the first cells layer and the free stream. For the coarse mesh cells were too large to have a smooth transition between the viscous layer and the domain, the drastic change in cells size at the edge of the boundary layer led to L_2 stagnation around the vessel (in the order of $L_2 = 10^{-3}$). The cells of the medium mesh were small enough to guarantee a smooth transition and avoid the mentioned problem. The difference between a smooth transition and a sharp one can be observed in Fig. 4.21. Therefore the grid used with the turbulence model was the medium mesh with a time step $\frac{T}{200}$ and $L_2 = 3 * 10{-}5$ (this was the lowest steady convergence achievable).

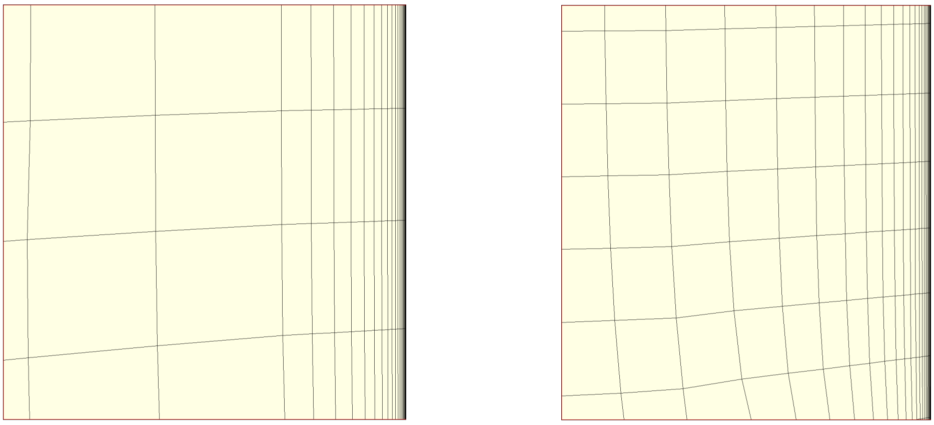

(a) Coarse mesh (b) Medium mesh

Figure 4.21: Particular of the transition between the viscous layer and the free stream at the stern vessel

4.13.2. Results

Simulations involving $k-\epsilon$ turbulence model diverged, a deeper investigation on the settings used has been conducted unfortunately the problem was not fixed. A possible explanation is the low y^+ value used, a higher y^+ with wall function would have probably shown a higher stability, however it was not investigated for a lack of time. $k-\omega$ showed a better behaviour however it was not possible to reduce the dissipation (ω) steady residuals below $5 * 10^{-3}$. Results are reported in appendix B.14 for sake of completeness, however its choice was disregarded.

Due to time limit of the project two equation models were dropped in favour of the more stable one equation model. Both results from SKL and MENTER provided similar results. They are summarized in table 4.8, post processed data are summarized respectively in appendix B.12 and B.13. Differences for all the data are smaller than 2%, the two turbulence models provides the same results. For future simulations involving the turbulence model the SKL was chosen.

Table 4.8: Results for the SKL and MENTER turbulence model

	$\bar{a}_{abs}$ $\frac{m}{m}$	F_x N	F_z N
SKL	0.93 ± 1.3 %	191.87 ± 0.17 %	347.26 ± 0.07 %
MENTER	0.92 ± 1.3 %	191.74 ± 0.19 %	346.25 ± 0.13 %

Fig. 4.23 compared the data from SKL turbulence model and laminar model, respectively on the left and right column of the page. An extensive presentation of the solution both for the turbulence model and the laminar model are reported respectively in appendix B.12 and B.11. $\bar{a}_{abs}$ decreases due to the increase in damping produced by the turbulence model. A reduction in the wave amplitude reduces the flow motion and directly influences the pressure distribution around the moonpool, consequently F_z is reduced as well. This is visible from a comparison of results in table 4.8 and 4.9 or by a comparison of the pressure distribution over the hull in Fig. 4.22. The violet area around the moonpool edges disappears applying the turbulence model. Other areas of the bottom do not show differences as large. On the opposite F_x (Fig. 4.23c and 4.23d) does not show significant variations including turbulence model. This is explained by the minor contribution that the water motion inside the moonpool has on F_x.

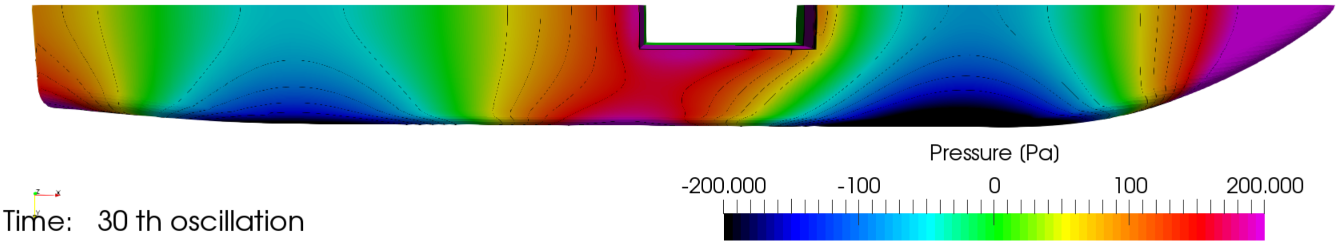

(a) Laminar model

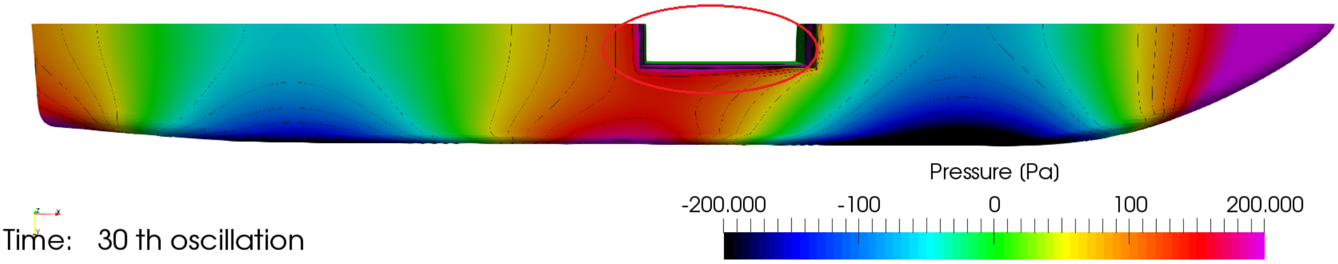

(b) SKL model

Figure 4.22: Comparison of the pressure distribution over the hull at the last time step

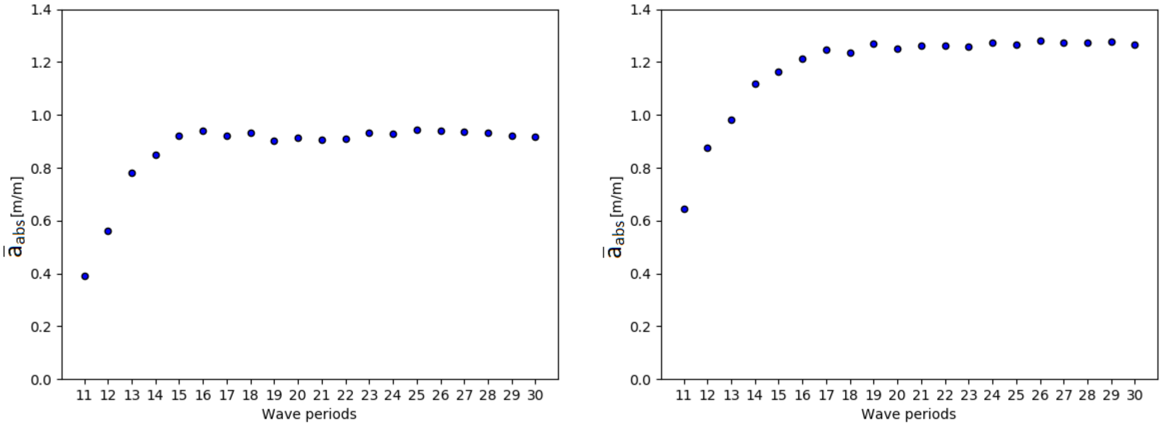

(a) wave amplitude with SKL model

(b) wave amplitude with Laminar model

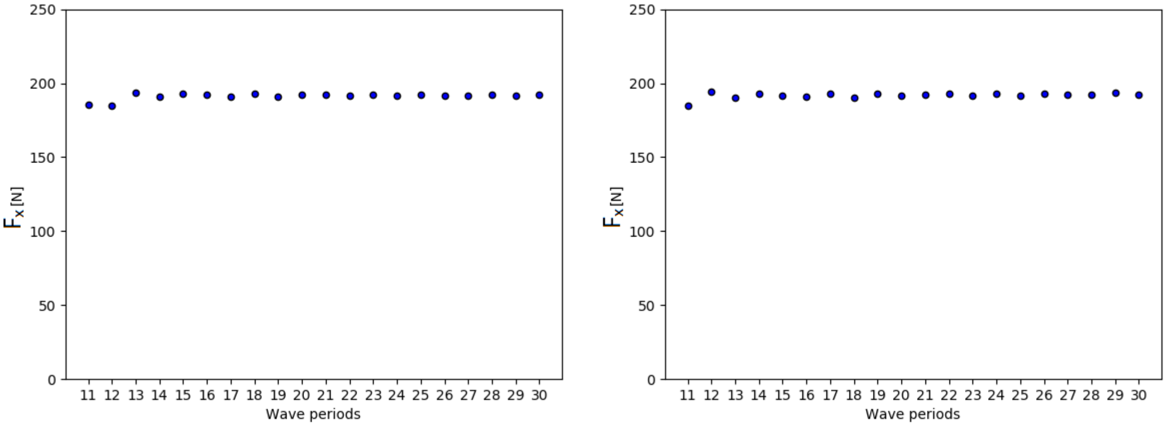

(c) F_x with SKL model

(d) F_x with Laminar model

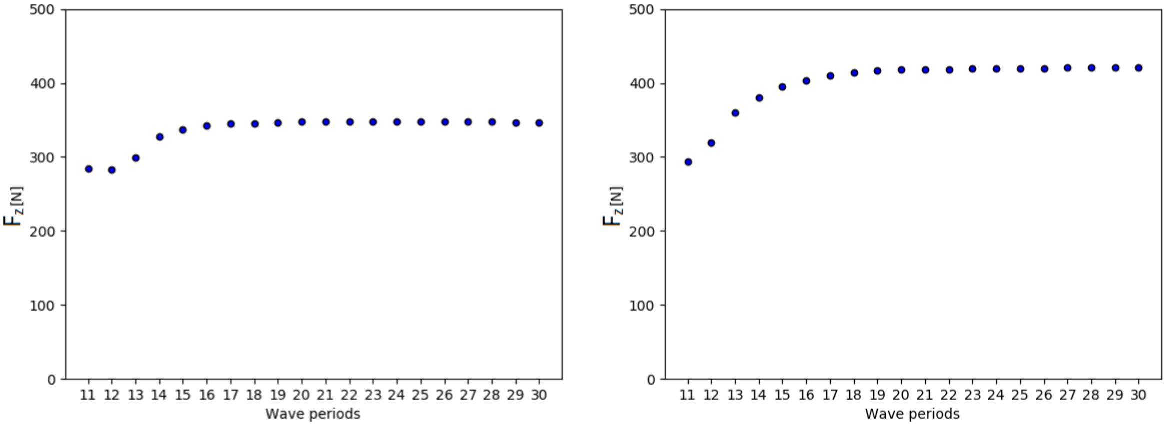

(e) F_z with SKL model

(f) F_z with Laminar model

Figure 4.23: On the left column results with SKL turbulence model, on the right with Laminar model

4.14. Numerical uncertainty

In Abeil [6] experiments were conducted with H = 4 m at full scale which correspond to 0.138 m at model scale. This value was used to asses the numerical uncertainty. Results are reported in table 4.9. Simulations presented in this chapter required a higher computational effort compared to the empty domain case, for this reason and for the limited time available the refinement study for the fixed vessel involved less simulations than the empty domain case. The time step refinement was limited to $\frac{T}{400}$. The steady convergence tolerance stopped at $L_2 = 10^{-5}$, non negligible differences are visible between 10^{-4} and 10^{-5} and a lower steady convergence tolerance should be simulated to define the correct tolerance level for the steady residuals. Nevertheless, thanks to the relaxation zone an additional refinement of the convergence tolerance proved to be challenging and time consuming, for these reasons $L_2 = 10^{-5}$ was considered sufficient. Steady residuals for simulations with time step $\frac{T}{100}$, medium and fine mesh did not reach the desired convergence tolerance due to high Courant Number (respectively 1.9 and 8.0) and they were not used to estimate the numerical uncertainty. They are here reported for sake of completeness. Simulation with fine mesh, time step $\frac{T}{100}$ and $L_2 = 10^{-4}$ stopped due to node failure (one of the node used to run the simulation crashed for unknown reason), due to the poor convergence behaviour of the simulation involving $L_2 = 10^{-5}$ the simulation was not restarted. By cause of the limited amount of time available for this project the refinement study was conducted using only the laminar model. Numerical uncertainty for the SKL turbulence model was not established.

The method to asses the numerical uncertainty is the same used for the empty domain case, refer to section 3.5 and Eça and Hoekstra [12] for additional reading. Results are summarized in table 4.10 and Fig. 4.24. In Fig. 4.24 the x and y axis are respectively the mesh and time step refinement. Values are expressed as fraction of the finest settings; for example $\frac{t_i}{t_1} = 2$ means the time step used is two times larger than the finest one. On the vertical axis the analysed data are displayed. Red dots represent the results of the refinement study (every dot corresponds to a value in table 4.9). Green bars represents the numerical uncertainty for ϕ_1. ϕ_0 is estimated at the intersection of the grey surface with the vertical axis ($\frac{t_i}{t_1} = 0$ and $\frac{h_i}{h_1} = 0$).

Table 4.9: Results of wave amplitude inside the moonpool and forces acting on the hull from the refinement study.

Grid	Timestep	Converge Level	$\bar{a}_{abs}$ $\frac{m}{m}$	F_x N	F_z N
Coarse	$\frac{T}{100}$	10^{-4}	1.253 ± 0.5%	185.278 ± 0.6%	409.053 ± 0.3%
		10^{-5}	1.252 ± 0.5%	185.226 ± 0.6%	409.588 ± 0.3%
	$\frac{T}{200}$	10^{-4}	1.284 ± 0.6%	187.250 ± 0.4%	419.575 ± 0.4%
		10^{-5}	1.284 ± 0.6%	187.581 ± 0.4%	419.445 ± 0.4%
	$\frac{T}{400}$	10^{-4}	1.257 ± 0.6%	183.393 ± 0.4%	407.884 ± 0.4%
		10^{-5}	1.262 ± 0.7%	184.442 ± 0.4%	409.211 ± 0.3%
Medium	$\frac{T}{100}$	10^{-4}	1.230 ± 0.5%	192.226 ± 0.4%	406.396 ± 0.2%
		10^{-5}	1.230 ± 0.7%	192.196 ± 0.6%	406.041 ± 0.2%
	$\frac{T}{200}$	10^{-4}	1.269 ± 0.5%	192.363 ± 0.3%	420.063 ± 0.2%
		10^{-5}	1.268 ± 0.5%	192.356 ± 0.3%	420.069 ± 0.3%
	$\frac{T}{400}$	10^{-4}	1.259 ± 0.5%	188.198 ± 0.3%	409.393 ± 0.1%
		10^{-5}	1.260 ± 0.6%	188.666 ± 0.3%	410.756 ± 0.1%
Fine	$\frac{T}{100}$	10^{-4}			
		10^{-5}	1.160 ± 0.8%	190.142 ± 0.6%	386.786 ± 0.7%
	$\frac{T}{200}$	10^{-4}	1.256 ± 0.4%	194.985 ± 0.4%	420.794 ± 0.1%
		10^{-5}	1.254 ± 0.4%	194.784 ± 0.4%	422.163 ± 0.1%
	$\frac{T}{400}$	10^{-4}	1.260 ± 0.6%	190.940 ± 0.4%	414.793 ± 0.1%
		10^{-5}	1.261 ± 0.6%	191.029 ± 0.3%	414.697 ± 0.1%

From table 4.10 the largest numerical uncertainty refers to F_z. In Fig. 4.24c one can notice how the fitting curve shows a parabolic behaviour along the y axis, consequently the estimated solution ϕ_0 is far from ϕ_1 and

Table 4.10: Results for the uncertainty analysis for the fixed vessel in waves.

Item	ϕ_0	ϕ_1	U_ϕ
$\bar{a}_{abs}$	$1.26 \times 10^{+0}$	$1.27 \times 10^{+0}$	1.7%
F_x	$1.93 \times 10^{+2}$	$1.91 \times 10^{+2}$	1.4%
F_z	$3.93 \times 10^{+2}$	$4.15 \times 10^{+2}$	14.9%

the uncertainty is large. Only when solutions are in the asymptotic range an accurate ϕ_0 estimation is possible. Probably the simulation with coarse mesh and $\frac{T}{100}$ is outside the asymptotic range and it badly influence the fitting surface, however to prove it simulations involving finer time step than $\frac{T}{400}$ should be tried. On the opposite $\bar{a}_{abs}$ and F_x show a numerical uncertainty one order of magnitude smaller than U_ϕ for F_z.

In table 4.11 and 4.12 the influence of the time step and the mesh refinement are highlighted, they are expressed as difference in percentage from the finest settings, for additional explanation refer to section 3.4.2. Different error sources can counteract each other, this explain why some differences increase refining the settings (for example in table 4.11 for the coarse mesh). As already explained in the previous chapter the numerical uncertainty is not a measure of the difference between ϕ_0 and ϕ_1. Here this is further confirmed looking at the differences of F_z refining the settings. Even if differences are always lower than 3.0% the numerical uncertainty is 14.9%. To conclude the numerical uncertainty is function of the fitting surface, the parabolic trend leads to a relatively large numerical uncertainty.

Table 4.11: Comparison between time steps for the fixed vessel case.

Grid	Timestep	a_{abs} %	F_x %	F_z %
Coarse	$\frac{T}{100}$	0.90	1.83	2.65
	$\frac{T}{200}$	1.58	1.70	2.47
	$\frac{T}{400}$	0.00	0.00	0.00
Medium	$\frac{T}{200}$	0.43	1.83	2.65
	$\frac{T}{400}$	0.00	0.00	0.00
Fine	$\frac{T}{200}$	1.38	1.75	1.84
	$\frac{T}{400}$	0.00	0.00	0.00

Table 4.12: Comparison between mesh size for the fixed vessel case.

Timestep	Grid	a_{abs} %	F_x %	F_z %
$\frac{T}{200}$	Coarse	2.97	2.97	0.34
	Medium	1.36	0.87	0.02
	Fine	0.00	0.00	0.00
$\frac{T}{400}$	Coarse	0.01	2.91	0.97
	Medium	0.44	0.94	0.79
	Fine	0.00	0.00	0.00

4.15. Conclusion

In this chapter the simulation case was a fixed vessel with incoming waves. Only one incoming frequency ($\omega = 0.8 \frac{rad}{s}$ at full scale) and one incoming direction (head waves) were tested. The objective were assess the numerical uncertainty and find the best settings in terms of absorption capacity and domain dimensions. The waves absorption is a great concern in simulations without forward speed. If waves are not completely absorbed by boundaries the reflected component can influence the solution around the vessel. In ReFRESCO two absorption methods are available. The Sommerfeld 1 boundary condition and the relaxation zone. Despite the theoretical disadvantages of the relaxation zone, the latter ensures a better wave absorption if compared to Sommerfeld 1. Even if theoretically the relaxation zone requires a larger space compared to Sommerfeld 1, the final domain has smaller dimensions compared to the one required by Sommerfeld 1 to obtain satisfactory results.

Mesh settings proved to be as important as the controls settings in ReFRESCO. For the refinement study meshes were generated using the method suggested by Rapuc [27]. This method has already been used in other projects at MARIN with solid results.

Both one equation and two equations turbulence model were tested. One equation turbulence model used were SKL and MENTER. Two equations turblence model were $k-\epsilon$ and $k-\omega$. Two equations models showed convergence problems and were dropped in favour of one equation turbulence model. SKL and

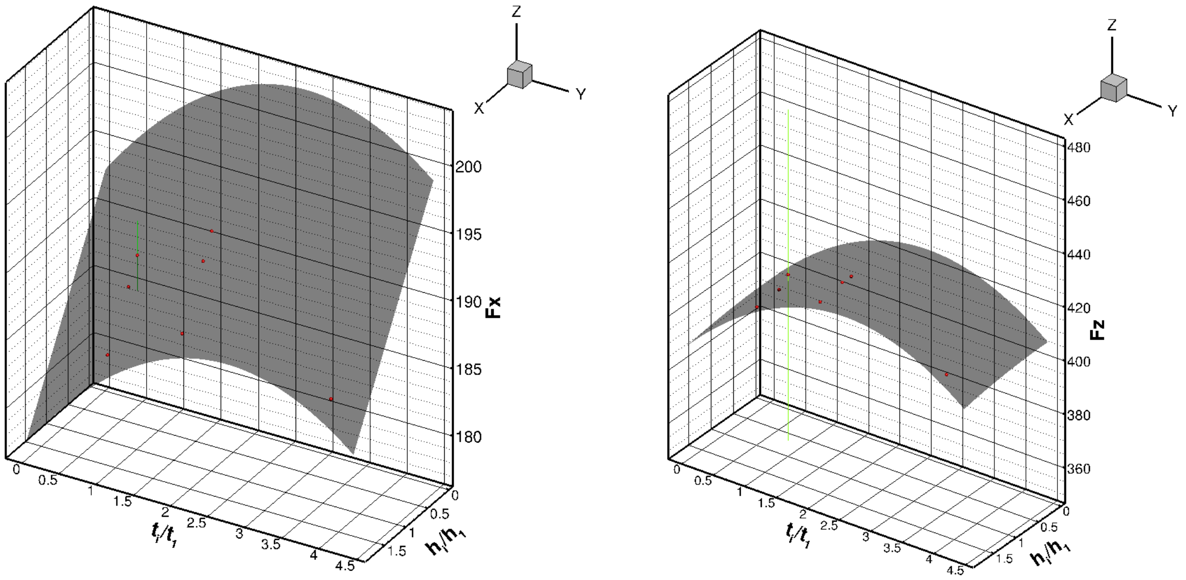

(a) F_x (b) F_z

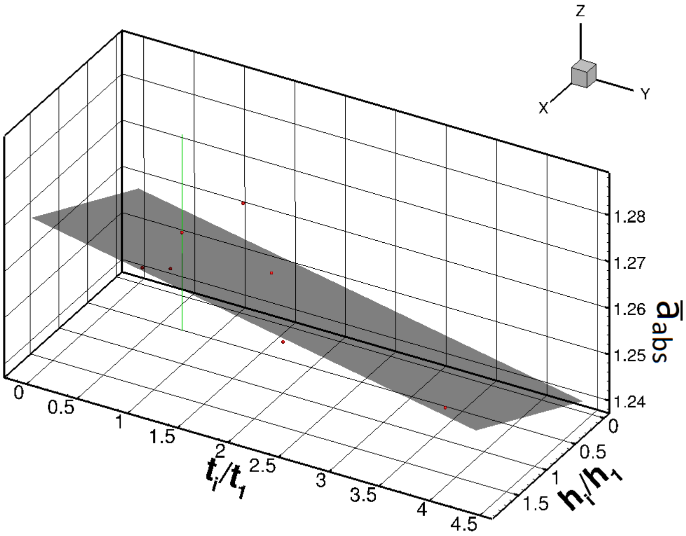

(c) $\bar{a}_{abs}$

Figure 4.24: Fitting surfaces for fixed vessel uncertainty

MENTER provided results within 2% of difference. The turbulence model increases the dissipated energy. As a consequence, $\bar{a}_{abs}$ reduces of 31% compared to laminar model. A reduction in the water motion influences F_z. The latter is reduced of 20% compared to F_z obtained with laminar model. No significant variations are noticeable for F_x.

Due to tight time constrain on the completion of this project an extensive refinement study as presented in section 3.5 was not possible. Lower convergence tolerance for the steady residuals should be investigate. To reduce the relatively larger uncertainty of F_z simulations involving finer settings are necessary.

5

Forced heave oscillation

The forced heave oscillation case is now investigated. This chapter has two main goals: The first one is to investigate the validity of the settings defined for the fixed vessel, now applied to the forced heave oscillation. The second one is to estimate the added mass and damping for the oscillation frequency. These results will be used at the end of the chapter to tune the potential flow solver DIFFRAC. The chapter is organized as follow: At first a description of the domain and the physichal problem studied. Additional monitors are included to check the absorption capabilities of the relaxation zone, they are described in section 5.2. In this section is also included a description of the method used to estimate added mass and damping. Simulations with forced heave oscillations require the introduction of new settings in the controls file, they are described in section 5.3. Then sections 5.4 and 5.5 deal with refinement study and numerical uncertainty. Turbulence model introduced in the previous chapter is applied to the present case, results are reported in section 5.6. Finally, DIFFRAC is tuned according to the added mass and damping obtained from the CFD simulations. All the results are collected in appendix C.

5.1. Domain description

Domain dimensions and monitors are shown in Fig. 5.1. Boundary conditions were established in chapter 4, only the bottom boundary changes from BC SlipWall to BC Pressure, the reason is explained in section 5.3. For this case a flat free surface is initialized and wave generation is disabled. The water inside the moonpool is now excited only by vessel heave, the force monitors record the buoyancy force and the radiation force (F_r). Equation 4.1 reduces to:

$$F_{tot} = \rho g \nabla + F_r \tag{5.1}$$

5.2. Mesh generation & monitors

The same meshes generated for the fixed vessel case were used, both for the laminar and turbulence models. A very-fine mesh was included in the refinement study to estimate with higher accuracy the numerical uncertainty. The very-fine mesh was generated refining the fine grid by a factor of 1.2 in every direction. Cells distribution for the very-fine mesh is represented in table 5.1 , the total number of cells is 9.0 millions.

To prevent wave reflection at boundaries the relaxation zone should completely damp the radiated waves. This is a particular case in which the capability of the relaxation zone can be easily investigated. To monitor

Table 5.1: Cells distribution for the very fine mesh

	Very Fine
Free surface	$55\ \frac{cells}{\lambda}$
	$15\ \frac{cells}{H}$
Vessel surface	$110\ \frac{cells}{B}$
Vessel & moonpool box	$55\ \frac{cells}{\lambda}$
	$15\ \frac{cells}{H}$

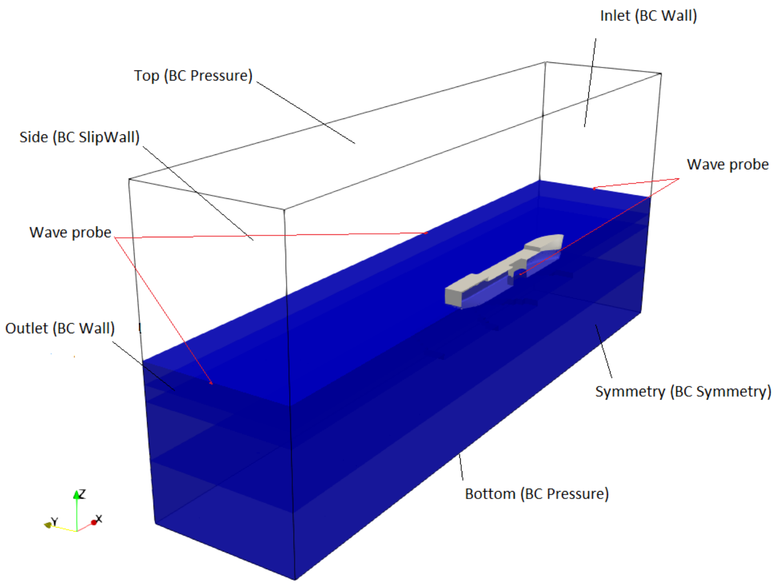

Figure 5.1: Forced heave oscillation domain and boundary conditions

whether the relaxation zone is correctly defined three new wave probes are included inside the domain, one near each edge. The expected wave elevation at the domain boundaries is $\eta_{abs} = 0$ for the entire simulation. As already explained in chapter 4 the wave probes extract the absolute free surface elevation. However, in this case the vessel motion needs to be taken into account in order to define the relative water motion inside the moonpool. In the previous chapters the free surface elevation and the wave amplitude were normalized by the incoming wave amplitude. In this chapter an incoming wave amplitude is missing. Therefore the non dimensional free surface and wave amplitude are obtained dividing them by the amplitude motion (z_a). For this specific case equation 2.14 becomes equation5.2.

$$\bar{\eta}_{rel} = \frac{\eta_{abs} - z}{z_a} \tag{5.2}$$

In the force heave oscillation case it is not necessary to wait for the generated waves to reach the vessel, therefore the simulation time is decreased. It was observed that forces and water motion are completely excited after 10 oscillations; simulations were stopped at 15^{th} oscillation and data were extracted from the last 5. If not different specified $\bar{a}_{rel}$ refers to the wave amplitude monitored at M MID.

5.2.1. Added mass and damping

In a force oscillation test the vessel motion and the monitored forces can be expressed as harmonic functions. In this specific condition the added mass and damping are easily computed. The equation of motion is:

$$(m+a)\ddot{z} + b\dot{z} + cz = F_a sin(\omega t + \epsilon_{Fz}) \tag{5.3}$$

m is the vessel mass, a the added mass and b the damping. c is the stiffness and it is computed by the vessel geometry. ϵ_{Fz} is the phase between the vessel motion and the force. F_a is the force amplitude and z the heave motion($\dot{z}$ and $\ddot{z}$ are respectively the heave velocity and acceleration):

$$\begin{aligned} z &= z_a sin(\omega t) \\ \dot{z} &= z_a \omega cos(\omega t) \\ \ddot{z} &= -z_a \omega^2 sin(\omega t) \end{aligned} \tag{5.4}$$

Substituting the heave motion, velocity and acceleration in equation 5.3 and solving respect to added mass and damping lead to:

$$
\begin{aligned}
a &= \frac{c - \frac{F_a}{z_a} cos(\epsilon_{Fz})}{\omega^2} - m \\
b &= \frac{\frac{F_a}{z_a} sin(\epsilon_{Fz})}{\omega}
\end{aligned}
\tag{5.5}
$$

The added mass is function of the force component in phase with vessel motion, the damping with the out of phase component. As described in Journée et al. [18] they are found by an integration respect to time of the force multiplied by the $\cos\omega t$ or $\sin\omega t$ over the wave period, respectively:

$$
\begin{aligned}
F_a sin(\epsilon_{Fz}) &= \frac{2}{NT} \int_0^{NT} F_z(t) cos(\omega t) dt \\
F_a cos(\epsilon_{Fz}) &= \frac{2}{NT} \int_0^{NT} F_z(t) sin(\omega t) dt
\end{aligned}
\tag{5.6}
$$

T is the oscillation period and N is the number of oscillations investigated. For the present case the integrals do not start from 0 but from the 10^{th} oscillation and N correspond to 5. Free body have 6 degrees of freedom, every motion has an influence on each degree of freedom. Therefore there are 36 added mass and damping coefficients. They are expressed with double subscript. For example A_{xy} is the added mas coefficient along the x axis due to the motion along the y axis. For the present case a and b become A_{33} and B_{33}, respectively the added mass and damping representing the vertical hydrodynamic reaction due to heave.

It is important to remember that A_{33} and B_{33} estimated with the presented method are valid only for the oscillation frequency, and they are function of the amplitude motion. For additional reading on the equation of motion and potential coefficient refer to Journée et al. [18]. The added mass and damping were extracted applying the theory described above and using a Matlab script coded by MSc. Frédérick Jaouën.

5.3. Controls settings

As mentioned in the introduction of this chapter the forced heave oscillation requires additional settings in ReFRESCO controls file. First of all, the grid is not static any-more but it is deformed every time step according to the imposed motion. In ReFRESCO the motion is obtained by moving or deforming the grid. The moving grid option moves or rotates the entire mesh, boundaries are moved as well and the cells shape do not change. For example, in the present case the heave motion will be simulated moving the entire mesh (the free surface obviously fixed) up and down. On the opposite, the deforming grid keep fixed the boundaries and deform the cells shape inside the grid to simulate the vessel motion. The second method is more complex and slower compared with the moving grid because every time step ReFRESCO needs to compute a new mesh according to the motion. However, the moving grid cannot be always used. Fig. 5.2 displays the effect of the moving grid when the mesh rotates. If the rotation angle is too large the free surface reaches the top or the domain bottom (longer is the domain smaller angles will cause this problem).

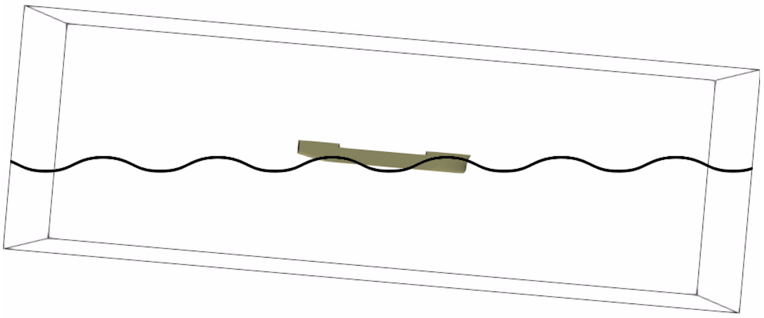

Figure 5.2: Example of moving grid effect

As the only motion allowed in this chapter is a vertical translation, the moving grid was used, however the bottom boundary needs to be changed from BC SlipWall to BC Pressure. With BC SlipWall the entire water

Table 5.2: Numerical settings forced heave

Parameters	Momentum	Pressure	Free surface
Solver	GMRES	GMRES	GMRES
Pre-conditioner	JACOBI	BJACOBI	BJACOBI
Convergence tolerance	0.01	0.01	0.01
Maximum iterations	200	500	500
Discretization Scheme	QUICK	-	REFRICS
Imp. relaxation Max.	0.5	-	0.5
Imp. relaxation Min.	0.9	-	0.9
Imp. relaxation Factor	40	-	40
Exp. relaxation	0.25	0.15	0.25

volume would moved together with the mesh. On the opposite, with a BC Pressure only the grid moves and the free surface do not. In the free floating case (chapter 6) the vessel will be free to pitch and the deform method will be used.

In the forced heave case the imposed motion consists of a periodic translation along the vertical axis. The oscillation frequency was set equal to the incoming wave frequency of the fixed vessel case (4.3 $\frac{rad}{s}$ at model scale, 0.8 $\frac{rad}{s}$ at full scale). In Abeil [6] the RAO for heave at the mentioned frequency is 0.2 $\frac{m}{m}$. The amplitude motion is set equal to:

$$z_a = 0.2a_{inc} \tag{5.7}$$

The amplitude and frequency motion were defined to reproduce the heave motion experienced by the vessel in the free floating case. To reproduce the same heave motion experienced by the vessel during the free floating case, a_{inc} was set equal to the incoming wave amplitude described for the fixed vessel.

Simulations carried out with the moving grid showed more difficulties to reach an acceptable convergence tolerance ($L_2 = 10^{-4}$ or lower). The implicit and explicit relaxation factors for the equations were gradually decreased until the solution provided a satisfactory convergence behaviour. In table 5.2 the new numerical settings are reported. A decrease in the relaxation factor (be aware that the relaxation factor analysed in chapter 4 referred to waves propagation, now the relaxation factors refer to the set of solved equations) stabilize the convergence, but at the same time requires more outerloops to reach the steady convergence tolerance increasing the computational time.

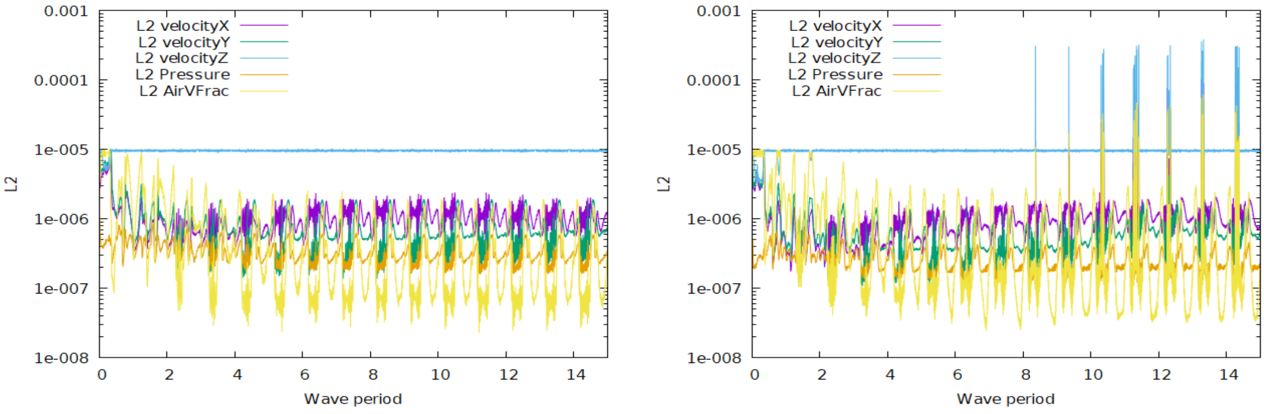

(a) Medium mesh Time step $\frac{T}{400}$ (b) Fine mesh Time step $\frac{T}{200}$

Figure 5.3: Steady Residuals for the medium and the very fine mesh convergence level $L_2 = 10^{-5}$

In Fig. 5.3 comparison between a good convergence (Fig. 5.3a) and a bad convergence (Fig. 5.3b) is shown. On one hand, in Fig. 5.3a the steady residuals for all the interested quantities are lower than the steady convergence tolerance for the entire simulation. On the other hand, in Fig.5.3b convergence problems regularly affects the simulation.

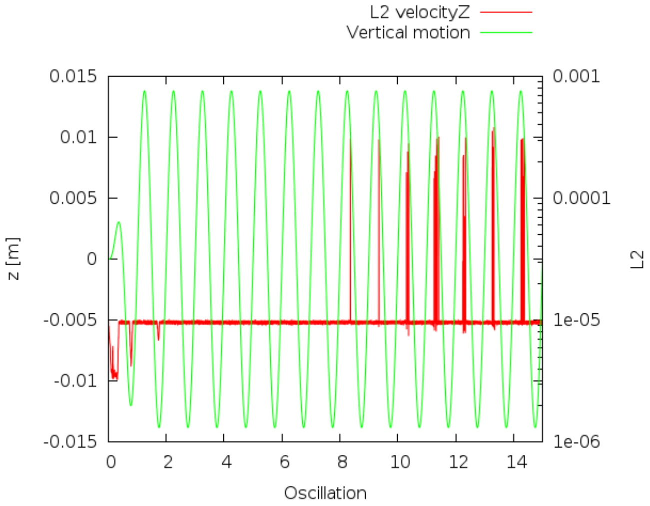

Figure 5.4: imposed motion and steady residuals for the fine mesh with time step $\frac{T}{200}$ and $L_2 = 10^{-5}$

In order to better understand the causes of this problem in Fig. 5.4 the steady residuals (only L_2 velocity z is reported for sake of clarity) and the imposed motion are plotted together. The imposed motion values (represented by the green line) refer to the left y axis, the right y axis represents the L_2 value (red line). The convergence problems arise after the 8^{th} oscillation and tend to increase in time. High values of L_2 occur when the vessel translation approaches the zero and $\dot{z}$ is at maximum. Additional help to visualize the residuals distribution in the domain comes from Fig. 5.5. Cells with the highest residuals (highlighted by the red color) are uniformly distributed only on the first cells layer. The unusual distribution (they drastically decrease their value in the second cells layer) and their location in an area where the flow velocity is almost zero suggests that they are produced by numerical error. Different settings configuration were investigated, such as a different deformation method or lower relaxation factors for the equations. Unfortunately none of them improved the results.

A Courant number lower than 0.3 was observed for simulations with satisfactory convergence behaviour. This value is lower than the maximum Courant number allowed in the previous chapters (in the empty domain and in the fixed vessel a Courant number lower than 1.0 was sufficient to guarantee a good convergence). In Denisart [11], a Courant number lower than 0.2 is suggested to avoid steady residuals stagnation, nevertheless the reason for this residuals distribution remains unclear.

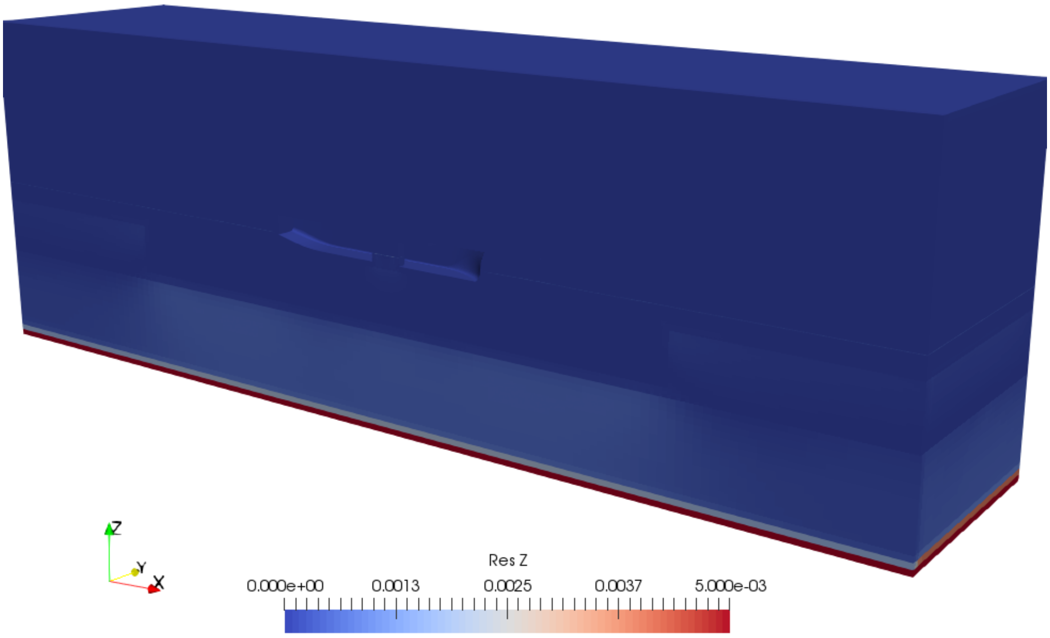

Figure 5.5: Vertical velocity residuals distribution for the fine mesh with time step $\frac{T}{200}$ and $L_2 = 10^{-5}$

5.4. Refinement study

Settings presented in section 5.3 were used for the refinement study necessary for the estimation of the numerical uncertainty. Results from the refinement study are in table 5.3. Due to the convergence problem explained above, only fine time steps could be used. Therefore a complete refinement study as presented in chapter 3 was not possible due to project time limit. At first, the very fine mesh was not included. Unfortunately the number of simulations was not enough to provide acceptable results. The numerical uncertainty was in the order of magnitude of 50% or higher for all the data. To reduce the numerical uncertainty a very fine mesh with a time step $\frac{T}{500}$ was included. Only one L_2 convergence tolerance was investigated for the very fine mesh, because the results from previous simulations showed a non negligible contribution of the iterative error for simulations with steady convergence tolerance equal to 10^{-4}. The convergence refinement stopped at $L_2 = 10^{-5}$, however non negligible differences are noticeable between 10^{-4} and 10^{-5} and lower convergence levels should be investigated to ensure that the iterative error is now at least two order of magnitude lower than the discretization error. Simulations with lower steady residuals tolerance were not launched due to a lack of time in the project. Added mass and damping were extracted only for the simulations used to compute the numerical uncertainty.

Grid	Timestep	Converge Level	$\bar{a}_{rel}$ $\frac{m}{m}$	F_x N	F_z N	A_{33} kg	B_{33} $\frac{kg}{s}$
Coarse	$\frac{T}{100}$	10^{-4}					
		10^{-5}					
	$\frac{T}{200}$	10^{-4}	2.071 ± 1.2%	28.747 ± 0.2%	402.826 ± 0.4%		
		10^{-5}	6.749 ± 0.7%	20.886 ± 0.2%	650.030 ± 0.2%	1459.8	4067.8
	$\frac{T}{400}$	10^{-4}	0.564 ± 8.0%	40.062 ± 0.4%	515.354 ± 0.4%		
		10^{-5}	6.567 ± 0.7%	20.375 ± 0.3%	624.043 ± 0.2%	1495.4	3976.2
Medium	$\frac{T}{100}$	10^{-4}					
		10^{-5}					
	$\frac{T}{200}$	10^{-4}	3.811 ± 1.8%	26.900 ± 0.4%	539.520 ± 0.8%		
		10^{-5}	6.661 ± 1.1%	20.880 ± 0.3%	639.969 ± 0.1%	1443.0	3866.9
	$\frac{T}{400}$	10^{-4}	0.661 ± 20.0%	41.442 ± 1.37%	468.068 ± 0.5%		
		10^{-5}	6.504 ± 1.2%	20.431 ± 0.2%	616.247 ± 0.1%	1480.3	3762.0
Fine	$\frac{T}{100}$	10^{-4}					
		10^{-5}					
	$\frac{T}{200}$	10^{-4}					
		10^{-5}					
	$\frac{T}{400}$	10^{-4}					
		10^{-5}	6.526 ± 1.9%	20.327 ± 1.0%	620.471 ± 0.1%	1453.7	3669.6
Very Fine	$\frac{T}{800}$	10^{-5}	6.545 ± 1.9%	20.575 ± 1.3%	610.0 ± 0.1%	1460.1	3581.4

Table 5.3: Analysis of wave amplitude inside the moonpool, forces on the hull, added mass and damping.

5.4.1. Convergence level

Two steady convergence tolerance were investigated, $L_2 = 10^{-4}$ and $L_2 = 10^{-5}$. Results for the medium mesh with time step $\frac{T}{400}$ and $L_2 = 10^{-4}$ and 10^{-5} are reported respectively in appendix C.1 and C.2. Large differences are noticeable between the two simulations, meaning the iterative error plays a major role as error source for $L_2 = 10^{-4}$. In Fig 5.6 the time traces for the relative wave elevation and the forces at M MID are compared. On the left column the results with L_2 equal to 10^{-4} are reported and on the right results with $L_2 = 10^{-5}$. It is clearly noticeable how the effect of the iterative error completely modifies the solution. Concluding, the iterative error for simulations involving a steady convergence tolerance = 10^{-4} is non negligible and the numerical uncertainty was evaluated for simulations with $L_2 = 10^{-5}$.

In the plot of $\bar{\eta}_{rel}$, the results from the moonpool probes located at the edges are included. They are reported as absolute wave elevation to ignore the influence of the vessel motion. The free surface at the edges of the domain is flat for the entire simulation. The small variations in time trace are in the order of magnitude of the cells height and they are produced by the free surface interpolation within a cell. This is confirmed looking at Fig. 5.7 where the time trace for the coarse mesh is reported. In this case the cells height is larger compared to the medium mesh and the wave elevation near the boundaries increases. η_{abs} at the edges is always in the order of magnitude of the cells height.

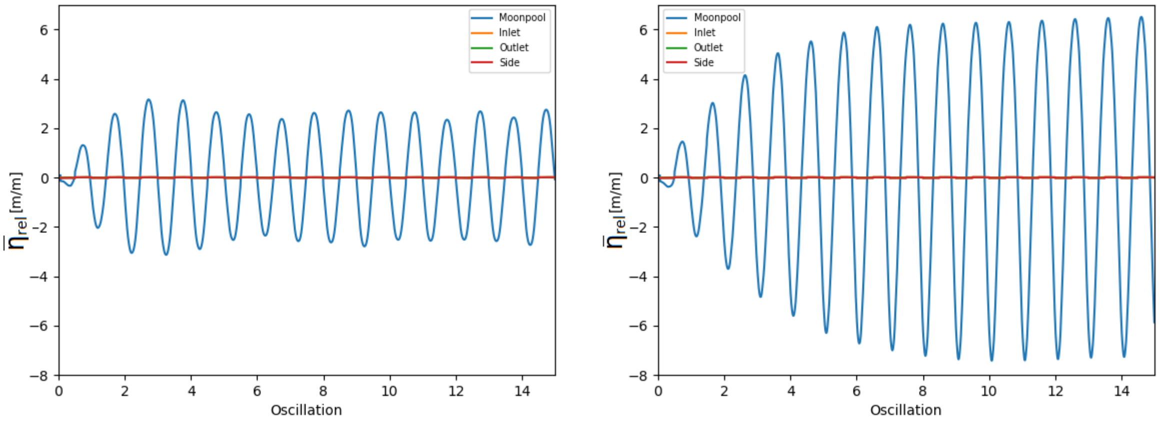

(a) η_{rel}, $L_2 = 10^{-4}$

(b) η_{rel} $L_2 = 10^{-5}$

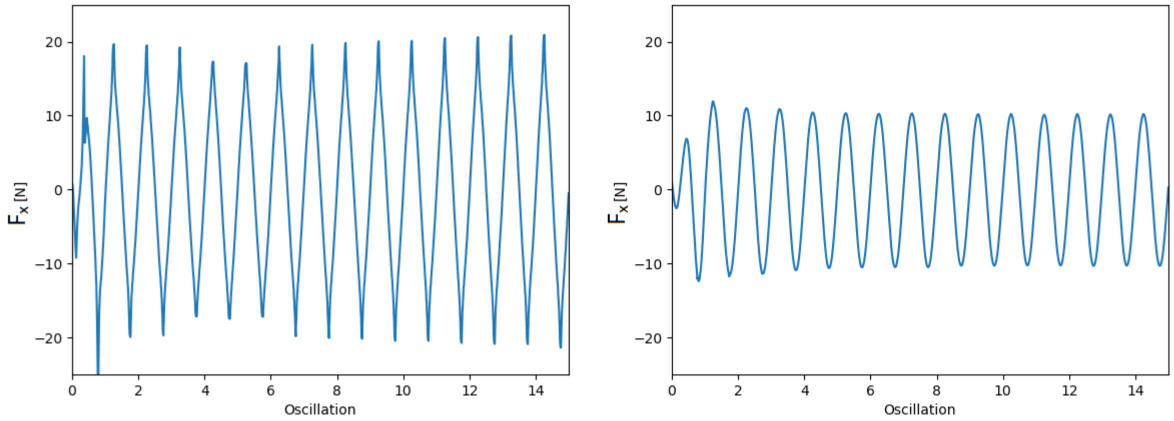

(c) Time trace F_x, $L_2 = 10^{-4}$

(d) Time trace F_x, $L_2 = 10^{-5}$

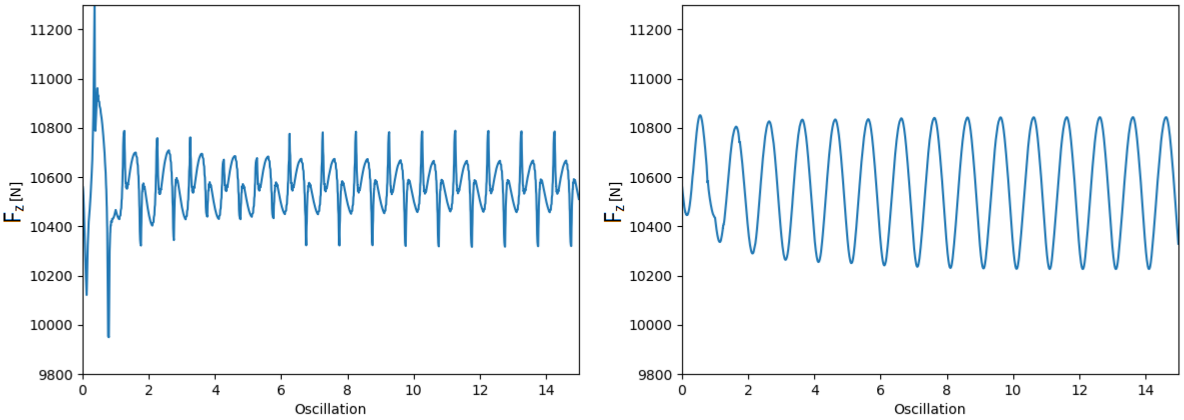

(e) Time trace F_z, $L_2 = 10^{-4}$

(f) Time trace F_z, $L_2 = 10^{-5}$

Figure 5.6: Comparison between different convergence level for the medium mesh and time step $\frac{T}{400}$

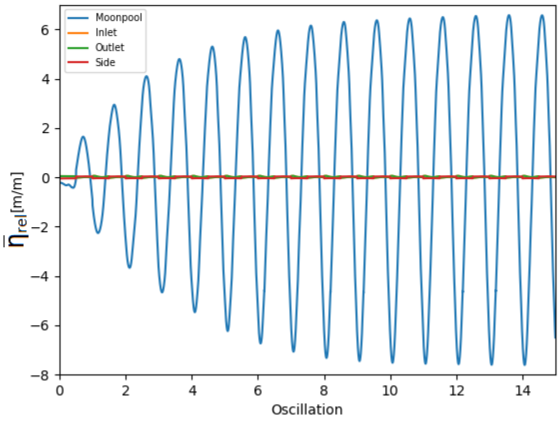

Figure 5.7: Time trace of the η_{rel} for the coarse mesh with time step $\frac{T}{400}$ and $L_2 = 10^{-5}$

Table 5.4: Comparison between time steps for the forced heave case.

Grid	Timestep	a_{rel} %	F_x %	F_z %	A_{33} %	B_{33} %
Coarse	$\frac{T}{200}$	1.84	2.47	4.08	2.41	2.28
	$\frac{T}{400}$	0.00	0.00	0.00	0.00	0.00
Medium	$\frac{T}{200}$	6.57	2.17	3.77	2.55	2.75
	$\frac{T}{400}$	0.00	0.00	0.00	0.00	0.00

5.5. Numerical uncertainty

The numerical uncertainty was estimated using the same method presented in the previous chapters (section 4.14 and 3.5). Despite the very fine mesh, the analysed data present relatively large numerical uncertainties (excluding F_z). The results from the uncertainty analysis are collected in table 5.6 and plotted in Fig. 5.8. For sake of clarity the plots are represented from different point of view, ϕ_0 is always extrapolated at the origin of the axis $\frac{t_i}{t_1}$ and $\frac{h_i}{h_1}$. The data are also collected in table 5.4 and 5.5 (respectively the time step and the mesh refinement are highlighted) where the differences are expressed in percentage from the finest settings.

F_x is more sensitive to time step than mesh refinement. Looking at the results in the table 5.4 it is noticeable how the largest differences occur refining the time step. This can also be observed in Fig. 5.8a, the steepest slope of the fitted surface is along $\frac{t_i}{t_1}$ axis which means the largest variation occurs refining the time step. The same approach is applied to the other results. F_z and A_{33} are more sensitive to the time step refinement. On the opposite $\bar{a}_{rel}$ and B_{33} show larger sensitivity to the mesh refinement. Concluding, it is difficult to define the best settings configuration for all the interested quantities, the time step and the mesh refinement should be defined according to the interested data.

Even if differences between refinement level are always lower than 5.1%, the final uncertainties are much larger. In the method proposed by Eça and Hoekstra [12], the numerical uncertainty is obtained multiplying by a safety factor the estimated numerical error. The numerical error is function of the solution convergence order, the safety factor is defined according the scatter in the data set. Therefore, the differences between solutions in the refinement study are not sufficient to define the numerical uncertainty. For a deeper explanation of the mentioned method refer to Eça and Hoekstra [12].

5.6. Turbulence model

Conclusions from section 4.13 highlighted a non negligible effect of the turbulence model on the final results. The effect of the latter is investigated for the forced heave as well. Only the SKL model is used since differences with MENTER model are negligible. Results are collected in appendix C.3. For the same reason

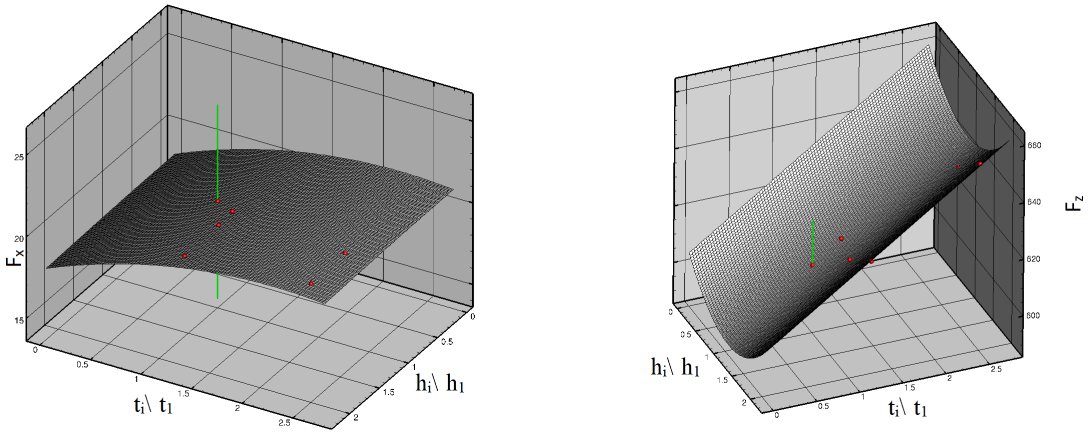

(a) F_x (b) F_z

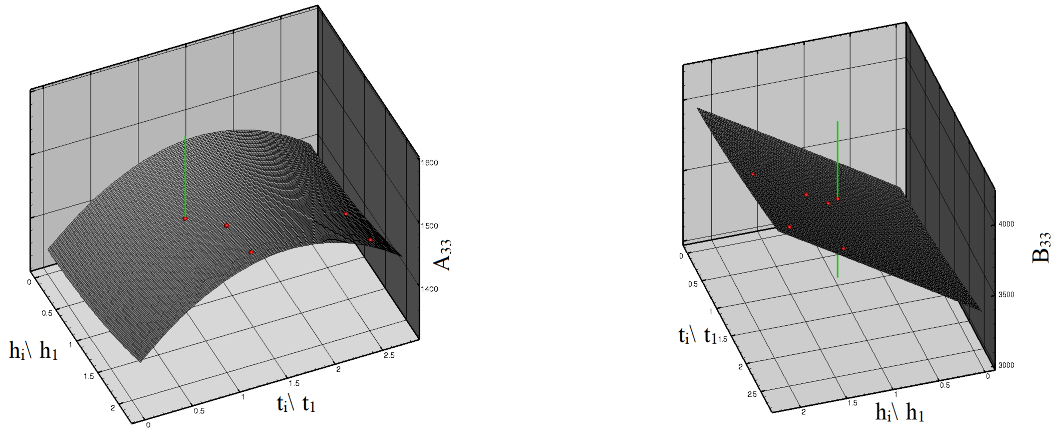

(c) A_{33} (d) B_{33}

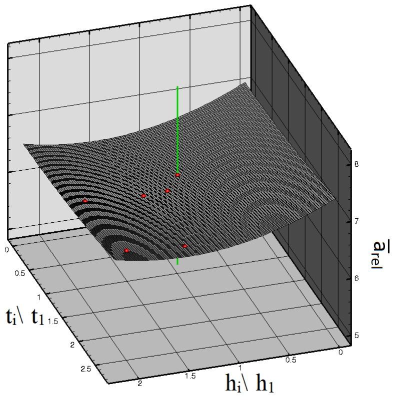

(e) a_{rel}

Figure 5.8: Fitting surfaces of the numerical uncertainty for the forced heave case

Table 5.5: Comparison between mesh size for forced heave case.

Timestep	Grid	a_{rel} [%]	F_x [%]	F_z [%]	A_{33} [%]	B_{33} [%]
$\frac{T}{200}$	Coarse	2.98	0.02	1.56	1.16	5.04
	Medium	0.00	0.00	0.00	0.00	0.00
$\frac{T}{400}$	Coarse	1.46	0.23	2.27	2.88	8.02
	Medium	4.53	0.51	1.02	1.86	2.49
	Fine	0.00	0.00	0.00	0.00	0.00

Table 5.6: Results for the uncertainty analysis for the forced heave

Item	ϕ_0	ϕ_1	U_ϕ
$\bar{a}_{rel}$	$7.06 \times 10^{+0}$	$6.54 \times 10^{+0}$	23.9%
F_x	$1.82 \times 10^{+1}$	$2.02 \times 10^{+1}$	29.5%
F_z	$6.04 \times 10^{+2}$	$6.09 \times 10^{+2}$	2.6%
A_{33}	$1.36 \times 10^{+3}$	$1.46 \times 10^{+3}$	9.0%
B_{33}	$3.14 \times 10^{+3}$	$3.58 \times 10^{+3}$	15.4%

explained in section 4.13 the medium grid and the time step $\frac{T}{200}$ were chosen for the simulation involving the turbulence model.

With turbulence model the water motion inside the moonpool results in a lower amplitude since part of the energy is dissipated by eddies. A lower wave elevation means a smaller net flux trough the bottom opening. As a consequence the pressure over the hull decreases resulting in a lower F_z. Results are summarized here below:

- $\bar{a}_{rel} = 5.11 \pm 1.0\ \%\ \frac{m}{m}$
- $F_x = 21.34 \pm 0.1\ \%$ N
- $F_z = 567.07 \pm 0.2\ \%$ N

Concluding, the influence of the turbulence model is non negligible even for the forced heave case. Results show a reduction in the wave elevation which affects the vertical force on the hull (the influence on F_x is negligible).

5.7. DIFFRAC

The added mass and the damping extracted from the forced heave simulations have been used to tune the potential flow solver DIFFRAC. DIFFRAC is a wave diffraction program (developed by MARIN) capable of calculating the wave loads and motion response of free floating or moored structures in regular waves, including their hydrodynamic interaction. The program is applicable to both shallow and deep water and has been validated against many physical model test results. DIFFRAC is based on a three dimensional source distribution technique for the solution of the linearised velocity potential problem. For the computations, the mean wetted part of the hull is approximated by a number of plane elements. Each element represents a distribution of source singularities, each of which contributes to the velocity potential describing the fluid flow. The rigid lid method is used to suppress the effect of irregular frequencies. A damping lid may be used to damp resonant water motions [1].

It is standard procedure in DIFFRAC to model the whole vessel at full scale, the same wave condition as described in table 3.1 were used. Extensive work were conducted by Peyredieu du Charlat [25] on the application of DIFFRAC for the moonpool case. He investigated the effect of mesh refinement and different boundary conditions. As a result of his work, guidelines about grid refinement and boundary conditions were provided. His guidelines are applied to the present case. For additional reading about DIFFRAC settings refer to Peyredieu du Charlat [25]. The relaxation zone in ReFRESCO showed a good absorption capacity and in DIFFRAC was not necessary to simulate the domain edges as walls, the open water condition was used. The potential theory assumes water as an incompressible, non rotational and inviscid flow. The viscous damping is consequently neglected which results in an overestimation of the water motion in the range next to the resonant frequency. In DIFFRAC, it is possible to specify a damping lid on the free surface to reduce the response amplitude. The damping factor (ϵ) influences the strength of the damping lid. A higher damping means a lower response amplitude. Although in this work ϵ already defines the phase difference, it is also used for the damping factor. This choice was made to keep the nomenclature of this work consistent with the DIFFRAC manual and the related literature. ϵ without subscripts will refer to the damping factor, with subscripts to a phase difference. In the present case, a damping lid was place over the free surface inside the moonpool. A range of values between $\epsilon = 0.001$ and 0.1 was investigate to define the right settings according to the CFD results. The range was chosen in accordance with Peyredieu du Charlat [25], he observed how a value larger than 0.1 completely suppressed the wave elevation inside the moonpool. Fig. 5.9 displays the vessel geometry used for DIFFRAC calculations. Only the mean wetted area is modelled in DIFFRAC. In the top view (Fig. 5.9b) the red area represents the damping lid applied to the free surface. The ϵ value is constant all over the free surface inside the moonpool.

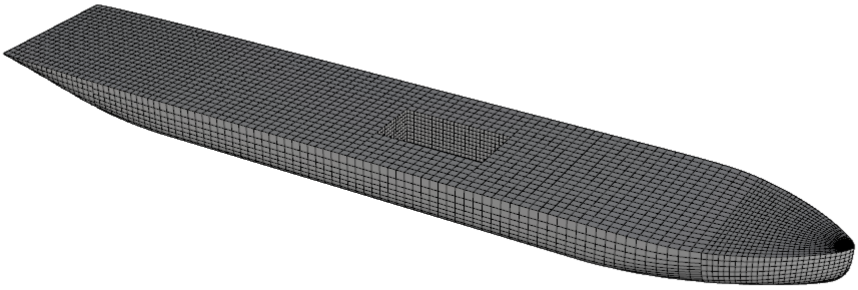

(a) Perspective view.

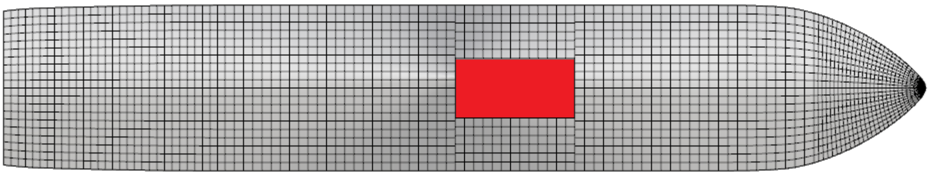

(b) Top view.

Figure 5.9: Vessel geometry used for DIFFRAC computations

DIFFRAC results are reported in table 5.7. Added mass and damping were estimated for 3 frequencies and different damping factors. The range of investigated frequencies is in accordance with results presented in chapter 7, for additional explanation about this choice refer to the mentioned chapter. Amplitude and phase of F_z are here reported for sake of completeness. DIFFRAC results are extracted simulating the floating vessel. The ReFRESCO results are reported in table 5.8 at full scale. CFD results are reported at full scale to compare them with results from potential flow solver.

To compare the two method results are plotted in Fig. 5.10. Results obtained with DIFFRAC are represented by circles (different colors for different ϵ values). Added mass and damping have been extracted both for laminar and turbulence model using medium mesh, time step $\frac{T}{200}$ and $L_2 = 10^{-5}$ to compared the two methods. As explained in section 4.13 the viscous layer could not be satisfactory modelled for the coarse mesh. The blue triangle represents the results obtained from the refinement study (ϕ_0) with the numerical uncertainty. Added mass and damping are amplitude dependent; the linear potential theory assumes amplitude an velocities small enough so hydrodynamic reaction forces are proportional to motion amplitude. To take into account the amplitude dependence a simulation with half the oscillating amplitude was performed, results are expressed by the green triangles.

In order to avoid misunderstanding is important to remember that the damping presented in this section is the damping produced by the vessel, while ϵ is a numerical value which increases the damping of the

Table 5.7: Results from DIFFRAC, F_z expressed in N, ϵ_{Fz} in rad, A_{33} in ton and B_{33} $\frac{ton}{s}$

	$\omega = 0.75$ $[\frac{rad}{s}]$				$\omega = 0.775$ $[\frac{rad}{s}]$				$\omega = 0.80$ $[\frac{rad}{s}]$			
ϵ	F_z	$\epsilon_{F_z - z_a}$	A_{33}	B_{33}	F_z	ϵ_{Fz}	A_{33}	B_{33}	F_z	ϵ_{Fz}	A_{33}	B_{33}
0.001	2401	2.08	79573	34706	4180	2.20	83696	43124	10911	1.40	42864	77145
0.02	2470	2.02	77543	34939	4197	2.08	77488	42268	7896	1.50	50274	53995
0.04	2538	1.95	75585	34817	4125	1.99	73067	40245	6561	1.64	55209	43985
0.06	2597	1.90	73917	34429	4022	1.95	70401	38055	5850	1.74	58298	38673
0.08	2646	1.85	72566	33886	3917	1.94	68871	36090	5413	1.85	60382	35389
0.10	2685	1.83	71511	33273	3822	1.95	68020	34439	5118	1.90	61875	33162

Table 5.8: Damping and added from ReFRESCO

	Laminar				SKL			
ω	F_z N	ϵ_{Fz} rad	A_{33} ton	B_{33} $\frac{ton}{s}$	F_z N	ϵ_{Fz} rad	A_{33} ton	B_{33} $\frac{ton}{s}$
0.750	21919	5.83	89990	32898	21252	5.82	86816	32555
0.775	22706	5.75	83604	38315	21722	5.79	81944	33949
0.800	21041	5.73	71596	35673	21304	5.80	75742	31559

water inside the moonpool. In addition the damping extracted by DIFFRAC has only the contribution of the potential damping while the results extracted from ReFRESCO include the estimation of the viscous damping.

The added mass shows a decreasing trend increasing the oscillation frequency. ϵ has an influence on both F_z and ϵ_{Fz} which represents the phase difference between the monitored force and the vessel motion. A decreasing trend of F_z increasing ϵ is noticeable for all the frequency, however due to the phase change the added mass does not follow a constant trend(the added mass is function of the force amplitude and phase difference). $\epsilon = 0.1$ is within 9% of accuracy compared with ϕ_0 and ϕ_1 for the added mass. $\epsilon = 0.1$ has the closest agreement to A_{33} estimated by ReFRESCO. In Fig. 5.10a it is shown how reducing z_a the added mass estimated by ReFRESCO approaches DIFFRAC results. The solutions obtained with laminar and turbulent model show the same decreasing trend even if it is less accentuate than data estimated with DIFFRAC.

An opposite trend compared to the added mass is reported for damping. A decrease in the damping lid on the moonpool increases F_z and consequently the damping produced by the vessel (refer to equation 5.5). Including the turbulence model in ReFRESCO slightly reduces F_z and ϵ_{Fz} and consequently the estimated B_{33}. This differences increase with the oscillation frequency. For $\omega = 0.75$ $\frac{rad}{s}$ all the simulations tend to similar B_{33} values. In addition, the damping tend to a constant line increasing ϵ. B_{33} is more sensitive to the amplitude oscillation than A_{33}. Dividing the oscillation amplitude by two increases B_{33} by 20%. Damping estimated by DIFFRAC with $\epsilon = 0.06$ differs of 4% from B_{33} estimated with ReFRESCO oscillating the vessel at half of the amplitude.

Finally, according to the added mass and damping estimated by ReFRESCO ϵ values between 0.06 and 0.1 will be used to tune DIFFRAC.

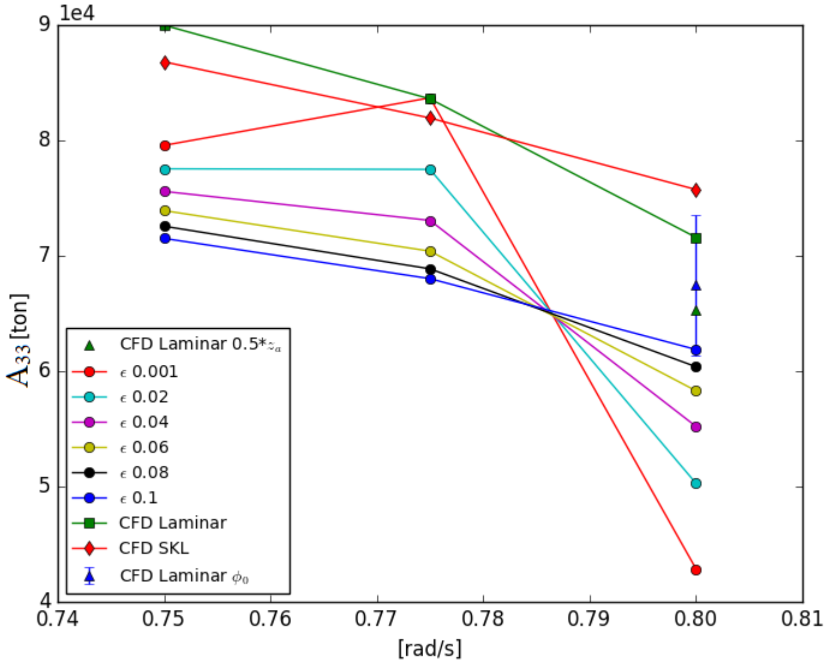

(a) A_{33}

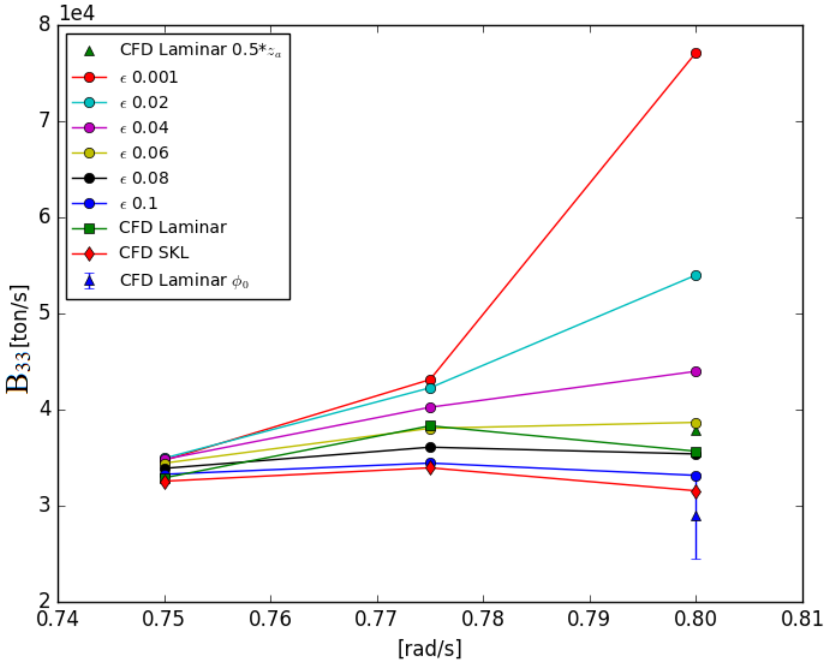

(b) B_{33}

Figure 5.10: Comparison between the added mass and damping calculated with ReFRESCO and DIFFRAC

5.8. Conclusion

The settings obtained in chapter 4 in terms of domain dimensions, grid refinement and boundary conditions were the starting point of this chapter. In order to simulate the vessel heaving the moving grid was used. For this case, insignificant differences were noticed between moving and deforming grid. Moving grid was chosen as faster. However, the bottom of the domain has to be changed from BC Wall to BC Pressure.

The forced heave oscillation is a special case where the capabilities of the relaxation zone can be easily investigated. 3 wave probes were added inside the domain. One near each domain edge, except for the symmetry boundary. η_{abs} was equal to zero during the entire simulation for each of the mentioned probes. Finally, at the edges of the domain the relaxation zone completely damp the free surface elevation. Therefore no reflection is expected from the domain boundaries.

A lower Courant number compared to the previous cases is necessary to reach the desired steady convergence tolerance. For the fixed vessel case a Courant number lower than 1.0 was sufficient. In this chapter the maximum Courant number acceptable was 0.3. The lower Courant number required finer settings for the refinement study. Thanks this reason less simulations were performed compared to the fixed vessel case. A very fine mesh was necessary to reduce the numerical uncertainty. A steady convergence of $L_2 = 10^{-4}$ showed a non negligible influence of the iterative error on the final results. For the numerical uncertainty $L_2 = 10^{-5}$ was used. Lower steady convergence tolerance should be investigated to ensure that the iterative error is now insignificant compared to the discretization error. However such simulations would require a too long computational time according to the time limit of this project.

In this chapter diffraction calculations were computed using the potential flow code DIFFRAC. A damping lid was placed inside the moonpool to include the effect of the viscous damping on the free surface elevation. The damping factor ϵ was tuned according to the added mass and damping extracted from URANS computations. For the added mass, $\epsilon = 0.1$ displayed 9% of difference compared to the estimated added mass by ReFRESCO for ω= 0.80 $\frac{rad}{s}$. For the same frequency, $\epsilon = 0.06$ showed the best agreement for the damping estimation. DIFFRAC and ReFRESCO results differed of 3%. ϵ between 0.06 and 0.1 will be used to tune DIFFRAC and compare the free surface elevation with ReFRESCO and experimental results..

6

Free floating vessel

In this chapter the simulations involve the free floating case in head waves. The aim of this unit is to define the right settings for simulations involving the free floating vessel. Steady residuals will be monitored to ensure a control over the iterative error. In this chapter the results obtained previously in terms of domain dimensions, mesh and controls settings are applied to the free floating case. The present simulations involve the solution of the equations of motion and the mesh deformation. Both of them greatly affect the performance of the computations in terms of time. Simulations for the free floating case require three or four times more time than fixed vessel simulations (using the same mesh and settings). Due to tight time constrain on the completion of this project, few simulations are conducted at this stage and only the coarse mesh is investigated. No refinement study is conducted and the numerical uncertainty is not assessed. For sake of simplicity the turbulence model was not included. The chapter is organized as follow. At first the loading condition and soft spring set-up used for the experimental tests by Abeil [6] are described in section 6.1. A new version of ReFRESCO was launched during the last period of the project and it was used for the free floating case. As suggested by the developers few settings were investigated, their results are reported in 6.2.

In this chapter the attention is focused on the numerical settings necessary to perform a good simulation for the free floating case. A physical analysis, together with a comparison of the results with experiments are provided in the next chapter.

6.1. Simulation set-up

To accurately reproduce the test set-up used in Abeil [6], the same loading condition and soft spring stiffness are modelled in the CFD simulations. For sake of completeness they are here reported in table 6.1 and 6.2. As for the previous cases only half of the vessel was simulated. Due to the symmetry conditions not all the degrees of freedom were enabled. Heave, pitch and surge were the motions allowed. The properties of the incoming waves were already presented in table 3.1. For additional reading about domain dimensions and mesh generation refer to chapter 3 and 4.

Table 6.1: Loading condition.

Description	Full scale	model scale
∇	52216 m^3	2.16 m^3
x_{CoG}	99.98 m	3.46 m
y_{CoG}	0.00 m	0.00 m
z_{CoG}	14.56 m	0.50 m
k_{xx}	14.52 m	0.50 m
k_{yy}	50.38 m	1.74 m
k_{zz}	50.77 m	1.76 m

Table 6.2: Spring stiffness per mode

Mode	Stiffness full scale	Stiffness Model scale
Surge	1.07E+02 $\frac{kN}{m}$	1.28E+02 $\frac{N}{m}$
Sway	2.65E+02 $\frac{kN}{m}$	3.17E+02 $\frac{N}{m}$
Yaw	3.03E+06 $\frac{kNm}{rad}$	4.33E+03 $\frac{Nm}{rad}$

6.2. Convergence tolerance

When the project started, at MARIN the latest version of REFRESCO was the 2.3.0. In the previous chapters this version was used for all the simulations. During the time of this project a new version of REFRESCO (2.4.0 trunk 2) was deployed on the server. This new version was used for the present chapter. The reason for this change is the new possibility available in ReFRESCO 2.4.0 t2 to combine the deforming mesh together with the equations of motion, in the old version this was not possible. All the following simulations involve the coarse mesh, time step $\frac{T}{400}$ and $L_2 = 10^{-5}$. The steady convergence level was chosen according to the results obtained in the previous chapters. The time step was defined in conformity with the Courant number. As explained in chapter 5 a Courant number higher than 0.3 resulted in a poor convergence of the steady residuals. Simulations with time step $\frac{T}{200}$ have a maximum Courant number of 0.9, with $\frac{T}{400}$ the maximum Courant number is 0.2.

The vessel motion is obtained deforming the grid every 20 outerloops. Deforming the mesh every few outerloops increases the accuracy of the simulation but, at the same time the computational time drastically increases. 20 outerloops is the default value used at MARIN. The choice of the deforming grid instead of moving grid has been already explained in section 5.3. Simulations with deforming grid showed greater difficulties to converge compared to simulations with fixed grid. The software developers suggested to investigate the effect of two different discretization schemes for the momentum equation, and a lower unsteady convergence tolerance for all the equations. The convergence tolerance which is referred now is not related to the steady but to the unsteady residuals. Results are collected in appendix D. The two discretization schemes are QUICK (Quadratic Upwind Interpolation for Convective Kinematics) and LIMITED QUICK (QUICK scheme with flux limiter). Refer to section 3.3 for a description of the discretization schemes. At first, simulations for this case were carried out with QUICK without flux limiter. The influence of the flux limiter is noticeable in the convergence of the steady residuals in Fig. 6.1. The solution without flux limiter is occasionally influenced by poor steady convergence with peaks up to an order of magnitude larger than the desired tolerance. Applying the flux limiter these peaks disappear. Results of the two simulations are reported in table 6.3 . Concluding, the flux limiter provides a better steady residuals convergence and it is included in the next simulations.

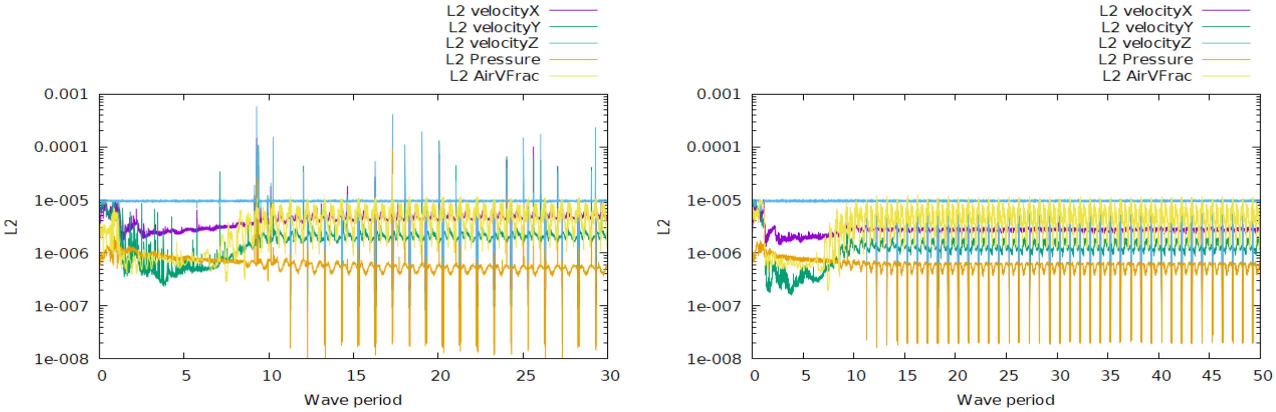

(a) steady residuals without flux limiter

(b) steady residuals with flux limiter

Figure 6.1: Steady residuals for the coarse mesh, time step $\frac{T}{400}$ and steady convergence $L_2 = 10^{-5}$

Table 6.3: Result comparison between QUICK and LIMITED QUICK

	QUICK	LIMITED QUICK
$\bar{a}_{rel}$	1.43 ± 3.3%	1.38 ± 1.9%
F_x	89.36± 3.1%	91.51± 3.1%
F_z	478.65 ± 1.2%	481.6± 1.1%

The next investigated setting is L_1. L_1 is the unsteady residuals tolerance, for a definition of it refer to chapter 2. The default value of L_1 in ReFRESCO is 10^{-2} for each equation. This value was gradually decreased

Table 6.4: L_1 refinement study

L_1	10^{-2}	10^{-3}	10^{-4}
$\bar{a}_{rel}$	1.38 ± 1.9%	1.40 ± 1.8%	1.40 ± 1.9%
F_x	91.51± 3.1%	91.66 ± 3.1%	92.40 ± 2.9%
F_z	481.6± 1.1%	485.97± 0.8%	490.67± 0.9%

for all the equations (momentum, pressure and free surface equation) until the differences between solutions became negligible. Results are summarized in table 6.4 and the post processed pictures are collected in appendices D.2 to D.4. The refinement of the convergence tolerance brings variations less than 1% in the results. However, a convergence tolerance of 10^{-3} showed a reduction in the computational time of 10.5%. This gain vanishes if the unsteady convergence tolerance is further decreased. Simulations with a lower L_1 require less outerloops to reach the desired steady convergence tolerance, reducing the number of outerloops per time step and consequently the computational time. Nevertheless, decreasing further L_1 implies more iterations per outerloop. Therefore the gain in time due to reduction of outerloops vanishes. Concluding, a $L_1 = 10^{-3}$ was chosen for the next simulations.

6.3. Conclusions

In this chapter the results obtained from the previous cases are applied to the free floating case. Domain and grid generation were not changed compared to the previous cases. In order to reproduce the test conducted at SMB a soft spring set-up was modelled. Due to the high computational time required for the simulations, only the coarse mesh with time step $\frac{T}{400}$ and steady convergence $L_2 = 10^{-5}$ was investigated. A new version of ReFRESCO was used for which the influence of unsteady convergence tolerance, and flux limiter on the discretization scheme for the momentum equations were investigated. Results obtained suggest the use of the flux limiter to stabilize the steady rediuals convergence and $L_1 = 10^{-3}$.

7

Results comparison

In the previous chapters the goal was to asses the numerical uncertainty for ReFRESCO applied to a vessel with a rectangular moonpool. In this chapter ReFRESCO is validated against experimental results for the free floating vessel. The solution verification was carried out only for $\omega = 0.80\ \frac{rad}{s}$. Therefore ReFRESCO is validated only for the mentioned frequency. Two additional frequencies are investigated in this unit to observe the solution trend. In section 7.6 and 7.7 fixed vessel and forced heave are compared to model tests. Even if a validation study is not possible (experimental results for fixed vessel and forced heave are missing) the results are still important. The objective is to show whether is possible or not to simplify the numerical model maintaining a the same degree of accuracy of the free floating case and, at the same time reduce the computational time. Solutions obtained with 3D potential flow are included to investigate their accuracy despite the simplifications (for additional reading on the software used and its tuning refer to section 5.7).

Simulations involve three different incoming wave angular frequencies: $\omega = 0.75$ - 0.775 -0.8 $\frac{rad}{s}$ at full scale. The resonance for the piston mode is observed for these frequencies [6]. The mesh should be adapted varying the incoming wave frequency in order to maintain a fixed number of cells per λ. Nevertheless, for the simulations presented in this chapter the same mesh (already described in the previous chapters) was used. There are two reasons for this choice. The first one deals with the time limit of the project. Theoretically a new mesh per incoming wave frequency should be generated, however it was not possible for the lack of time. Secondly, the mesh was generated tacking into account the incoming wave with the highest angular frequency in the interested range. Lower wave frequency means longer waves and consequently more cells per λ. Concluding, only one grid was used as the mesh accuracy do not deteriorate lowering the incoming wave frequency.

Simulations for the fixed vessel and the forced heave were performed with medium mesh, time step $\frac{T}{200}$ and steady convergence level $L_2 = 10^{-5}$. The reason for this choice is the possibility to compare the Laminar results with simulations involving SKL turbulence model. The free floating results were calculated with coarse mesh, time step $\frac{T}{400}$ and $L_2 = 10^{-5}$. For additional explanation refer to the related chapters.

7.1. Free floating

In the free floating case the turbulence model was not included and only data from laminar simulations are available. A refinement study was not conducted, so the numerical uncertainty was not estimated. Nevertheless the uncertainty in Fig. 7.1 is calculated including the numerical uncertainty from the forced heave case. Discretization is the main source of error, and to validate the model is necessary to assess its magnitude. Consequently to validate the free floating case, the numerical uncertainty for the forced heave oscillation was used. The choice is motivated by the larger uncertainty produced by the forced heave compared to the fixed vessel case.

The free floating case is reported in Fig. 7.2. Six plots are reported, each of them reports the wave amplitude at one position in the moonpool. For additional information about probes location refer to section 4.3. On the x axis the investigated frequency range is reported. The blue circles represent $\bar{a}_{rel}$ for the experiment.

The related uncertainty bar represents the experimental uncertainty (± 4 mm for the wave probes used at SMB). The experimental results are reported for two additional frequencies to show the $\bar{a}_{rel}$ trend. The green triangles are $\bar{a}_{rel}$ for the CFD simulations, the uncertainty bars for ω = 0.75 and 0.775 $\frac{rad}{s}$ include only the statistical uncertainty (no refinement study was carried out for these frequencies). CFD results for ω = 0.80 are reported with numerical and statistical uncertainty (to highlight the difference it is plotted with a different color). Results obtained with DIFFRAC are reported for different ϵ.

For ω = 0.80 $\frac{rad}{s}$ the results are validated against the experiment within 14 % of accuracy. The accuracy for every wave probe is reported in table 7.1.

ω = 0.80 $\frac{rad}{s}$

	M AFT	SB AFT	M MID	SB MID	M FOR	SB FOR
Accuracy	13.2 %	13.1 %	13.4 %	14.0 %	12.8%	12.0 %

Table 7.1: $\bar{a}_{rel}$ accuracy for each wave probe.

Comparison error and validation uncertainty are shown in table 7.2.

ω = 0.80 $\frac{rad}{s}$

	M AFT	SB AFT	M MID	SB MID	M FOR	SB FOR
U_{val}	0.33	0.33	0.34	0.34	0.32	0.32
|E|	0.18	0.18	0.19	0.20	0.17	0.16
	Validated	Validated	Validated	Validated	Validated	Validated

Table 7.2: Free floating vessel validation

For the aft and the forward area of the moonpool ReFRESCO is able to capture the trend expressed by the experiment. The largest differences occur in the central area for ω = 0.75 $\frac{rad}{s}$. Here the differences are up to 25%. In order to understand why this large discrepancy occurs only for the specified frequency and only in a restricted area of the moonpool, it is necessary to have a deeper look in the experimental results. For sake of completeness observation conducted by Abeil [6] for ω = 0.75 $\frac{rad}{s}$ are here mentioned:

> At the wave frequency of 0.75 rad/s, the vertical motions increase substantially and are not uniform anymore: while the motion at aft and fore moonpool seems synchronized, there is a dephasing at the center: at first the motion at the center appears delayed with respect to that at the sides, but then catches up to surpass the amplitude at the sides, yielding a sharp peak, up to 5 m above mean water line. The motion remains further symmetrical with respect to centerline.

As clearly expressed by Abeil [6], for ω = 0.75 $\frac{rad}{s}$ the water motion at M MID and SB MID takes longer to get excited compared to the aft and forward areas of the moonpool. For this reason an additional simulation was performed, increasing the total time from 30T to 50T. The results are expressed by the blue stars in Fig. 7.1. Despite the longer simulation, $\bar{a}_{rel}$ confirms the value obtained with 30T. Simulations involving even higher number of wave periods were not performed as the computational time required would be too long. To further investigate this difference, the heave and pitch motion of the whole vessel were compared between the three methods. They are reported in Fig. 7.2. For ω = 0.775 and 0.80 $\frac{rad}{s}$ both the ReFRESCO and DIFFRAC results lay within the uncertainty of the experiments. On the opposite, large discrepancies are noticeable for ω = 0.75 $\frac{rad}{s}$. The experimental estimation of the heave response is three time higher than numerical methods. Fredriksen et al. [15] observed how the water motion inside the moonpool is a phenomena driven by vessel heave. Consequently the discrepancy noticed in $\bar{a}_{rel}$ inside the moonpool can be explained by a different estimation of the heave response. In Fig. 7.2b it is noticeable how the numerical solutions lay within the uncertainty bar of the experiments for the pitch response. The largest differences occur for the highest frequency. Here the solution estimated with ReFRESCO shows 35% of difference compared to the experimental solution. However the influence of the pitch on $\bar{a}_{rel}$ is lower compared to the heave.

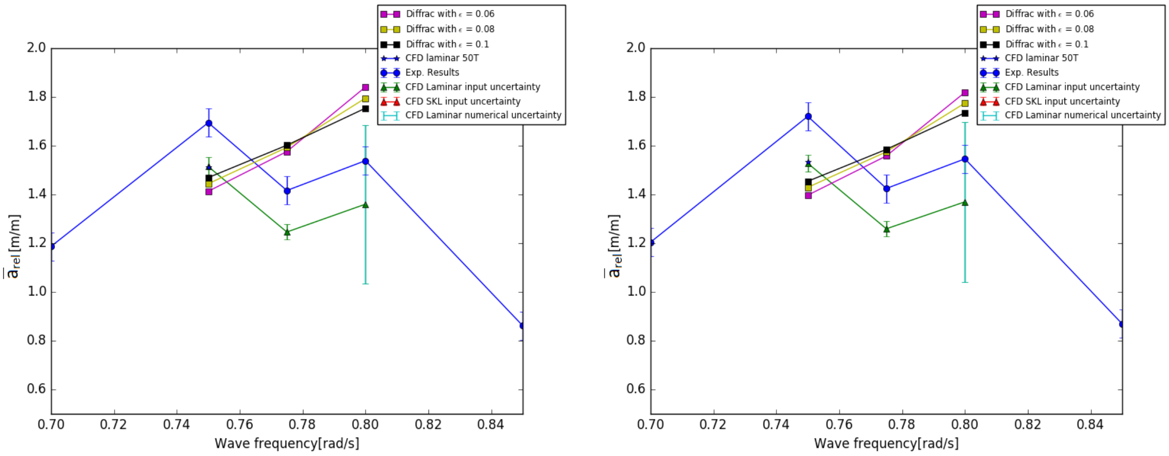

(a) M AFT

(b) SB AFT

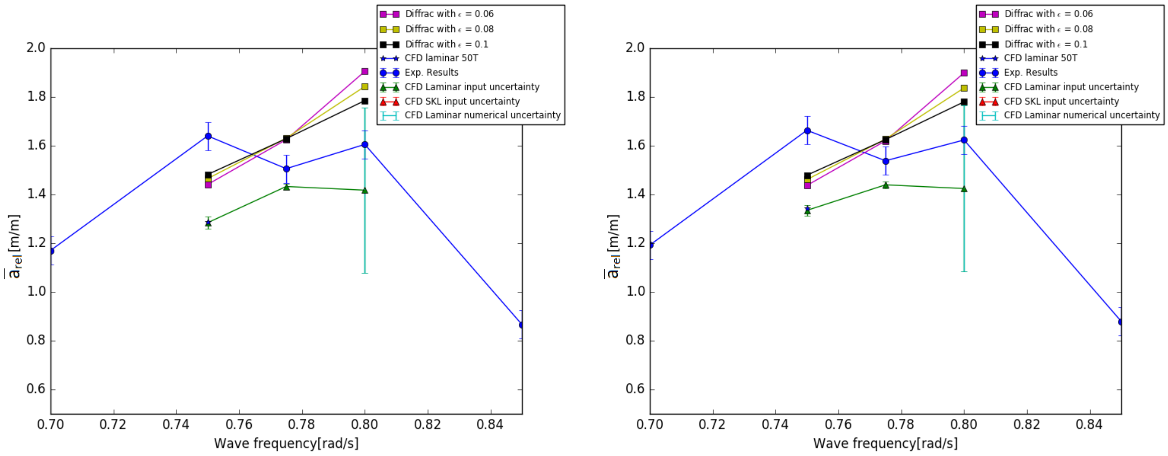

(c) M MID

(d) SB MID

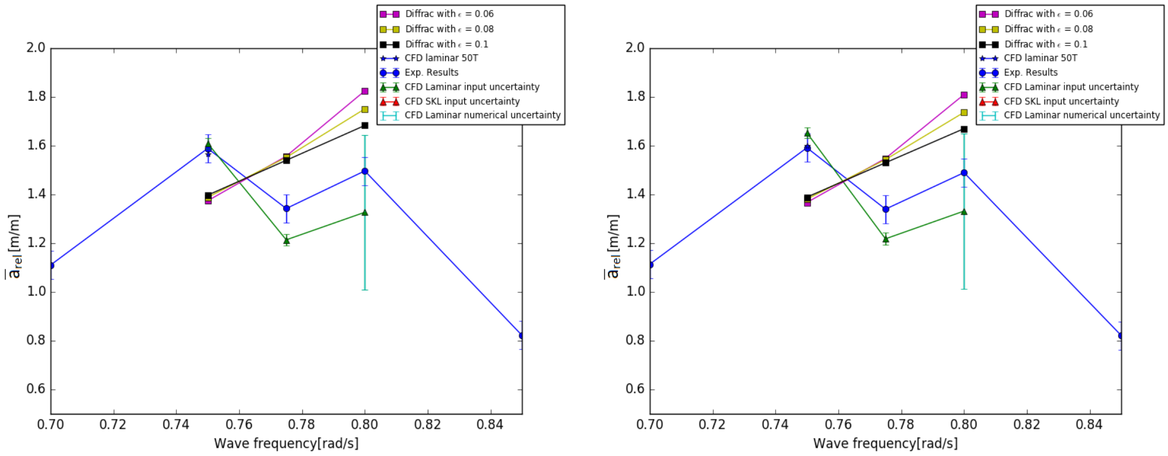

(e) M FOR

(f) SB FOR

Figure 7.1: Wave amplitude for the free floating vessel at different wave probes

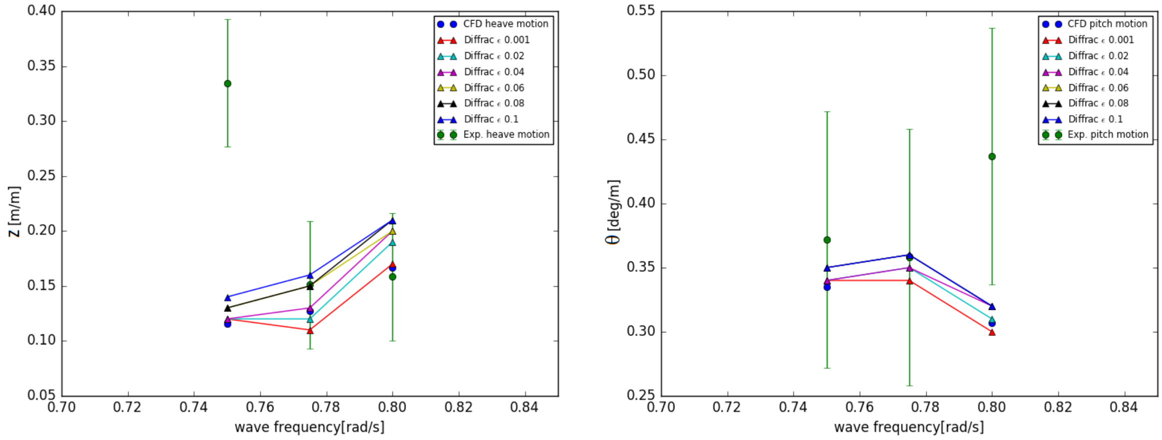

(a) Heave motion (b) Pitch motion

Figure 7.2: Comparison between heave and pitch motion estimated by experiment, ReFRESCO and DIFFRAC

7.1.1. Wave pattern

To further investigate the rate of agreement between the experiment and ReFRESCO results the time traces of $\bar{\eta}_{rel}$ are compared. In Abeil [6] for the investigated frequencies only the wave pattern for $\omega = 0.775\ \frac{rad}{s}$ along the mid line is displayed. Fig. 7.3 reports both the results from experiment (Fig. 7.3c), and numerical simulation. Plot of Fig. 7.3c has been copied from Abeil [6] for sake of comprehension. The reader can notice how the time trace along the mid line is not captured by ReFRESCO. The experiment clearly shows a non-harmonic behavior that is missing in the numerical solution. Only in Fig. 7.3b the influence of a second harmonic is noticeable, nevertheless a satisfactory agreement is still missing. To explain this difference is worthy to remember the low number of cells both for wave length and wave height in the coarse mesh (table 4.3). These values are below the recommended guidelines to correctly capture the wave distribution (implemented in the medium mesh). Unfortunately, as already explained in chapter 6, free floating simulations with the medium mesh were not performed.

In Fig. 7.4 are reported the 3D visualization of the water motion inside the moonpool for the analysed frequencies at the last simulated wave period. The white color represents value above the displayed scale. For $\omega = 0.75\ \frac{rad}{s}$ both the water motion at 30 and 50 T are reported. In addition to the free surface elevation the streamlines are plotted. The velocity magnitude is highlighted by the streamline colors. This is included to observe how the water motion changes modifying the incoming wave frequency. At $\omega = 0.75\ \frac{rad}{s}$ it is easy to recognize the observation done by Abeil [6]. A de-phase of the wave elevation is present in the central area of the moonpool while the highest regions are the forward and aft areas. The highest velocities are near the moonpool walls and they decrease moving to the center. For $\omega = 0.775\ \frac{rad}{s}$ the velocity distribution changes, the highest velocities are at the central area of the moonpool where free surface has the highest elevation. A more uniform motion is noticeable for $\omega = 0.80\ \frac{rad}{s}$.

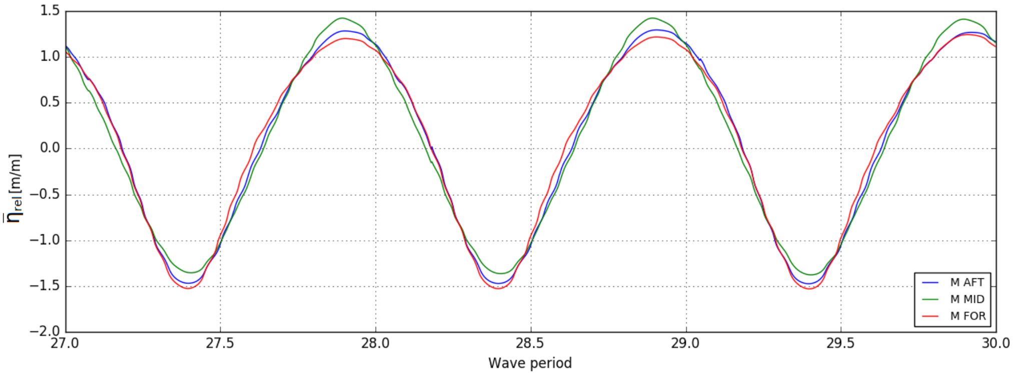

(a) Time trace estimated with ReFRESCO of $\bar{\eta}_{rel}$ inside the moonpool for $\omega = 0.775\ \frac{rad}{s}$

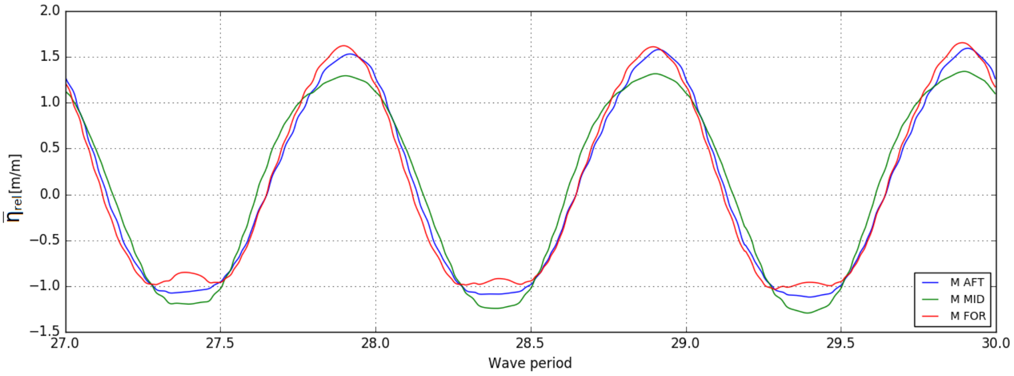

(b) Time trace estimated with ReFRESCO of $\bar{\eta}_{rel}$ inside the moonpool for $\omega = 0.75\ \frac{rad}{s}$

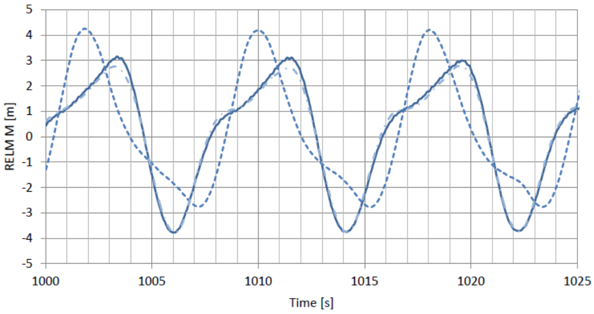

(c) Time trace of $\bar{\eta}_{rel}$ for $\omega = 0.755\ \frac{rad}{s}$ reported in Abeil [6]. $\bar{\eta}_{rel}$ are extracted along the centreline inside the moonpool. Dash line correspond to M MID, dotted and dash M FOR, continuous line M AFT

Figure 7.3: Comparison between time trace of $\bar{\eta}_{rel}$ estimated by ReFRESCO and the experiment.

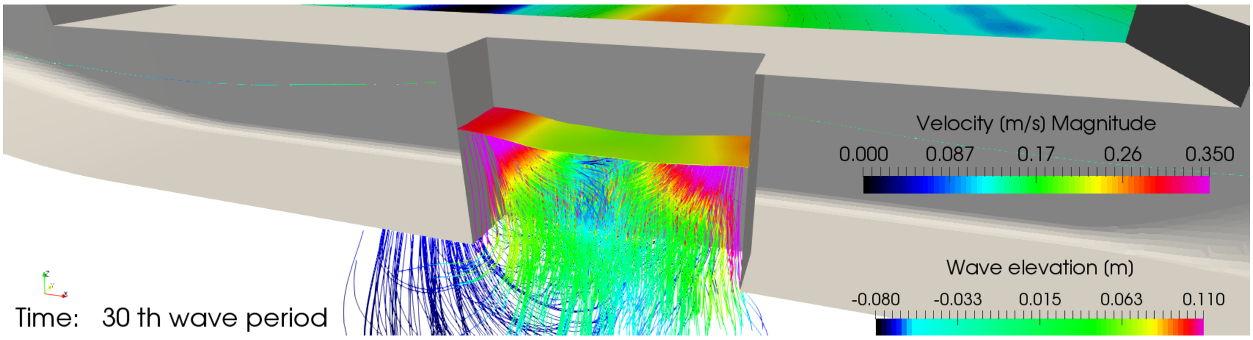

(a) T = 30, $\omega = 0.75\ \frac{rad}{s}$

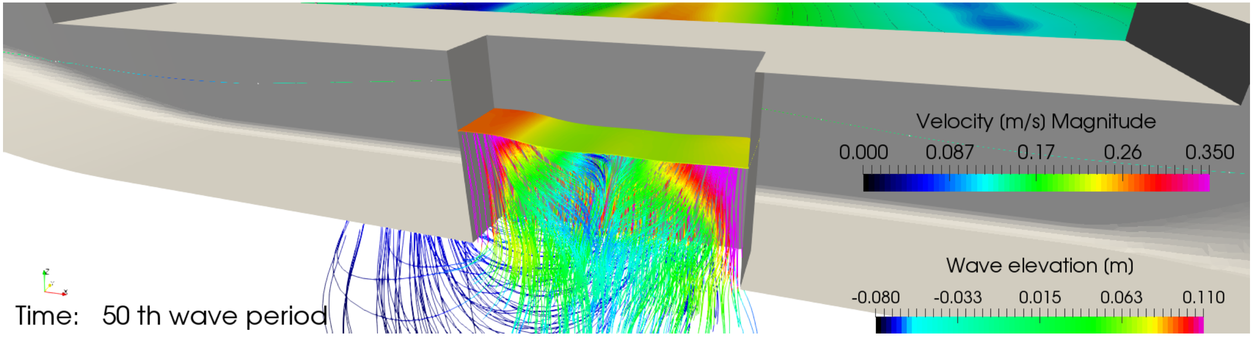

(b) T = 50, $\omega = 0.75\ \frac{rad}{s}$

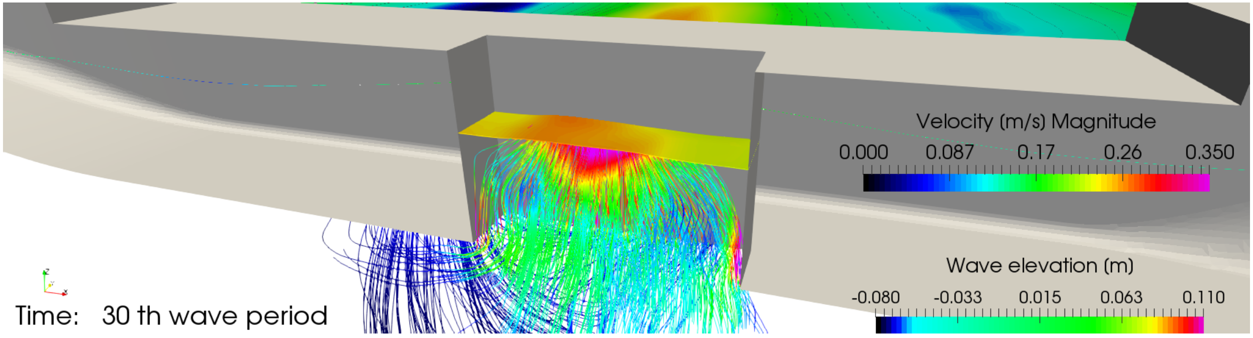

(c) T = 30, $\omega = 0.775\ \frac{rad}{s}$

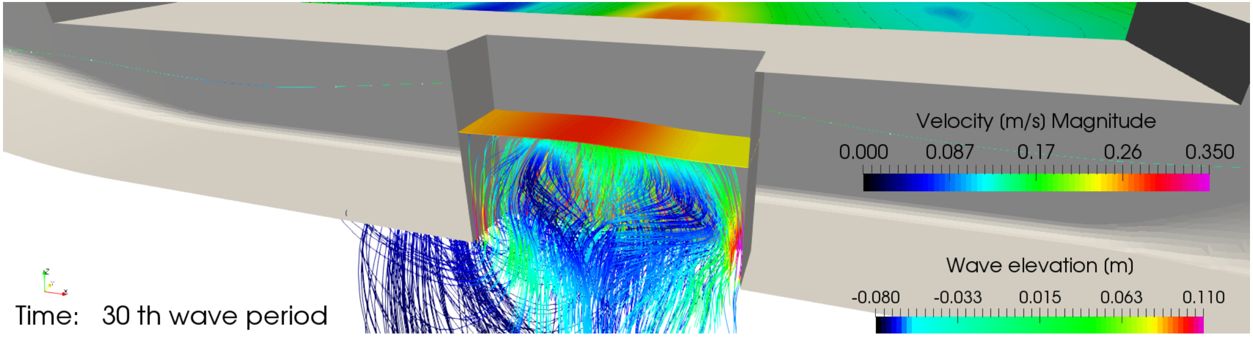

(d) T = 30, $\omega = 0.80\ \frac{rad}{s}$

Figure 7.4: Wave motion inside the moonpool

7.1.2. Diffrac results

The analysis of the DIFFRAC results start from the vessel motions reported in fig. 7.2. ϵ influences both the vessel heave and pitch. ϵ is only applied inside the moonpool which means the water motion inside the moonpool influences the global motion of the vessel. This is in accordance with results obtained by Fredriksen et al. [15]. Increasing ϵ increase the vessel response (Fig. 7.2a). In order to explain it let's recall the formula for the heave response amplitude operator:

$$z_a = \frac{F_a}{\sqrt{[(C-(M+A)\omega^2)^2]+[B\omega]^2}} \tag{7.1}$$

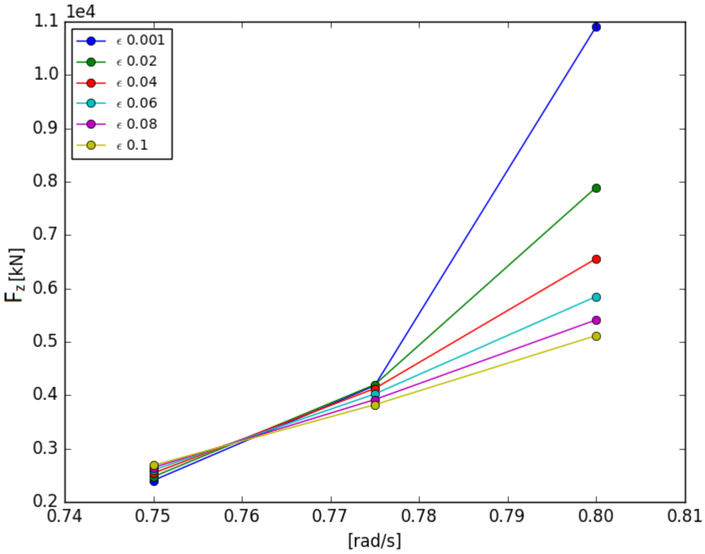

Figure 7.5: F_z estimation for different ϵ in DIFFRAC

In Fig. 7.5 the forces estimated by Diffrac are plotted, data are collected in table 5.7. As already described in section 5.7 DIFFRAC simulations were carried out at full scale. In table 5.8 CFD data were scaled to full model to make them comparable with solutions from potential slow solver. F_z increases with frequency. In the frequency resonant range the motion is driven by damping. For $\omega = 0.80\ \frac{rad}{s}$ the largest influence of ϵ are noticeable. The same conclusions can be observed looking at added mass and damping (Fig. 5.10). Increasing the incoming wave frequency increases the role played by B_{33} which means the resonant vessel motion is estimated by DIFFRAC around $\omega = 0.80\frac{rad}{s}$. Despite the increase of B_{33} with ϵ, the vessel motion increases, which means F_z grows faster than damping.

Looking at the water motion inside the moonpool (Fig. 7.2) ϵ has an interesting influence on $\bar{a}_{rel}$. Near the resonant frequency of the vessel increasing ϵ decrases $\bar{a}_{rel}$ which is an expected consequence. Nevertheless, moving out the resonant region ϵ inverts its influence, higher values mean higher $\bar{a}_{rel}$. However the largest influence of ϵ on $\bar{a}_{rel}$ is noticeable for $\omega = 0.80\ \frac{rad}{s}$. DIFFRAC accuracy in estimate the water motion and the vessel motion compared to the experimental results is in the same order of magnitude of ReFRESCO. $\epsilon = 0.1$ provides the best estimation compared to the experimental results. Although there is a the good agreement between the potential flow solver and the other methods, the wave amplitude trend is not captured. In addition, it is worthy to remember the results estimated with DIFFRAC are based on linear potential theory. According to different publications [5, 6, 15] the water motion inside the moonpool is a non linear phenomenon. Different incoming wave elevation should be modelled in ReFRESCO to further investigate the accuracy of a linear potential flow solver.

7.2. Fixed vessel

Comparison results for the fixed vessel case are displayed in Fig. 7.6. Fixed vessel experiment are missing, therefore experiments refer to relative wave amplitude extracted from the free floating case. Numerical solutions report the absolute wave amplitude ($\bar{a}_{abs}$). Red triangles are $\bar{a}_{abs}$ for simulations with turbulence model SKL.

The reader can notice how the CFD simulations underestimate the wave elevation at every location and every incoming wave frequency. The largest differences occur for $\omega = 0.75\ \frac{rad}{s}$. The trend described by the experiment is capture only in the forward area of the moonpool. As already discussed, the turbulence model significantly decreases $\bar{a}_{abs}$. Simulations for the fixed vessel conducted by DIFFRAC display different agreement for different wave probe. For $\omega = 0.80\ \frac{rad}{s}$ a damping lid of $\epsilon = 0.06$ shows a good agreement in the aft area of the moonpool. The central and the forward part requires a $\epsilon = 0.08$. $\epsilon = 0.1$ underestimates $\bar{a}_{abs}$ everywhere. The agreement between DIFFRAC and the experiment tend to decrease reducing the frequency. The trend displayed by the experiment is not captured by DIFFRAC as well.

To conclude, the fixed vessel case underestimate the wave amplitude inside the moonpool. The modelling error introduced neglecting the equations of motion is too large to be ignored.

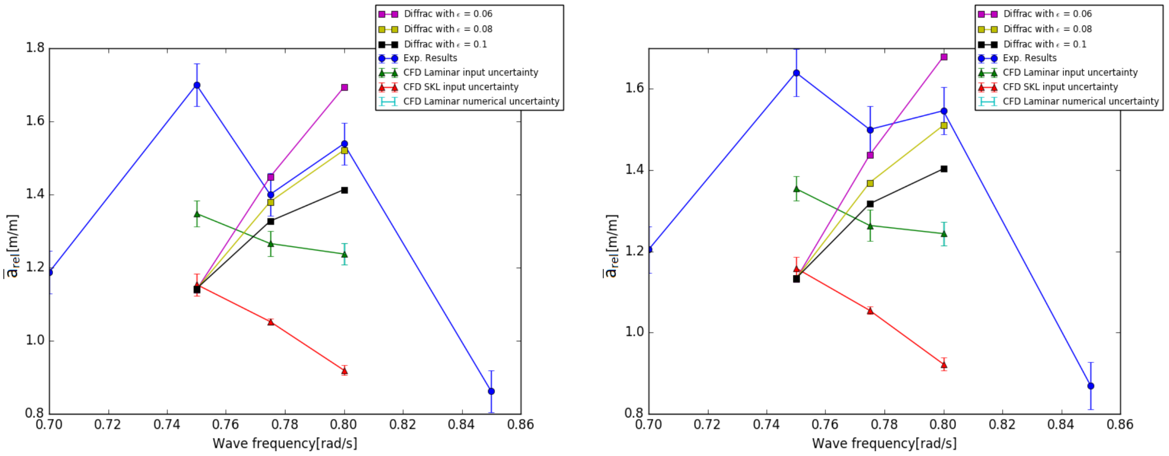

(a) M AFT (b) SB AFT

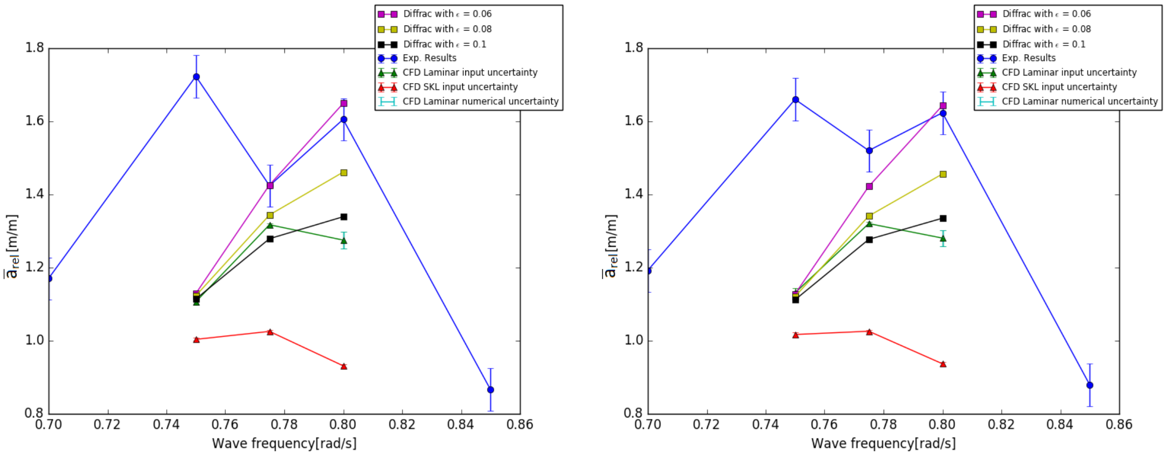

(c) M MID (d) SB MID

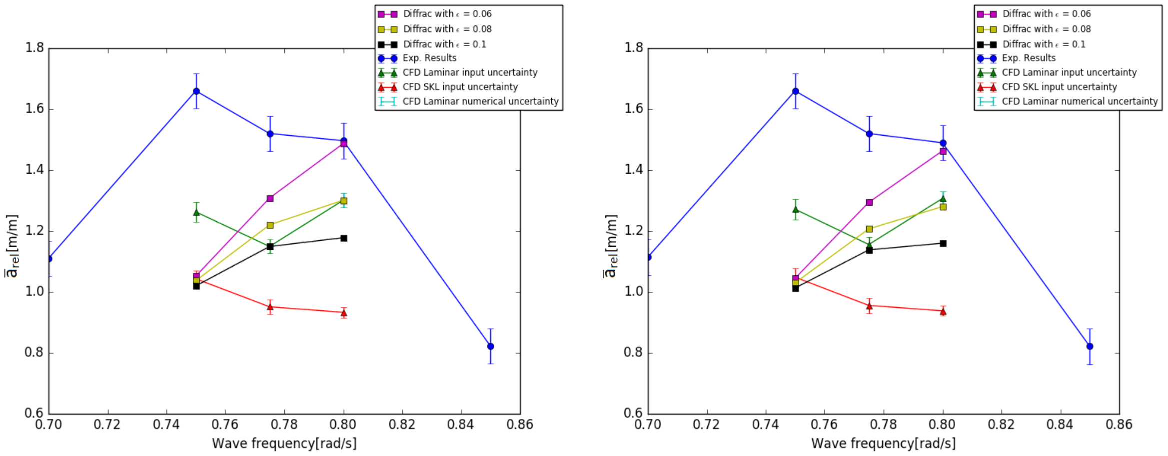

(e) M FOR (f) SB FOR

Figure 7.6: Wave amplitude for the fixed vessel at different wave probes

7.3. Forced Heave

In chapter 5, the relative wave amplitude was calculated using equation 7.2 because an incoming wave amplitude was missing.

$$\bar{a}_{rel} = \frac{a_{rel}}{z_a} \tag{7.2}$$

However, results from the forced heave cannot be directly compared to the free floating experiments because they are expressed using two different relative amplitude operators. In the forced heave case the RAO is calculated respect to the vessel heave. The relative amplitude operator of the experiment is calculated respect to the incoming wave amplitude. To compare them the experiments results have to be converted in an RAO respect to the vessel heave. This is done using the following equation:

$$\begin{aligned} \bar{a}_{rel} &= RAO_{a_{inc}} \frac{1}{RAO_{heave}} \\ RAO_{a_{inc}} &= \frac{a_{rel}}{a_{inc}} \\ RAO_{heave} &= \frac{a_{rel}}{z_a} \end{aligned} \tag{7.3}$$

Where $RAO_{a_{inc}}$ is the response amplitude operator calculated respect to the incoming wave amplitude. RAO_{heave} is the RAO respect to the vessel heave. Although the results are now comparable, it is important to be aware of the limit of this comparison. Vessel heave estimated by ReFRESCO differs from the experimental estimation (Fig. 7.2a). This is particularly true for $\omega = 0.75\ \frac{rad}{s}$. Results are reported in Fig. 7.7. As already described for in the previous sections only the relative amplitude estimated for $\omega = 0.80\ \frac{rad}{s}$ with laminar model was verified. The uncertainty bar for the other frequencies only include the statistical uncertainty. Both the laminar and the turbulence model underestimate $\bar{a}_{rel}$. The best agreement occurs for $\omega = 0.75\ \frac{rad}{s}$. Nevertheless, thanks to the large difference between the heave motion estimation between ReFRESCO and the experiments the accuracy of this comparison is questionable. To conclude, the forced heave oscillation case underestimate the relative wave amplitude respect to the experimental results.

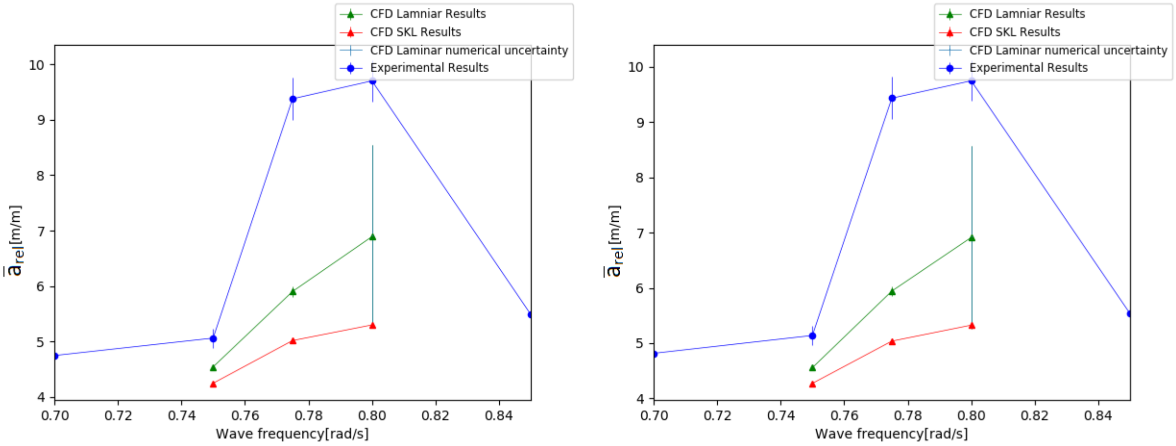

(a) M AFT (b) SB AFT

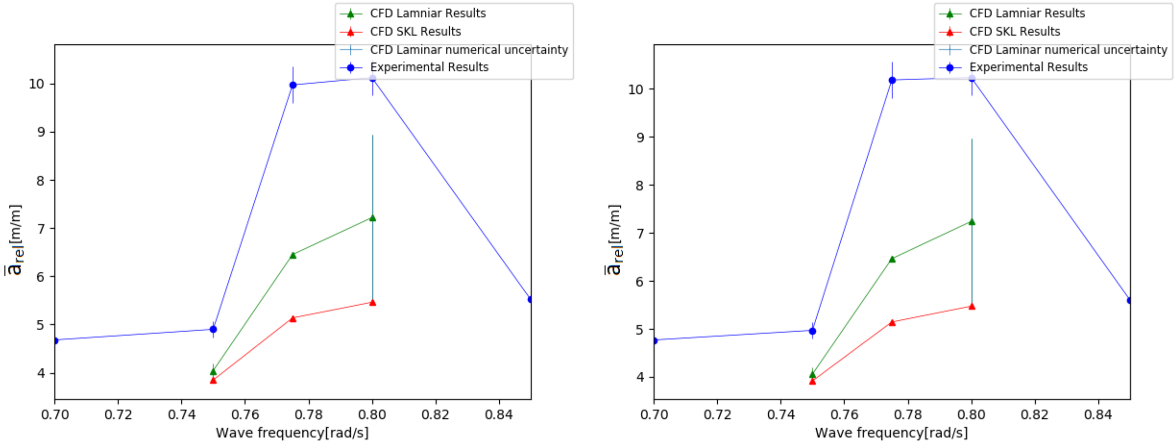

(c) M MID (d) SB MID

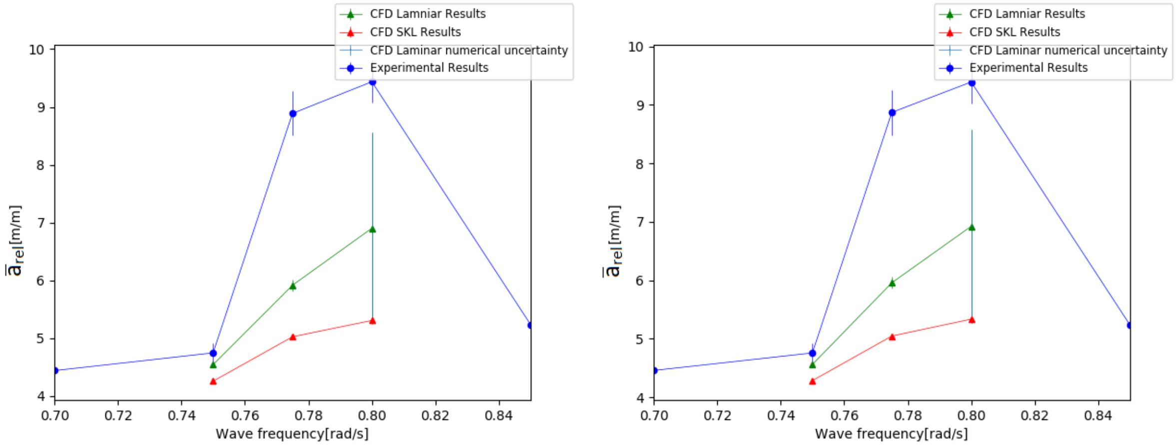

(e) M FOR (f) SB FOR

Figure 7.7: Wave amplitude for the forced heave oscillation at different wave probes

7.4. Conclusions

The aim of this chapter was to assess the accuracy of ReFRESCO for the free floating vessel compared to experimental results. ReFRESCO has been validated against the experimental results for $\omega = 0.8\ \frac{rad}{s}$. ReFRESCO results are within 14 % of accuracy compared to experimental results. The accuracy compared to model test varies across the domain. The lowest difference occurs in the forward area of the moonpool. Here the difference between ReFRESCO and experiments is within 12%. The largest difference occurs at the middle of the moonpool (14% of difference).

Fixed vessel and forced heave case were compared to model test results. Even if the results could not be validated the conclusions are still important. The aim was to investigate the possibility to simulated a simplify case compared to the real flow problem with an acceptable degree of accuracy. Both of the cases showed a modelling error too high to be neglected. Therefore, the water column inside the moonpool is excited by a combination of incoming wave and vessel heave. This conclusion is in accordance with results obtained by Fredriksen et al. [15] and Aalbers [5].

To further investigate the accuracy of ReFRESCO compared to experimental results, the vessel heave and pitch were investigated. For $\omega = 0.8\ \frac{rad}{s}$ the difference between the vessel heave motion estimated by ReFRESCO and the experiments is 6%. ReFRESCO solutions lay within the uncertainty bar of the experiment both for $\omega = 0.8$ and $0.775\ \frac{rad}{s}$. For $\omega = 0.75\ \frac{rad}{s}$ the vessel heave motion estimated by the experiment is three times larger than the CFD estimation. According to the conclusion above, this large difference is the leading factor for the differences in $\bar{a}_{rel}$ observed at the middle of the moonpool for the same frequency. The estimate pitch response for the numerical methods is in good agreement with the experiment except for the highest frequency. Nevertheless, pitch plays a minor role in $\bar{a}_{rel}$ estimation (the vessel CoG lay within the moonpool).

The linear potential flow solver DIFFRAC was tuned according to the added mass and damping estimated by the forced heave case. DIFFRAC shows differences up to 20% for the estimation of the vessel heave motion compared with ReFRESCO. Both heave and pitch are influenced by the damping factor. Therefore, the water motion inside the moonpool plays a significant role in the vessel motion. The conclusion is in accordance with Fredriksen et al. [15]. He observed how the water motion inside the moonpool has a non negligible influence on the vessel motion.

The relative wave elevation estimated with DIFFRAC has been compared to ReFRESCO and experiments. $\bar{a}_{rel}$ is affect by ϵ. For $\omega = 0.8\ \frac{rad}{s}$ the closest agreement between DIFFRAC and ReFRESCO osccurs for $\epsilon = 0.1$. In this case, $\bar{a}_{rel}$ estimated with DIFFRAC shows differences up to 25 % compared with ReFRESCO. Nevertheless, the largest difference between DIFFRAC and experimental results is 14%. However the DIFFRAC solutions have to be cautiously considered. Abeil [6] observed how the water motion for the investigated range of frequencies is a superposition of piston and second order sloshing mode. The trend displayed by the experiments shows this non-linearity. The trend captured by ReFRESCO and the experiment is not noticeable for DIFFRAC. To conclude, additional incoming wave amplitudes should be simulated to further investigate the accuracy of the linear theory applied to a non linear phenomenon.

Conclusions

The water column inside the moonpool of vessels operating in waves is excited by pressure fluctuations produced by external waves and vessel motions. Large water motions in the moonpool can lead to injuries for crew members and damage to deck equipment. The resonant frequency and water motions are functions of the moonpool dimensions, and therefore, moonpools are a critical aspect of the vessel design phase. CFD solvers had already been used in the design phase to predict the water motion and free surface elevation inside the moonpool. Nevertheless, a complete verification and validation study was still missing. In this project, the accuracy of ReFRESCO for water motion prediction inside a rectangular moonpool without additional damping devices has been investigated. This is a step forward in the applicability of numerical methods to moonpool designs.

To perform a validation study, experimental results are necessary. Model tests of a floating vessel in waves were carried out by Abeil [6]. His results were available for this project, and therefore, the validation has been made only for the mentioned case. Further, validation was performed only for regular head waves exciting the moonpool at the pumping frequency. As a result, ReFRESCO underestimates the wave amplitude inside the moonpool. Despite this underestimation, it has been validated against experimental results, showing and accuracy within 14%. The accuracy compared to model test depends on the position in the moonpool. The best agreement is in the forward area. Here, ReFRESCO and experiment results differ by 12%.

Simulations involving a fixed ship in waves or a heaving ship in calm water have been compared to model tests. The objective is to show whether it is possible or not to simplify the numerical model reducing the computational time. In reality, the relative wave elevation is caused by a combination (called coupling effect) of the incoming wave and vessel motion. As a result, the solution is underestimated if one of the factors is missing. This conclusion agrees with results obtained by Aalbers [5] and Fredriksen et al. [15].

Wave absorption at boundaries is a major problem in simulations with waves and without forward speed. The relaxation zone is able to absorb waves with different incoming directions and frequencies. However, it requires a larger domain than when the waves are absorbed by Sommerfeld 1. Moreover, the residuals are generally higher when the relaxation zone is used rather than the absorbing boundaries. In this project, an investigation into the relaxation zone parameters has been conducted. The objective was to optimize the absorption capacity keeping the iterative error insignificant compared to the discretization error. Concluding, the relaxation zone reveals a higher absorption capacity compared to Sommerfeld 1 boundary condition.

In addition to URANS computations, diffraction calculations were computed using the potential flow code DIFFRAC. A damping lid was located inside the moonpool to account for viscous damping that is not modelled by a potential flow solver as DIFFRAC. The damping factor was tuned according to added mass and damping estimated with ReFRESCO. At the angular wave frequency used for the validation study (0.8 $\frac{rad}{s}$ at full scale), the closest agreement between DIFFRAC and ReFRESCO occurs with ϵ (damping factor) equal to 0.1. For this case ReFRESCO and DIFFRAC show differences of 25% in the estimation of the wave amplitude inside the moonpool. Nonetheless, comparison between wave amplitude estimated with DIFFRAC (using ϵ = 0.1) and experiments reveal differences up to 13%. Therefore for this project, the combination of CFD and potential flow show a similar degree of accuracy compared to the use of CFD alone. However, thanks to the strong simplifications applied in the potential theory, DIFFRAC results have to be cautiously considered. The strongest simplification involves the use of linear theory to solve a non-linear problem [5, 6, 15]. As observed by Abeil [6], in the investigated range of frequencies the water motion is a superposition of the pumping mode and second-order sloshing mode. The result is a non-linear trend highlighted by the experiment. The same trend is not captured by DIFFRAC. To further estimate the accuracy of linear potential flow solver for non-linear phenomena, different incoming wave amplitudes should be investigated.

To conclude, the results of the present work are the starting point for future projects. In this thesis, the attention was focused on the piston mode. A complete verification and validation study should be performed for higher modes as well. The present work mainly dealt with the numerical aspects of the simulations. The next step is a deeper investigation into the physical phenomenon. At first how different incoming wave heights and directions influence the water motion inside the moonpool. Then, define which are the main design parameters which influence the water motion. Finally, identify which damping device has the highest efficiency to reduce the wave elevation.

Bibliography

[1] DIFFRAC. `http://www.marin.nl/web/Facilities-Tools/Software/Software-Sales.htm`. Accessed: 2017-11-12.

[2] "REFRESCO Controls". MARIN. Wageningen, the Netherlands, 4 2015.

[3] "Numerical Uncertainty Analysis". User Manual MARIN. Wageningen, the Netherlands, 4 2016.

[4] "Werkinstructie W0". Procedure Meshing. MARIN. Wageningen, the Netherlands, 2 2017.

[5] A. B. Aalbers. "The Water Motions in a Moonpool". *Ocean Engineering*, Vol.11(No.6):pp.557–559, 1984. Pergamon Press Ltd.

[6] B. Abeil. "Experimental Determination of Water Motions Inside a Moonpool". Proceeding of the ASME 2017 36th International Conference on Ocean, Offshore and Arctic Engineering, 2017. June 25-30, Trondheim, Norway.

[7] A. Bedos. "Moonpool Water Motion Prediction for a Ship at Zero-Speed in Sea Conditions". 08 2016. Report No. 70040.120-1-RD.

[8] T. Bunnik. "Implementation of Wave Generating and Absorbing Boundary Conditions in ReFRESCO". 2017. MARIN. Wageningen, the Netherlands.

[9] Y. Cao, F. Zhang, T. Joung, A. Ostman, and T. Kristiansen. "An Assessment of Prediction Methods for Waves Inside the Moonpool of a Vessel"'. Proceedings of the ASME 2015 34th International Conference on Ocean, Offshore and Arctic Engineering, 2015. May 31- June 5, St. John's, Newfoundland, Canada.

[10] H. W. Coleman and W. G. Steele. "Experimentation, Validation and Uncertainty Analysis for Engineers". *Jhon Wiley & Sons*, pages ISBN 978–0–470–16888–2, 2009. Third Edition.

[11] V. Denisart. "Discretization Error on Wave Propagation". Study of grid and time step refinement, MARIN. Wageningen, the Netherlands, 9 2017.

[12] L. Eça and M. Hoekstra. "A Procedure for the Estimation of the Numerical Uncertainty of CFD Calculations Based on Grid Refinement Studies". *Journal of Computational Physics 262*, pages pp.104–130, 2014. www.elsevier.com/locate/jcp.

[13] F. Fathi, L. Eça, and M. Borsboom. "An Example of Code Verification in the Simulation of Wave Propagation". Proceeding of the ASME 2011 30th International Conference on Ocean, Offshore and Arctic Engineering, 2011. June 19-24, Rotterdam, The Netherlands.

[14] J. H. Ferziger and M. Perić. *"Computational Methods for Fluid Dynamics"*. 2002. Third Edition.

[15] A. G. Fredriksen, T. Kristiansen, and O. M. Faltinsen. "Wave-induced Response of a Floating Two-dimensional Body with a Moonpool". *Philos Trans A Math Phys Eng Sci*, Vol.373(No.2033), 2015. ISSN 1471-2962 (Electronic) 1364-503X (Linking). doi: 10.1098/rsta.2014.0109.

[16] S. Haland. "Lowering and Lifting Operations through Moonpools: Hydrodynamic Investigations". Master's thesis, NTNU-Throndheim, Department of Marine Technology, 06 2014.

[17] L. H. Holthuijsen. *"Waves in Oceanic and Costal Waters"*. 2007. First Edition.

[18] J.M.J. Journée, W.W. Massie, and R.H.M. Huijsmans. *"Offshore Hydromechanics"*. 2015. Third Edition, Course OE4630.

[19] C. M. Klaij and C. Vuik. "Simple-type Preconditioner for Cell-centered, Collocated Finite Volume Discretization of Incompressible Reynolds-averaged Navier Stokes Equations". International Journal for Numerichal Methods in Fluids, 2013. 71(7), pp. 830-849.

[20] B. Le Méhauté. *"An Introduction to Hydrodynamics and Water Waves"*. 1976.

[21] T. Leboulleux. "CFD Verification of Waves Loads on a Fixed 2D Hull Section Equipped with Bilge Keels". 2016. Wageningen, The Netherlands.

[22] B. Molin. "On the Piston and Sloshing Modes in Moonpools". *Ecole Superieure d'Ingenieurs de Marseille*, Vol.430:pp.27–50, 2001. Cambridge University Press.

[23] B. Molin and X. Zhang. "On Resonant Modes in Moonpools with Restrictions or Recesses". The 32nd International Workshop on Water Waves and Floating Bodies, 2017. April 23-26, Dalian, China.

[24] N. Petrovskaya. "Solution Limiters and Flux Limiters for High Order Discontinuous Galerkin Schemes". *School of Mathematics, University of Birmingham. Edgbaston, B15 2TT, Birmingham, UK*. http://web.mat.bham.ac.uk/N.B.Petrovskaya.

[25] G. Peyredieu du Charlat. "Study of a Fix Vessel by Potential Flow Code DIFFRAC". MARIN, ENSTA Bretagne, 8 2017.

[26] A. Pistidda and H. Ottend. "CFD Modeling of Moonpool Behavior". Proceedings of the ASME 33rd International Conference on Ocean, Offshore and Arctic Engineering, 2014. June 8-13, San Francisco, California, USA.

[27] S. Rapuc. "SHIP IN WAVES Incoming Waves and Forced Oscillations". 2017. Wageningen, The Netherlands.

[28] S. Sadiq and Y. Xiongliang. "Multi-dimensional Numerical Free Surface VOF Modeling with Moonpool Experiments". Proceedings of the ASME 27th International Conference on Offshore Mechanics and Arctic Engineering, 2008. June 15-20, Estoril, Portugal.

[29] G. Vaz, F. Jaouen, and M. Hoekstra. "Free-surface Viscous Flow Computation. Validation of URANS Code FRESCO". Proceeding of the ASME 28th International Conference on Ocean, Offshore and Arctic Engineering, 2009. May 31-June 5, Honolulu, Hawaii.

[30] K. Zhuang, Y. Xiongliang, and S. Sadiq. "Experimental Research on Flow Induced Oscillations in Moonpool Encountered Through Waves". Proceedings of the 26th International Conference on Offshore Mechanics and Arctic Engineering, 2007. June 10 -15, San Diego, California, USA.

A

Appendix Empty domain

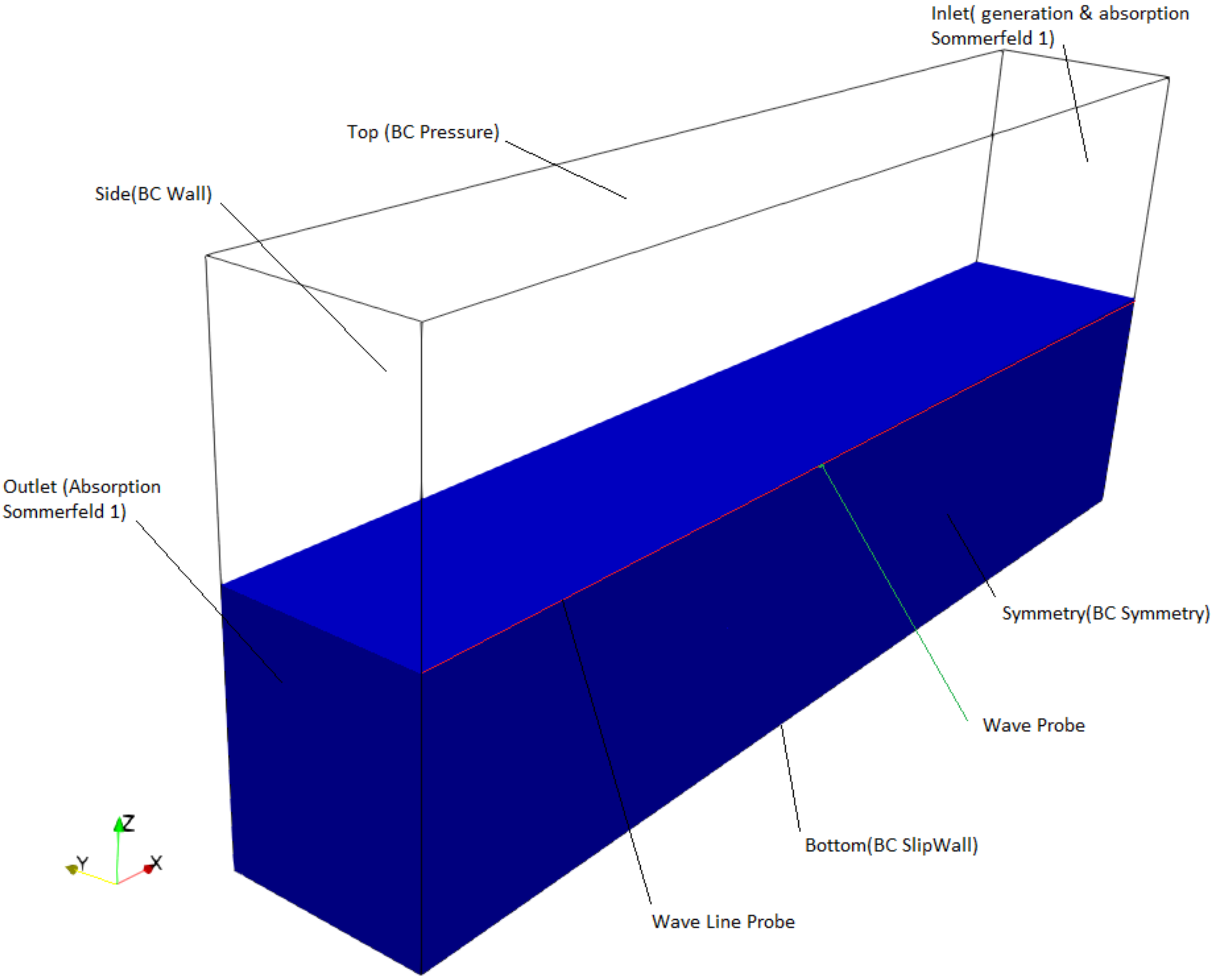

Figure A.1: Boundary conditions and monitors

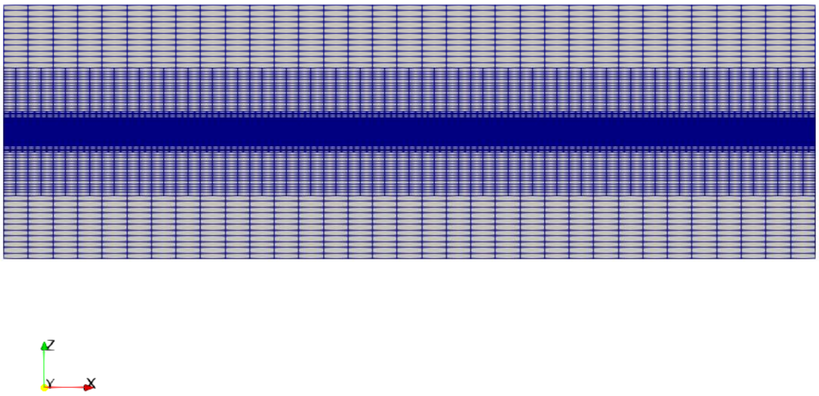

(a) Coarse

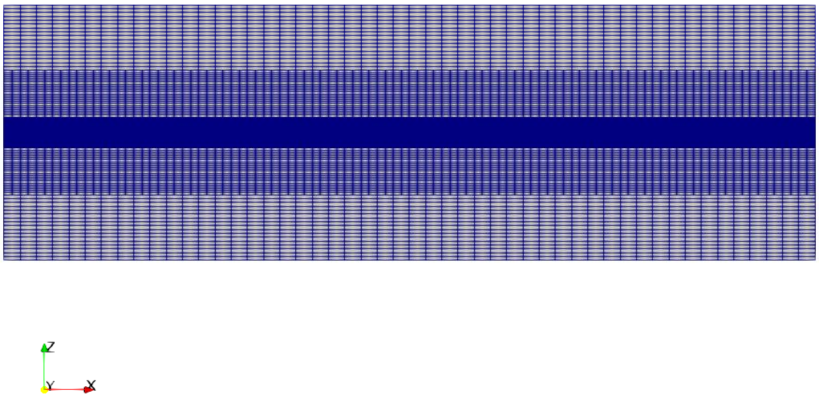

(b) Medium

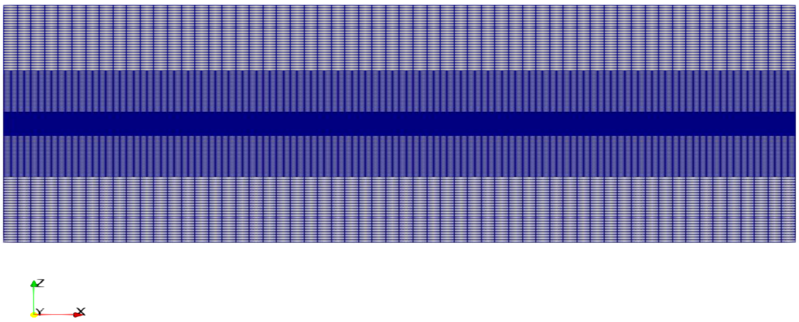

(c) Fine

Figure A.2: Mesh refinement for the empty domain case

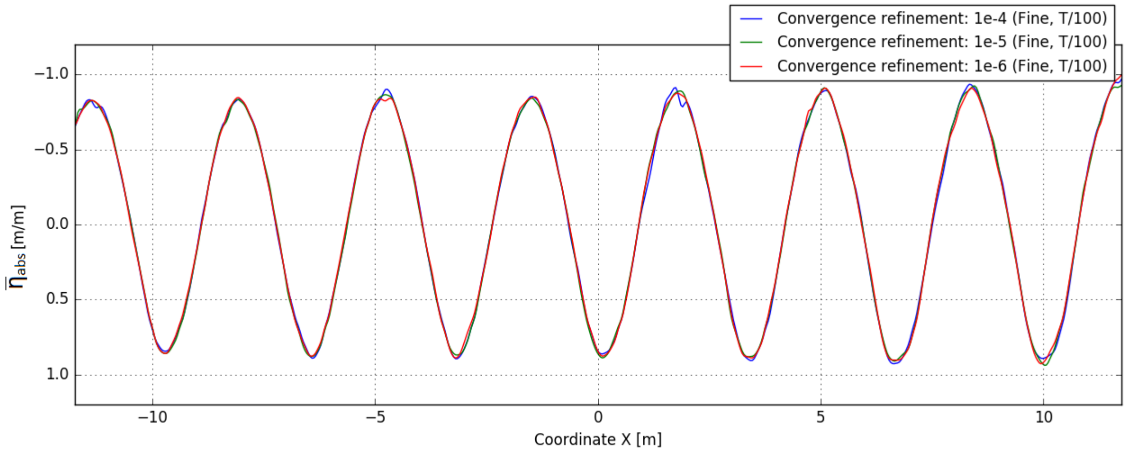

(a) Time step $\frac{T}{100}$

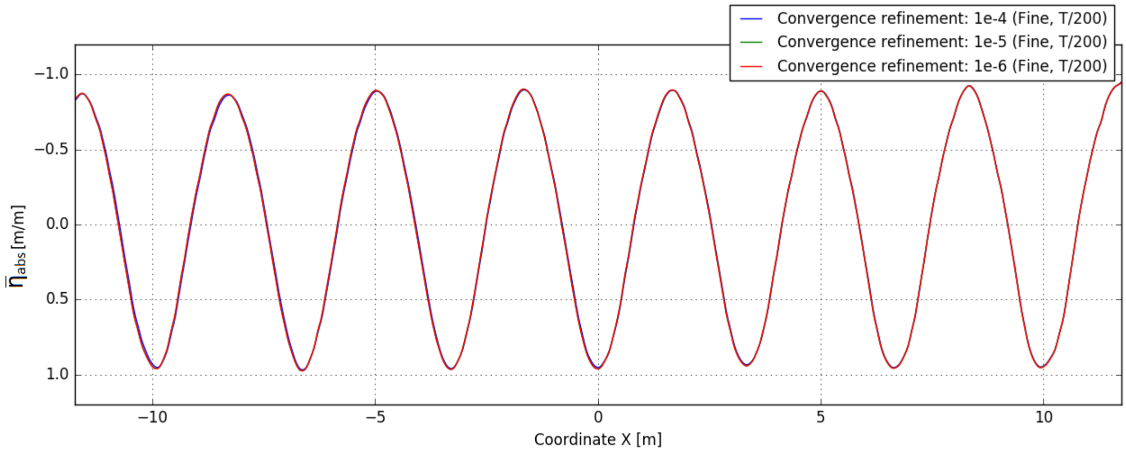

(b) Time step $\frac{T}{200}$

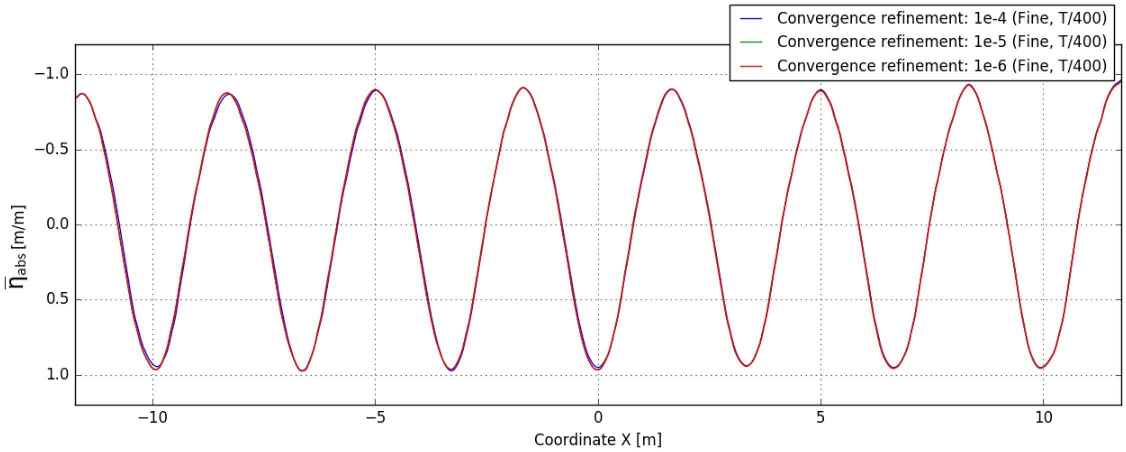

(c) Time step $\frac{T}{400}$

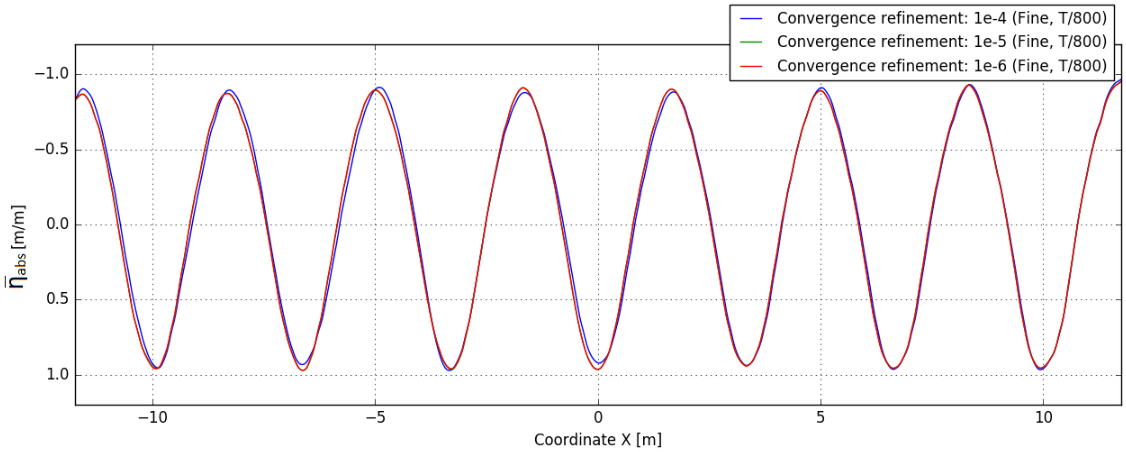

(d) Time step $\frac{T}{800}$

Figure A.3: Convergence refinement for the fine mesh

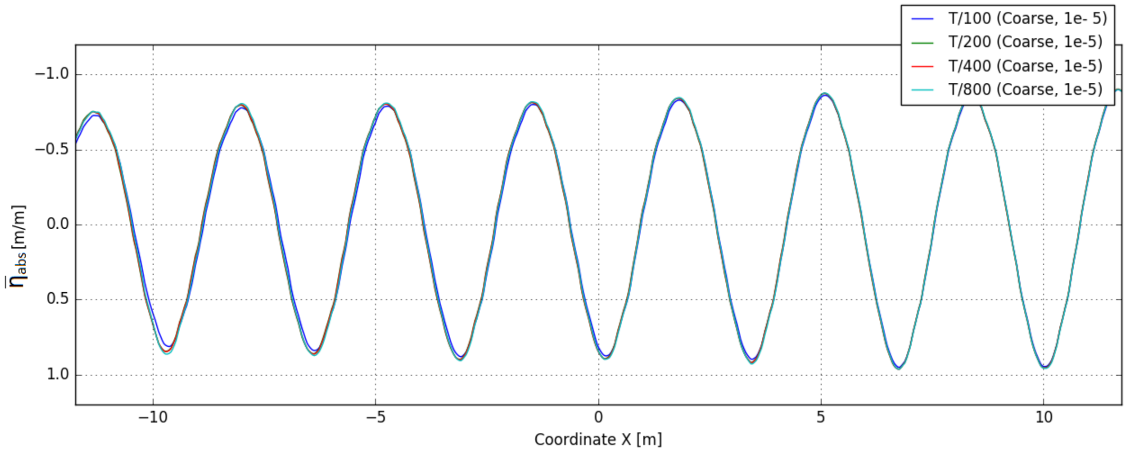

(a) Converge level 10^{-5}

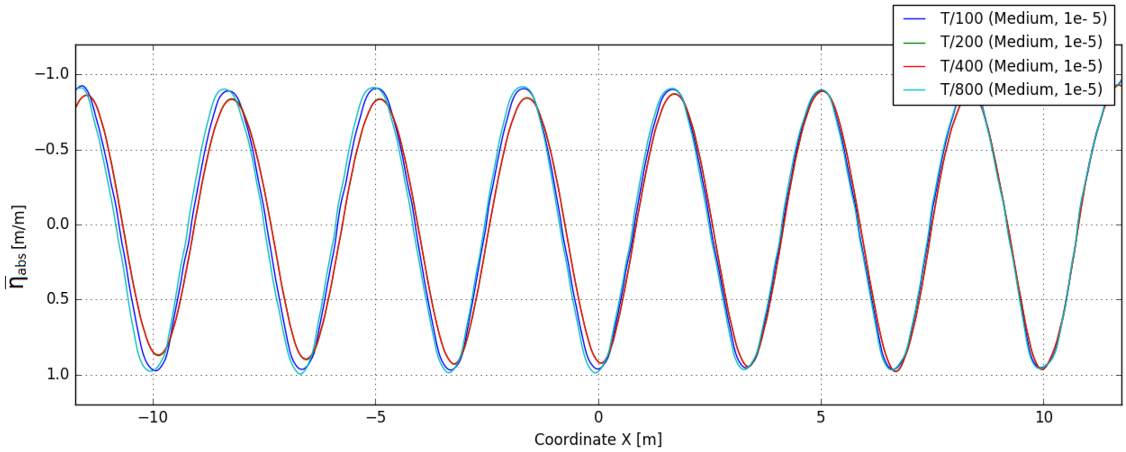

(b) Converge level 10^{-5}

Figure A.4: Time step refinement for the coarse and medium mesh

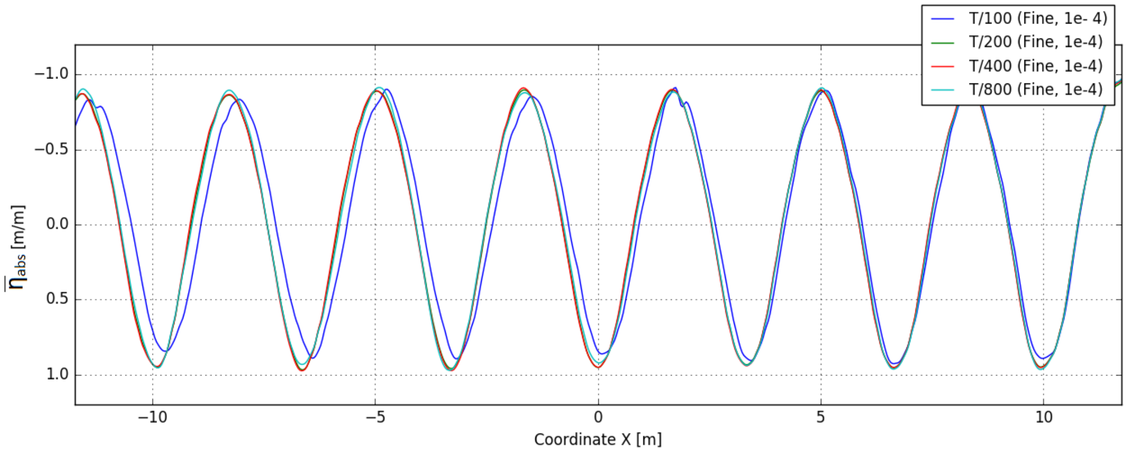

(a) Converge level 10^{-4}

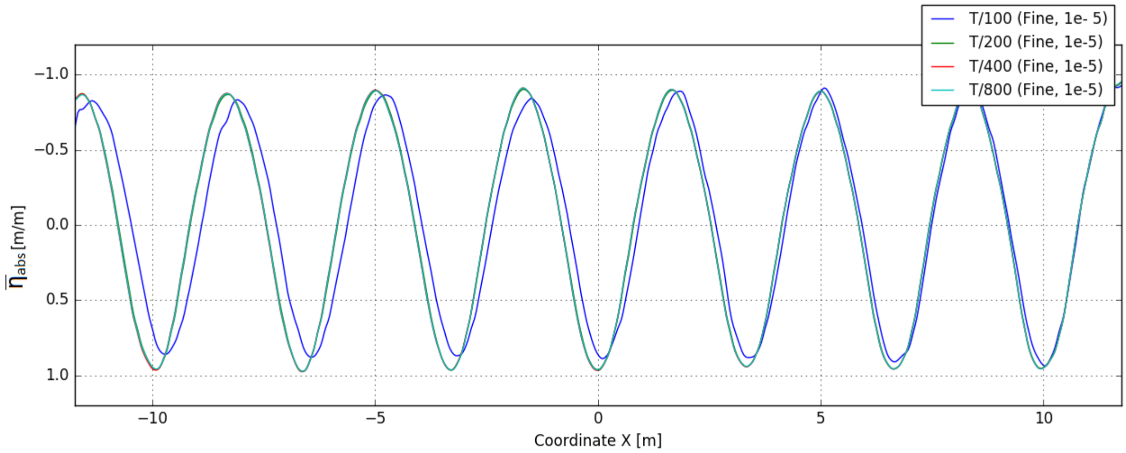

(b) Converge level 10^{-5}

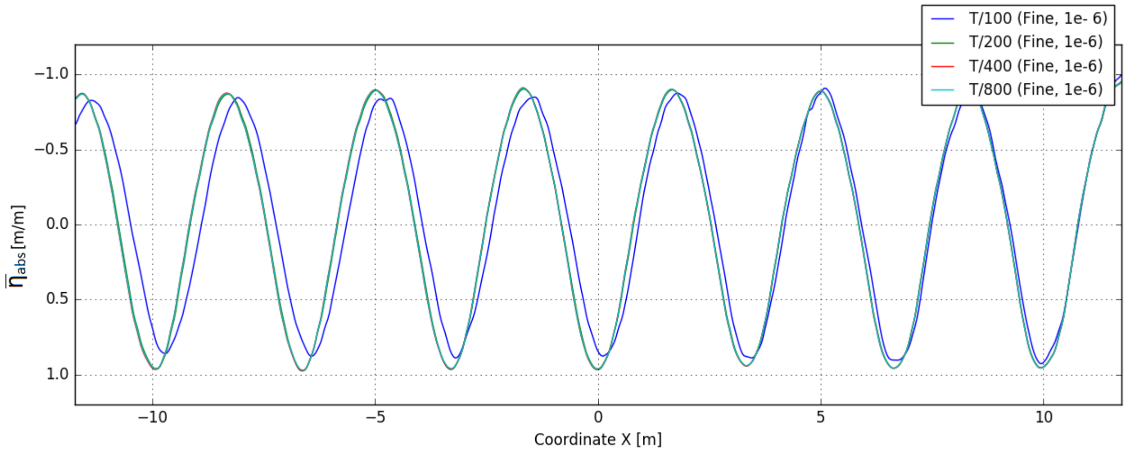

(c) Converge level 10^{-6}

Figure A.5: Time step refinement for the fine mesh

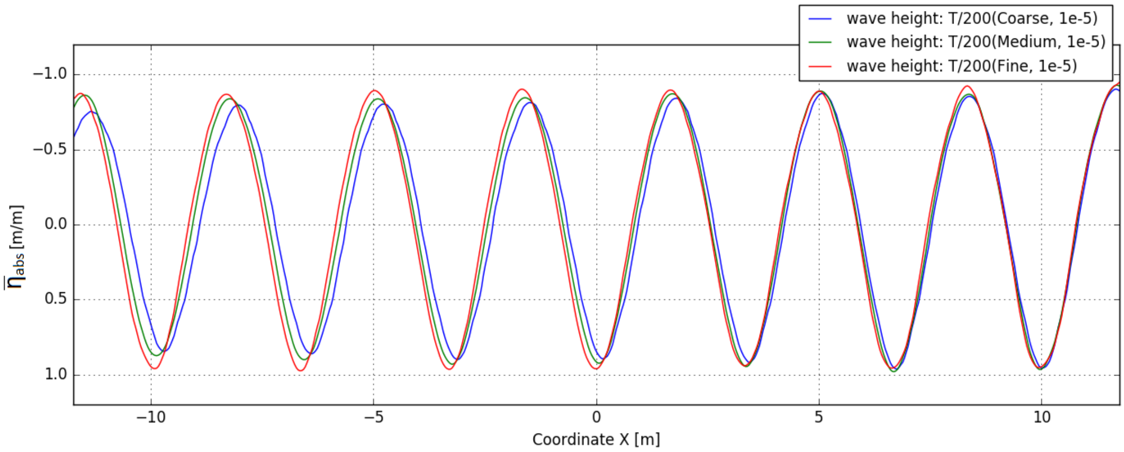

(a) Time step $\frac{T}{200}$

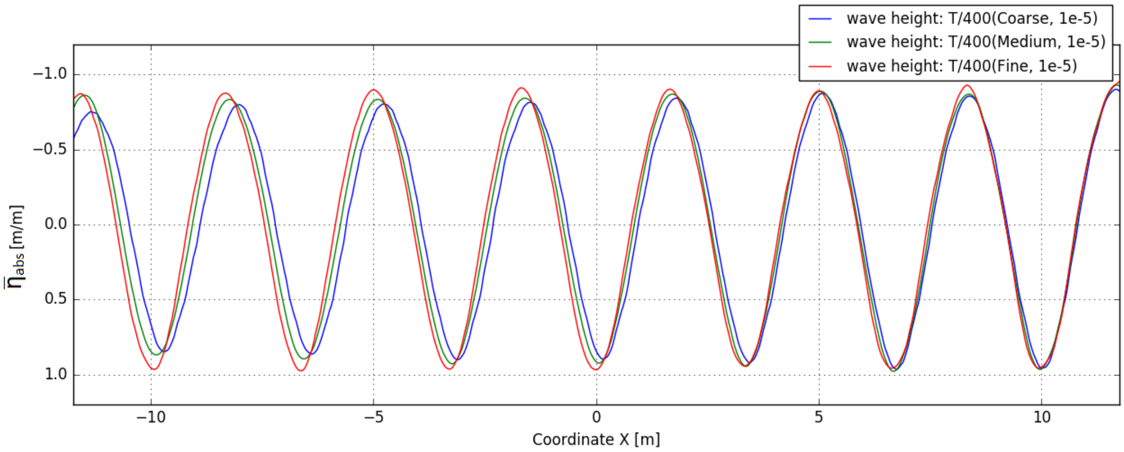

(b) Time step $\frac{T}{400}$

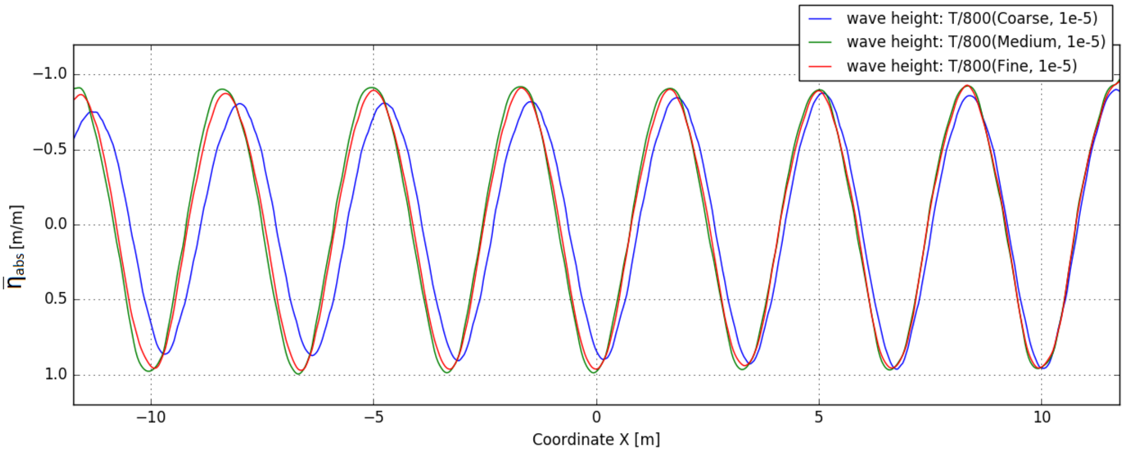

(c) Time step $\frac{T}{800}$

Figure A.6: Mesh refinement for the convergence 10^{-5}

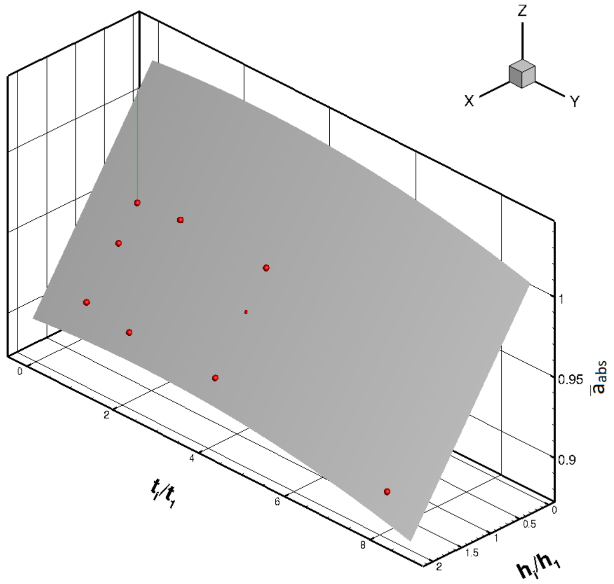

(a) Numerical uncertainty for a

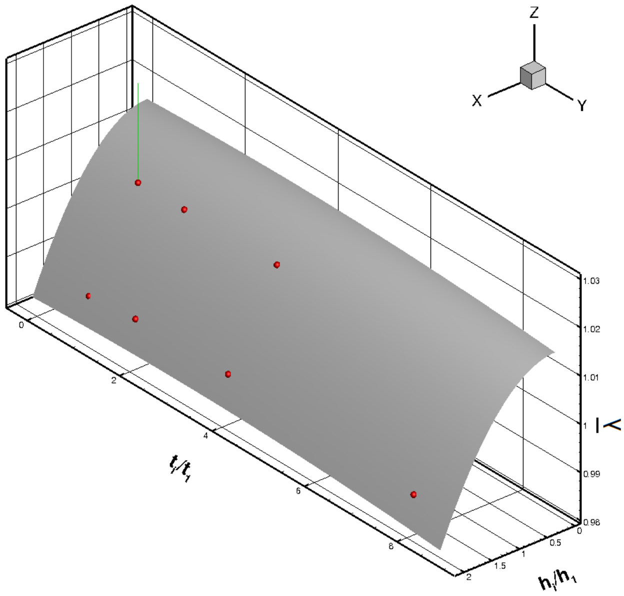

(b) Numerical uncertainty for λ

Figure A.7: Numerical uncertainty for the empty domain case

B

Appendix Fixed vessel

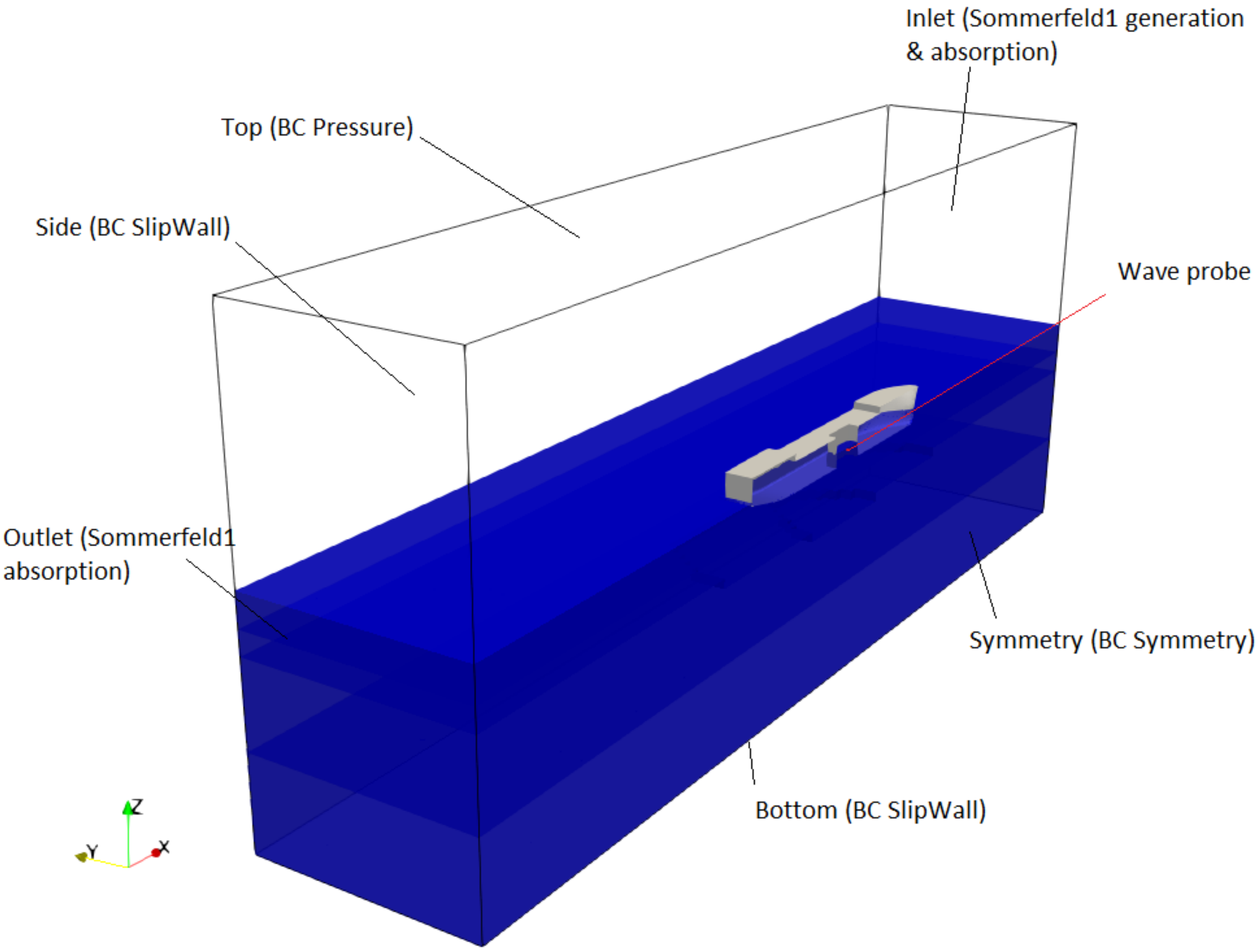

Figure B.1: Boundary conditions

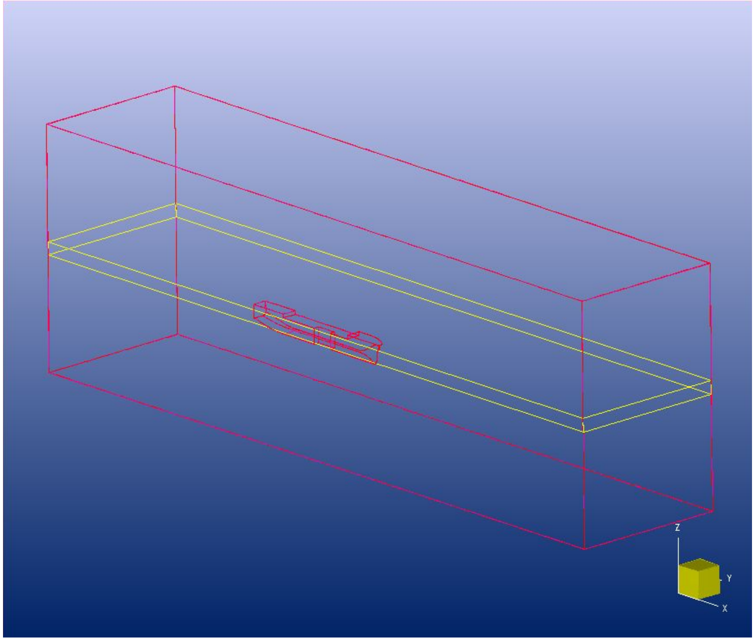

(a) Free surface refinement

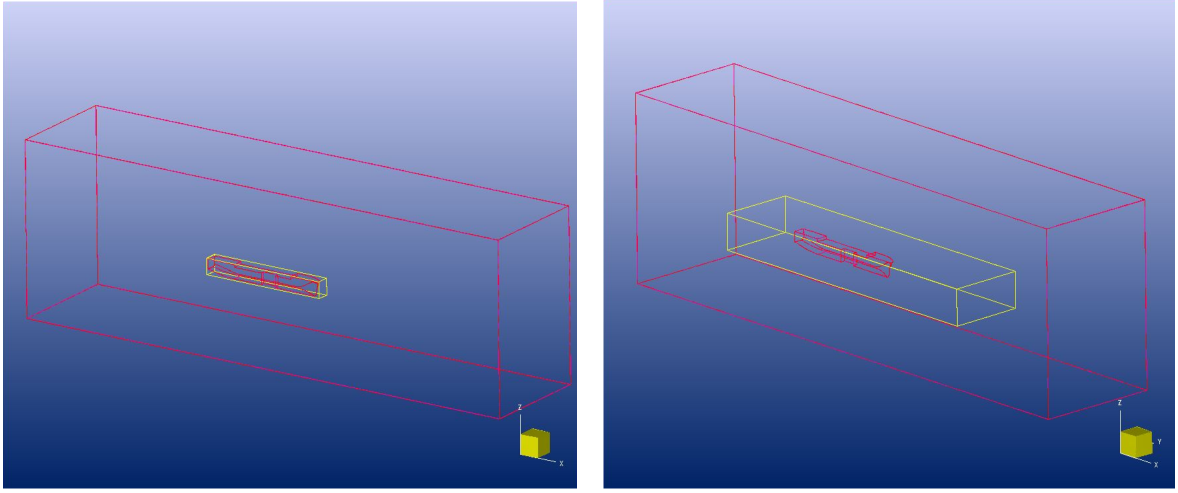

(b) First vessel box refinement

(c) Final vessel box refinement

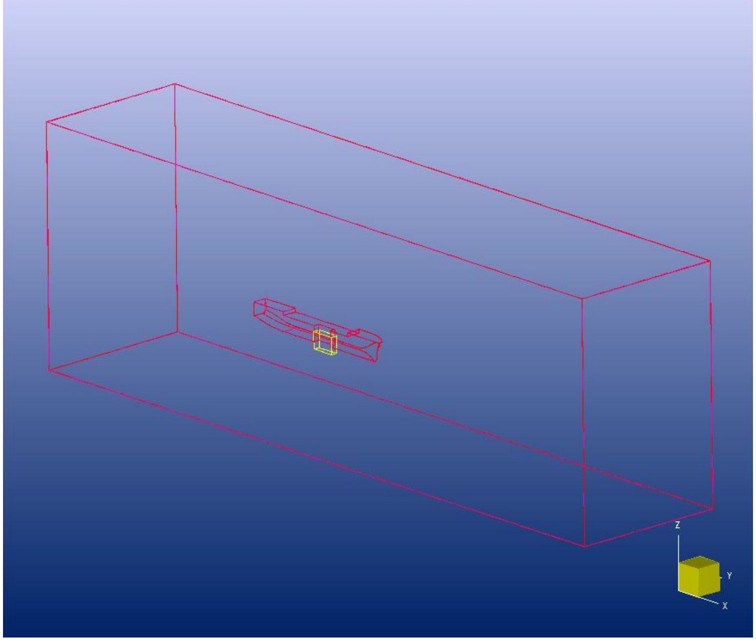

(d) Moonpool refinement

Figure B.2: Box refinements

B.1. Case A

- Grid: Coarse (1.8M cells)
- Timestep: T/100
- Convergence level : 10^{-4}
- Domain length: 2.5 λ in front and aft the vessel
- Domain width : 1.5 λ
- Boundary conditions:
  1. Inlet: Generation and absorption Sommerfeld 1
  2. Side: BC Wall
  3. Outlet: Absorption Sommerfeld 1

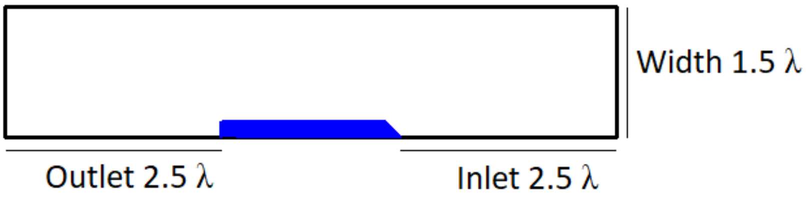

Figure B.3: Domain case A

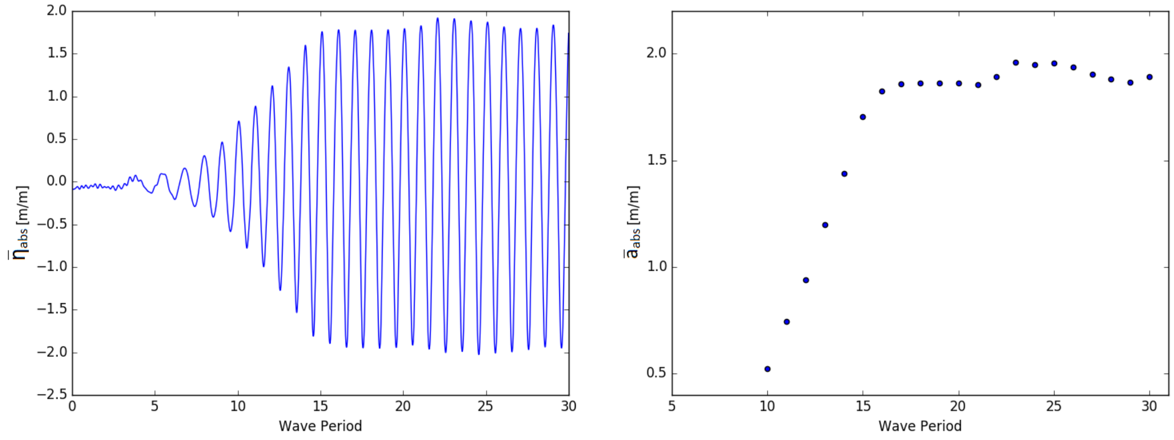

(a) Time trace wave elevation (b) Wave amplitude

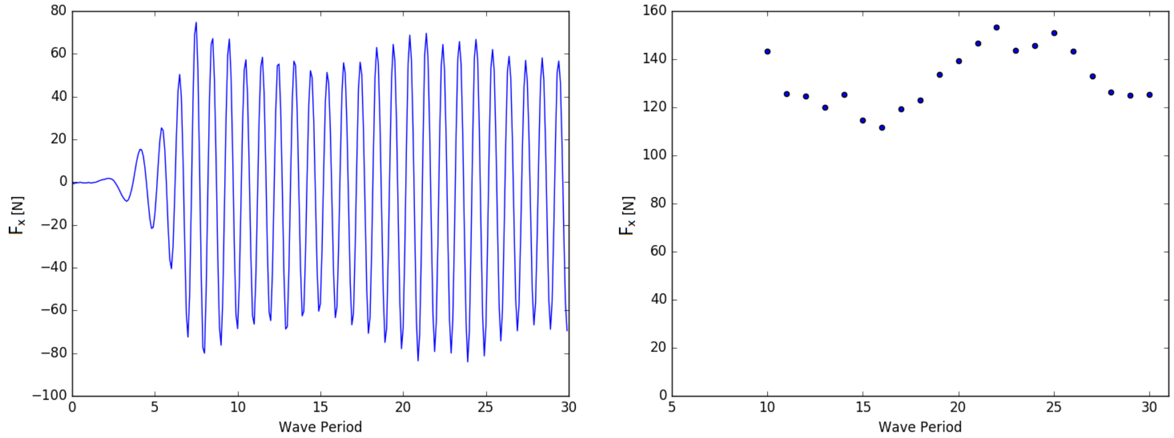

(c) Time trace F_x (d) Scatter F_x

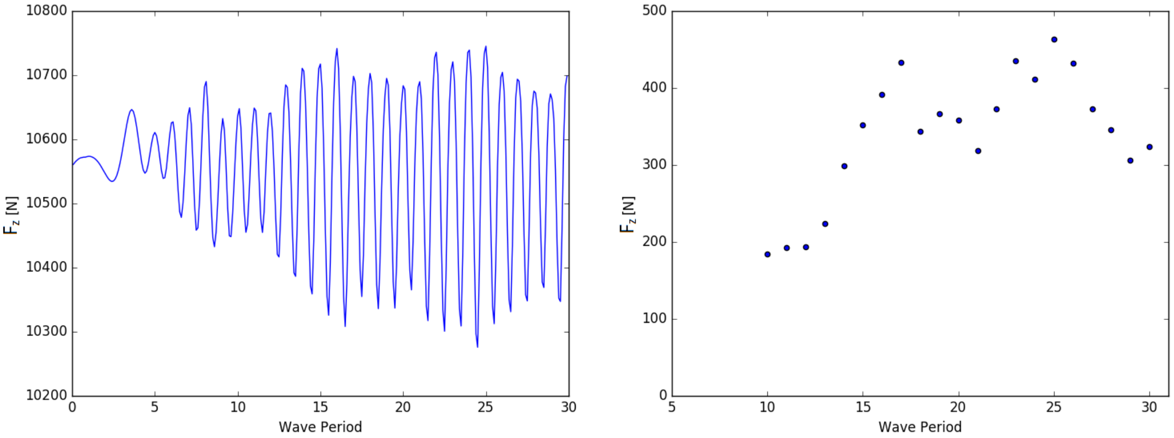

(e) Time trace F_z (f) Scatter F_z

Figure B.4: Case A

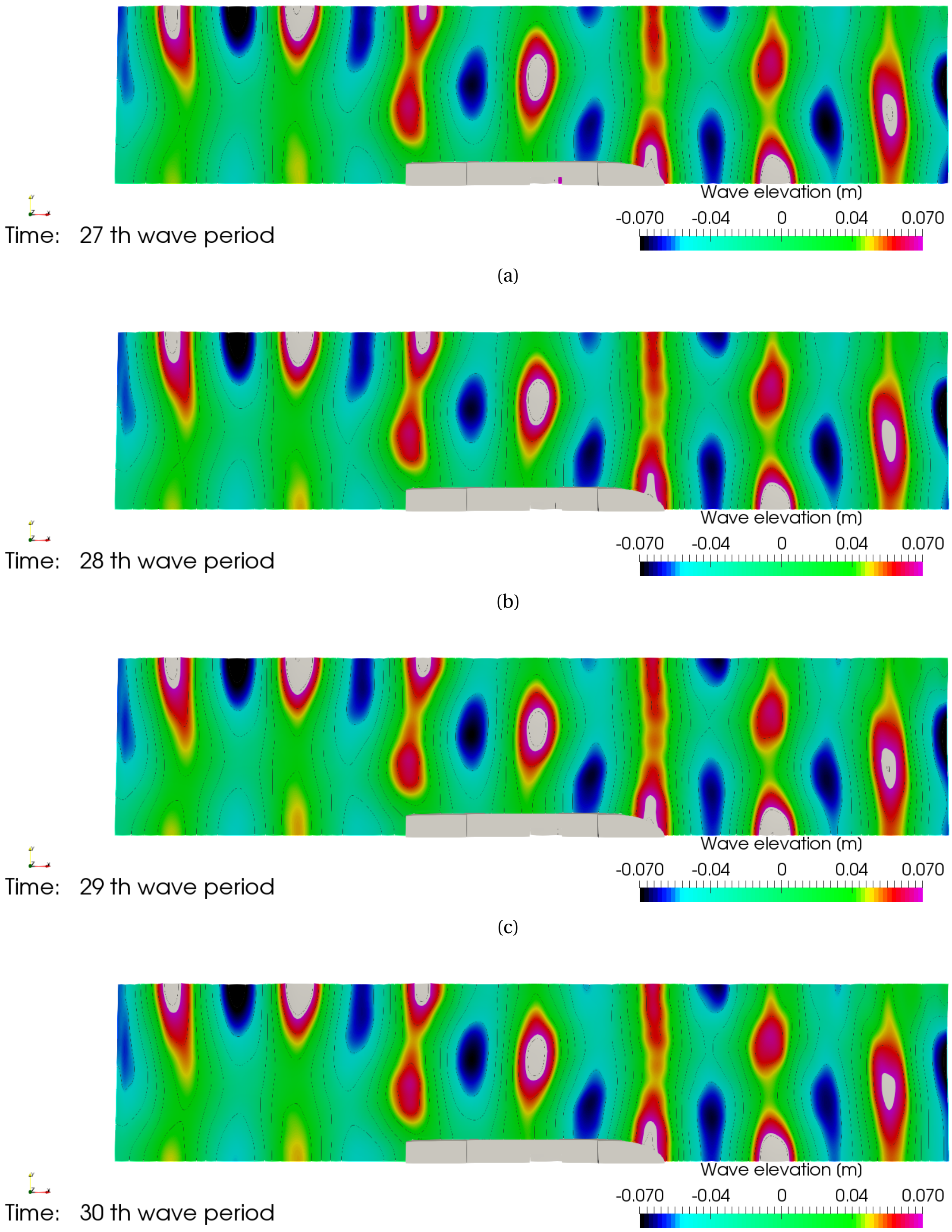

(a)

(b)

(c)

(d)

Figure B.5: Wave elevation case A

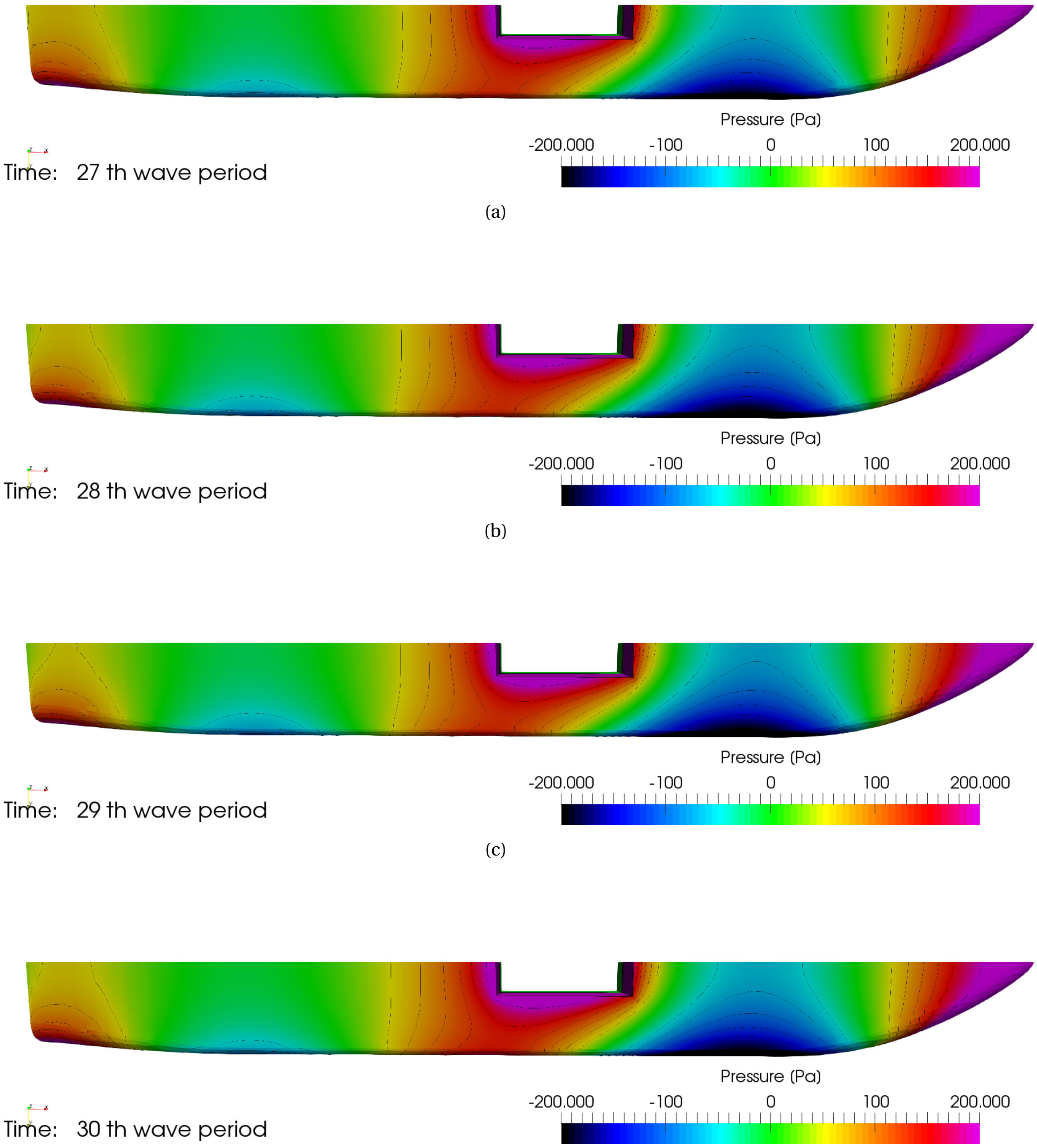

(a) (b) (c) (d)

Figure B.6: Pressure distribution along the bottom for case A

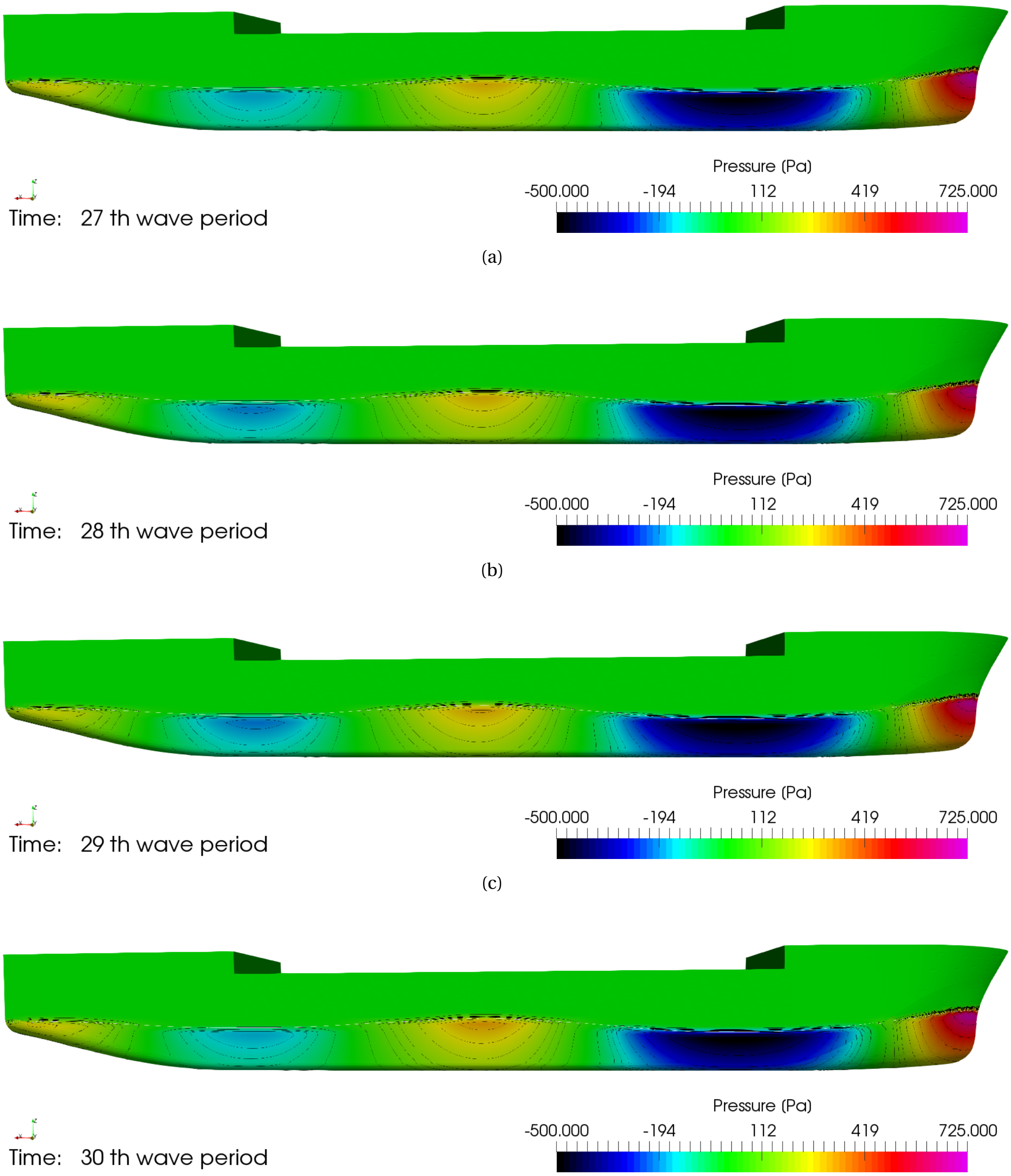

(a)

(b)

(c)

(d)

Figure B.7: Pressure distribution along the side for case A

B.2. Case B

- Grid: Coarse (7.0M cells)
- Timestep: T/100
- Convergence level : 10^{-4}
- Domain length: 5.0 λ in front and aft the vessel
- Domain width : 3.0 λ
- Boundary conditions:
  1. Inlet: Generation and absorption Sommerfeld 1
  2. Side: BC Wall
  3. Outlet: Absorption Sommerfeld 1

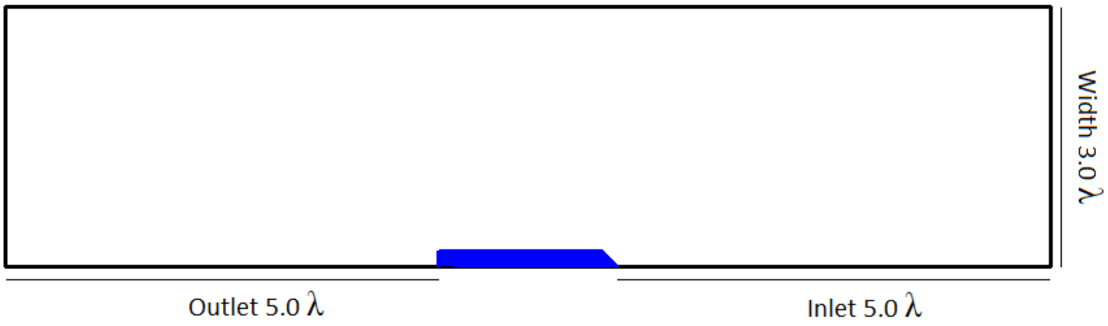

Figure B.8: Domain case B

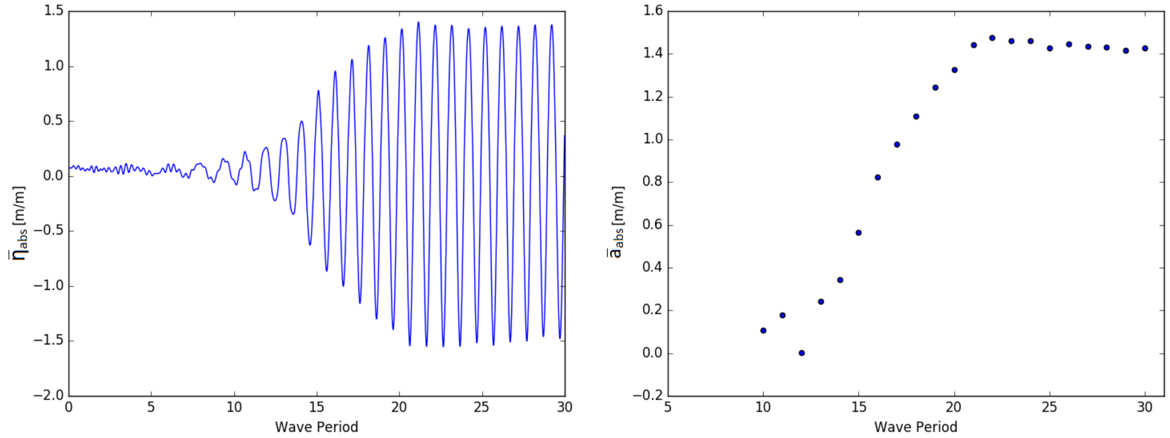

(a) Time trace wave elevation (b) Wave amplitude

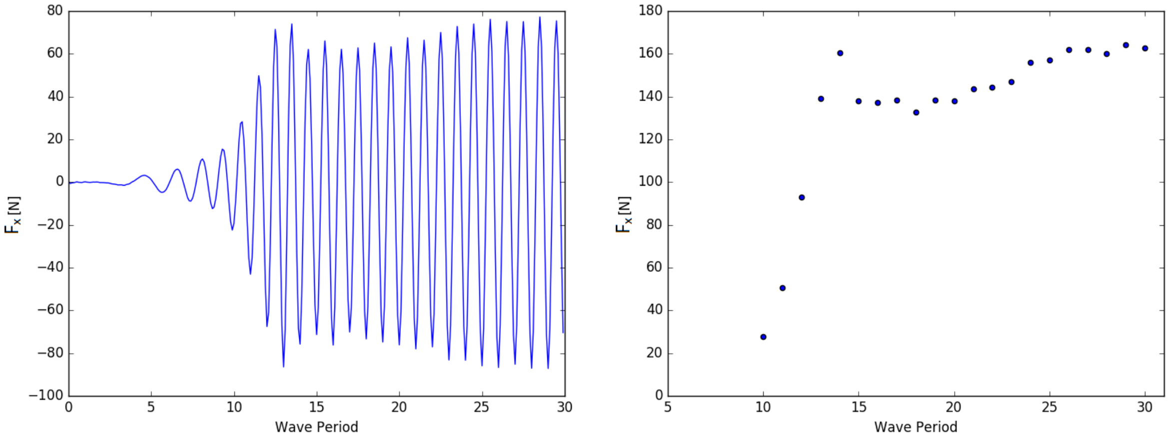

(c) Time trace F_x (d) Scatter F_x

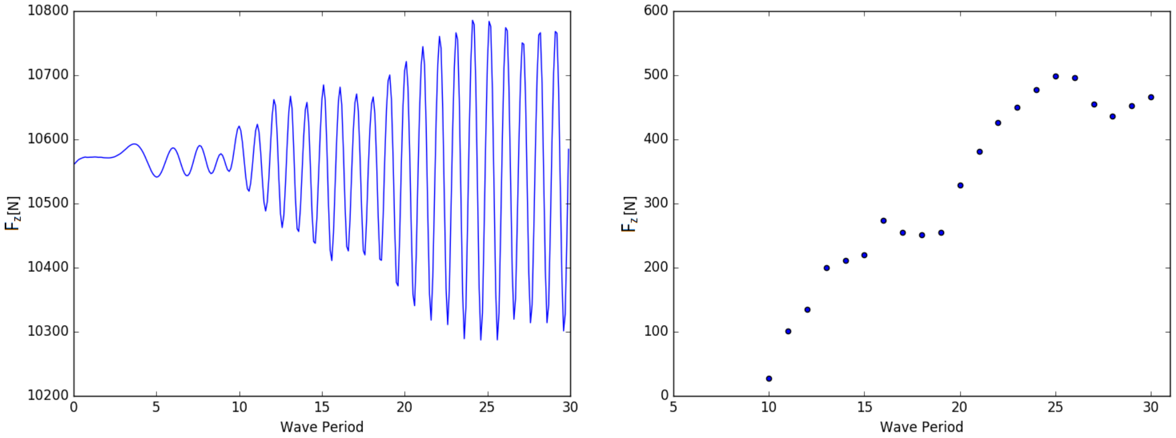

(e) Time trace F_z (f) Scatter F_z

Figure B.9: Case B

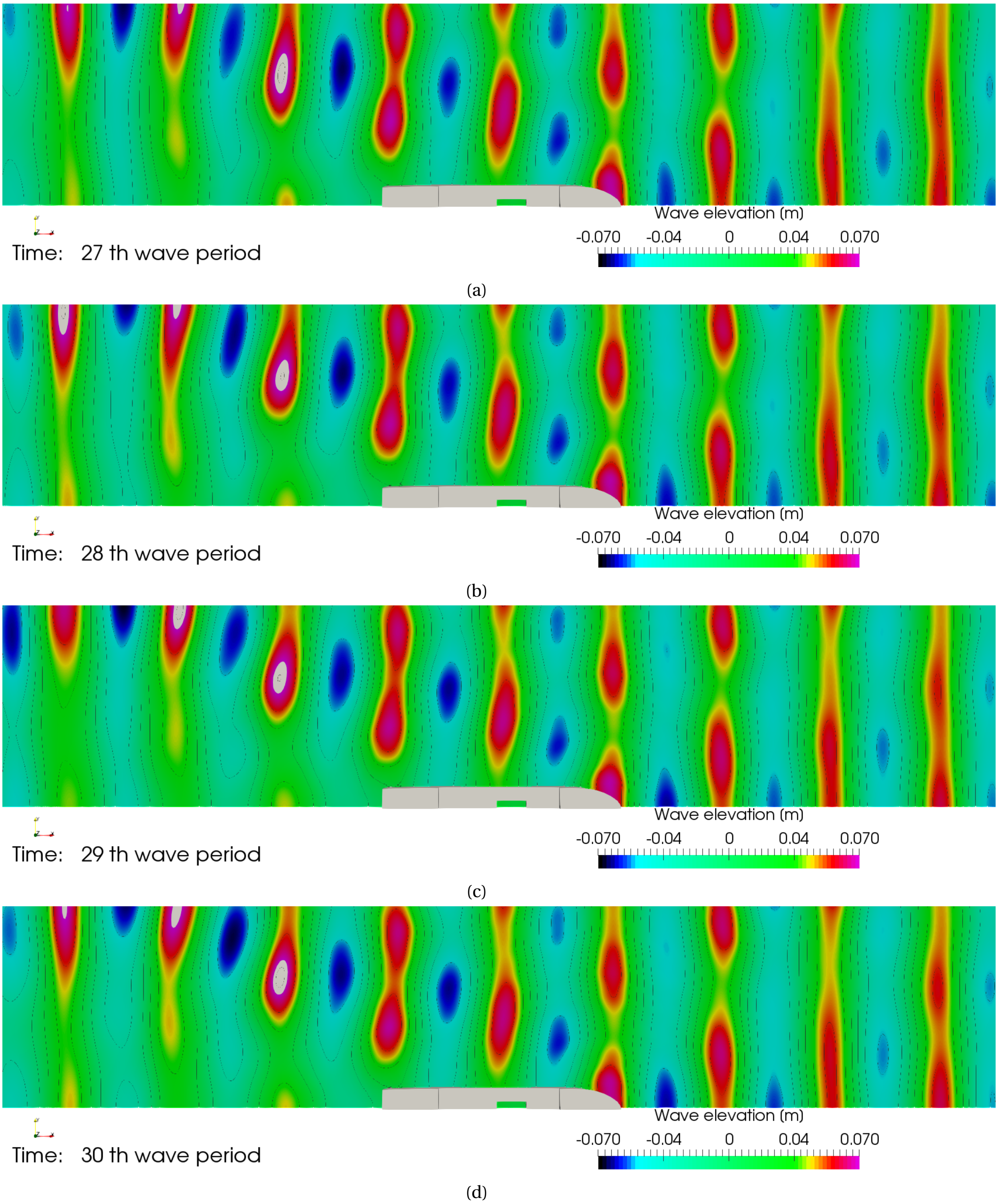

Figure B.10: Wave elevation case B

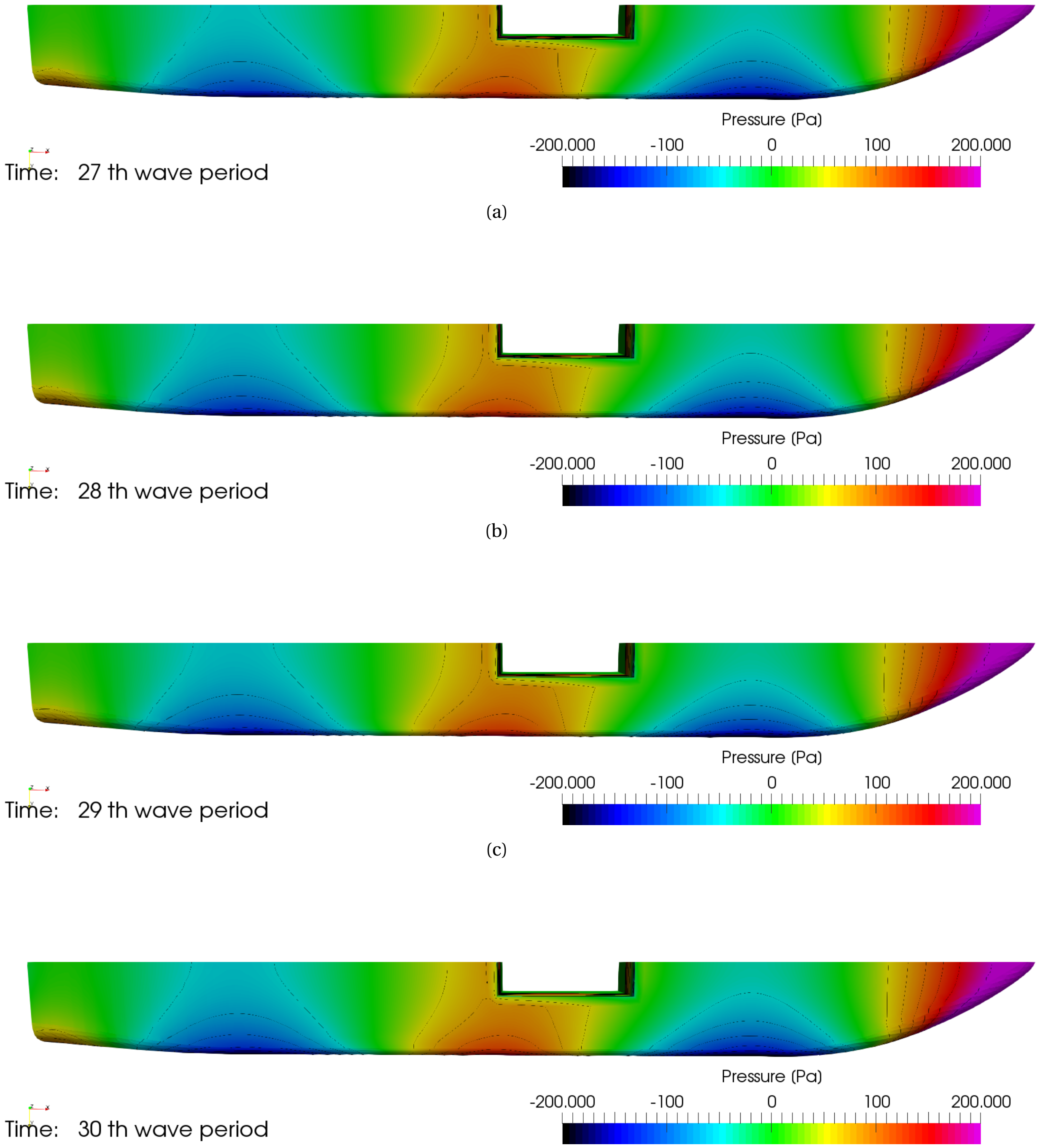

(a)

(b)

(c)

(d)

Figure B.11: Pressure distribution along the bottom for case B

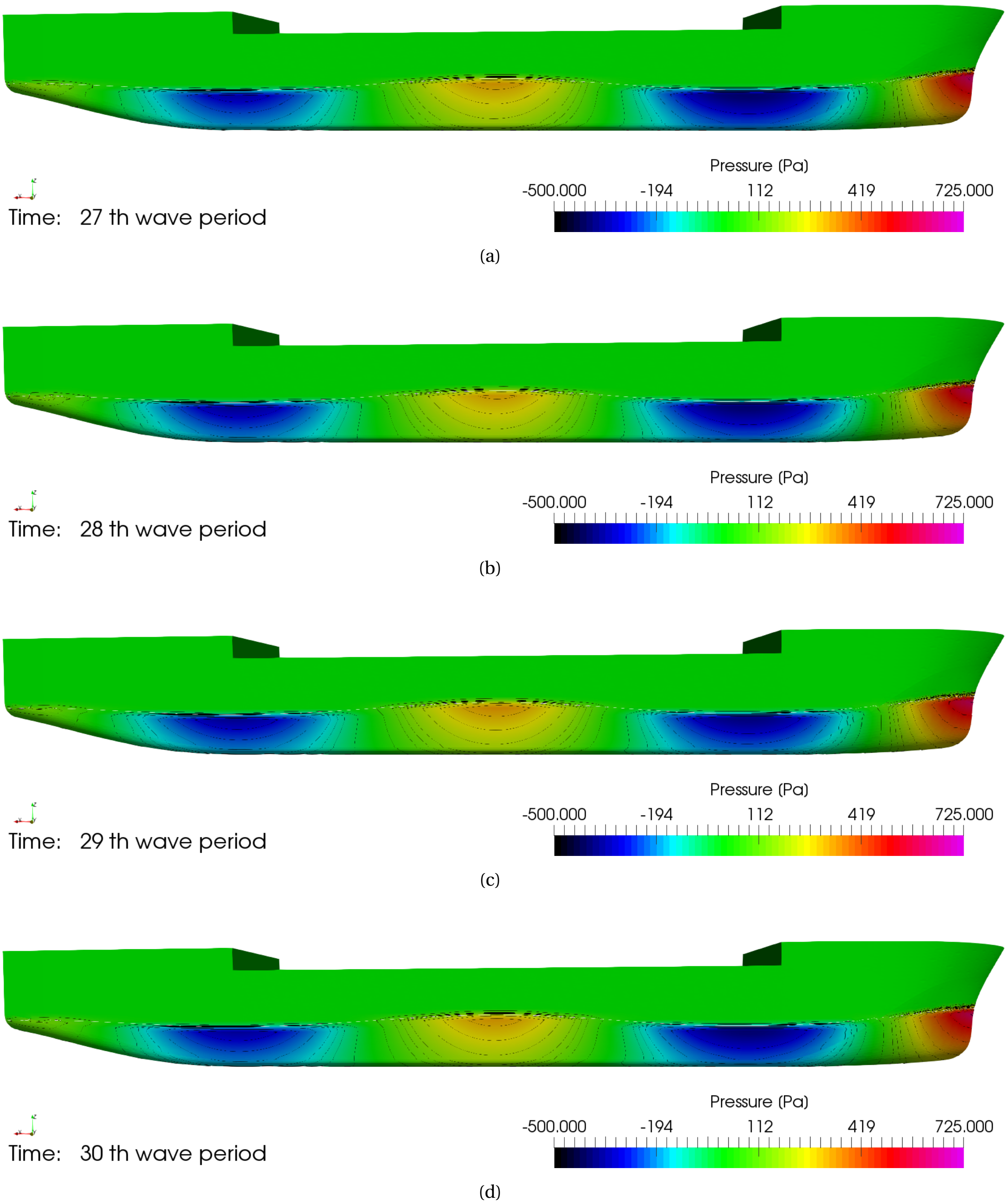

Figure B.12: Pressure distribution along the side for case B

B.3. Case C

- Grid: Coarse (2.5M cells)
- Timestep: T/10
- Convergence level : 10^{-4}
- Domain length: 2.5 λ in front and 3.5 L aft the vessel
- Domain width : 1.5 λ
- Boundary conditions:
    1. Inlet: Generation and absorption Sommerfeld 1
    2. Side: BC Wall
    3. Outlet: Absorption Sommerfeld 1

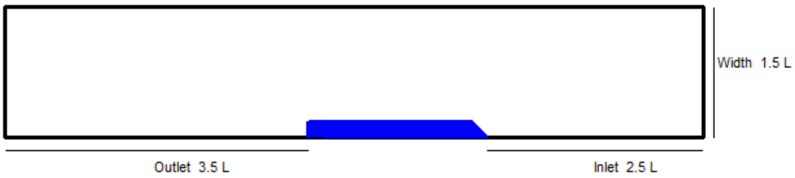

Figure B.13: Domain case C

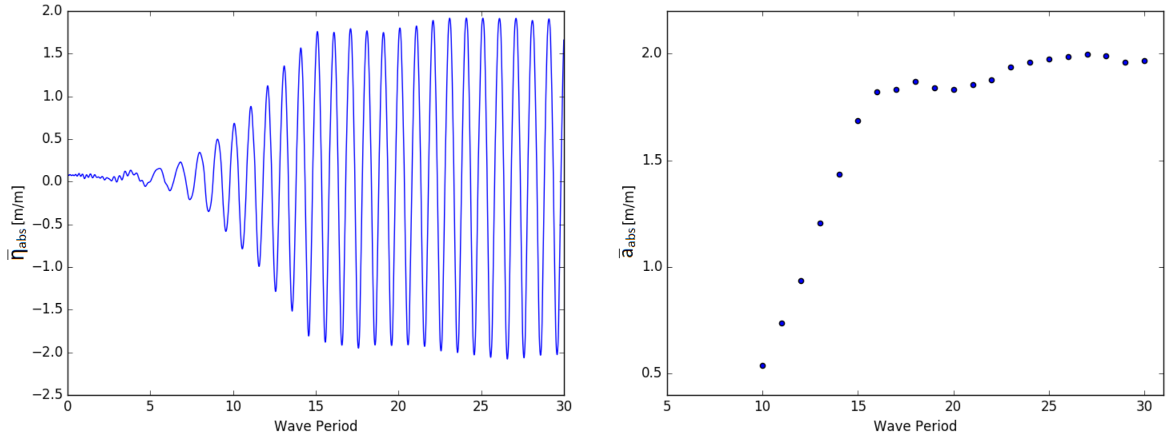

(a) Time trace wave elevation

(b) Wave amplitude

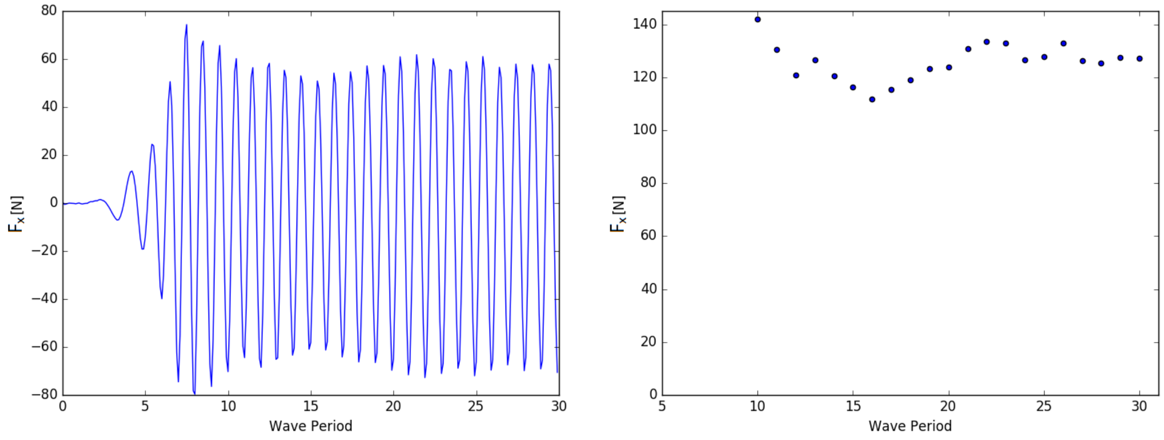

(c) Time trace F_x

(d) Scatter F_x

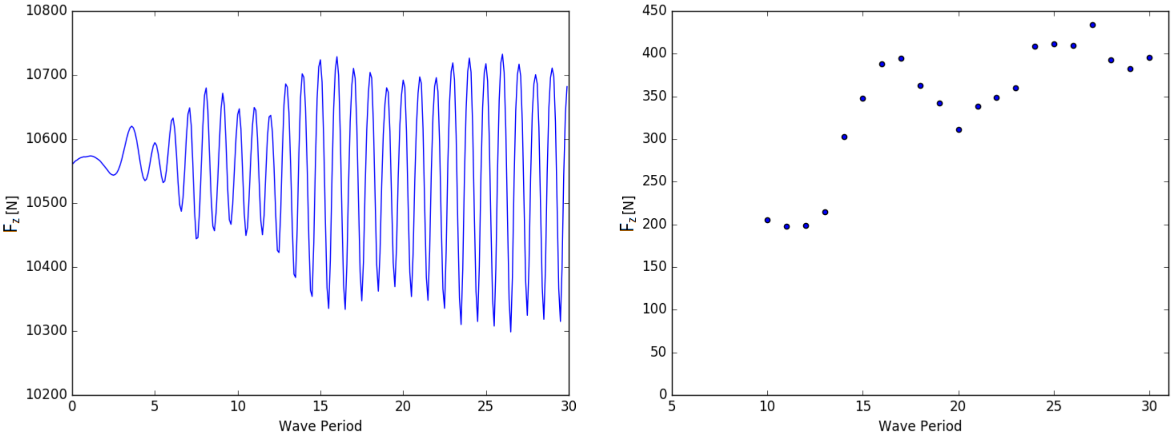

(e) Time trace F_z

(f) Scatter F_z

Figure B.14: Case C

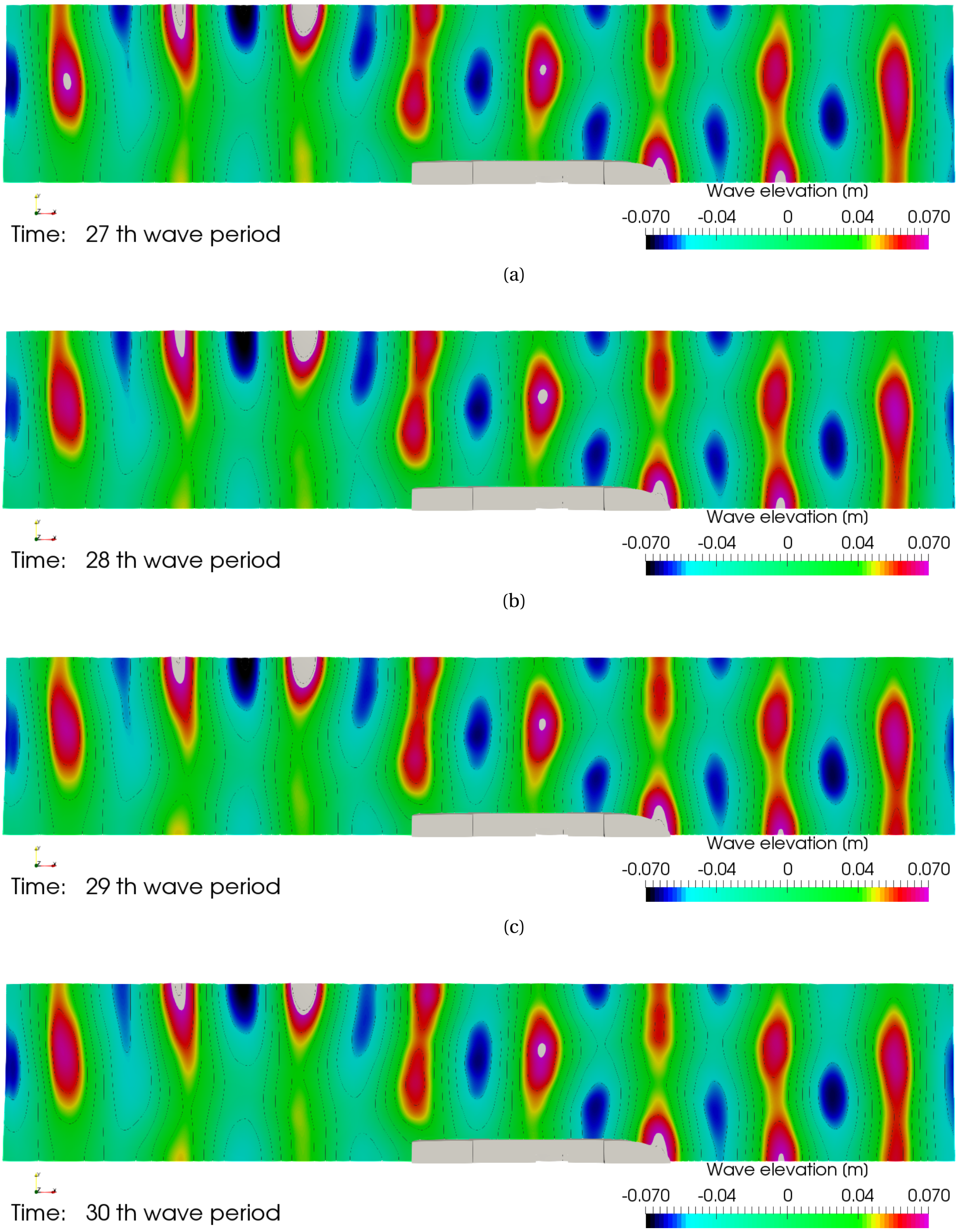

(a)

(b)

(c)

(d)

Figure B.15: Wave elevation case C

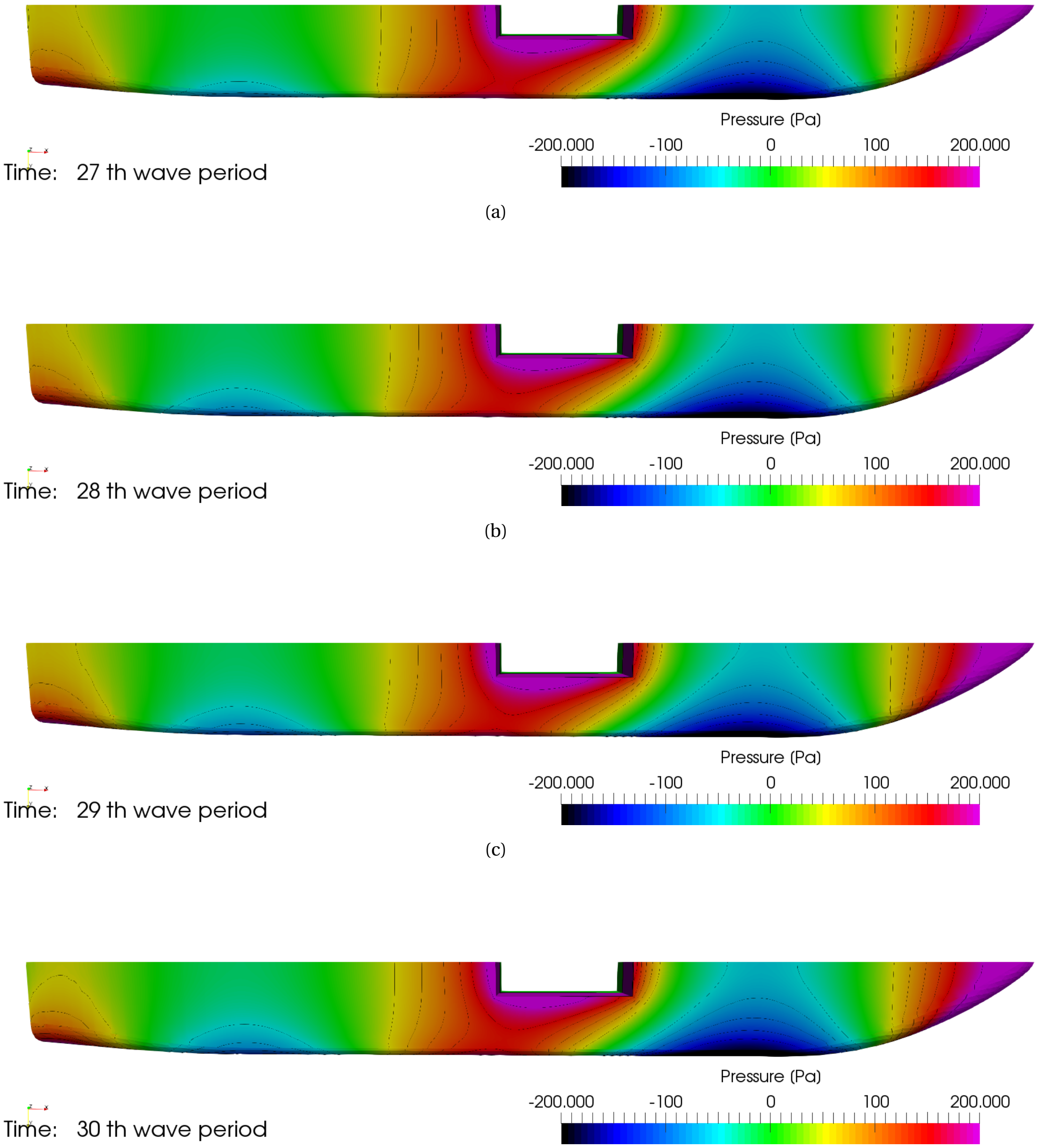

(a)

(b)

(c)

(d)

Figure B.16: Pressure distribution along the bottom for case C

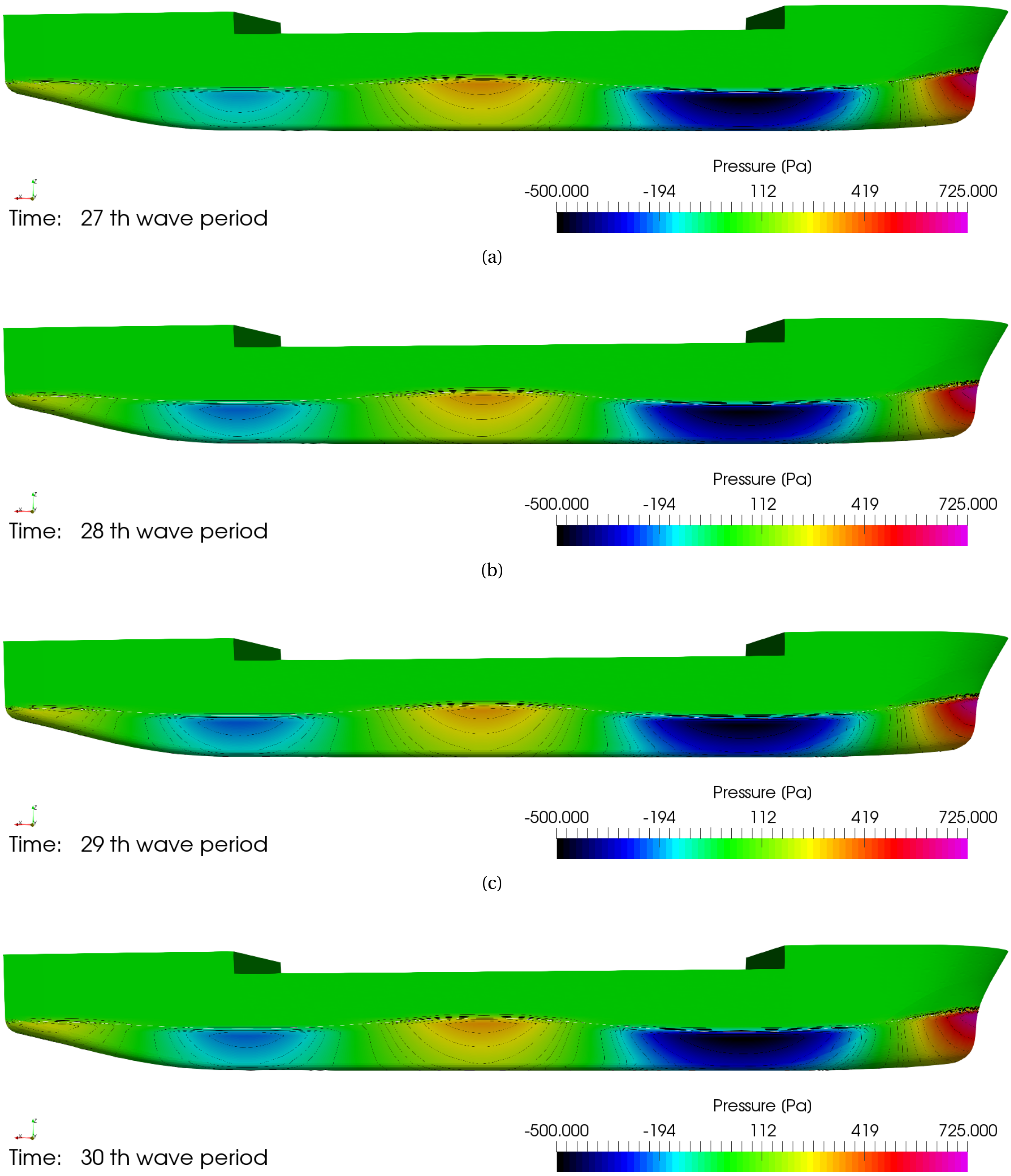

(a)

(b)

(c)

(d)

Figure B.17: Pressure distribution along the side for case C

B.4. Case D

- Grid: Very Coarse (2.8M cells)
- Timestep: T/100
- Convergence level : 10^{-4}
- Domain length: 3.5 λ in front and aft the vessel
- Domain width : 1.5 λ
- Boundary conditions:
  1. Inlet: Generation and absorption Sommerfeld 1
  2. Side: BC Wall
  3. Outlet: Absorption Sommerfeld 1

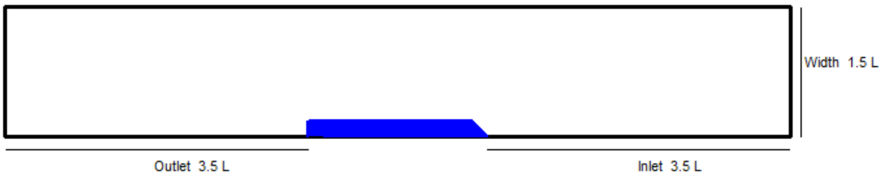

Figure B.18: Domain case D

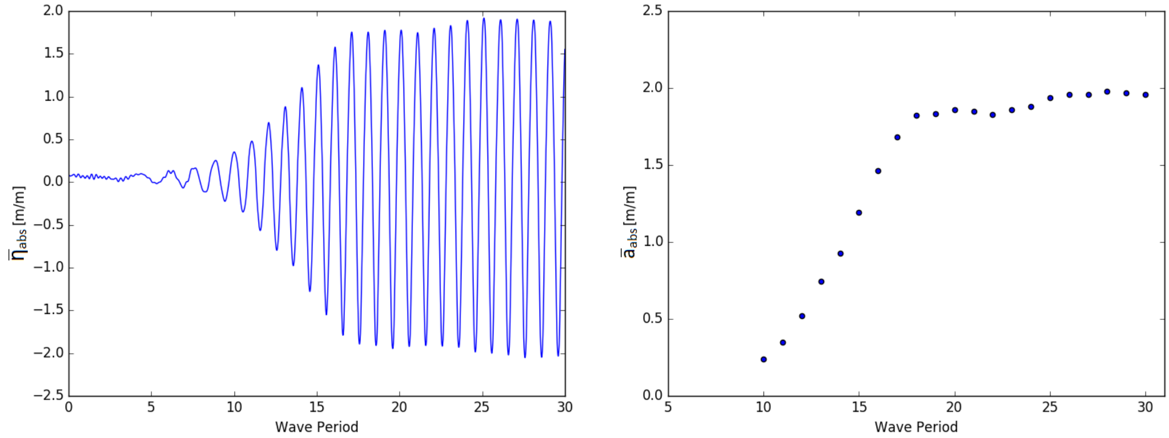

(a) Time trace wave elevation (b) Wave amplitude

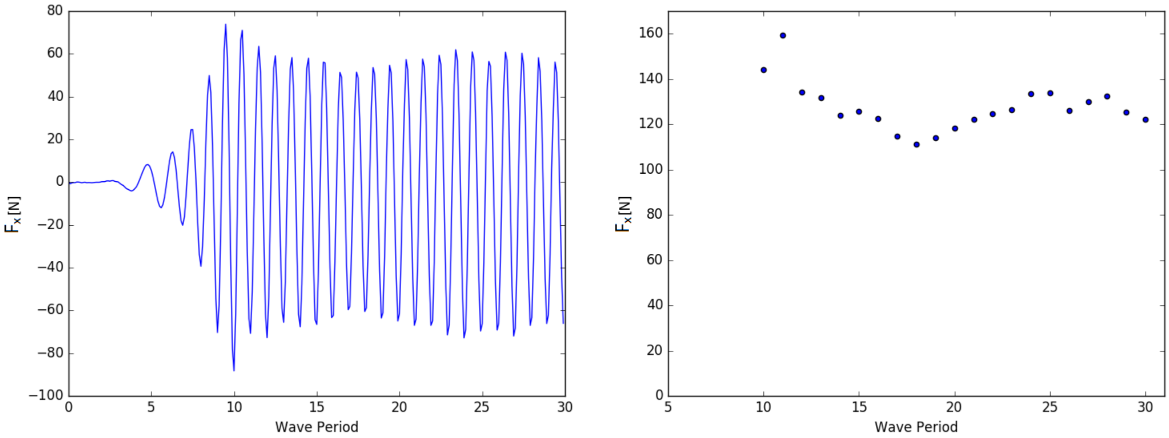

(c) Time trace F_x (d) Scatter F_x

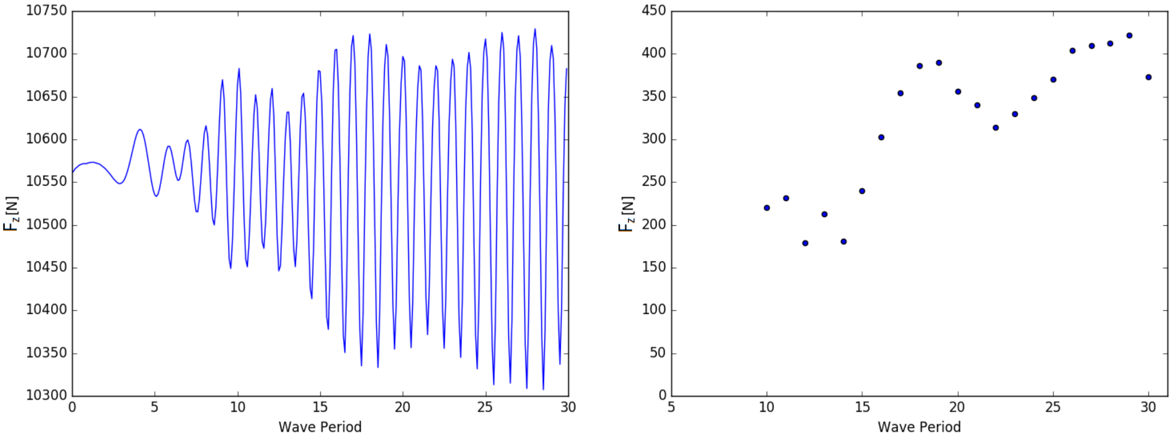

(e) Time F_z (f) Scatter amplitude F_z

Figure B.19: Case D

B.5. Case E

- Grid: Coarse (2.8M cells)
- Timestep: T/100
- Convergence level : 10^{-4}
- Domain length: 3.5 λ in front and aft the vessel
- Domain width : 1.5 λ
- Boundary conditions:
  1. Inlet: Generation and absorption Sommerfeld 1
  2. Side: BC Wall
  3. Outlet: Absorption Sommerfeld 1
- Relaxation zone:
  1. Inner radius along x direction: 1.5 L + $\frac{L_{pp}}{2}$
  2. Relaxation factor at Inlet & Outlet: 0.05
  3. Relaxation length: 2L
  4. Inner radius along y direction: 1.0 L
  5. Relaxation factor at Side: 0.05
  6. Relaxation length: 0.5 L

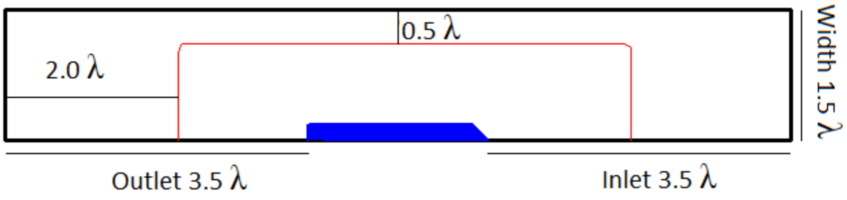

Figure B.20: Domain case E

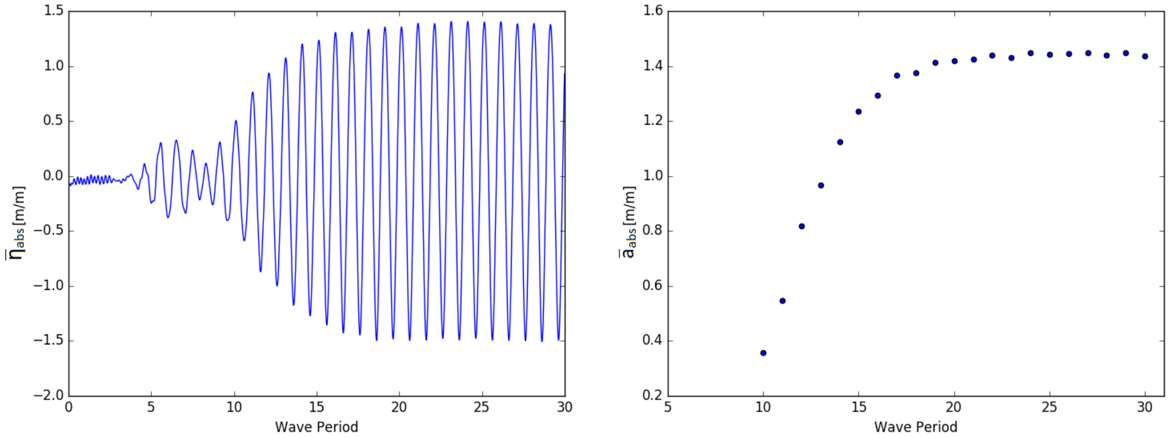

(a) Time trace wave elevation

(b) Wave amplitude

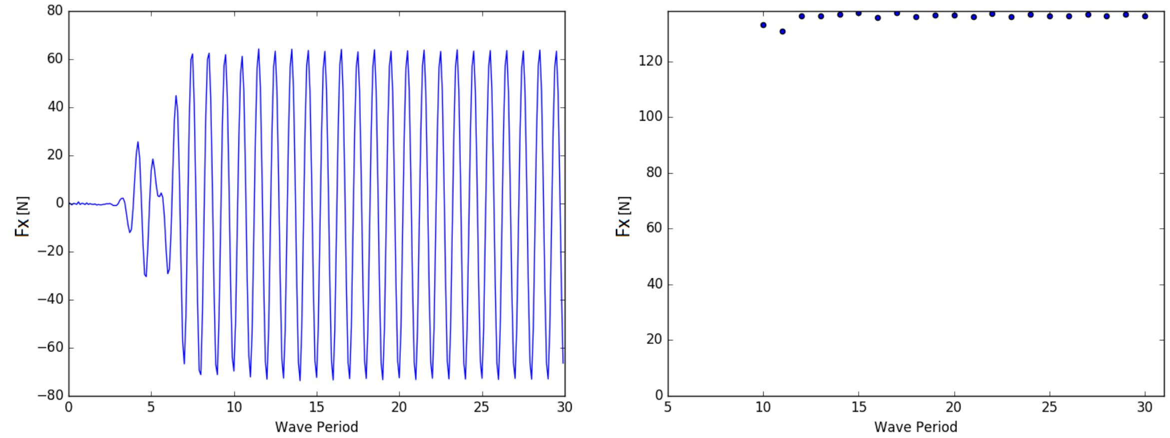

(c) Time trace F_x

(d) Scatter F_x

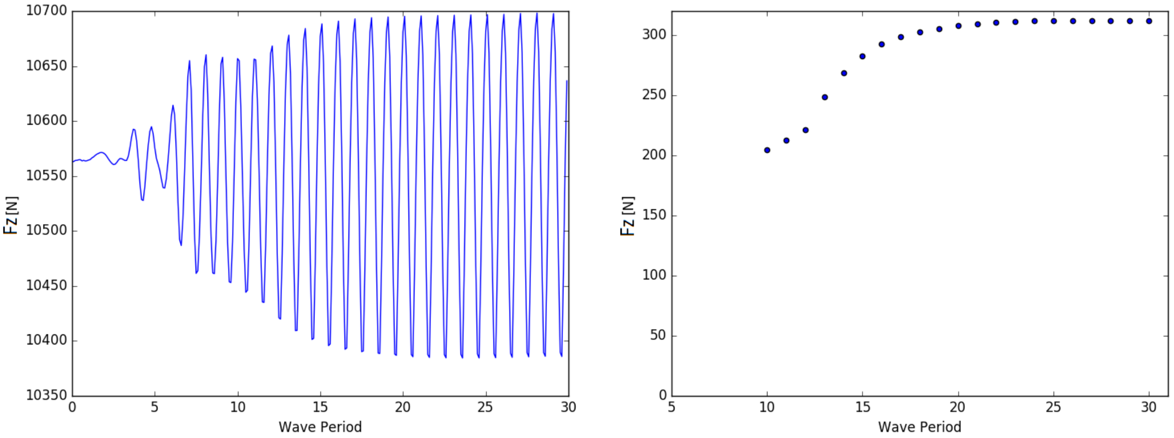

(e) Time trace F_z

(f) Scatter F_z

Figure B.21: Case E

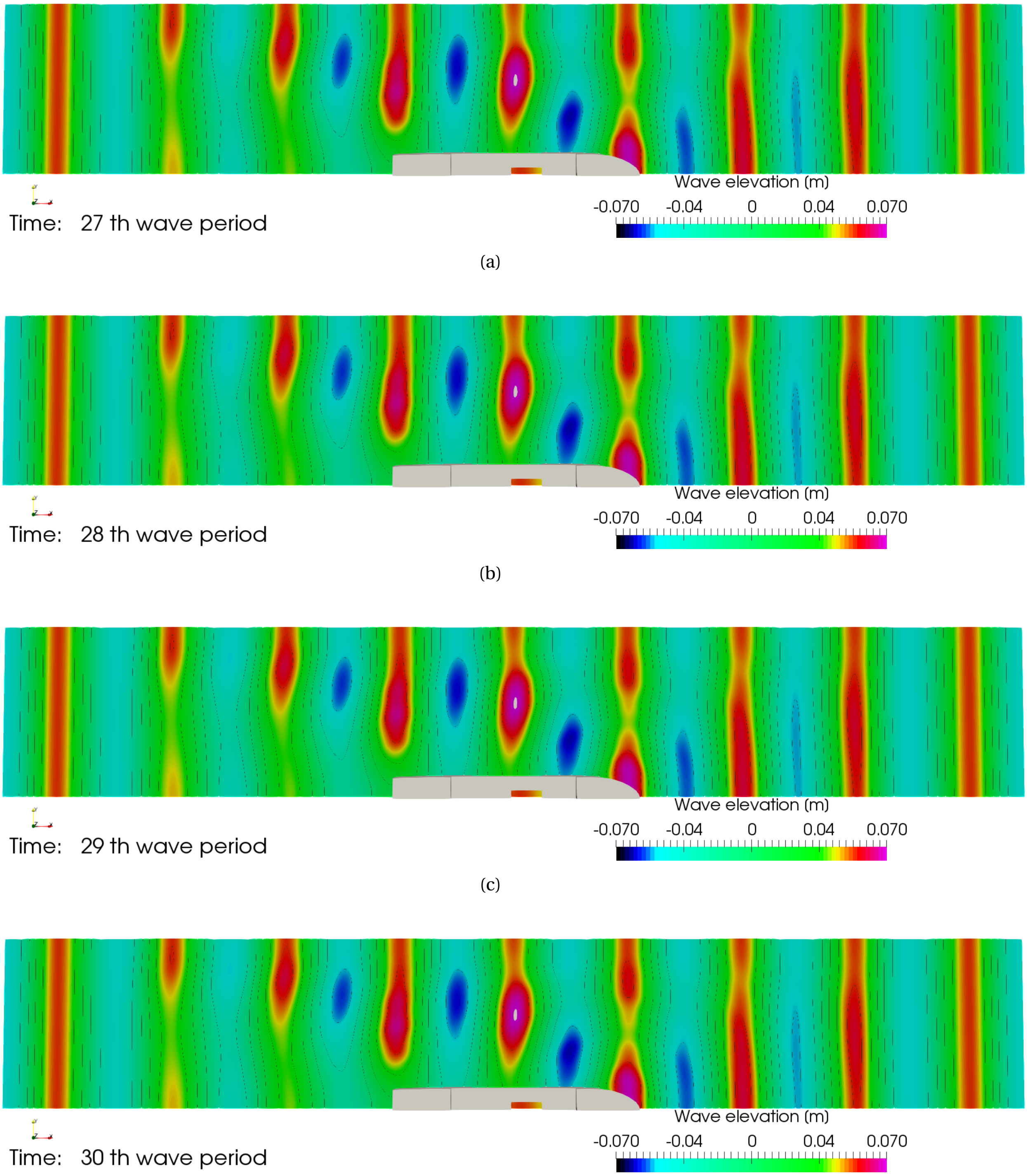

(a)

(b)

(c)

(d)

Figure B.22: Wave elevation case E

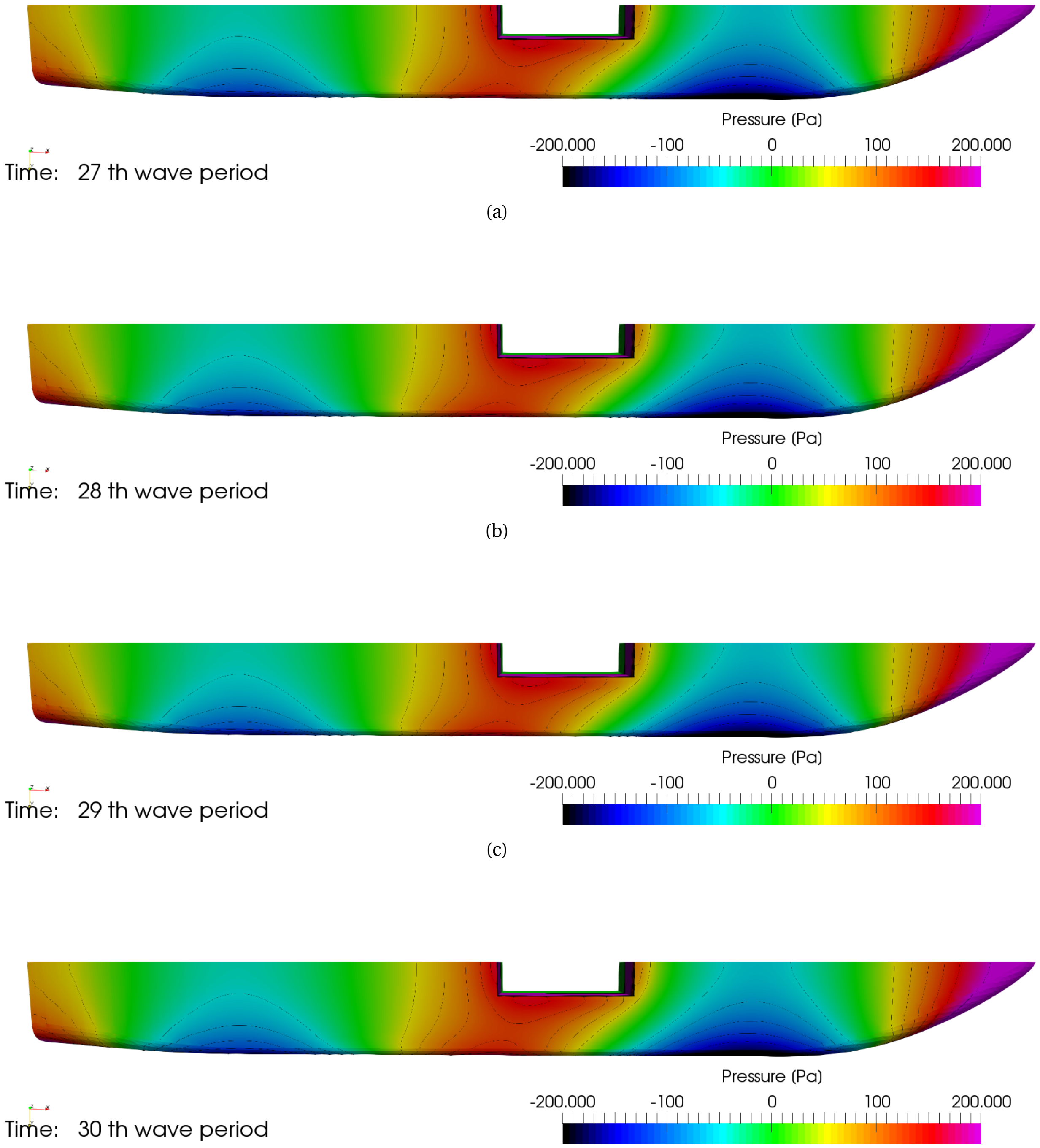

(a)

(b)

(c)

(d)

Figure B.23: Pressure distribution along the bottom for case E

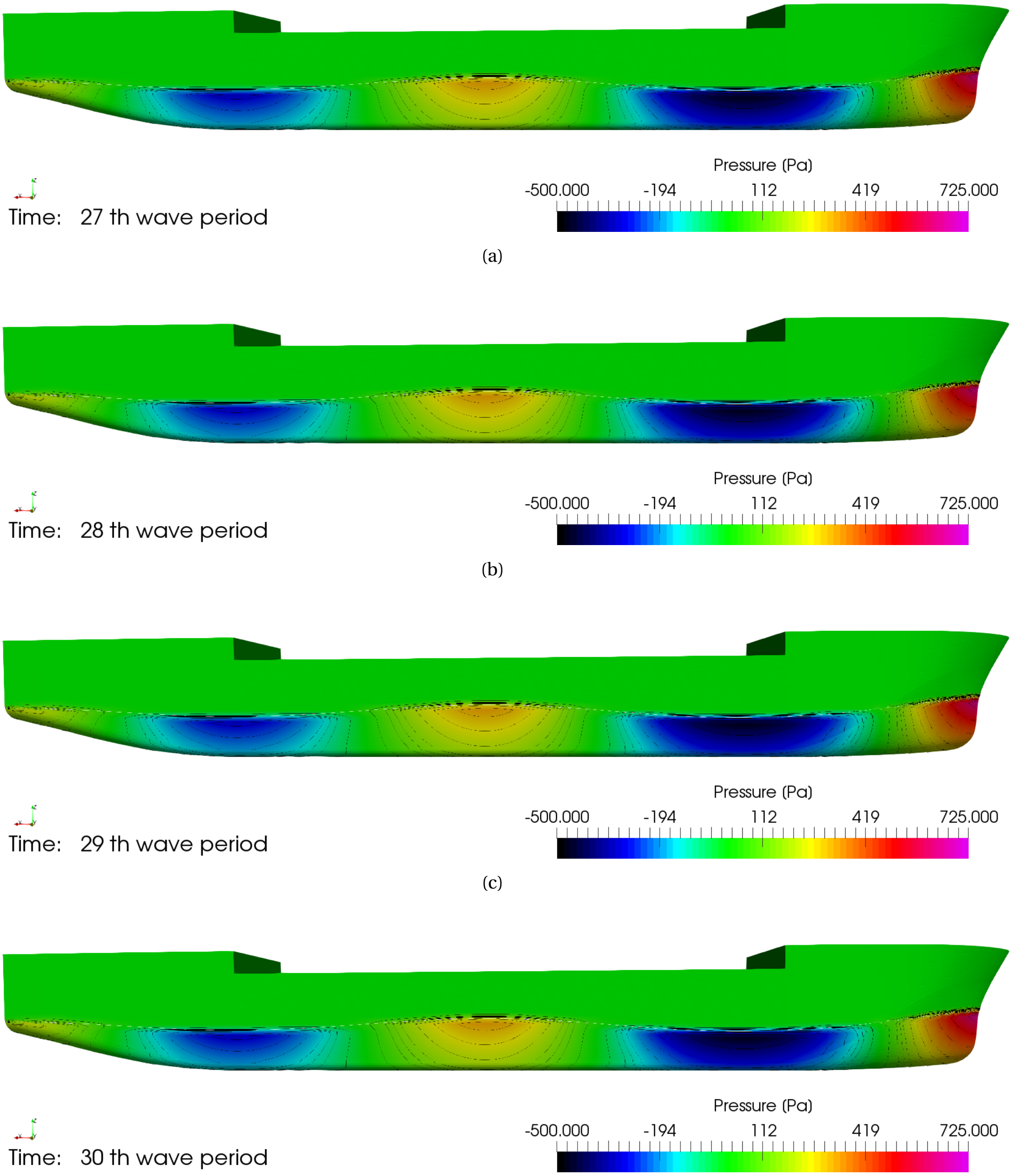

(a)

(b)

(c)

(d)

Figure B.24: Pressure distribution along the side for case E

B.6. Case F

- Grid: Coarse (2.8M cells)
- Timestep: T/100
- Convergence level : 10^{-4}
- Domain length: 3.5 λ in front and aft the vessel
- Domain width : 1.5 λ
- Boundary conditions:
    1. Inlet: Generation and absorption Sommerfeld 1
    2. Side: BC Wall
    3. Outlet: Absorption Sommerfeld 1
- Relaxation zone:
    1. Inner radius along x direction: 1.5 L + $\frac{L_{pp}}{2}$
    2. Relaxation factor at Inlet & Outlet: 0.10
    3. Relaxation length: 2L
    4. Inner radius along y direction: -
    5. Relaxation factor at Side: 0.00
    6. Relaxation length: 0L

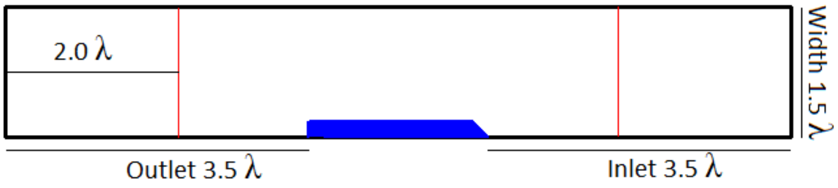

Figure B.25: Domain case F

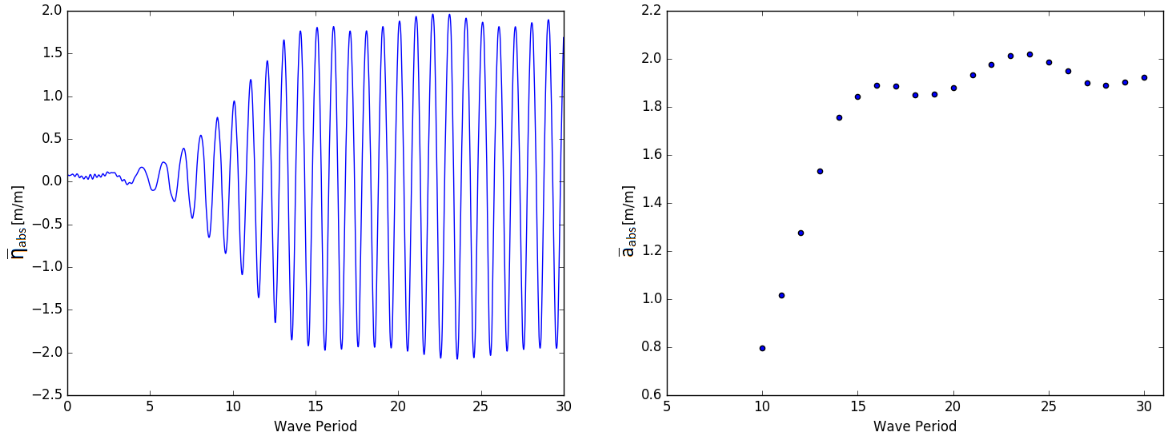

(a) Time trace wave elevation

(b) Wave amplitude

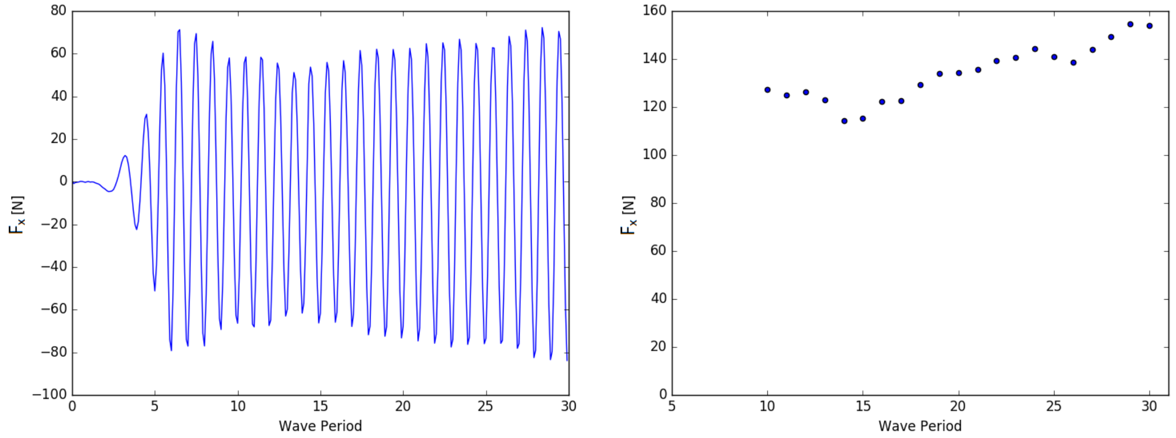

(c) Time trace F_x

(d) Scatter F_x

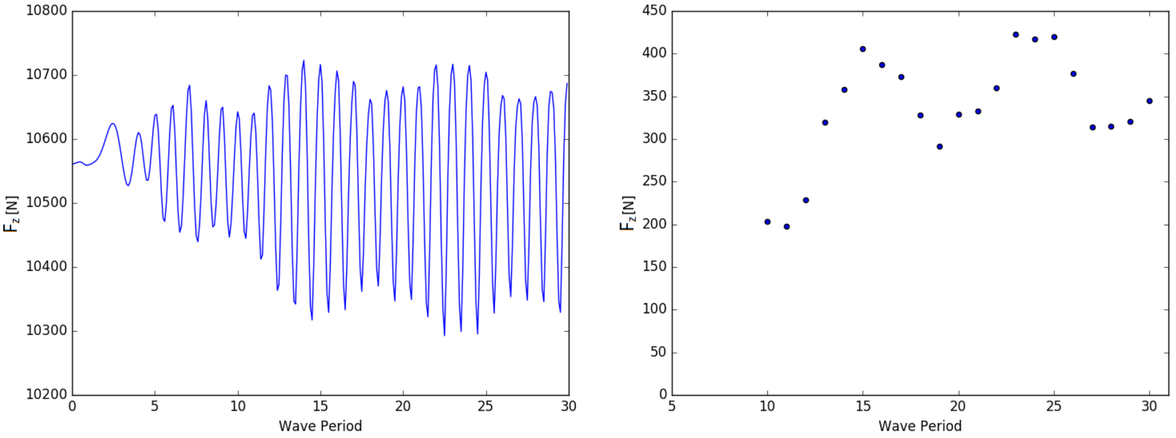

(e) Time trace F_z

(f) Scatter F_z

Figure B.26: Case E

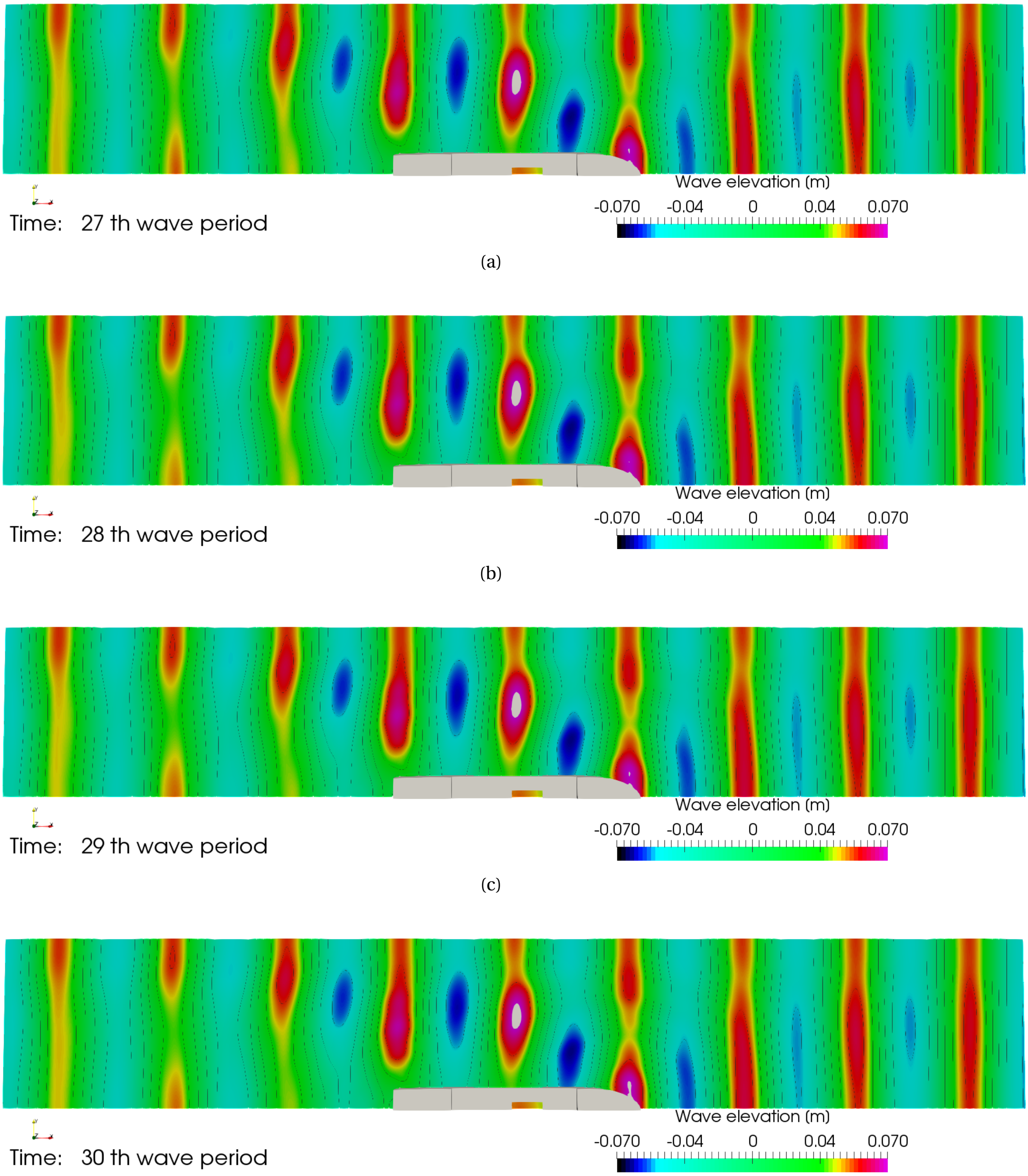

(a)

(b)

(c)

(d)

Figure B.27: Wave elevation case E

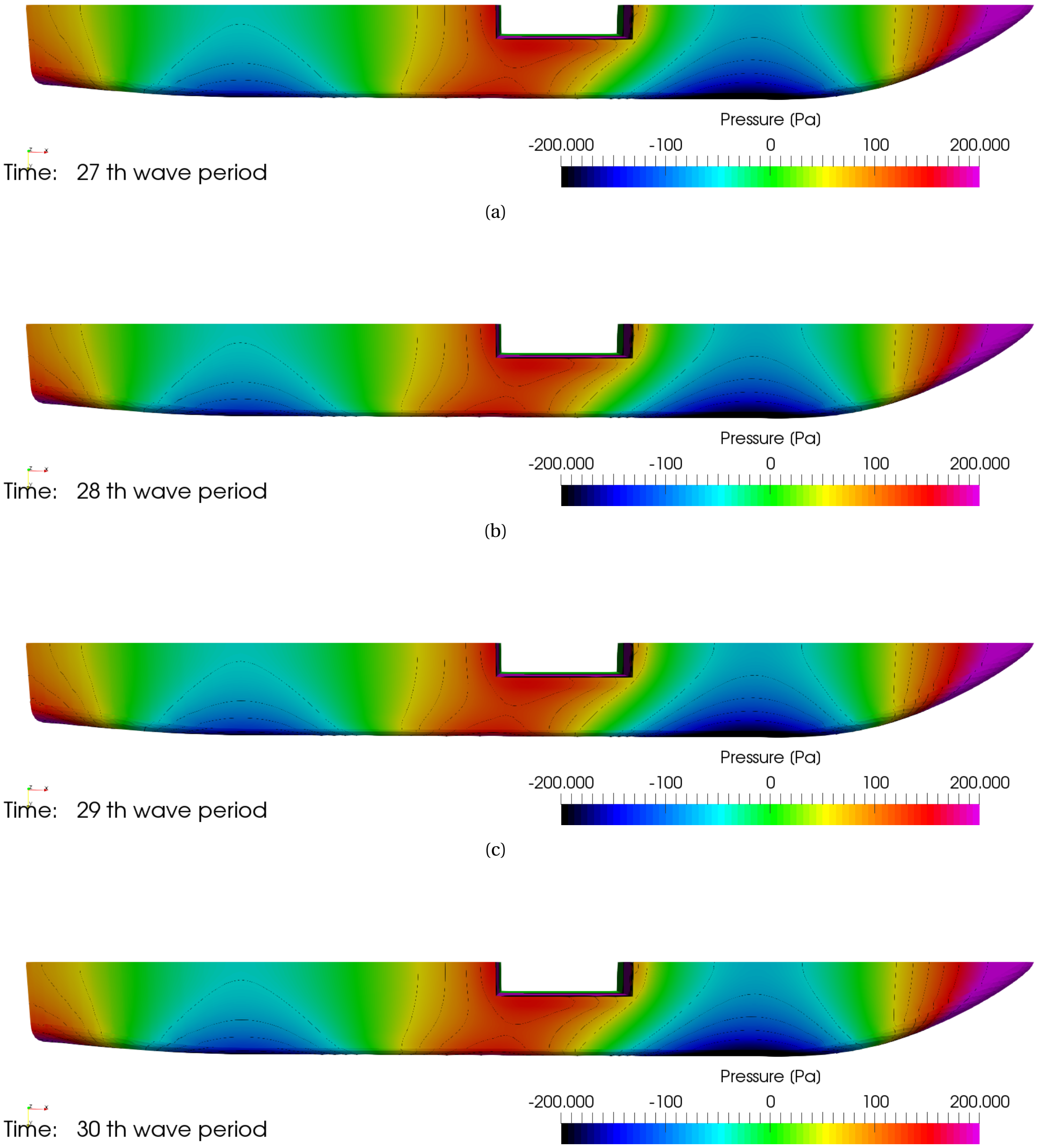

(a)

(b)

(c)

(d)

Figure B.28: Pressure distribution along the bottom for case E

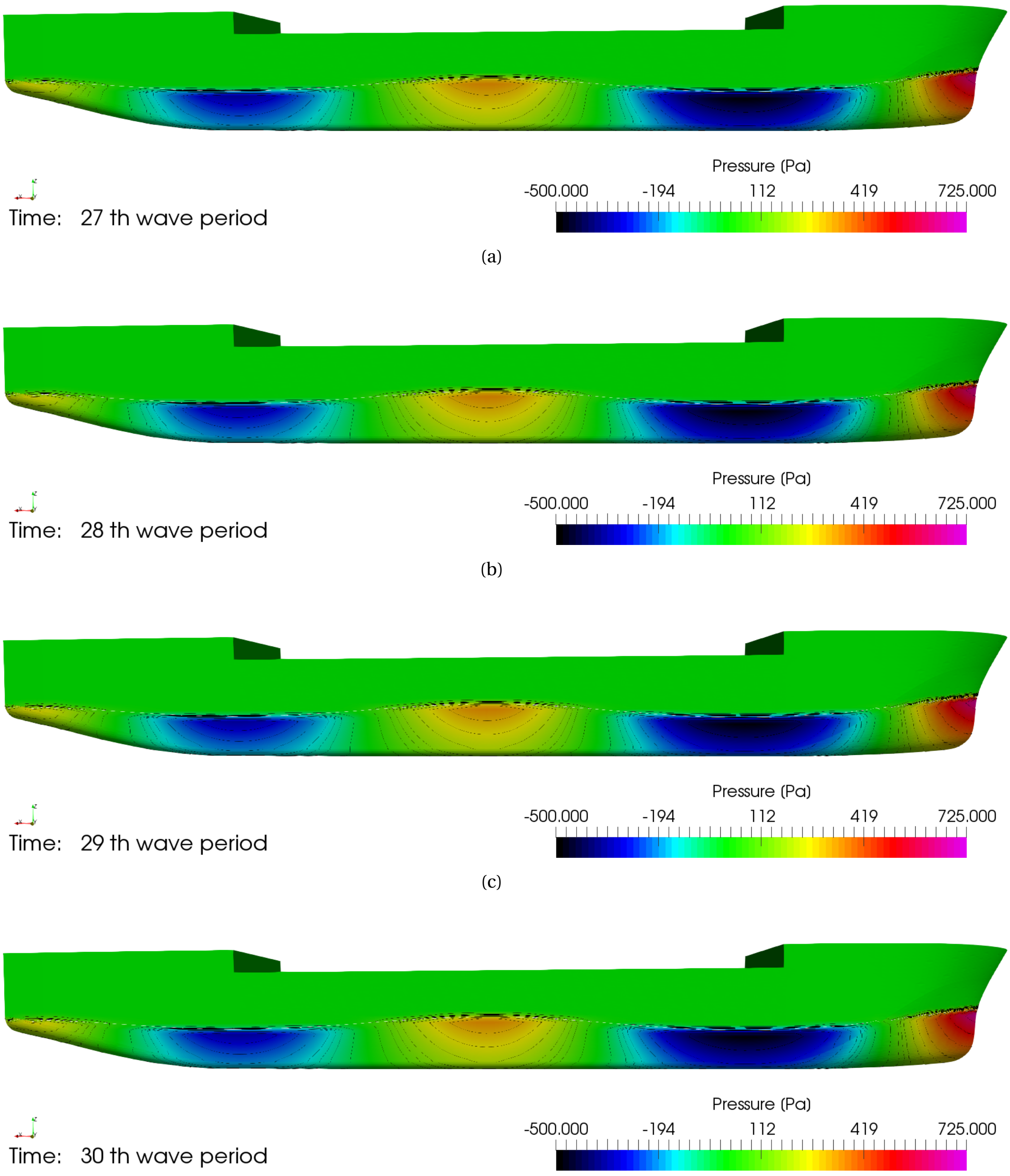

(a)

(b)

(c)

(d)

Figure B.29: Pressure distribution along the side for case E

B.7. Case G

- Grid: Coarse (2.8M cells)
- Timestep: T/100
- Convergence level : 10^{-4}
- Domain length: 3.5 λ in front and aft the vessel
- Domain width : 1.5 λ
- Boundary conditions:
  1. Inlet: Generation and absorption Sommerfeld 1
  2. Side: BC Wall
  3. Outlet: Absorption Sommerfeld 1
- Relaxation zone:
  1. Inner radius along x direction: -
  2. Relaxation factor at Inlet & Outlet: 0.00
  3. Relaxation length: 0 L
  4. Inner radius along y direction: 1 L
  5. Relaxation factor at Side: 0.05
  6. Relaxation length: 0.5 L

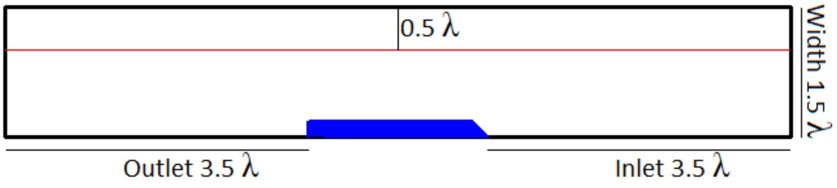

Figure B.30: Domain case G

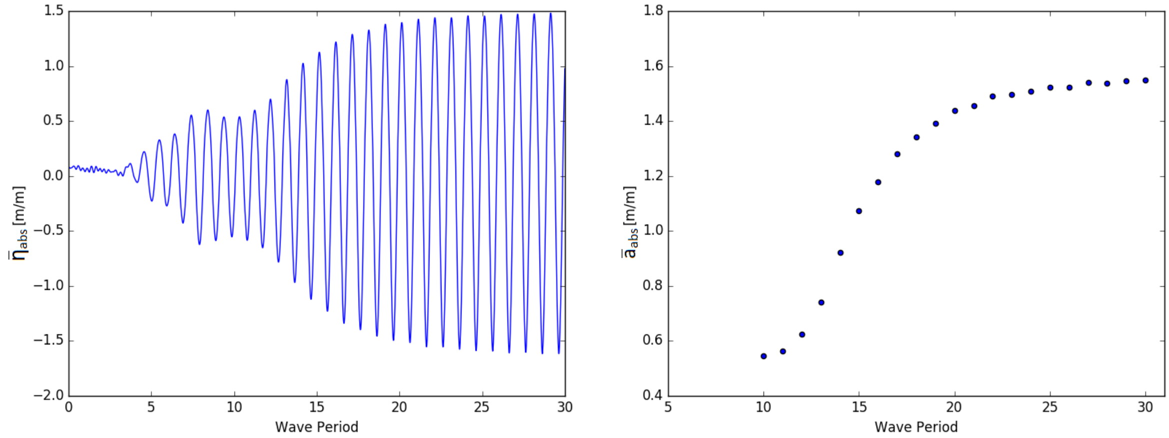

(a) Time trace wave elevation

(b) Wave amplitude

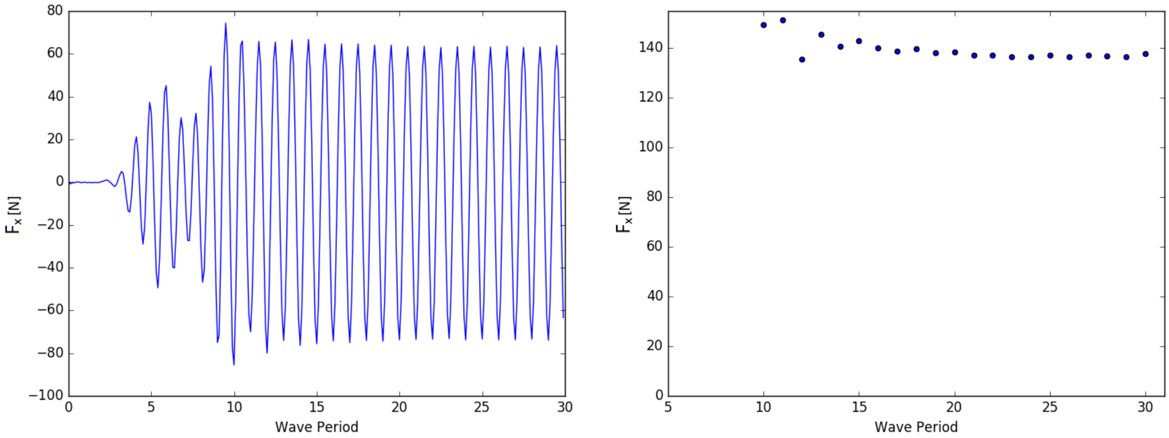

(c) Time trace F_x

(d) Scatter F_x

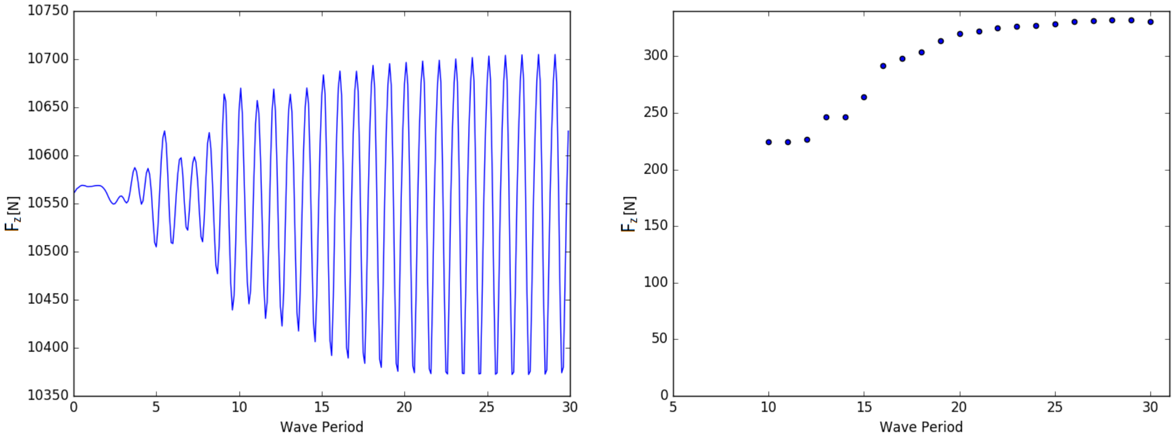

(e) Time trace F_z

(f) Scatter F_z

Figure B.31: Case G

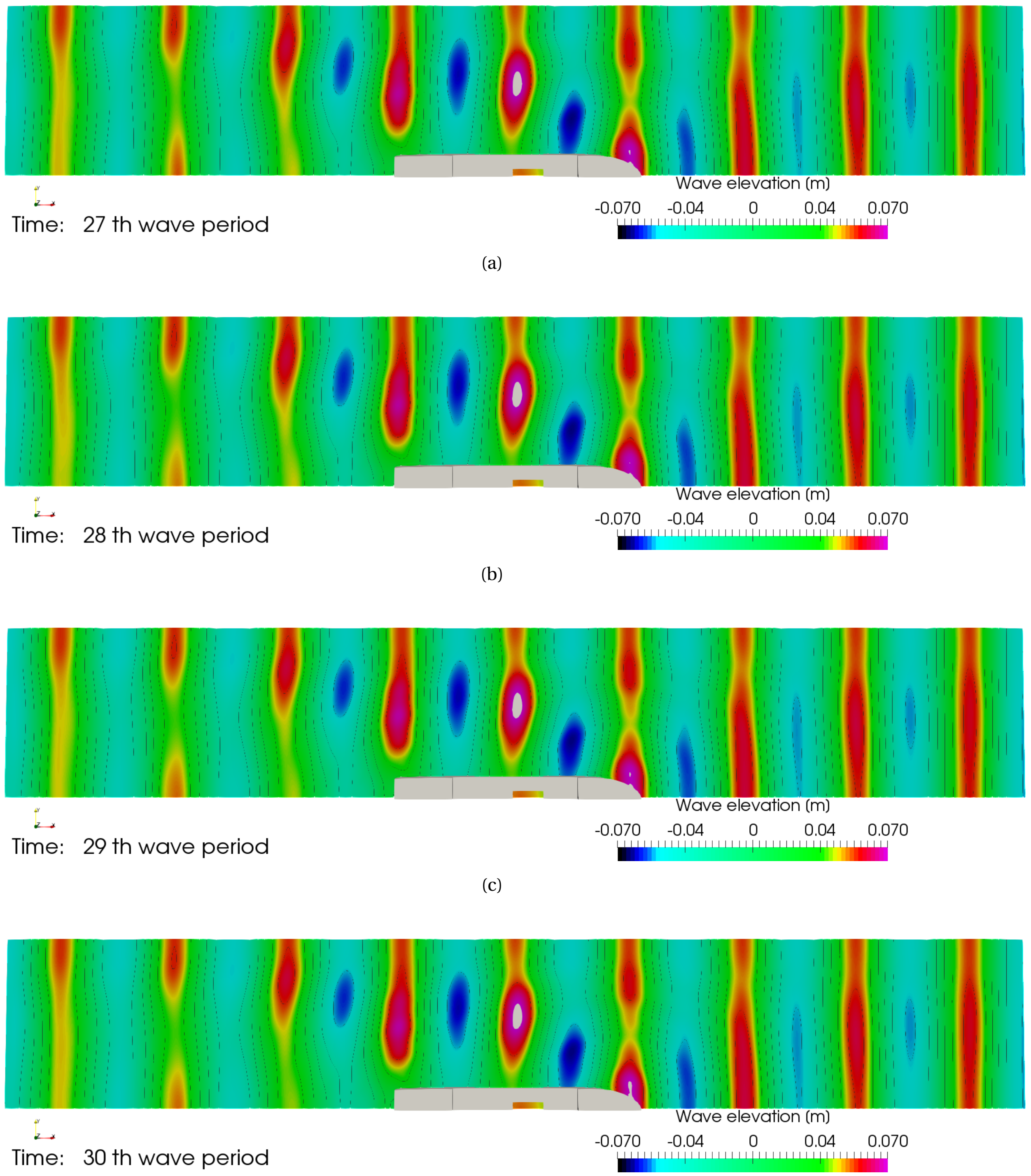

(a)

(b)

(c)

(d)

Figure B.32: Wave elevation case G

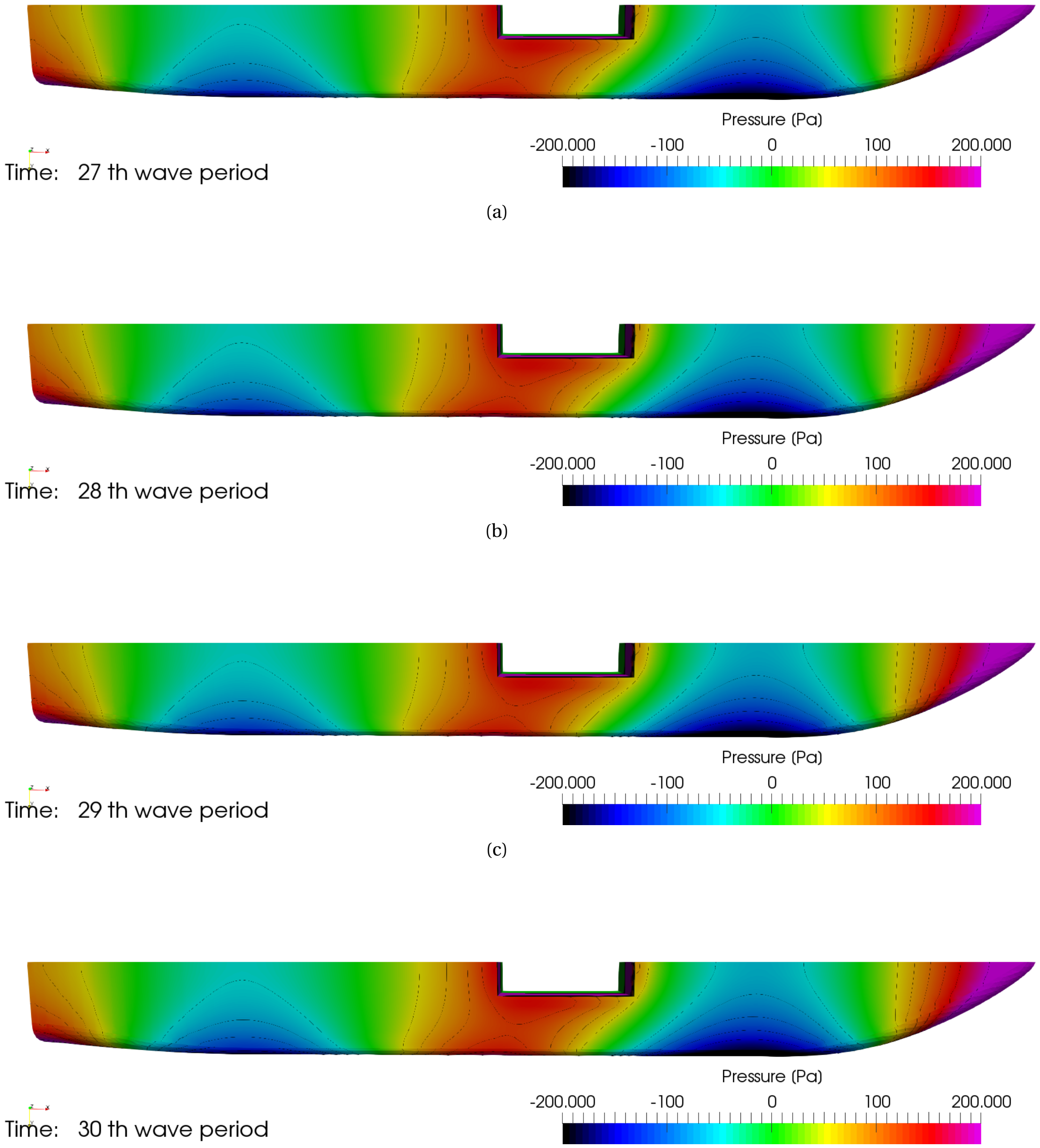

(a)

(b)

(c)

(d)

Figure B.33: Pressure distribution along the bottom for case G

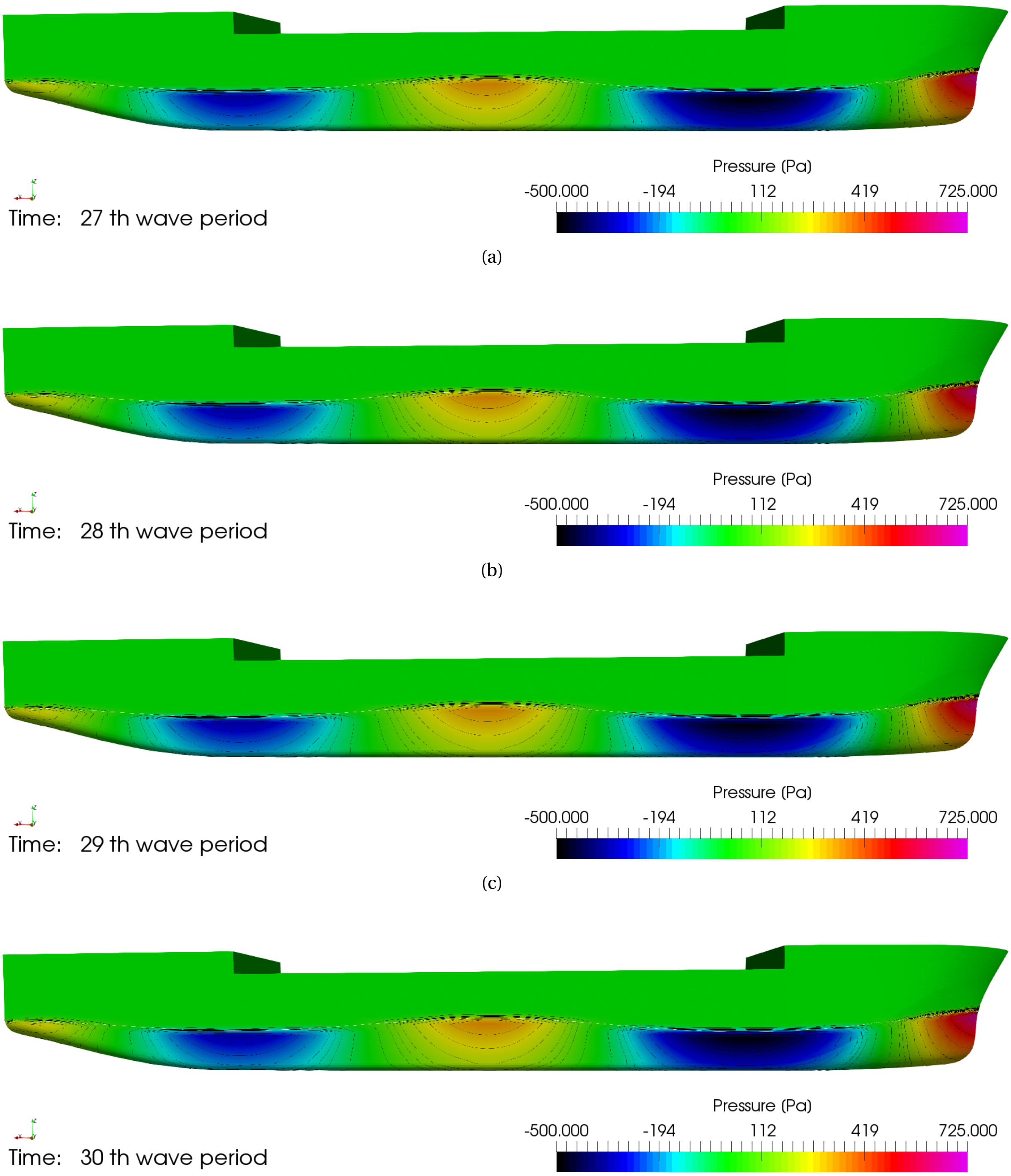

(a)

(b)

(c)

(d)

Figure B.34: Pressure distribution along the side for case G

B.8. Case H

- Grid: Coarse (4.2M cells)
- Timestep: T/100
- Convergence level : 10^{-4}
- Domain length: 3.5 λ in front and aft the vessel
- Domain width : 2.0 λ
- Boundary conditions:
  1. Inlet: BC Wall
  2. Side: BC Wall
  3. Outlet: BC Wall
- Relaxation zone:
  1. Inner radius along x direction: 1.5 λ
  2. Relaxation factor at Inlet & Outlet: 0.05
  3. Relaxation length: 2.0 λ
  4. Inner radius along y direction: 1.0 λ
  5. Relaxation factor at Side: 0.10
  6. Relaxation length: 1.0 λ

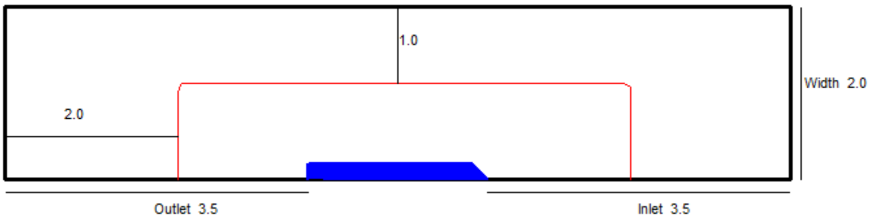

Figure B.35: Domain case H

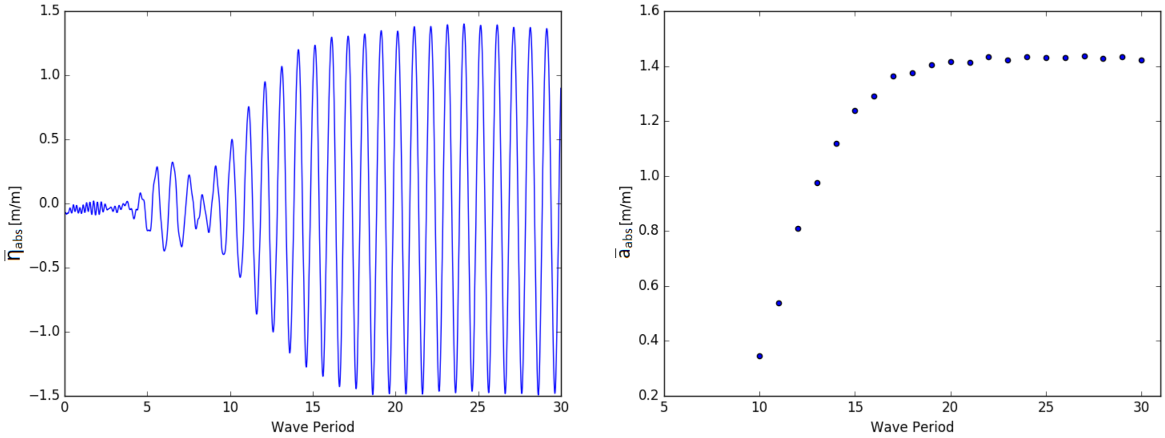

(a) Time trace wave elevation

(b) Wave amplitude

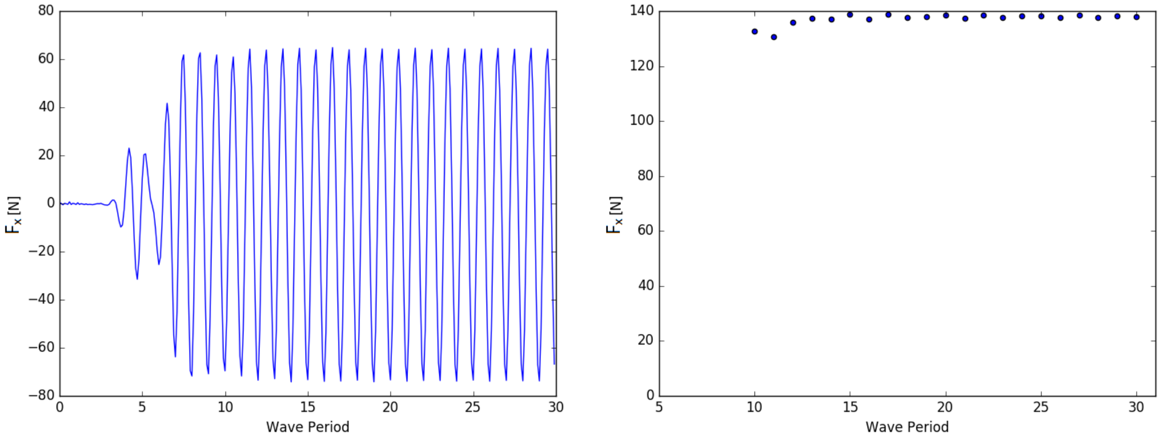

(c) Time trace F_x

(d) Scatter F_x

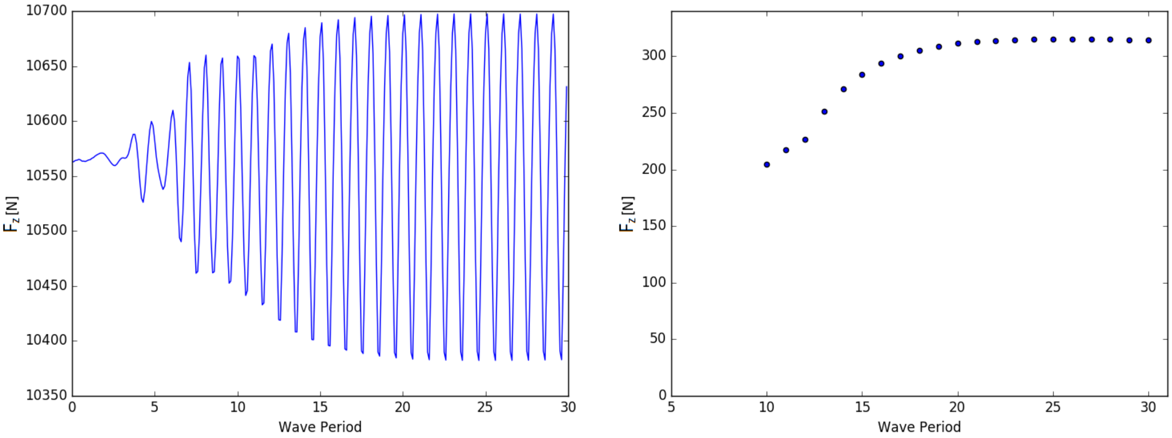

(e) Time trace F_z

(f) Scatter F_z

Figure B.36: Case H

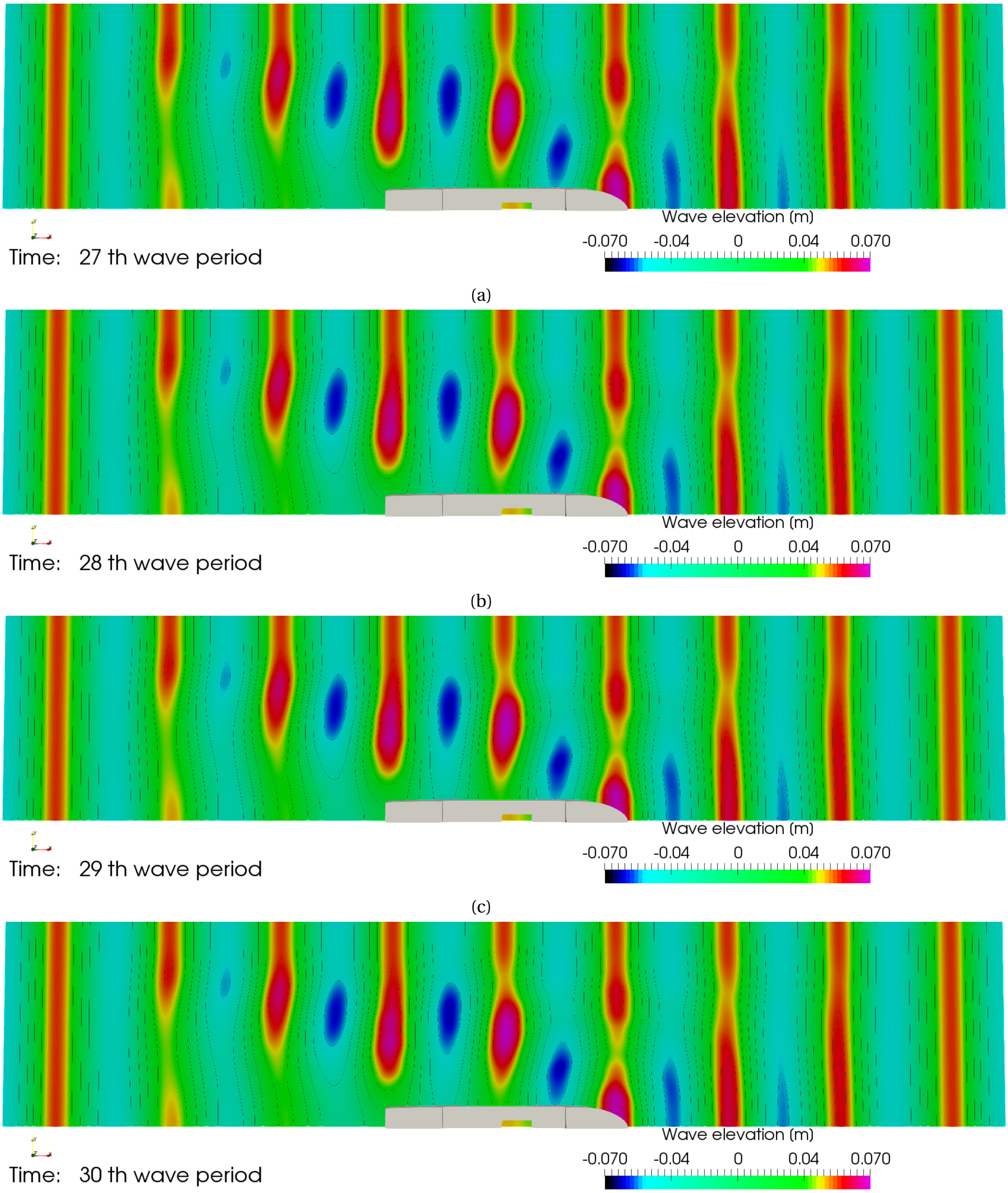

(a)

(b)

(c)

(d)

Figure B.37: Wave elevation case H

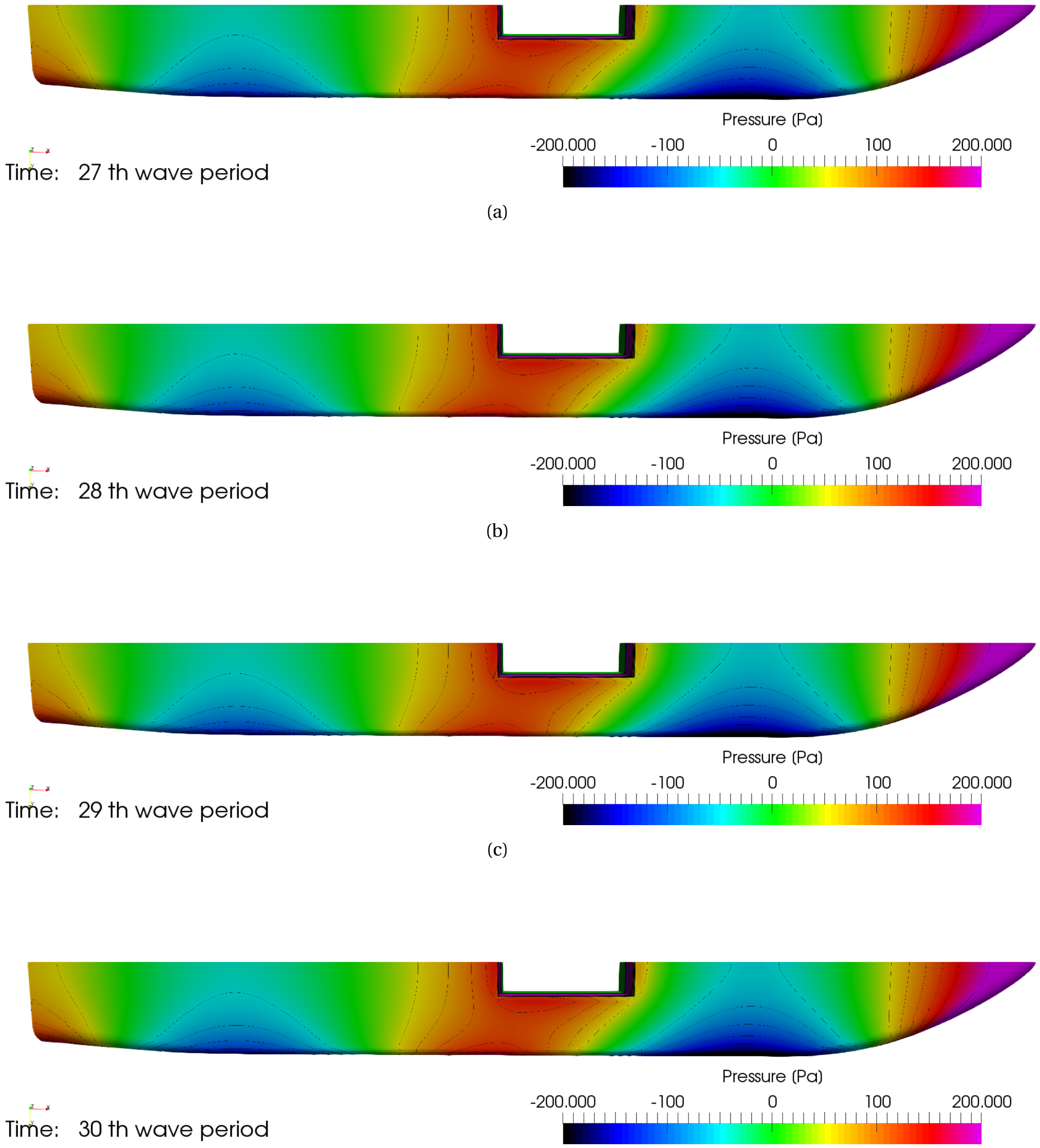

(a)

(b)

(c)

(d)

Figure B.38: Pressure distribution along the bottom for case G

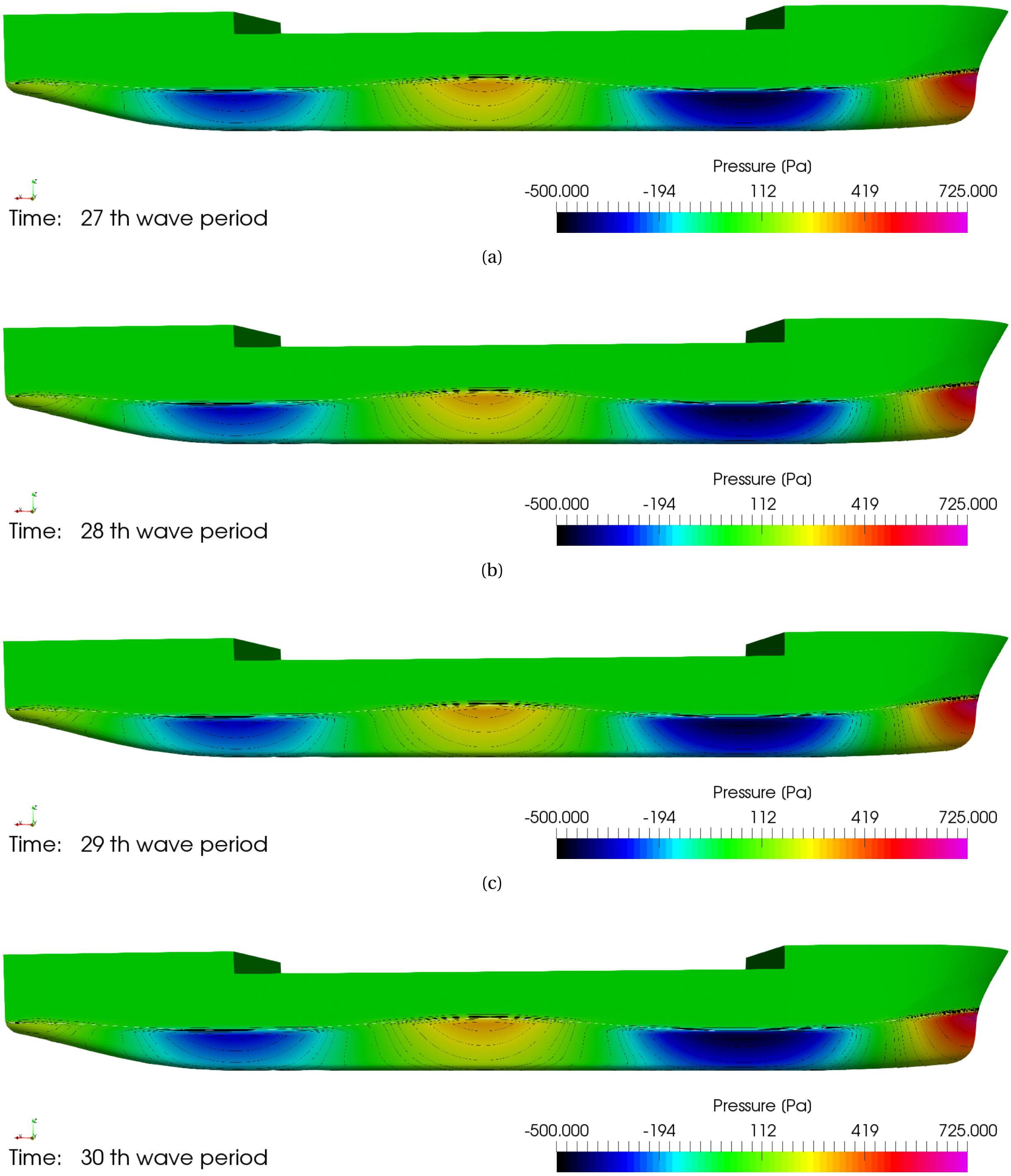

(a)

(b)

(c)

(d)

Figure B.39: Pressure distribution along the side for case H

B.9. Case I

- Grid: Medium (6.1M cells)
- Timestep: T/200
- Convergence level : 10^{-4}
- Domain length: 3.5 λ in front and aft the vessel
- Domain width : 2.0 λ
- Boundary conditions:
  1. Inlet: BC Wall
  2. Side: BC Wall
  3. Outlet: BC Wall
- Relaxation zone:
  1. Inner radius along x direction: 1.5 λ
  2. Relaxation factor at Inlet & Outlet: 0.05
  3. Relaxation length: 2.0 λ
  4. Inner radius along y direction: 1.0 λ
  5. Relaxation factor at Side: 0.10
  6. Relaxation length: 1.0 λ

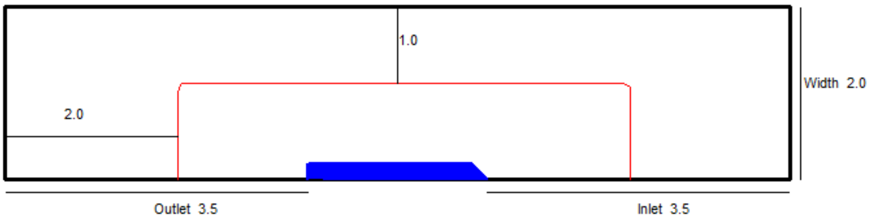

Figure B.40: Domain case I

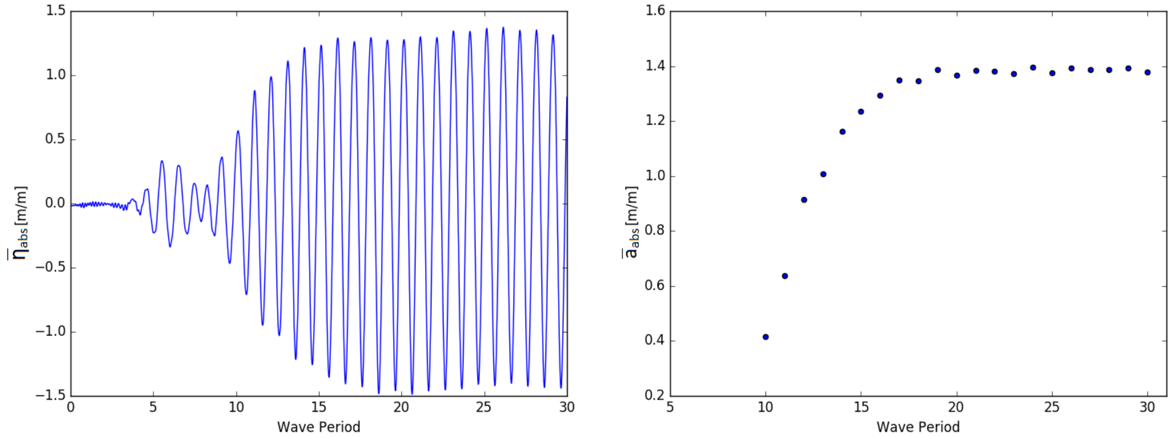

(a) Time trace wave elevation

(b) Wave amplitude

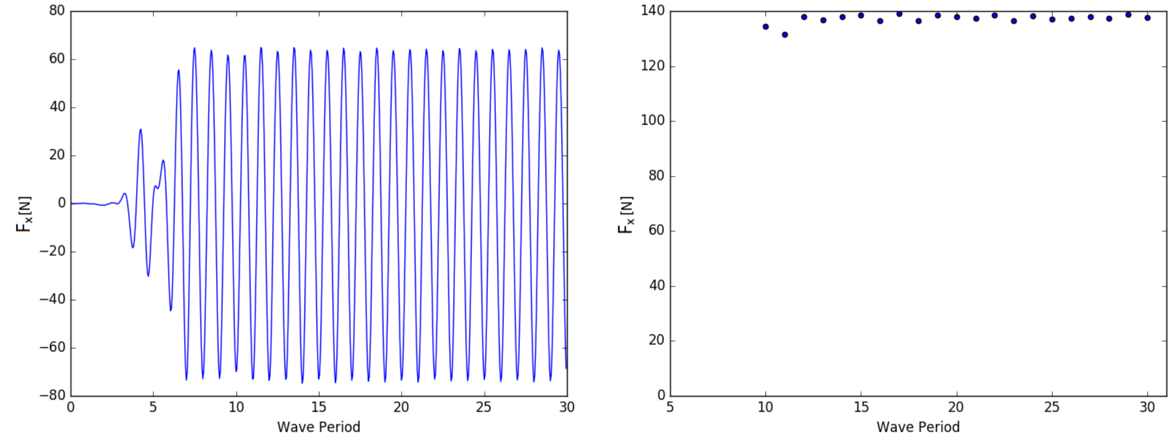

(c) Time trace F_x

(d) Scatter F_x

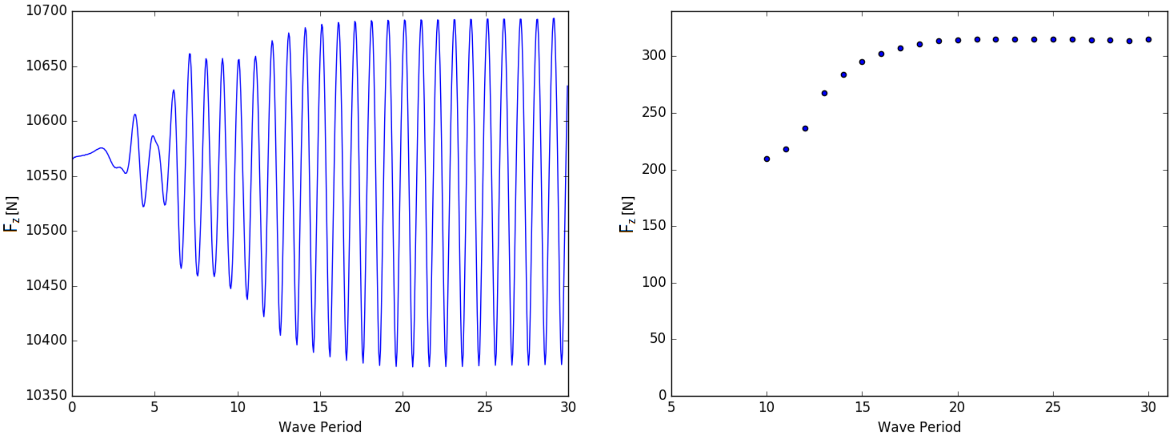

(e) Time trace F_z

(f) Scatter F_z

Figure B.41: Case I

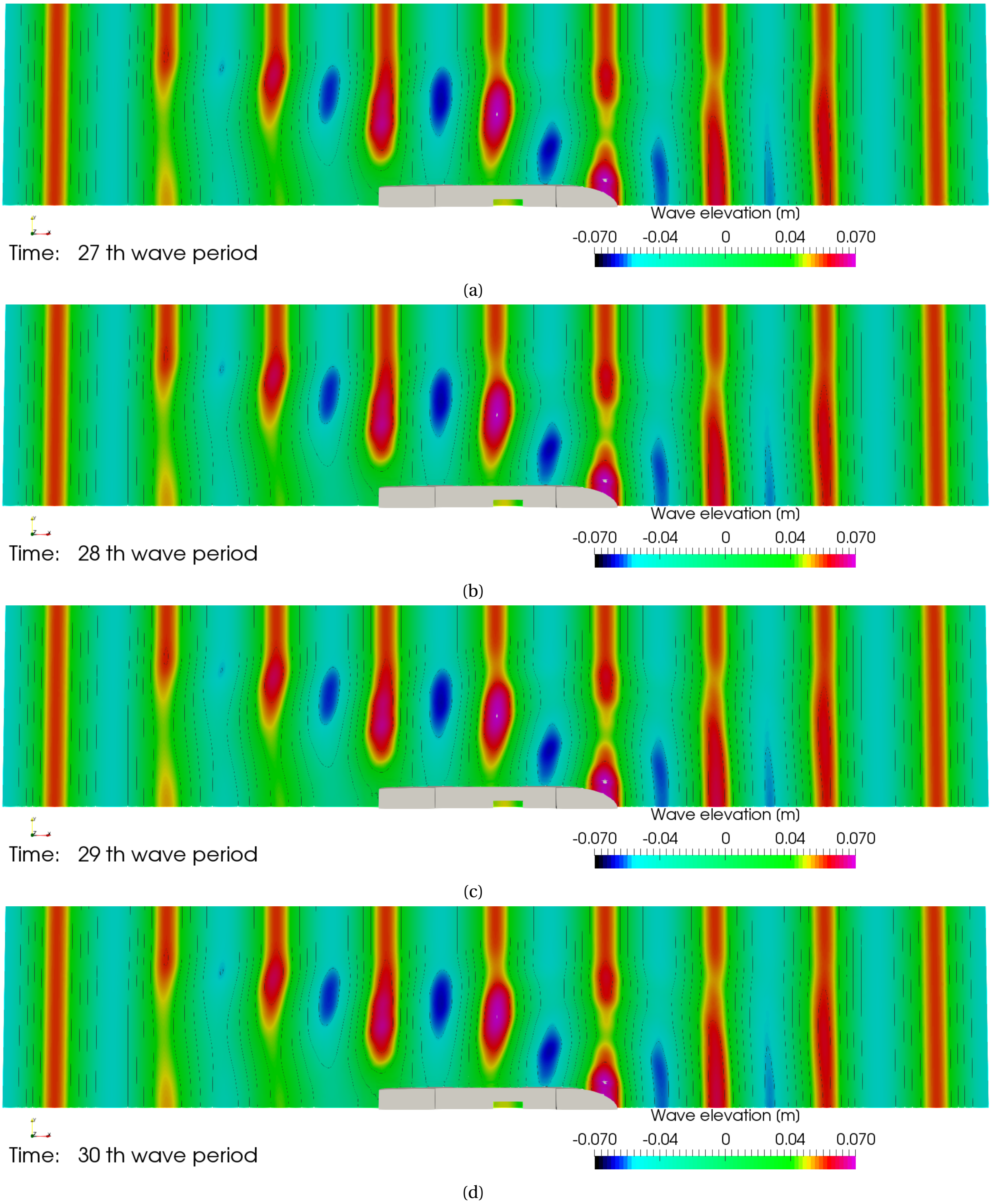

(a)

(b)

(c)

(d)

Figure B.42: Wave elevation case I

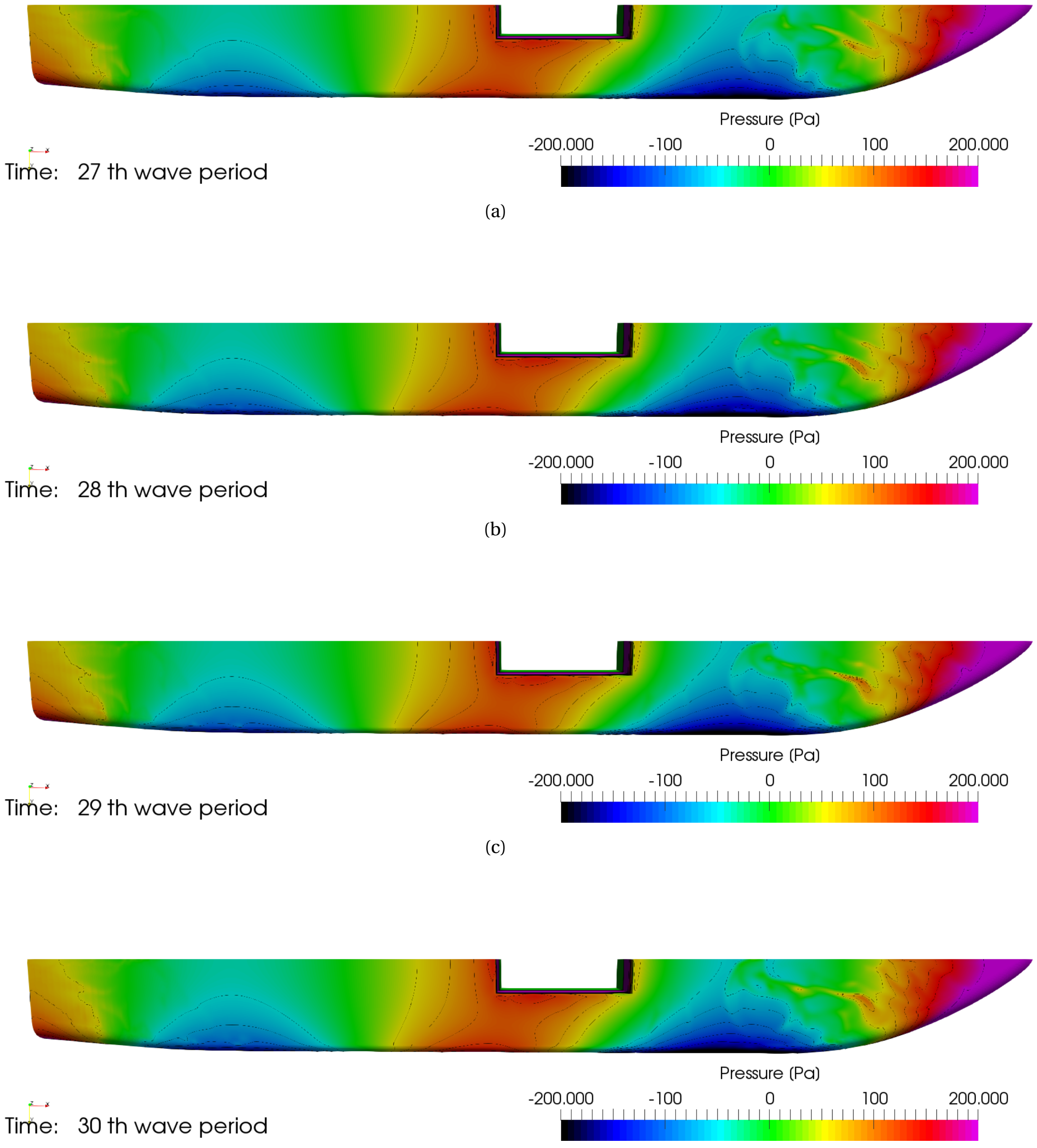

(a)

(b)

(c)

(d)

Figure B.43: Pressure distribution along the bottom for case I

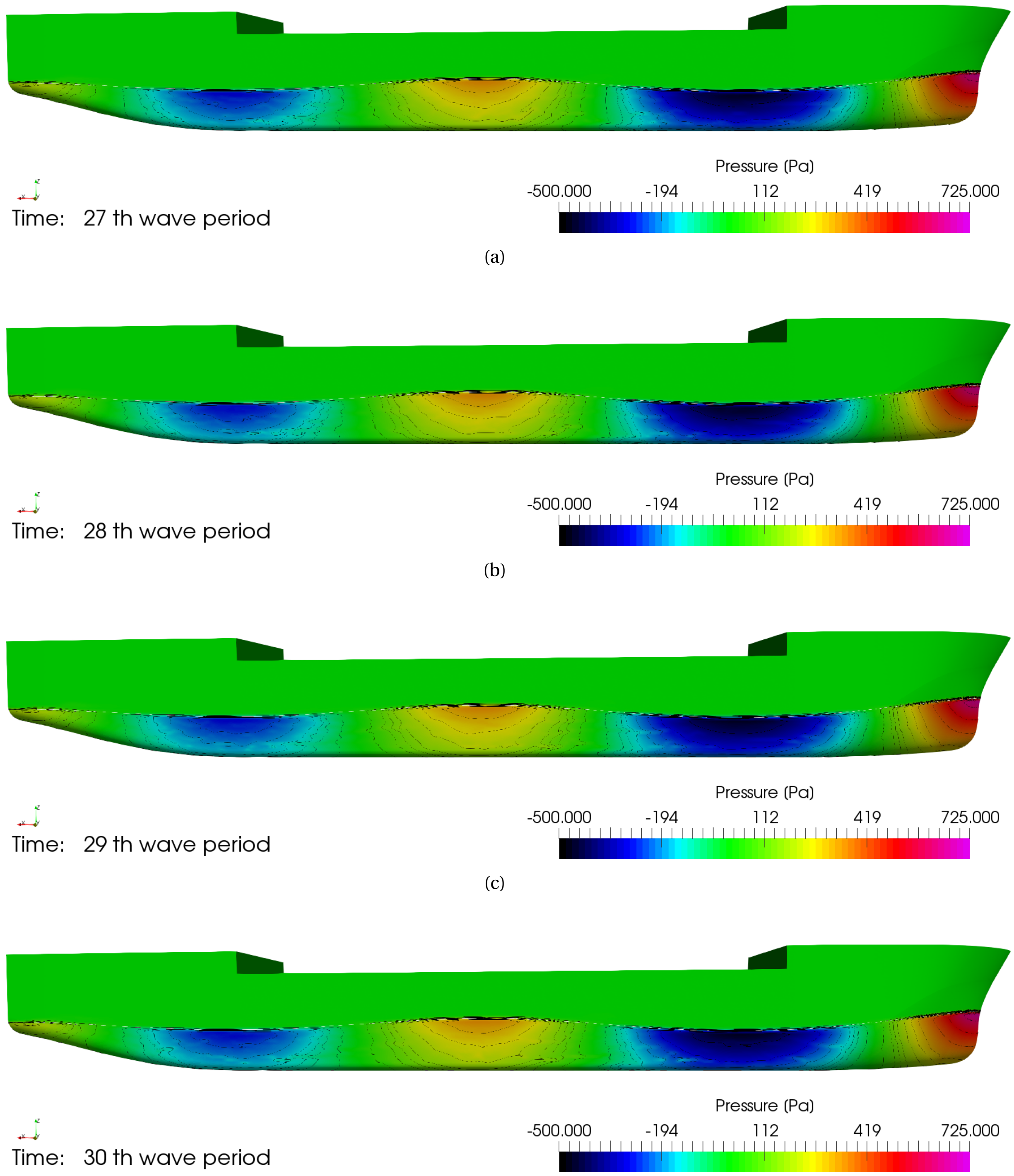

(a)

(b)

(c)

(d)

Figure B.44: Pressure distribution along the side for case I

B.10. Case J

- Grid: Medium (3.0M cells)
- Timestep: T/200
- Convergence level : 10^{-4}
- Domain length: 3.5 λ in front and aft the vessel
- Domain width : 2.0 λ
- Boundary conditions:
    1. Inlet: BC Wall
    2. Side: BC Wall
    3. Outlet: BC Wall
- Relaxation zone:
    1. Inner radius along x direction: 1.5 λ
    2. Relaxation factor at Inlet & Outlet: 0.05
    3. Relaxation length: 2.0 λ
    4. Inner radius along y direction: 1.0 λ
    5. Relaxation factor at Side: 0.10
    6. Relaxation length: 1.0 λ

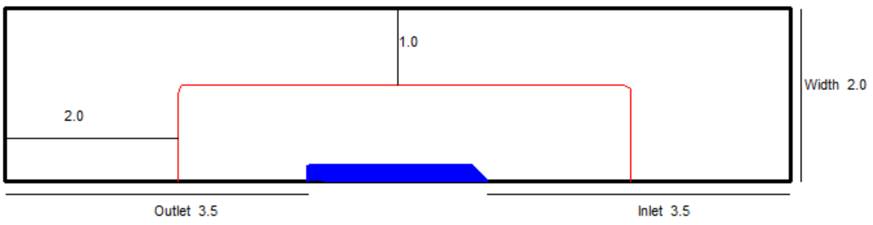

Figure B.45: Domain case J

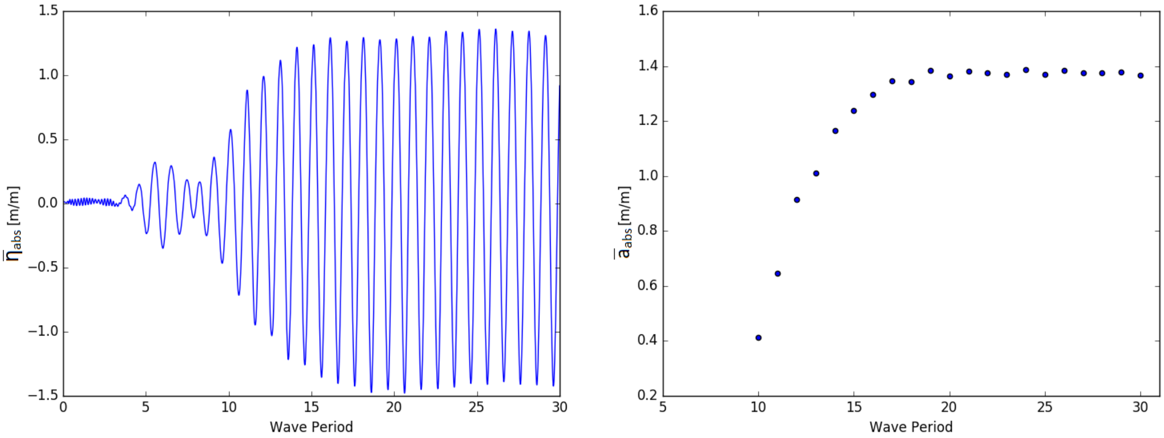

(a) Time trace wave elevation

(b) Wave amplitude

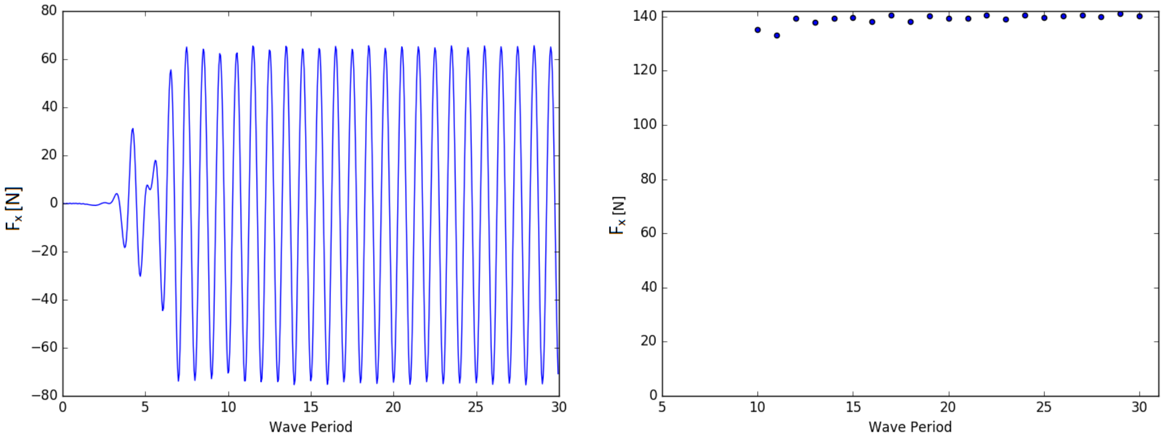

(c) Time trace F_x

(d) Scatter F_x

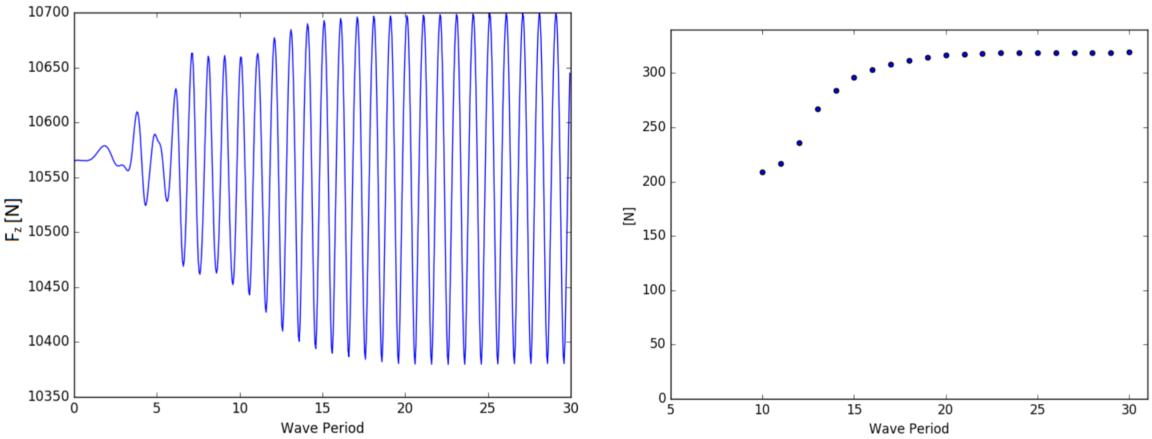

(e) Time trace F_z

(f) Scatter F_z

Figure B.46: Case J

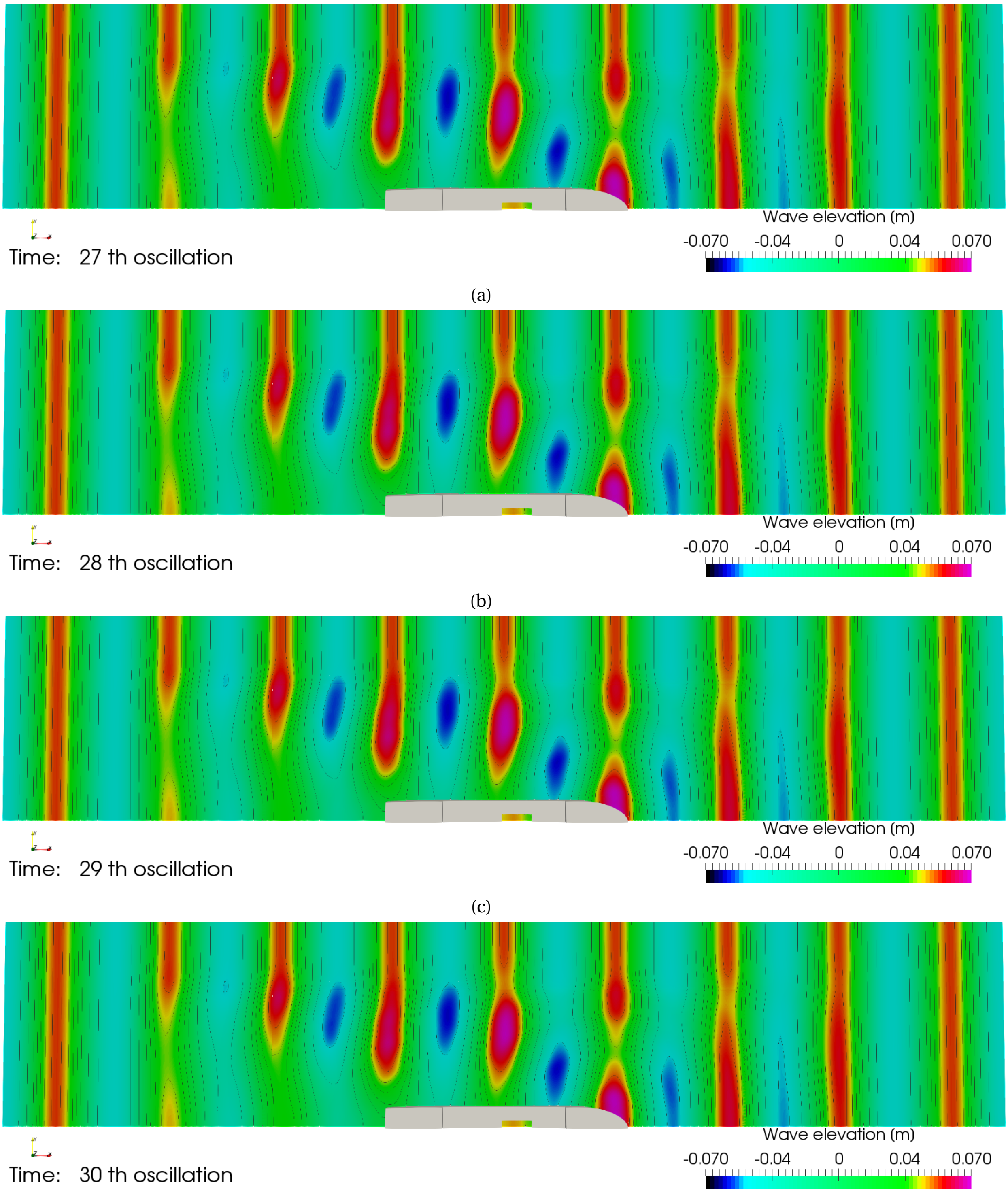

(a)

(b)

(c)

(d)

Figure B.47: Wave elevation case J

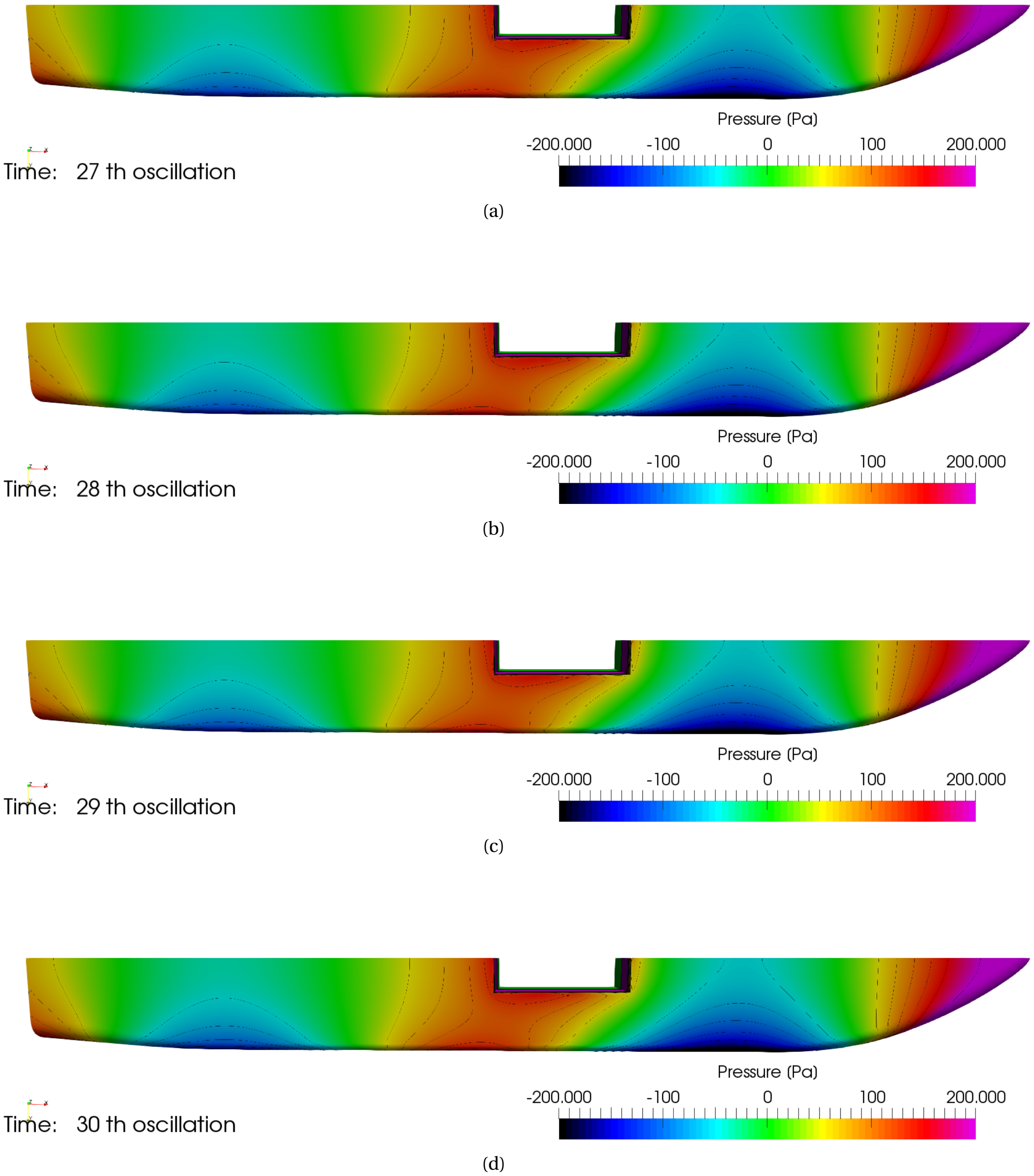

Figure B.48: Pressure distribution along the bottom for case J

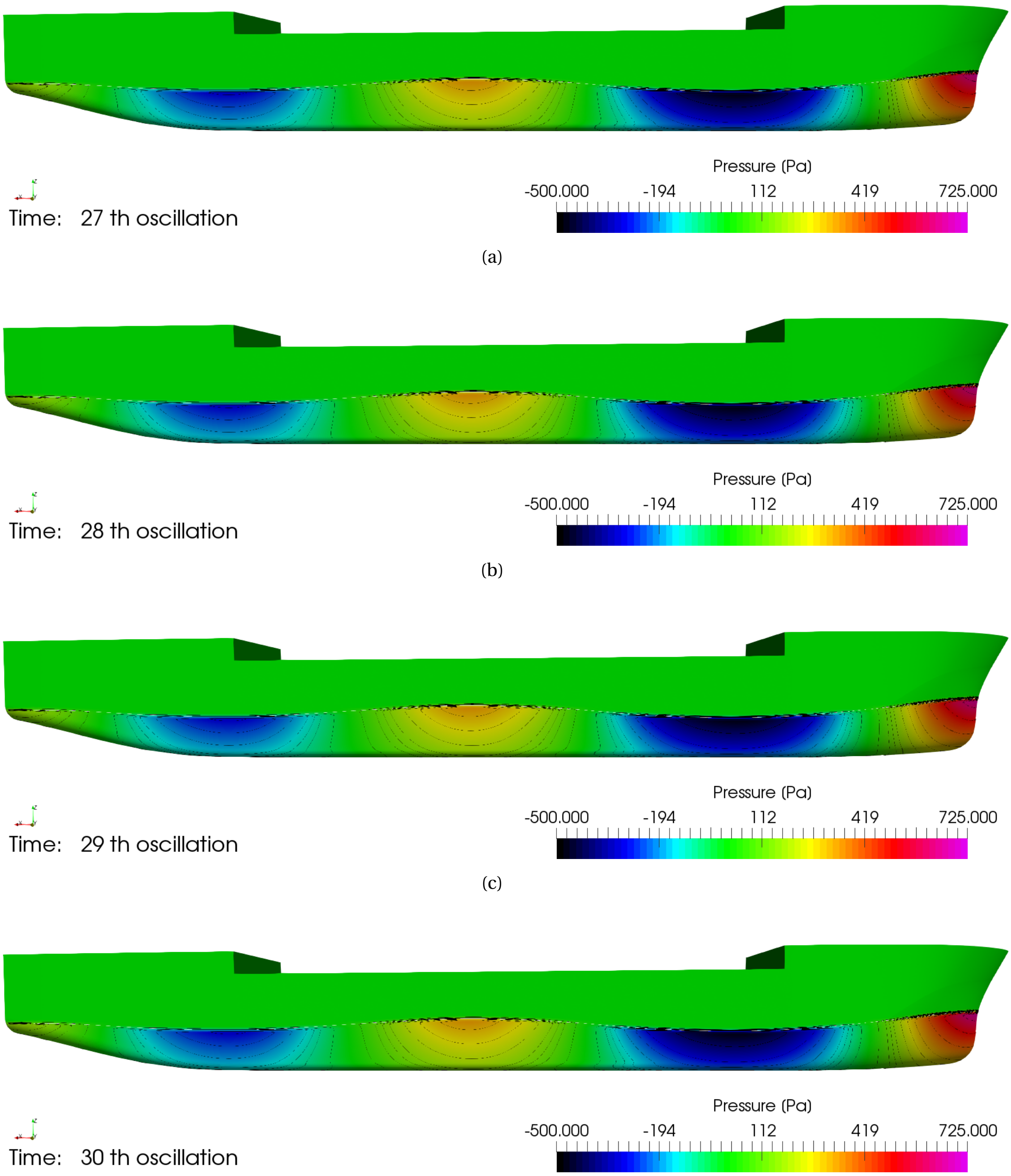

(a)

(b)

(c)

(d)

Figure B.49: Pressure distribution along the side for case J

B.11. Case J2

- Grid: Medium (3.0M cells)
- Timestep: T/200
- Convergence level : 10^{-4}
- Domain length: 3.5 λ in front and aft the vessel
- Domain width : 2.0 λ
- Boundary conditions:
    1. Inlet: BC Wall
    2. Side: BC Wall
    3. Outlet: BC Wall
- Relaxation zone:
    1. Inner radius along x direction: 1.5 λ
    2. Relaxation factor at Inlet & Outlet: 0.05
    3. Relaxation length: 2.0 λ
    4. Inner radius along y direction: 1.0 λ
    5. Relaxation factor at Side: 0.10
    6. Relaxation length: 1.0 λ

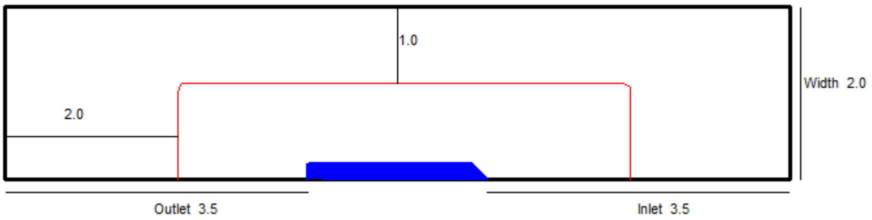

Figure B.50: Domain case J2

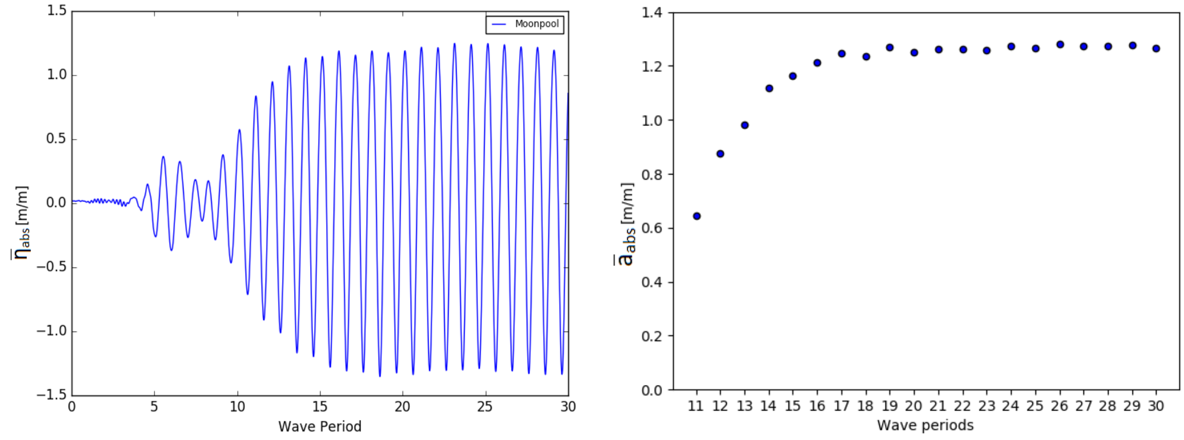

(a) Time trace wave elevation (b) Wave amplitude

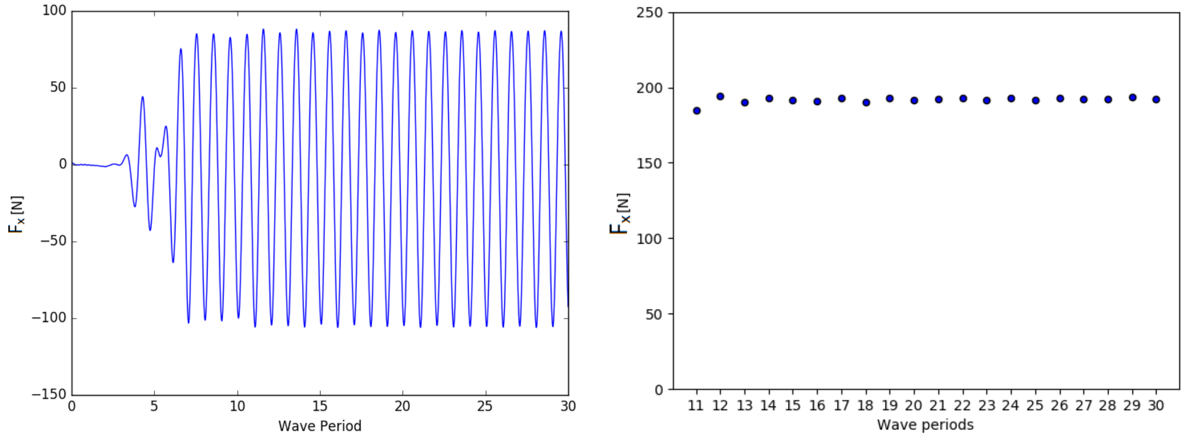

(c) Time trace F_x (d) Scatter F_x

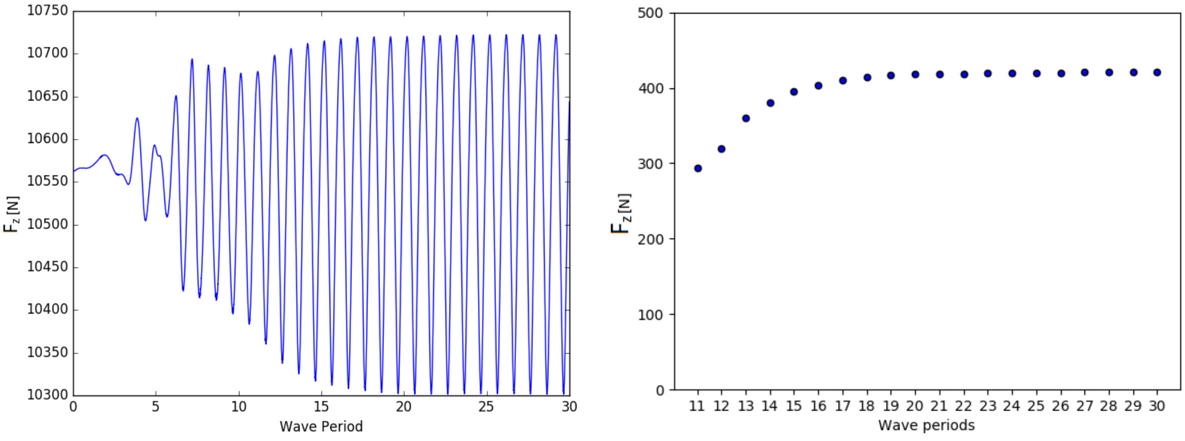

(e) Time trace F_z (f) Scatter F_z

Figure B.51: Case J2

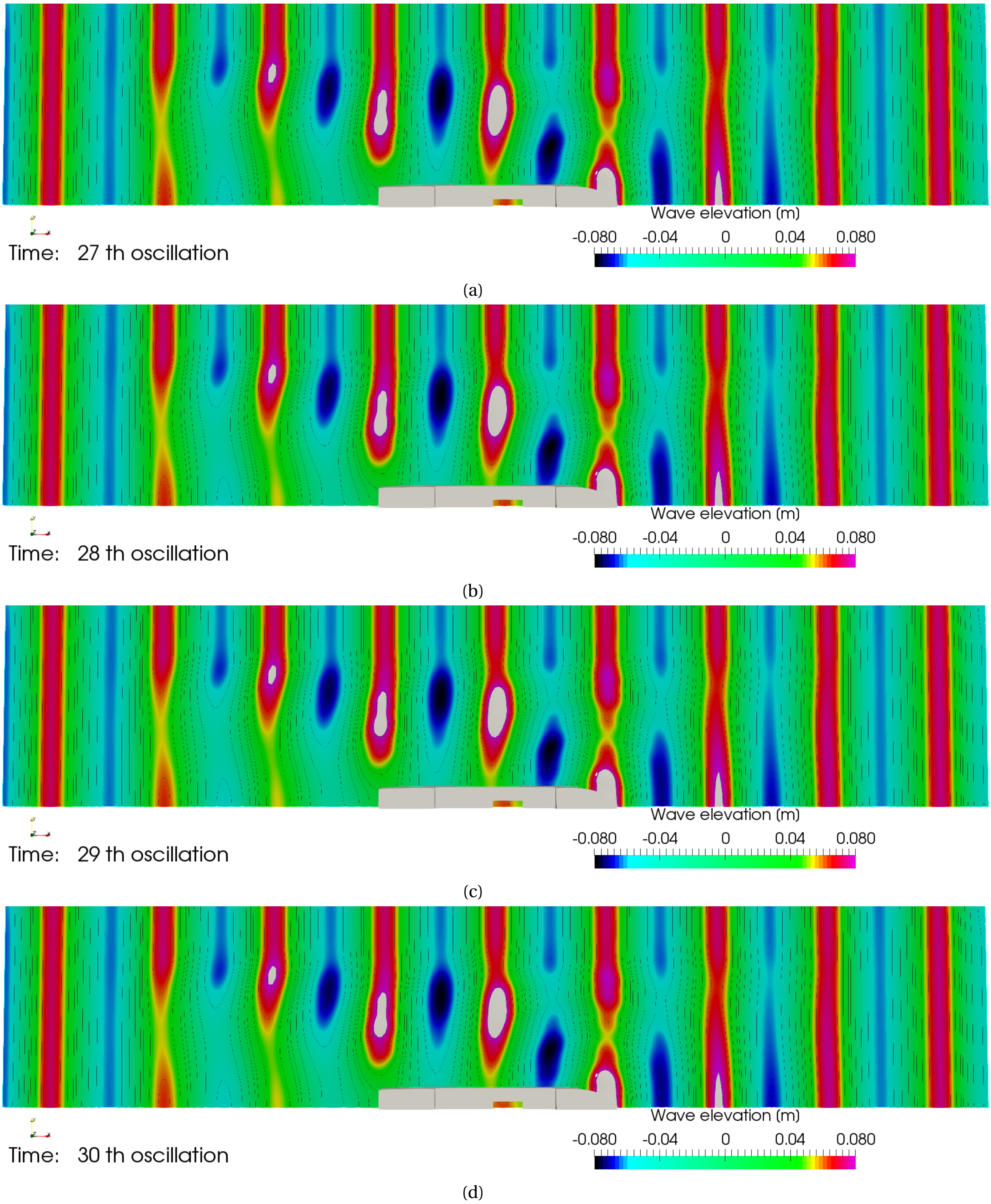

(a)

(b)

(c)

(d)

Figure B.52: Wave elevation case J2

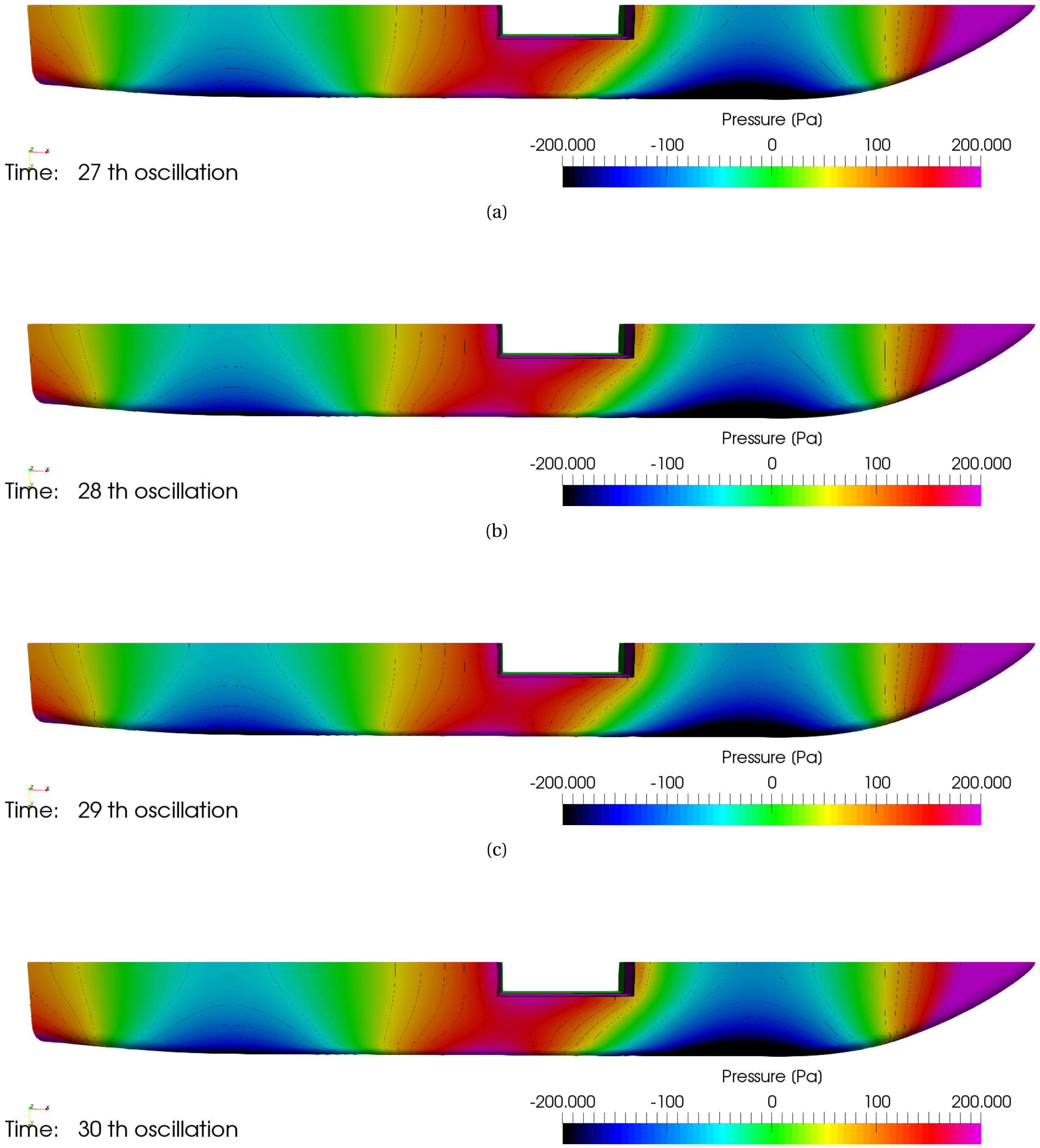

(a)

(b)

(c)

(d)

Figure B.53: Pressure distribution along the bottom for case J2

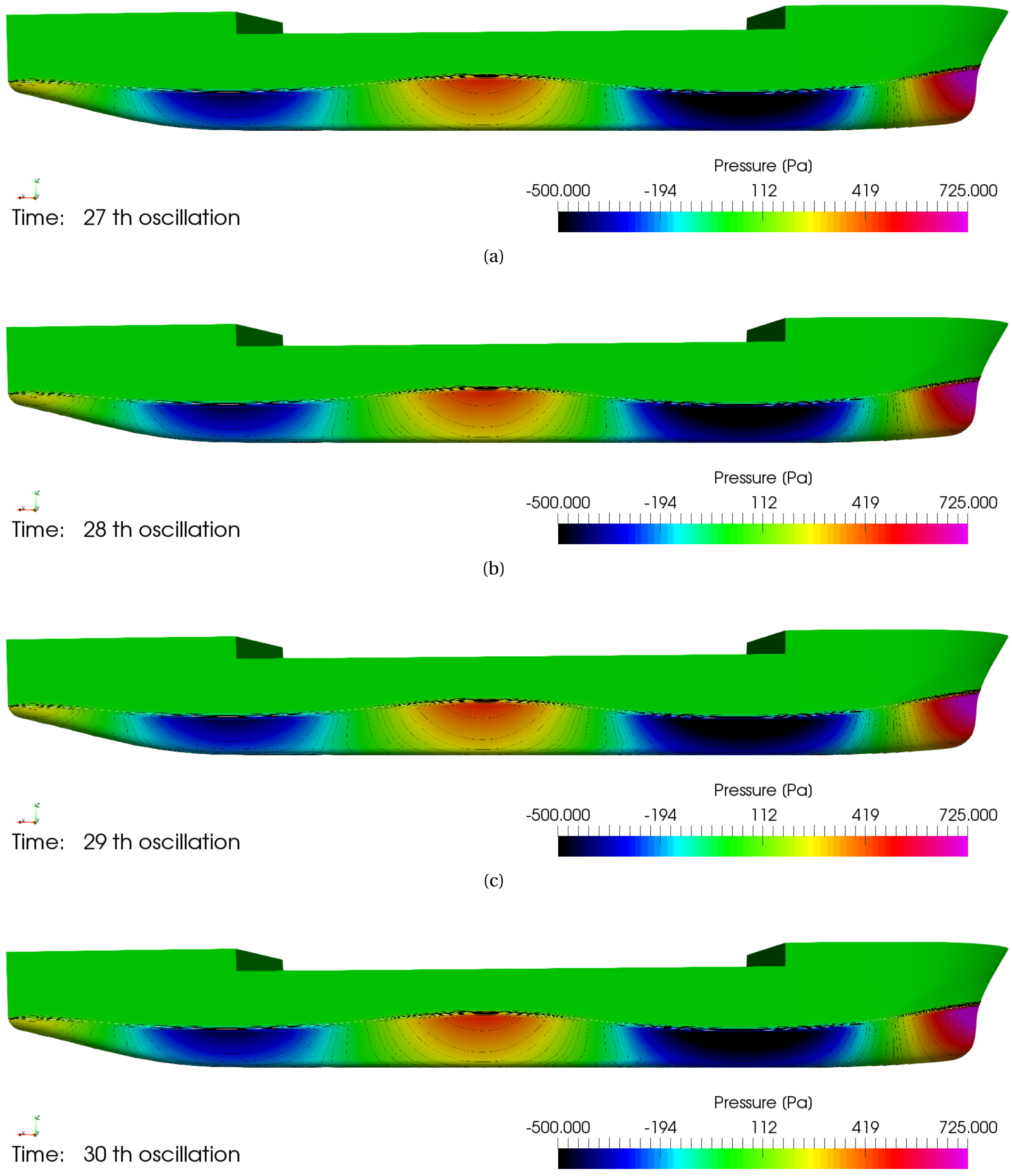

(a)

(b)

(c)

(d)

Figure B.54: Pressure distribution along the side for case J2

B.12. Case K

- Grid: Medium (4.4M cells)
- Timestep: T/200
- Convergence level : $3 * 10^{-5}$
- Domain length: 3.5 λ in front and aft the vessel
- Domain width : 2.0 λ
- Boundary conditions:
  1. Inlet: BC Wall
  2. Side: BC Wall
  3. Outlet: BC Wall
- Relaxation zone:
  1. Inner radius along x direction: 1.5 λ
  2. Relaxation factor at Inlet & Outlet: 0.05
  3. Relaxation length: 2.0 λ
  4. Inner radius along y direction: 1.0 λ
  5. Relaxation factor at Side: 0.10
  6. Relaxation length: 1.0 λ
- Turbulence model: SKL

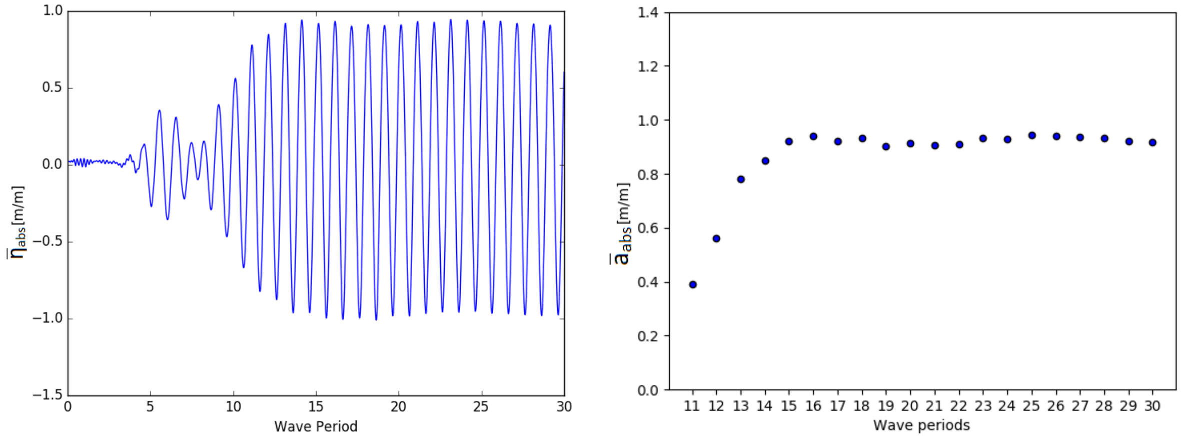

(a) Time trace wave elevation (b) Wave amplitude

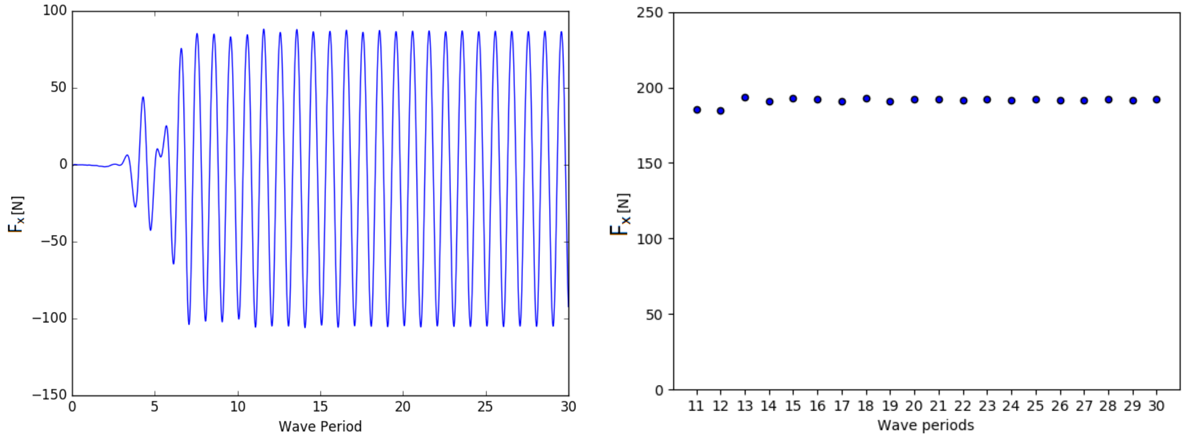

(c) Time trace F_x (d) Scatter F_x

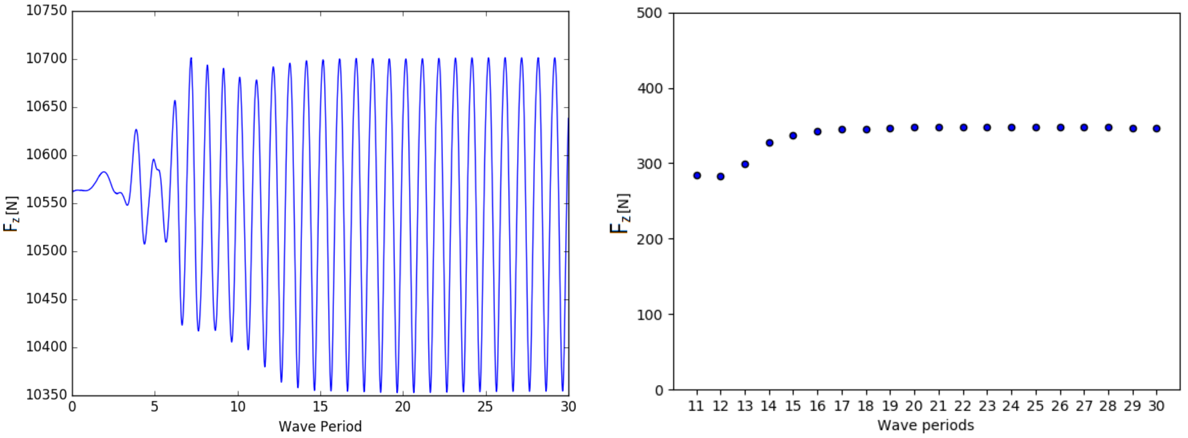

(e) Time trace F_z (f) Scatter F_z

Figure B.55: Case K

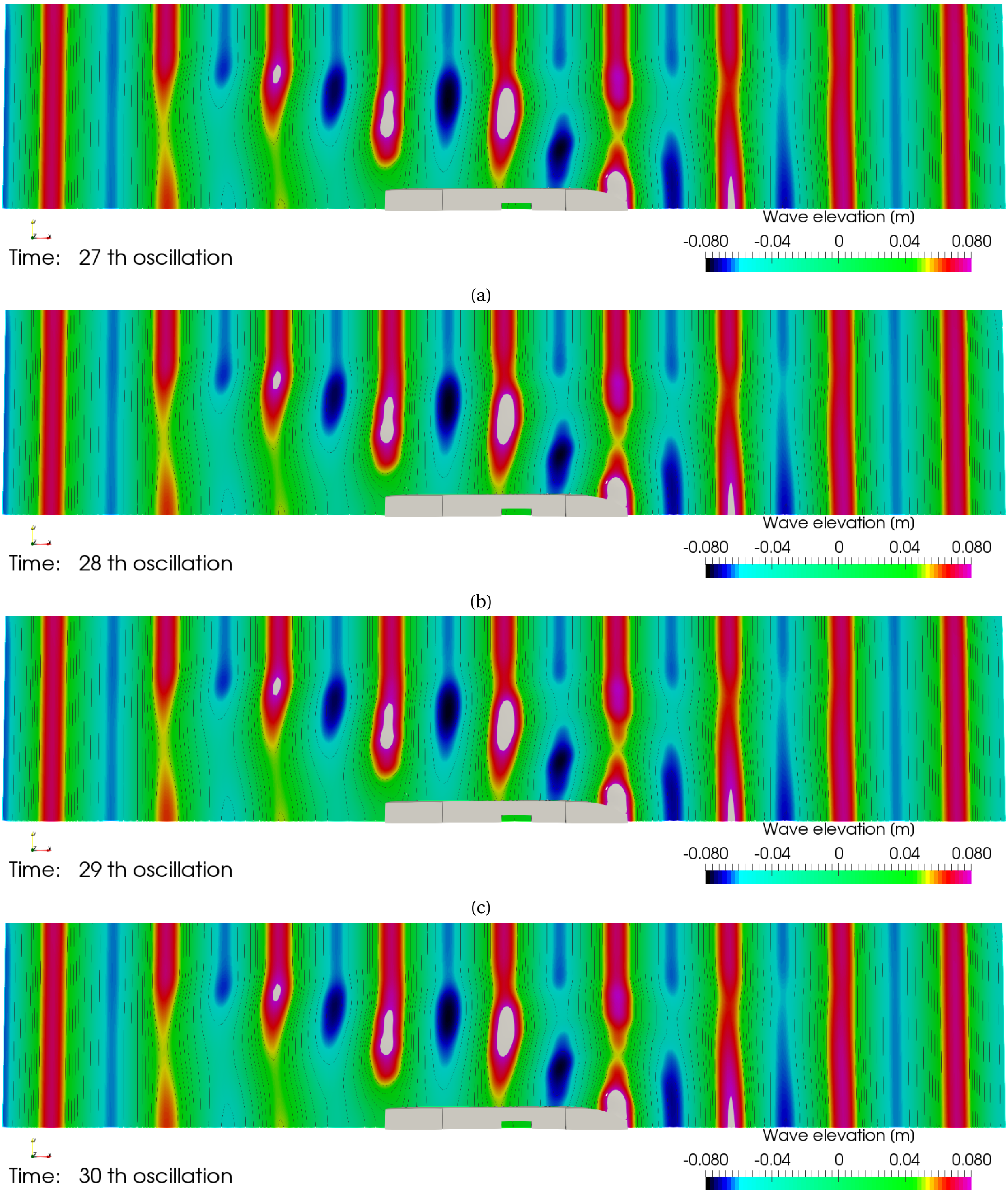

(a)

(b)

(c)

(d)

Figure B.56: Wave elevation case K

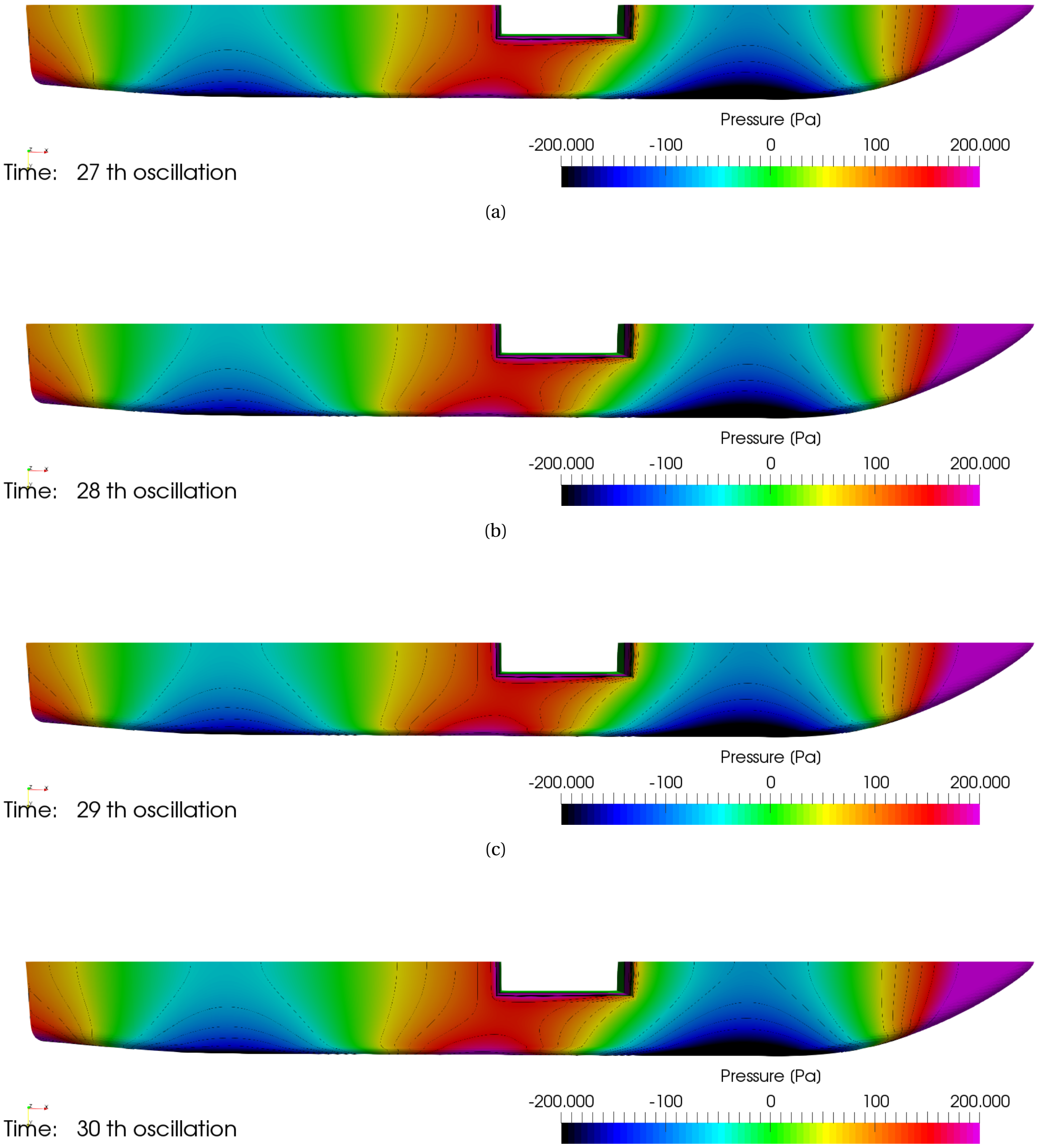

(a)

(b)

(c)

(d)

Figure B.57: Pressure distribution along the bottom for case K

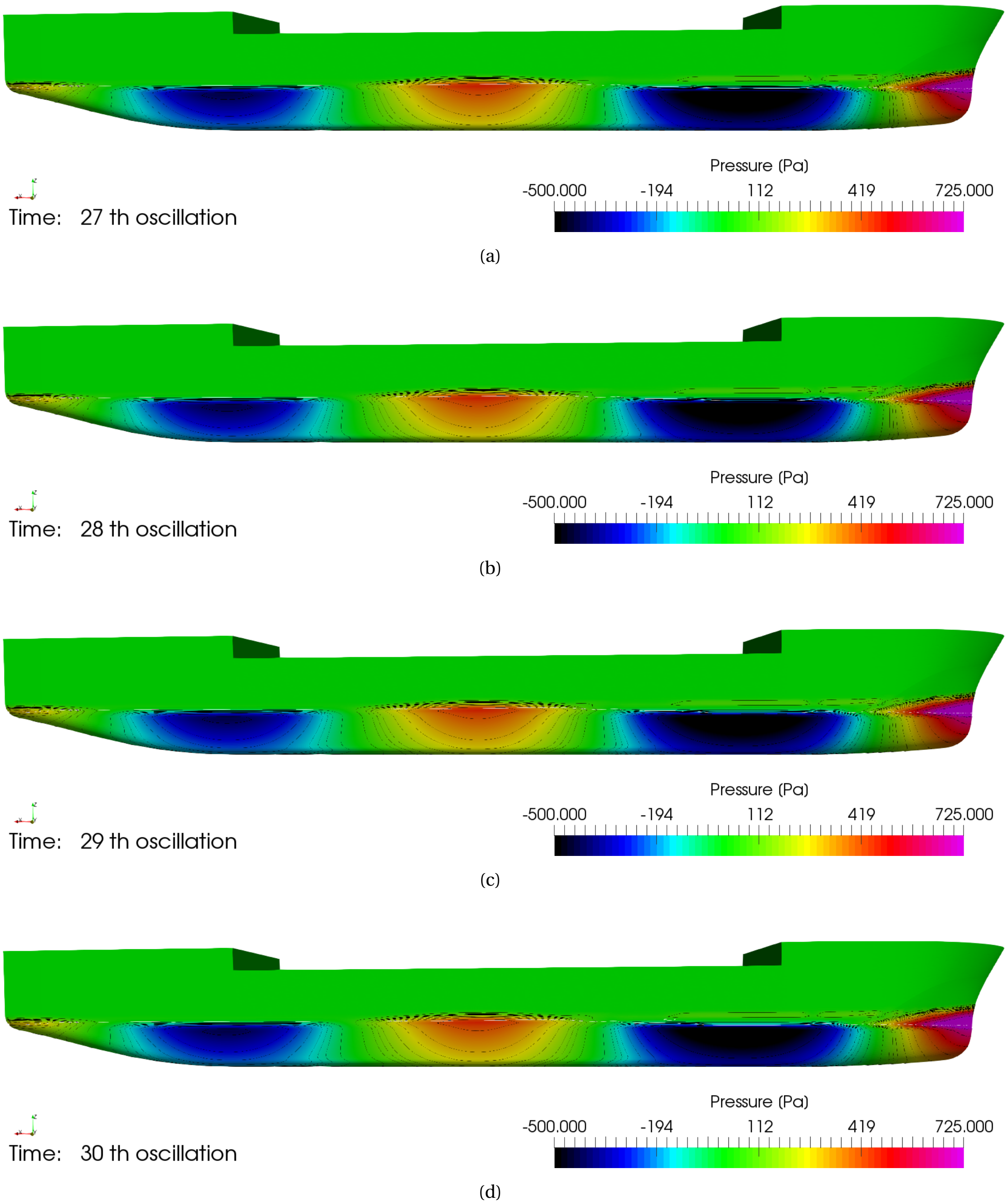

Figure B.58: Pressure distribution along the side for case K

B.13. Case L

- Grid: Medium (4.4M cells)
- Timestep: T/200
- Convergence level : $3 * 10^{-5}$
- Domain length: 3.5 λ in front and aft the vessel
- Domain width : 2.0 λ
- Boundary conditions:
    1. Inlet: BC Wall
    2. Side: BC Wall
    3. Outlet: BC Wall
- Relaxation zone:
    1. Inner radius along x direction: 1.5 λ
    2. Relaxation factor at Inlet & Outlet: 0.05
    3. Relaxation length: 2.0 λ
    4. Inner radius along y direction: 1.0 λ
    5. Relaxation factor at Side: 0.10
    6. Relaxation length: 1.0 λ
- Turbulence model: MENTER

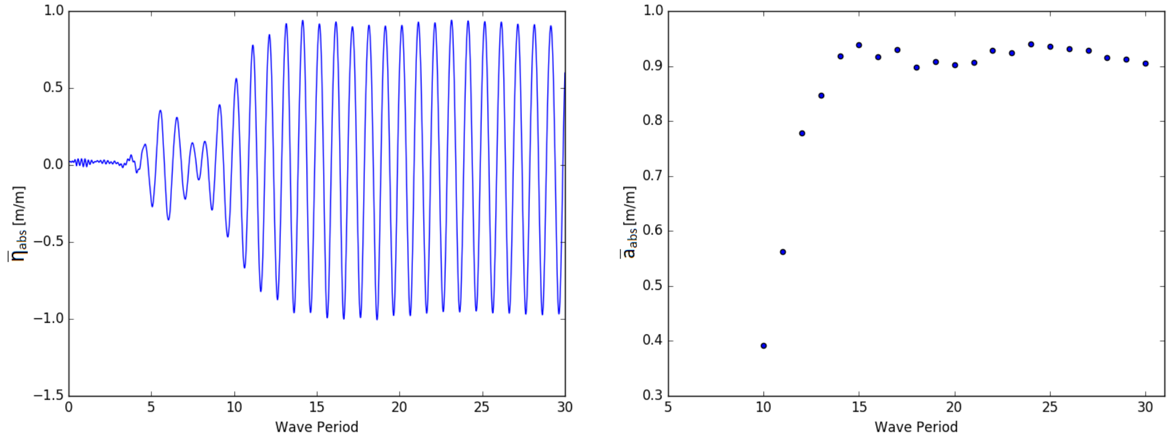

(a) Time trace wave elevation (b) Wave amplitude

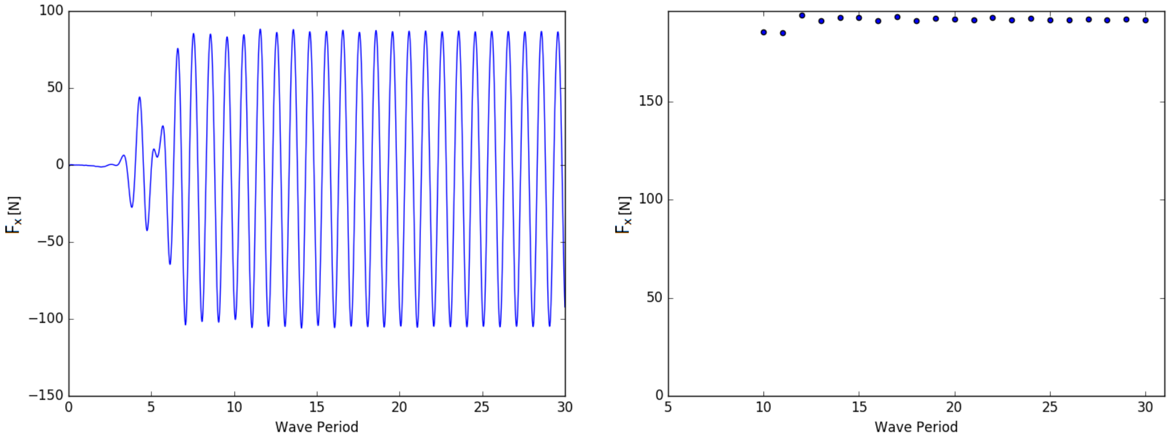

(c) Time trace F_x (d) Scatter F_x

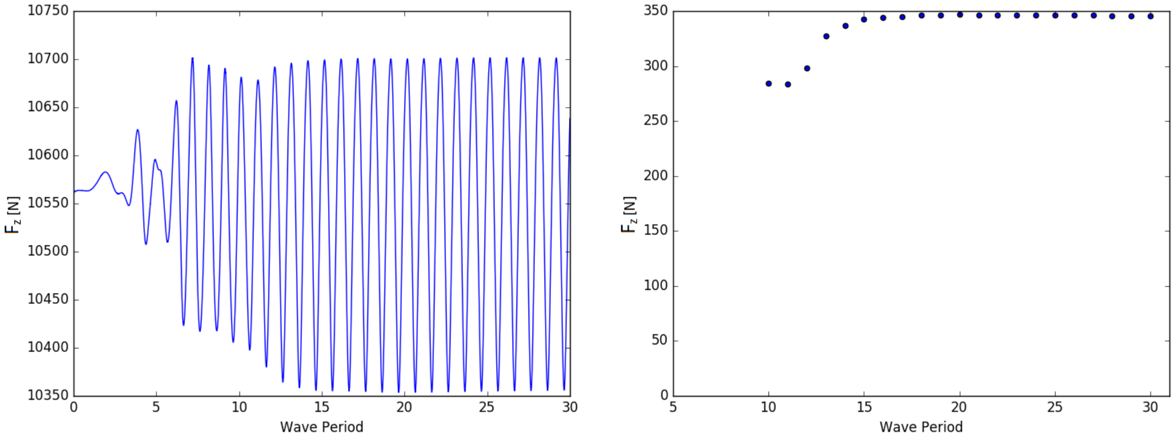

(e) Time trace F_z (f) Scatter F_z

Figure B.59: Case L

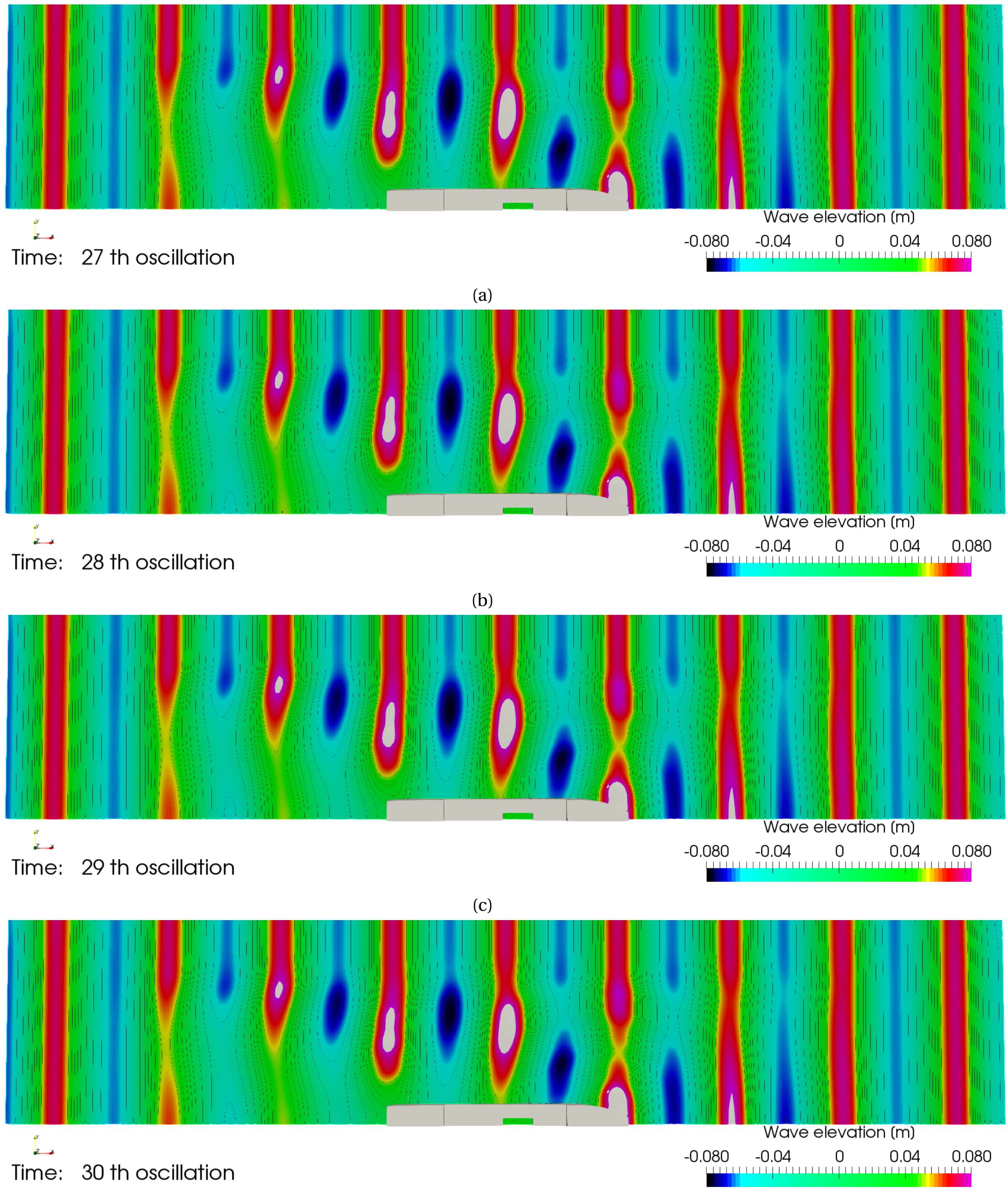

(a)

(b)

(c)

(d)

Figure B.60: Wave elevation case L

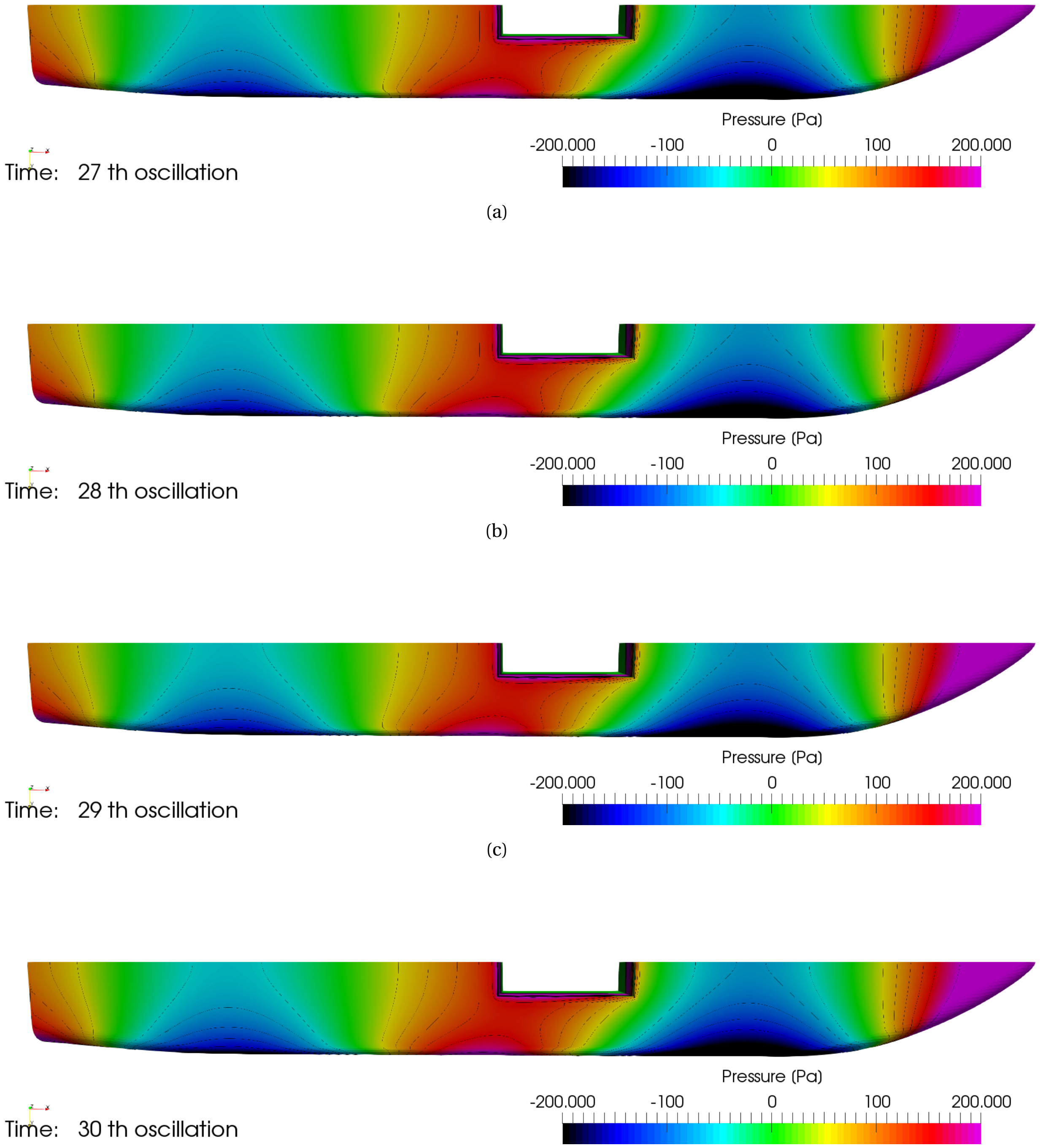

(a)

(b)

(c)

(d)

Figure B.61: Pressure distribution along the bottom for case L

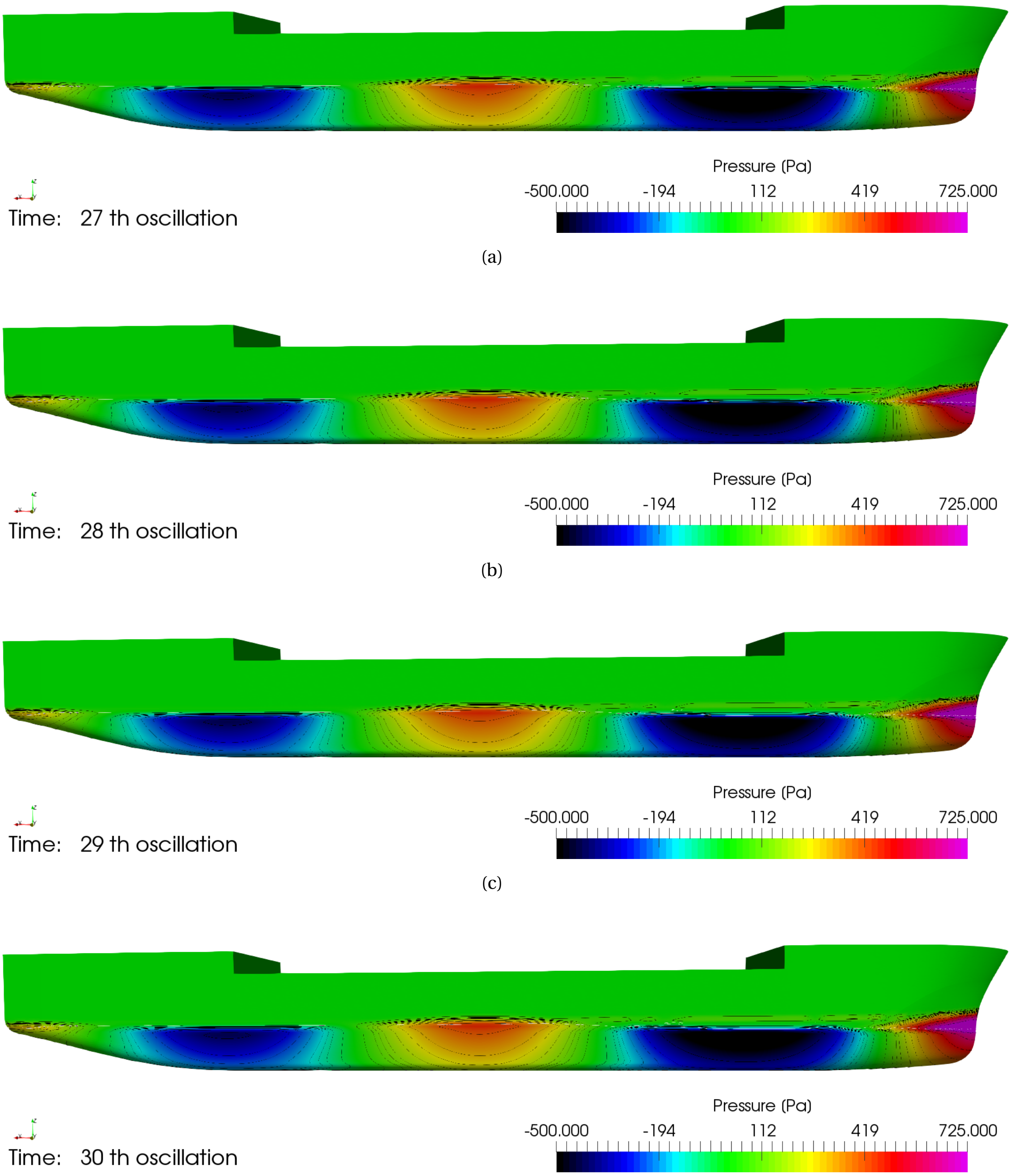

(a)

(b)

(c)

(d)

Figure B.62: Pressure distribution along the side for case L

B.14. Case M

- Grid: Medium (4.4M cells)
- Timestep: T/200
- Convergence level : $3 * 10^{-5}$
- Domain length: 3.5 λ in front and aft the vessel
- Domain width : 2.0 λ
- Boundary conditions:
    1. Inlet: BC Wall
    2. Side: BC Wall
    3. Outlet: BC Wall
- Relaxation zone:
    1. Inner radius along x direction: 1.5 λ
    2. Relaxation factor at Inlet & Outlet: 0.05
    3. Relaxation length: 2.0 λ
    4. Inner radius along y direction: 1.0 λ
    5. Relaxation factor at Side: 0.10
    6. Relaxation length: 1.0 λ
- Turbulence model: $k-\omega$

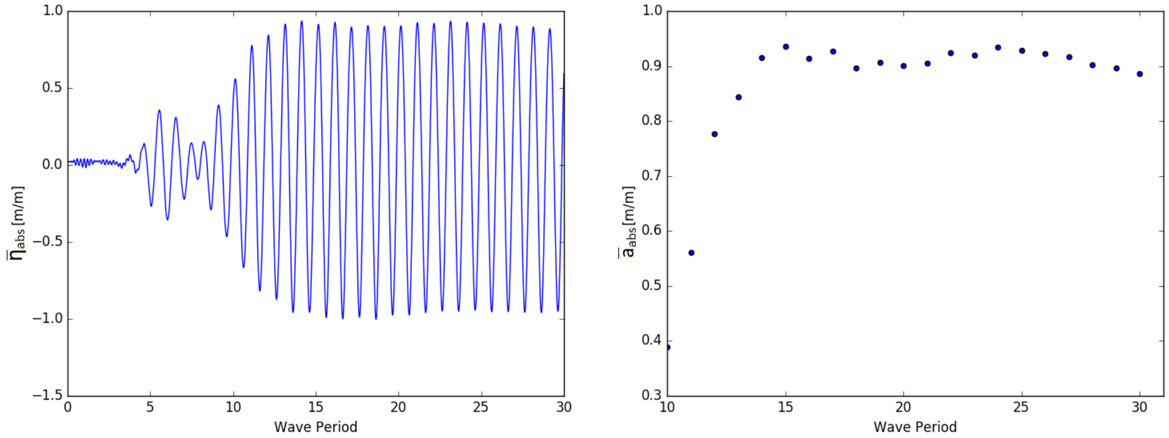

(a) Time trace wave elevation (b) Wave amplitude

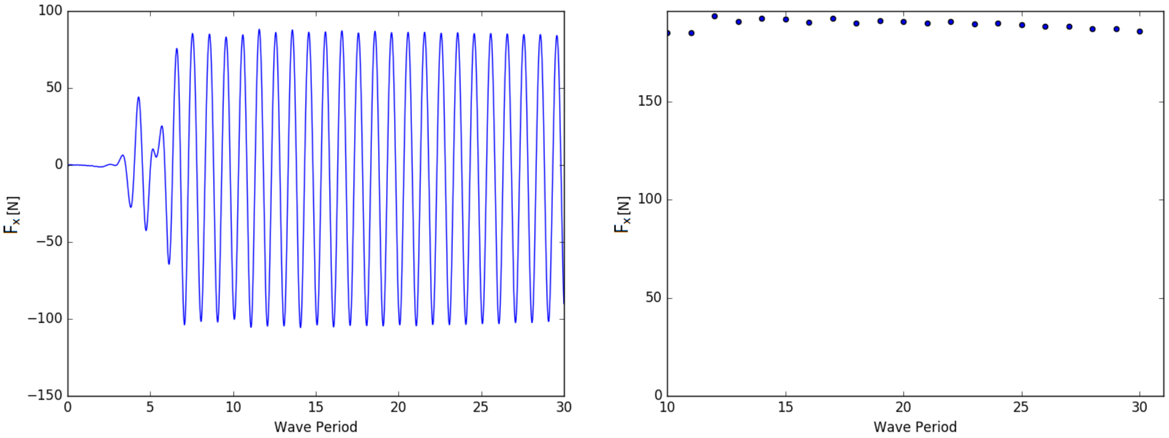

(c) Time trace F_x (d) Scatter F_x

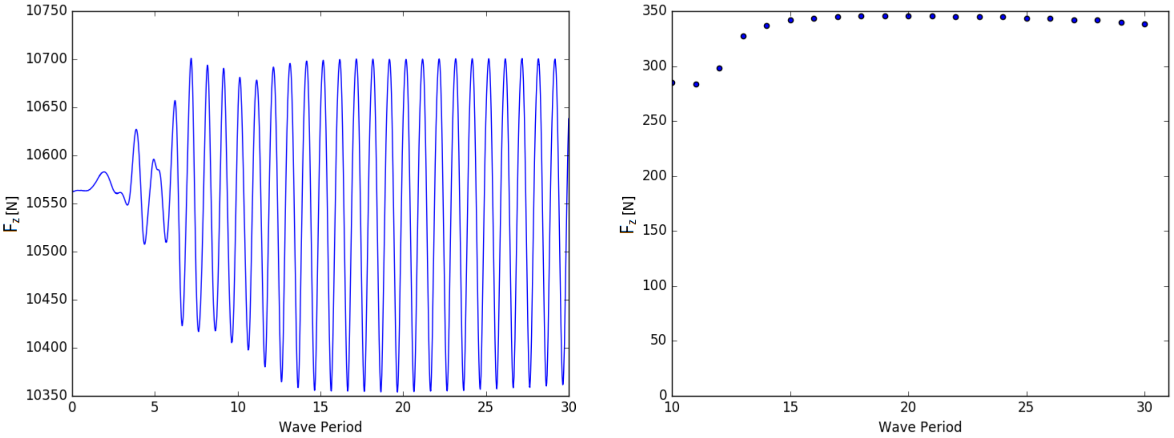

(e) Time trace F_z (f) Scatter F_z

Figure B.63: Case M

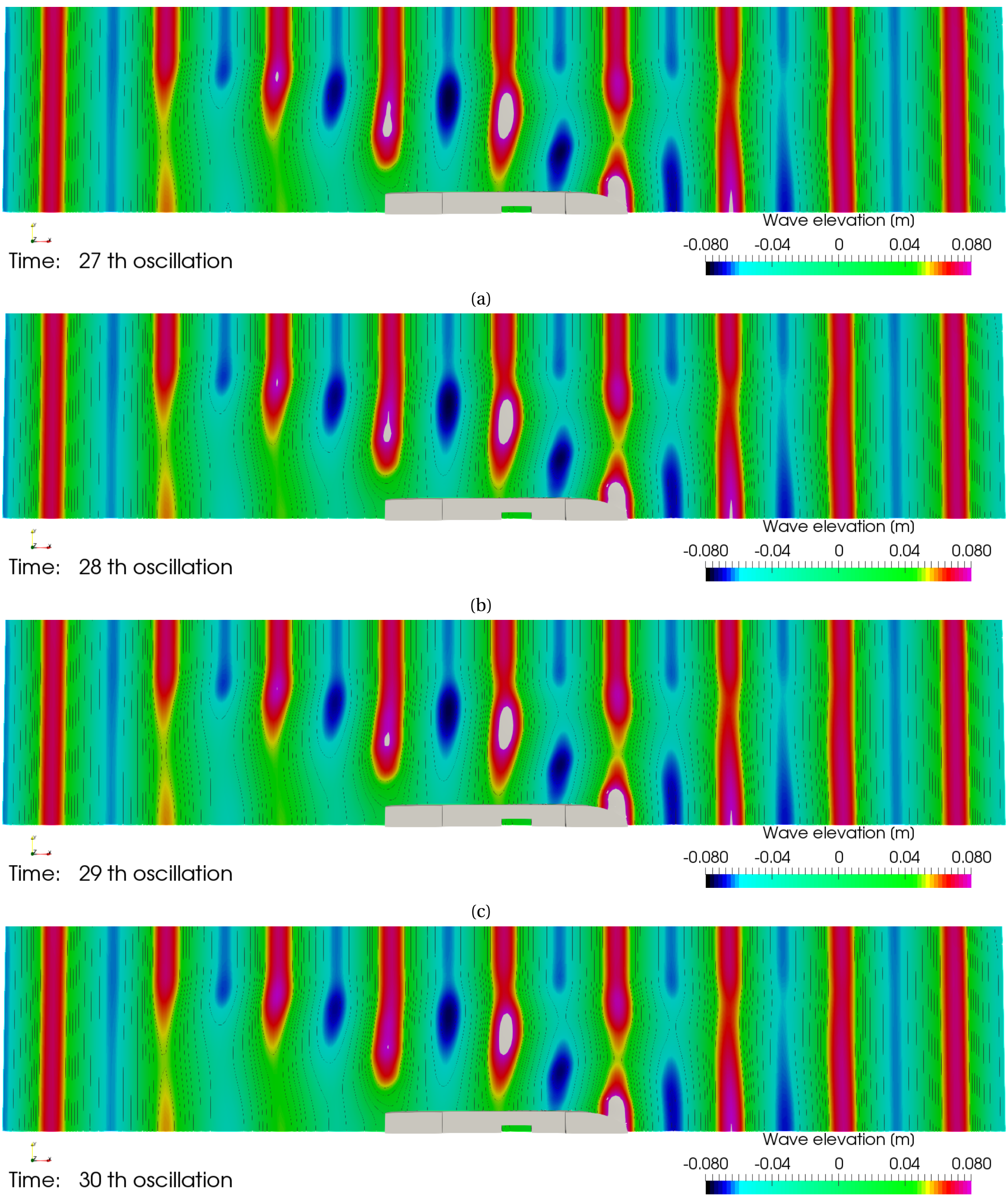

(a)

(b)

(c)

(d)

Figure B.64: Wave elevation case M

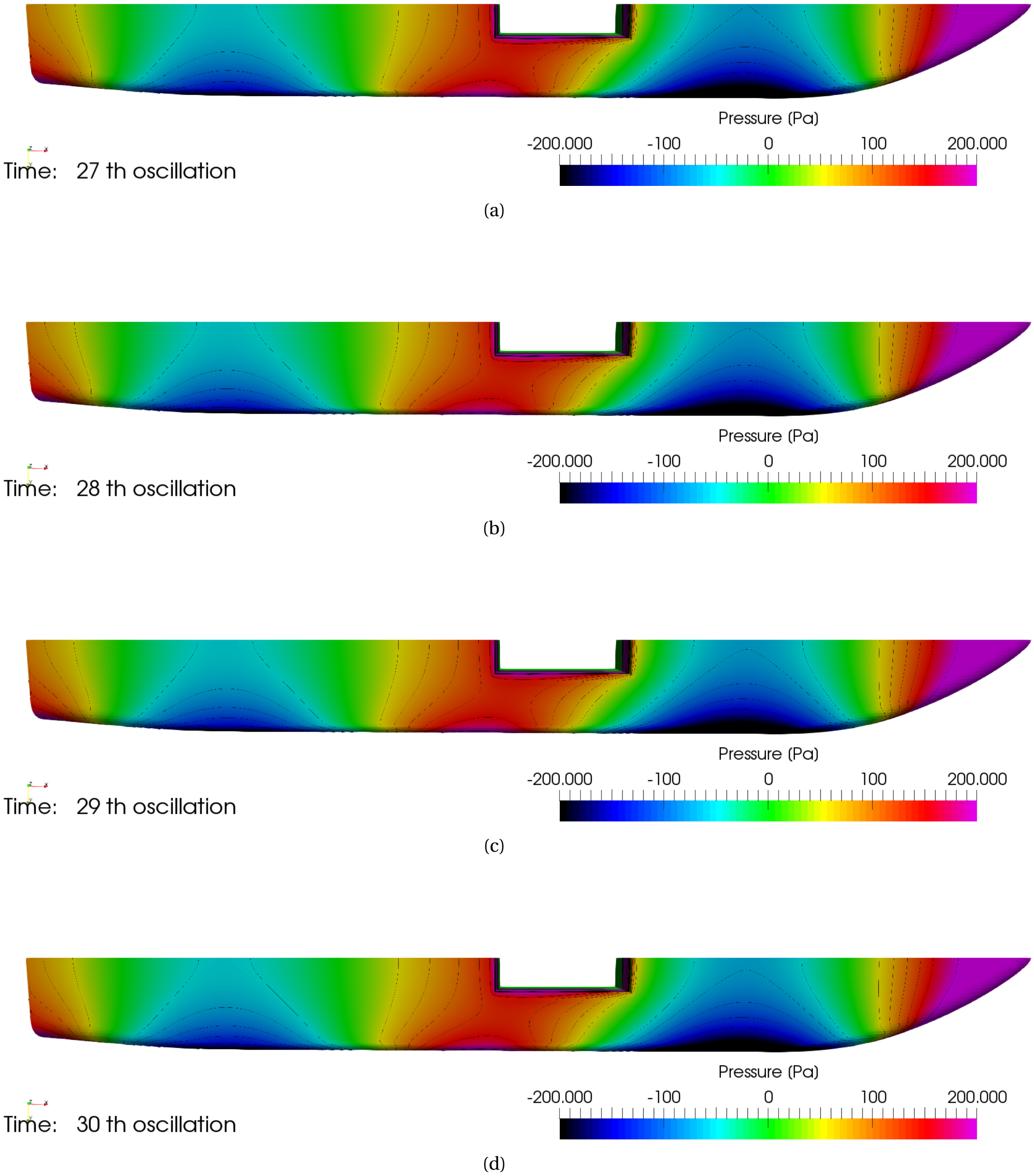

Figure B.65: Pressure distribution along the bottom for case M

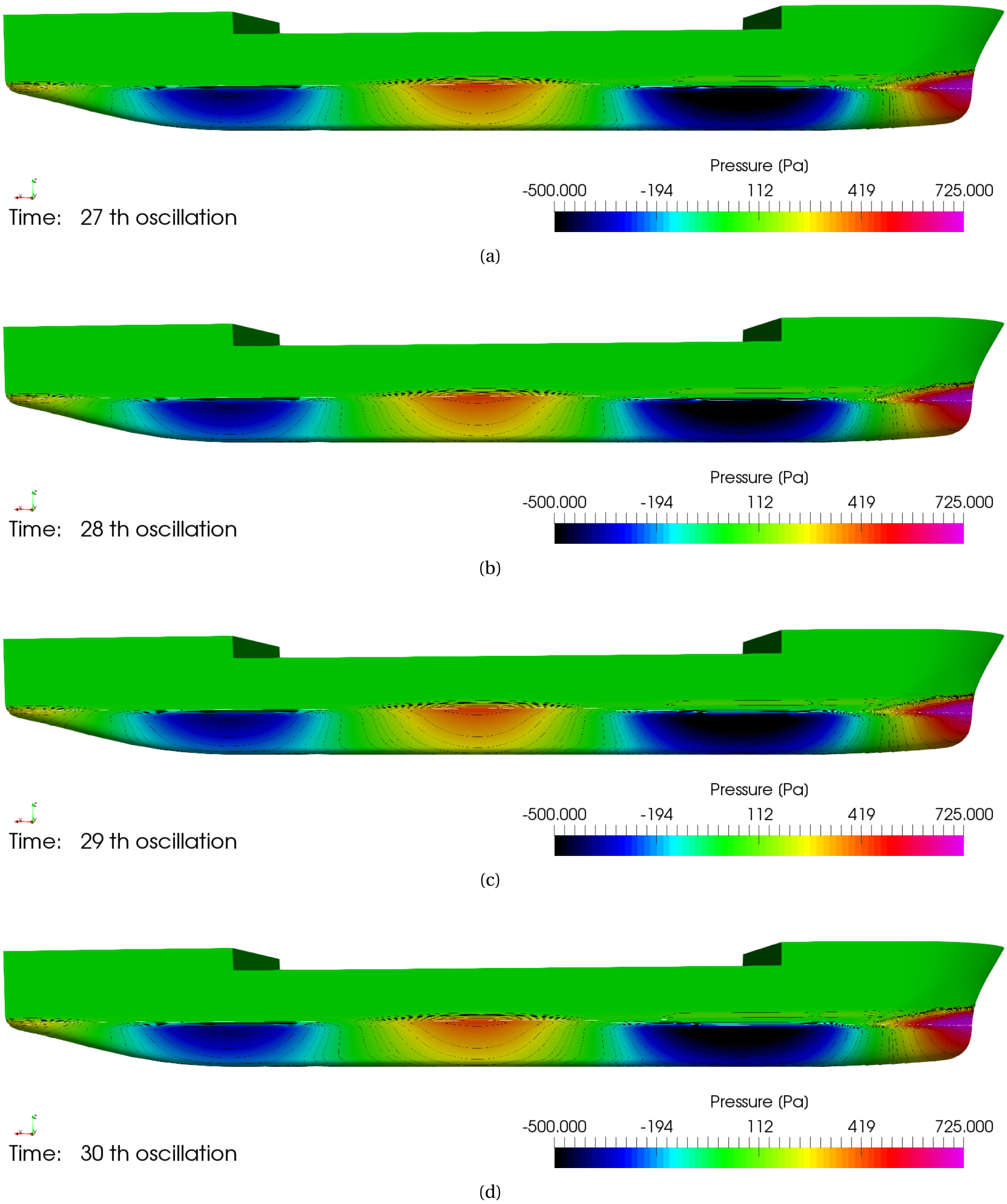

Figure B.66: Pressure distribution along the side for case M

C

Appendix Forced heave oscillation

C.1. Case A

- Grid: medium (6.1M cells)
- Timestep: T/400
- Convergence level : 10^{-4}
- Domain length: 2.5 λ in front and aft the vessel
- Domain width : 1.5 λ
- Boundary conditions:
    1. Inlet: BC Wall
    2. Side: BC Wall
    3. Outlet: BC Wall

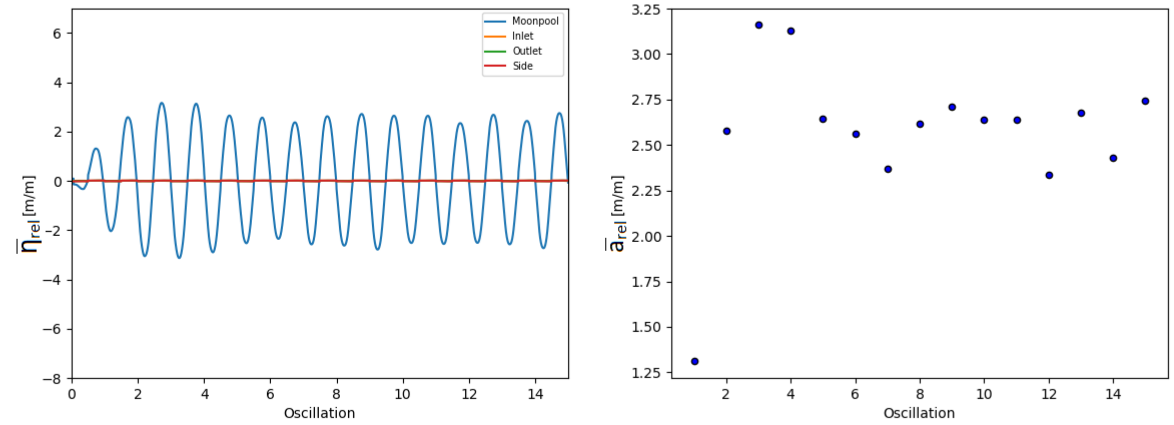

(a) Time trace wave elevation

(b) Wave amplitude

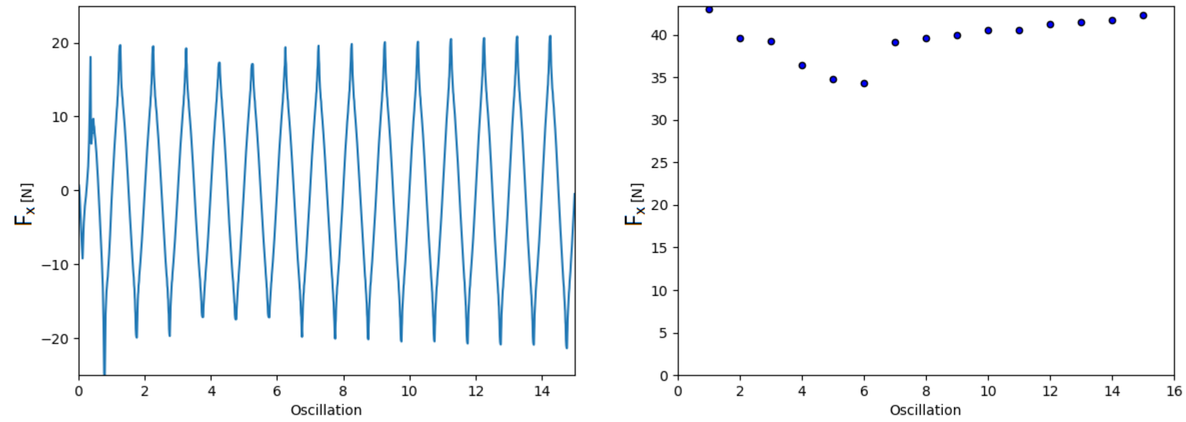

(c) Time trace F_x

(d) Scatter amplitude F_x

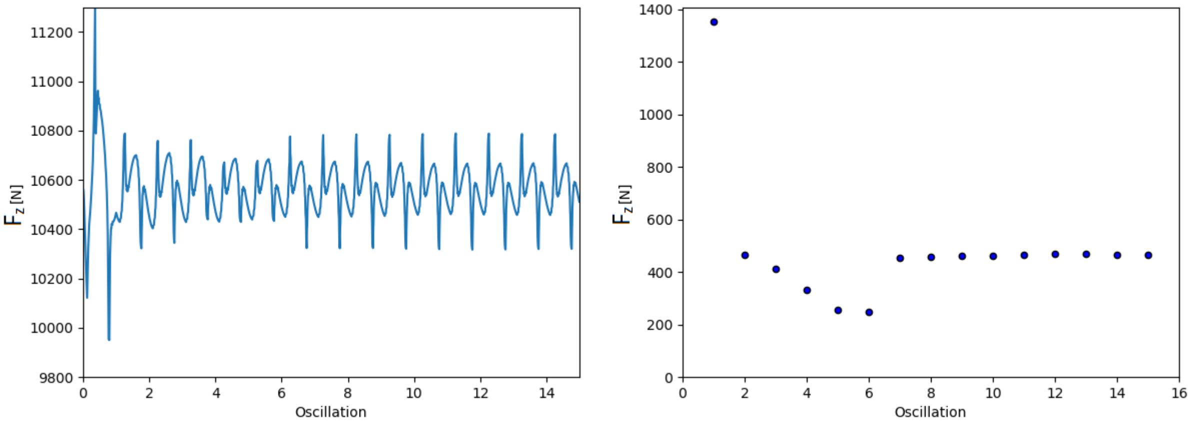

(e) Time trace F_z

(f) Scatter amplitude F_z

Figure C.1: Case A FH

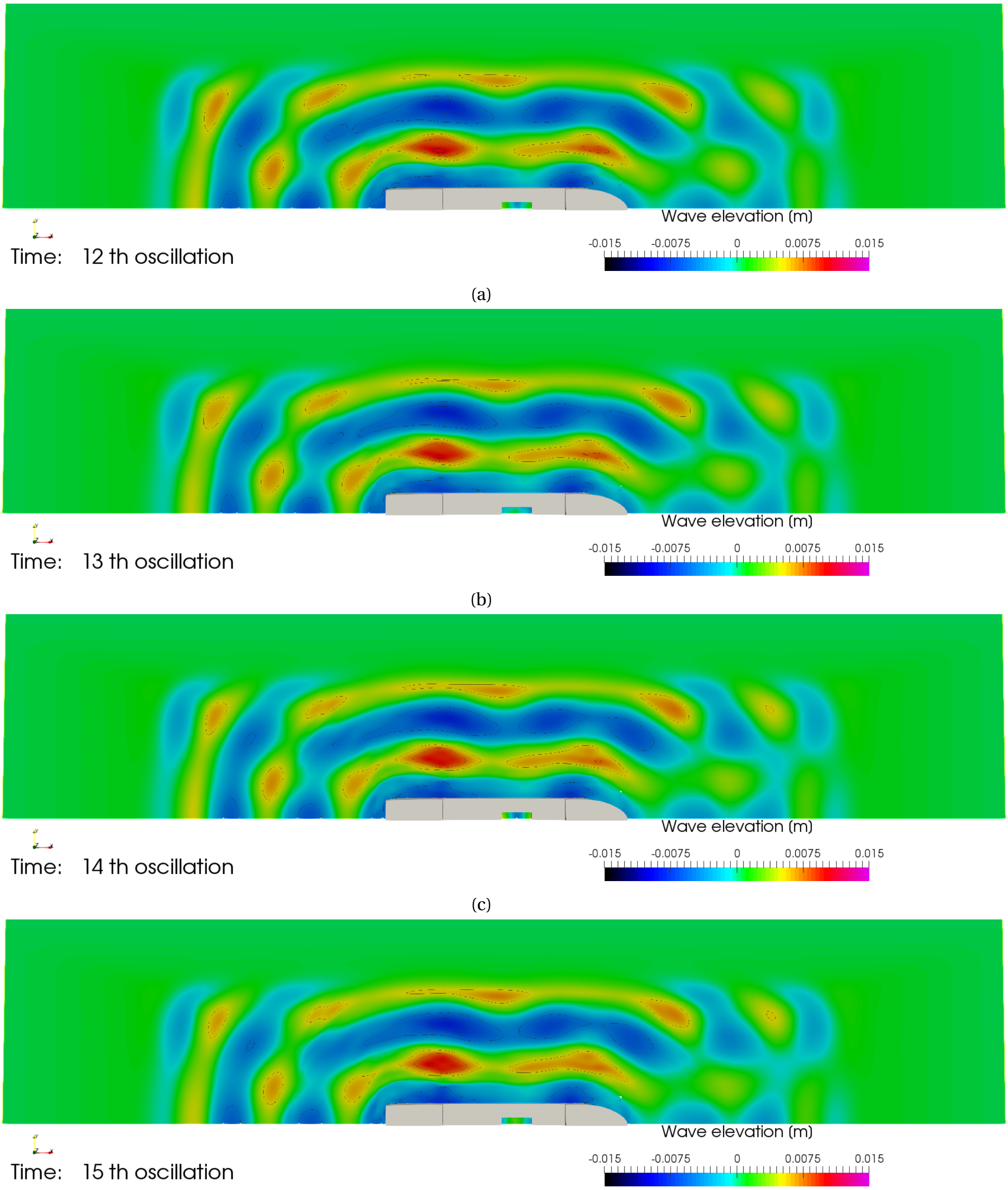

(a)

(b)

(c)

(d)

Figure C.2: Wave elevation case A

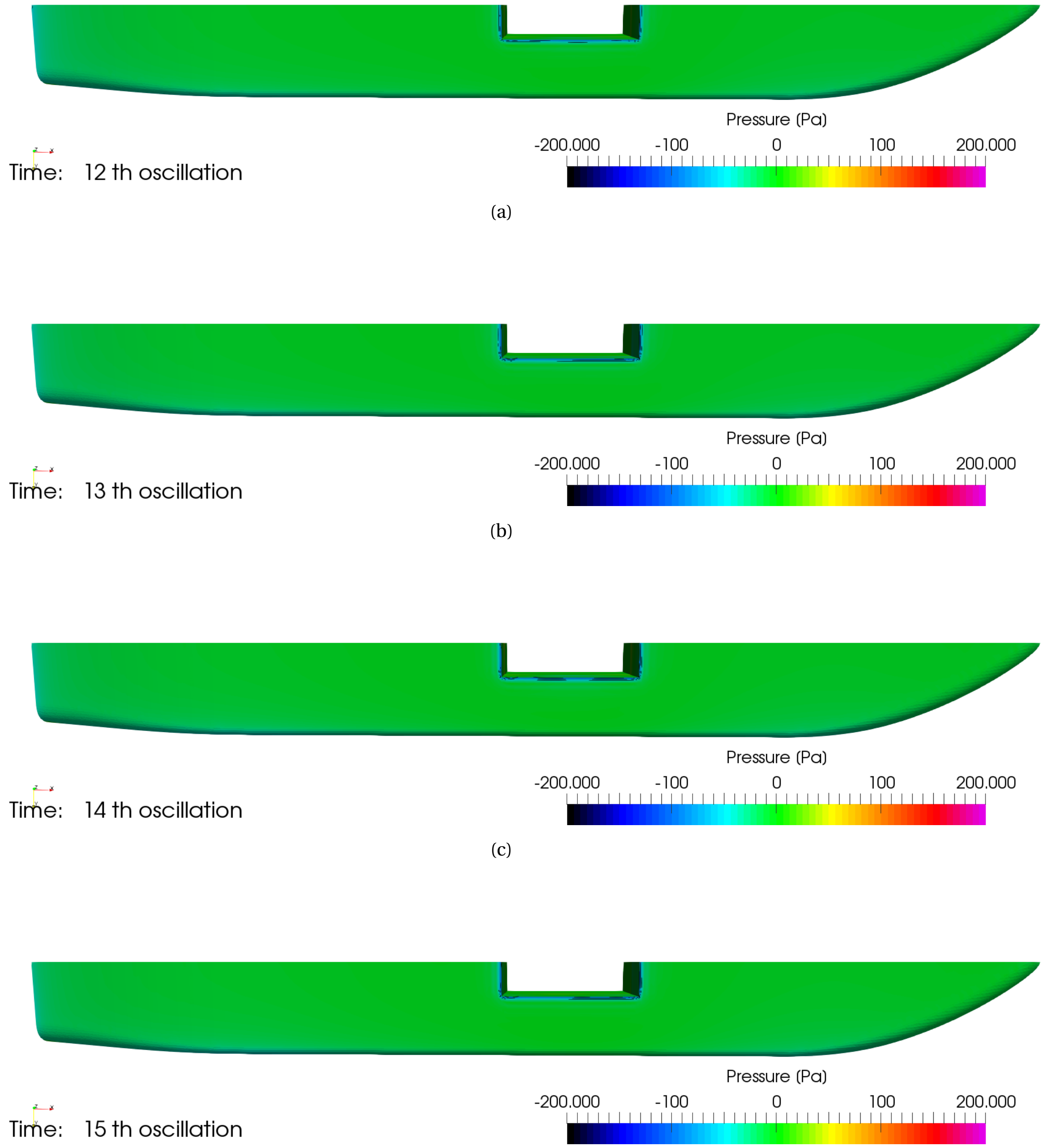

(a)

(b)

(c)

(d)

Figure C.3: Pressure distribution along the bottom for case A

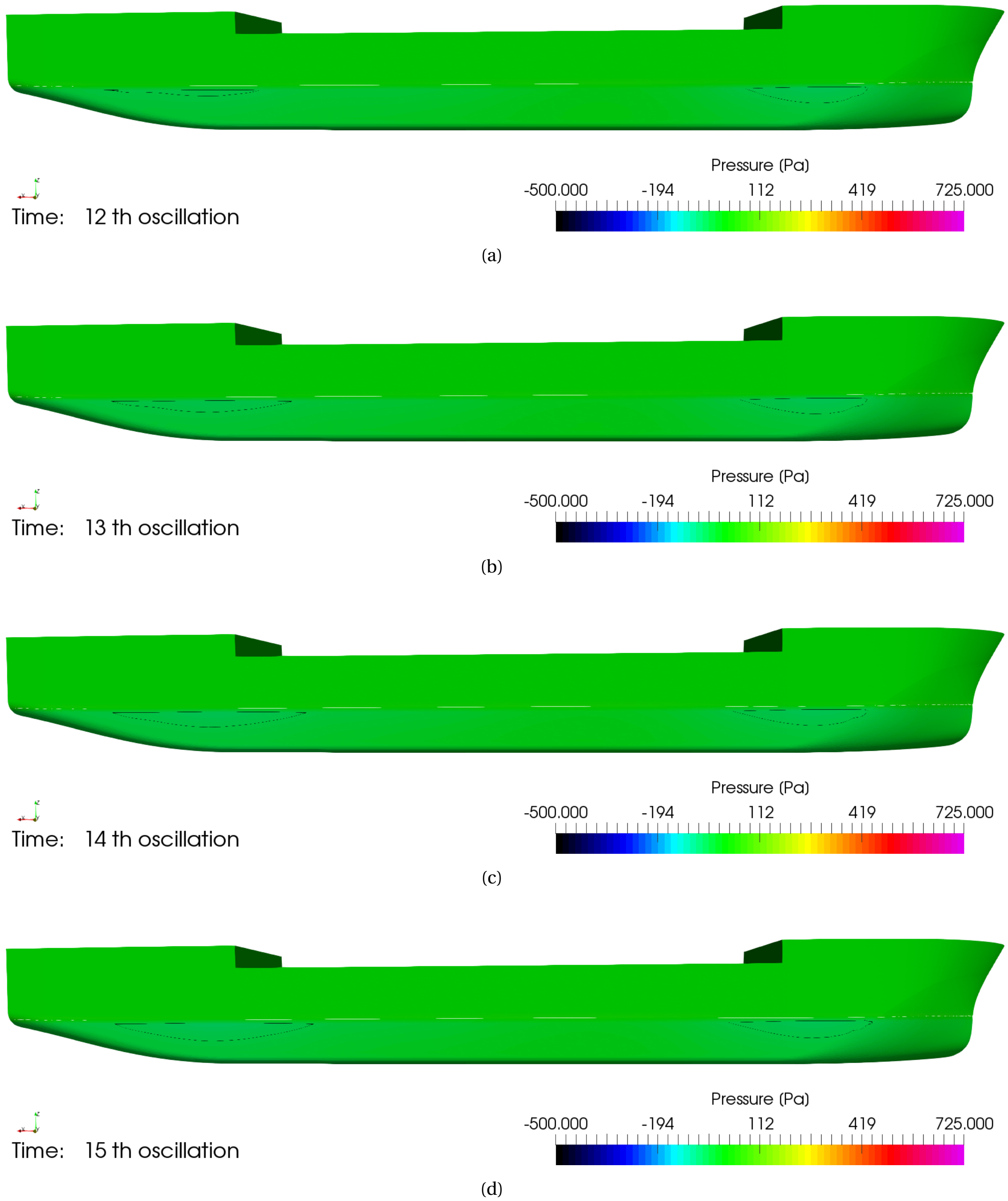

Figure C.4: Pressure distribution along the side for case A

C.2. Case B

- Grid: medium (6.1M cells)
- Timestep: T/400
- Convergence level : 10^{-5}
- Domain length: 2.5 λ in front and aft the vessel
- Domain width : 1.5 λ
- Boundary conditions:
    1. Inlet: BC Wall
    2. Side: BC Wall
    3. Outlet: BC Wall

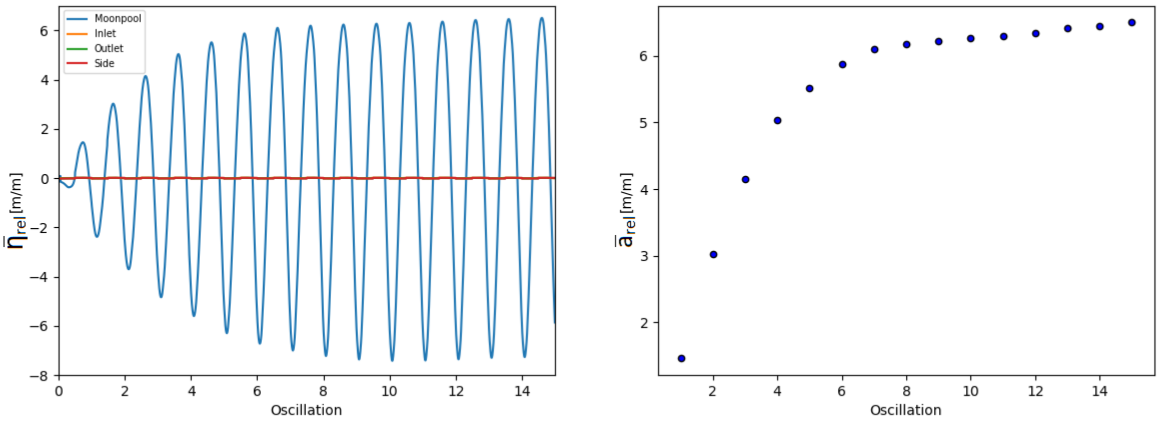

(a) Time trace wave elevation (b) Wave amplitude

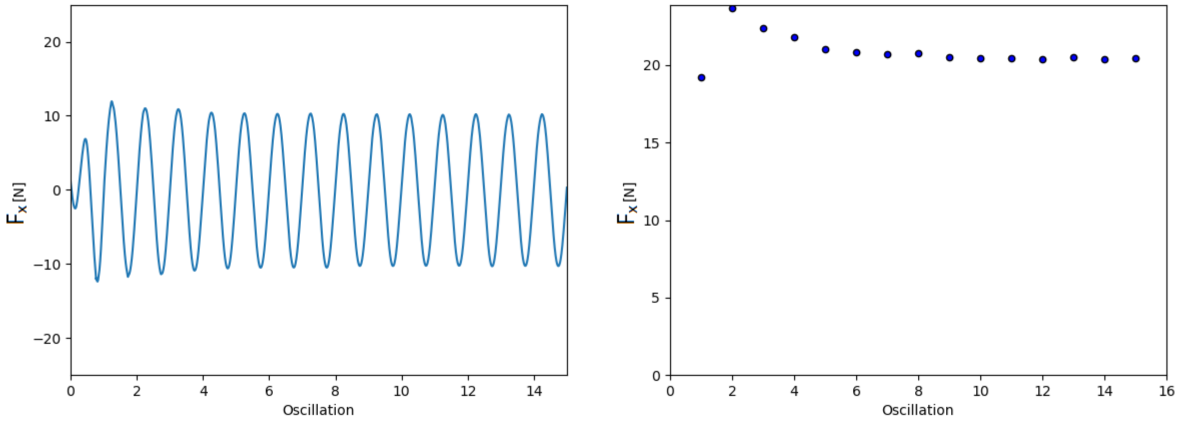

(c) Time trace F_x (d) Scatter amplitude F_x

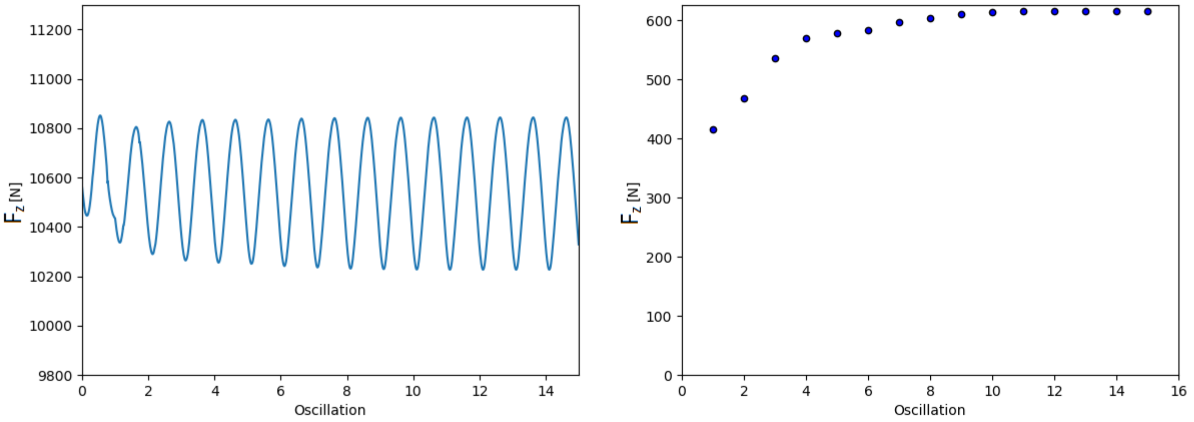

(e) Time trace F_z (f) Scatter amplitude F_z

Figure C.5: Case B FH

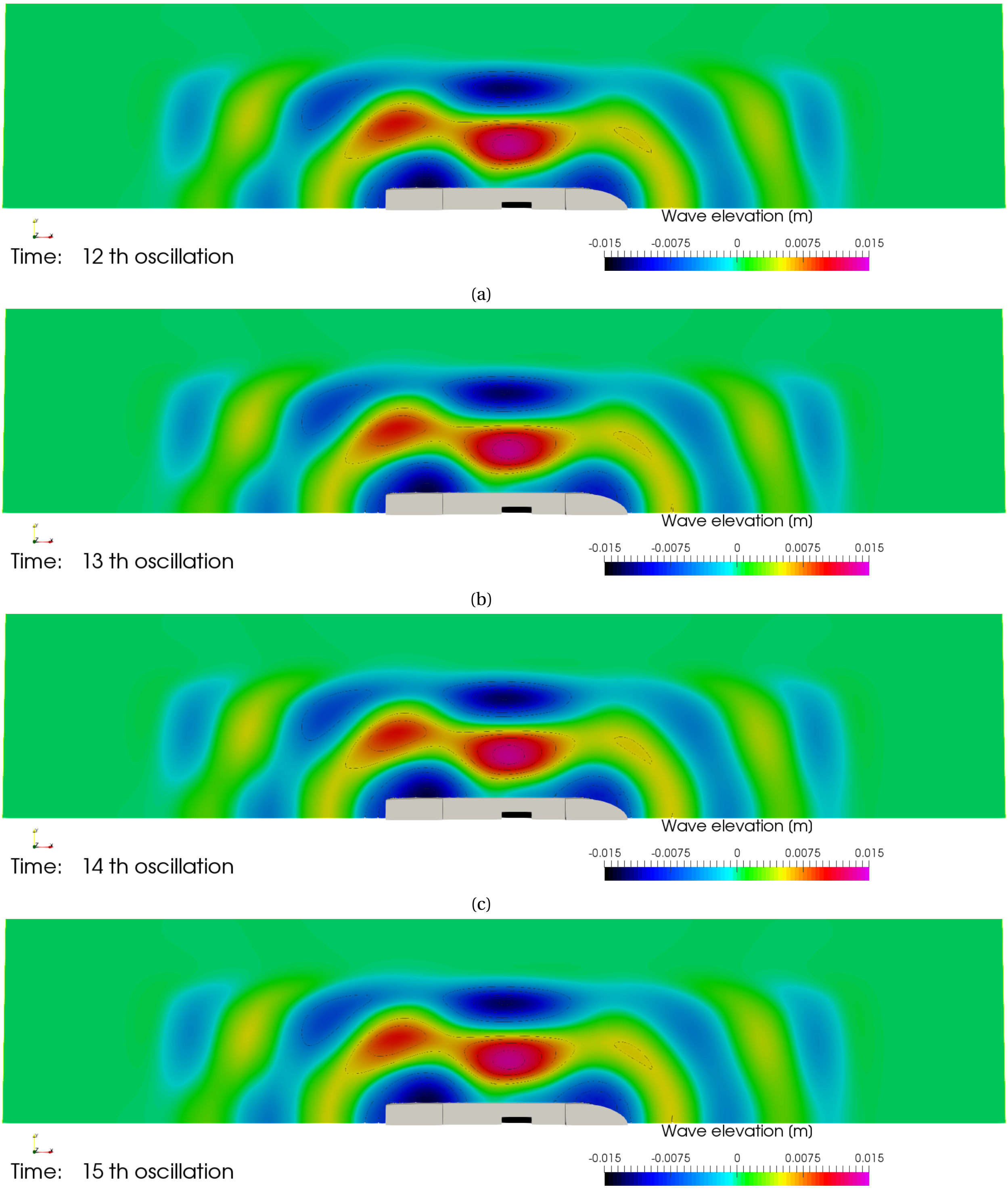

(a)

(b)

(c)

(d)

Figure C.6: Wave elevation case B

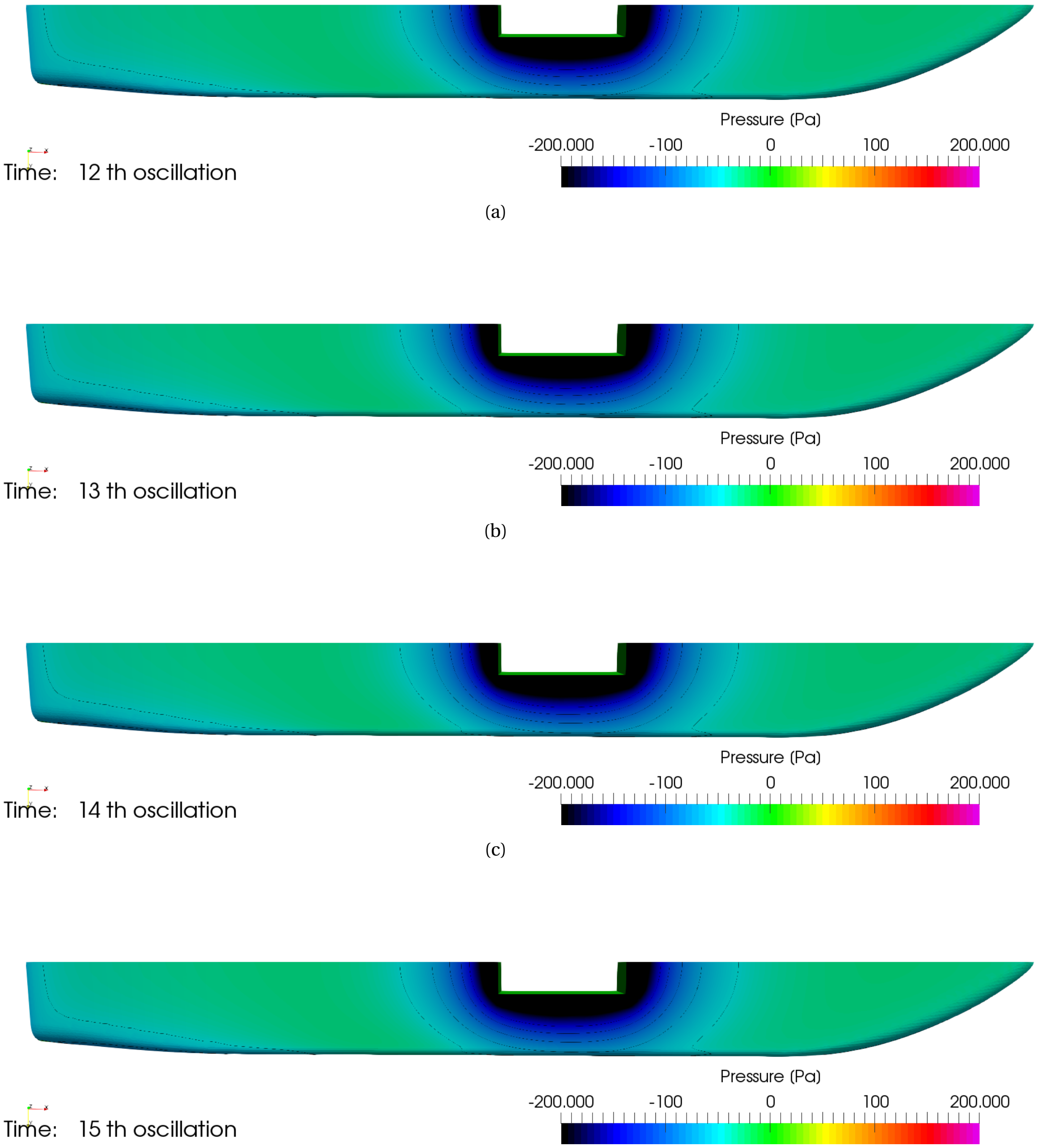

(a)

(b)

(c)

(d)

Figure C.7: Pressure distribution along the bottom for case B

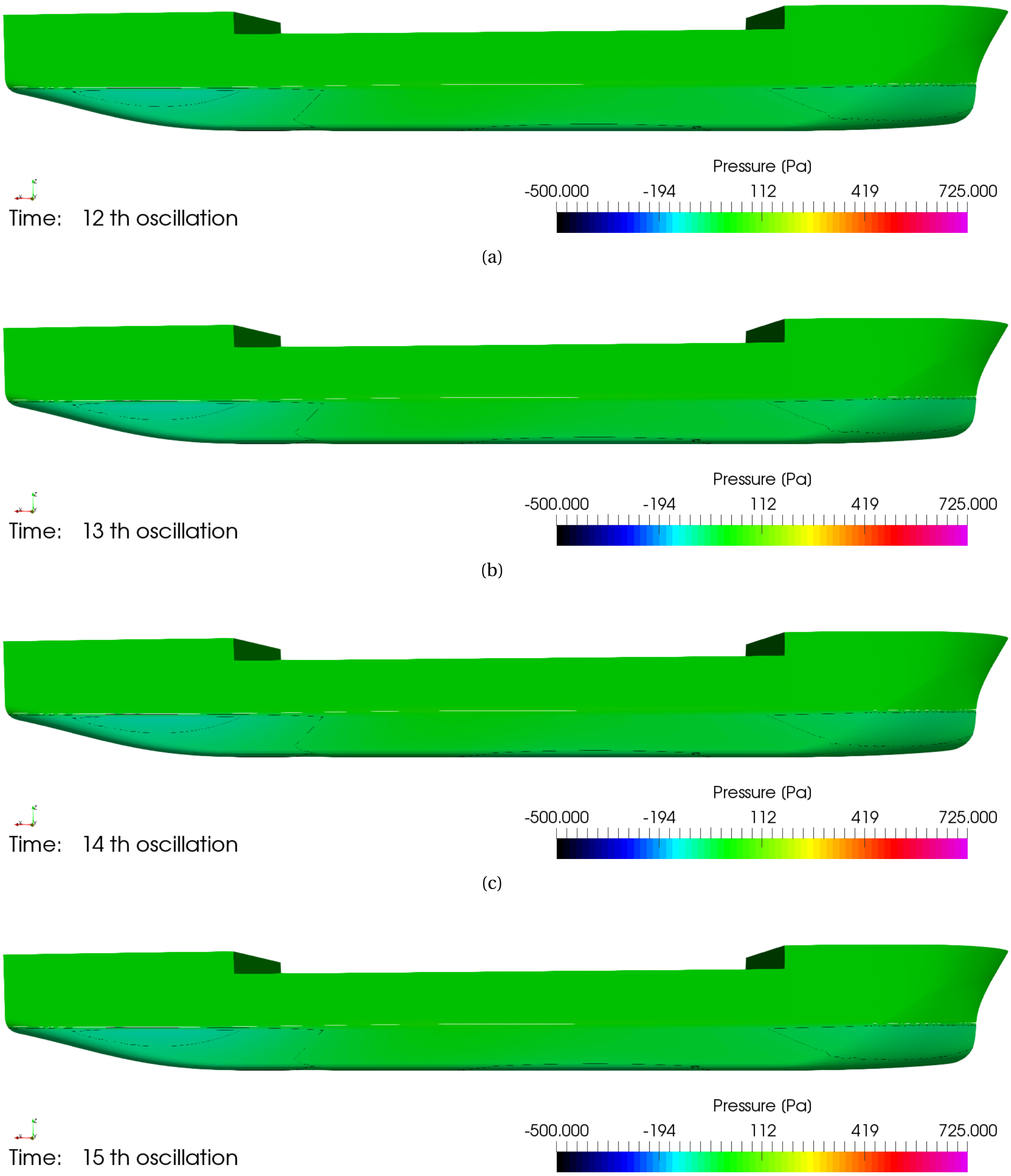

(a)

(b)

(c)

(d)

Figure C.8: Pressure distribution along the side for case B

C.3. Case C

- Grid: medium (6.1M cells)
- Timestep: T/200
- Convergence level : 10^{-5}
- Domain length: 2.5 λ in front and aft the vessel
- Domain width : 1.5 λ
- Boundary conditions:
    1. Inlet: BC Wall
    2. Side: BC Wall
    3. Outlet: BC Wall
- Turbulence model: SKL

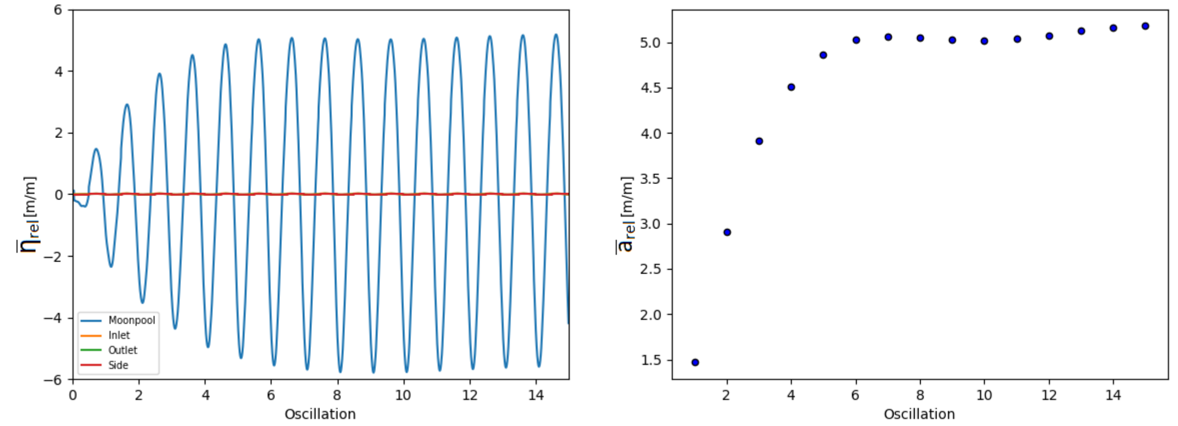

(a) Time trace wave elevation (b) Wave amplitude

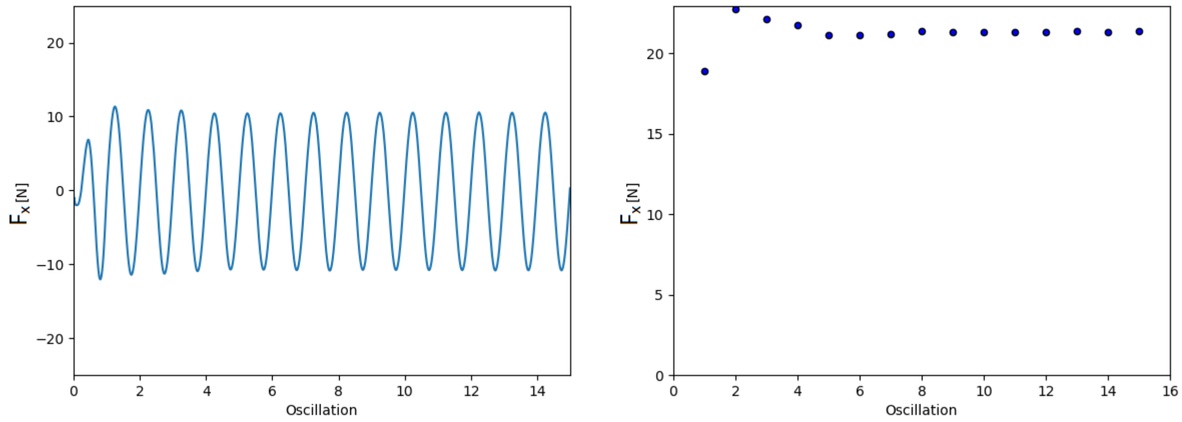

(c) Time trace F_x (d) Scatter amplitude F_x

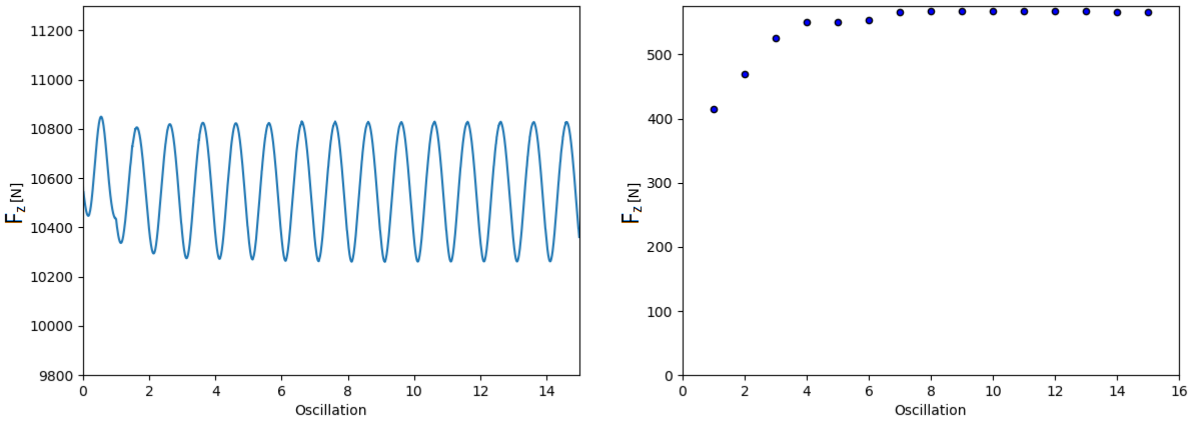

(e) Time trace F_z (f) Scatter amplitude F_z

Figure C.9: Case C FH

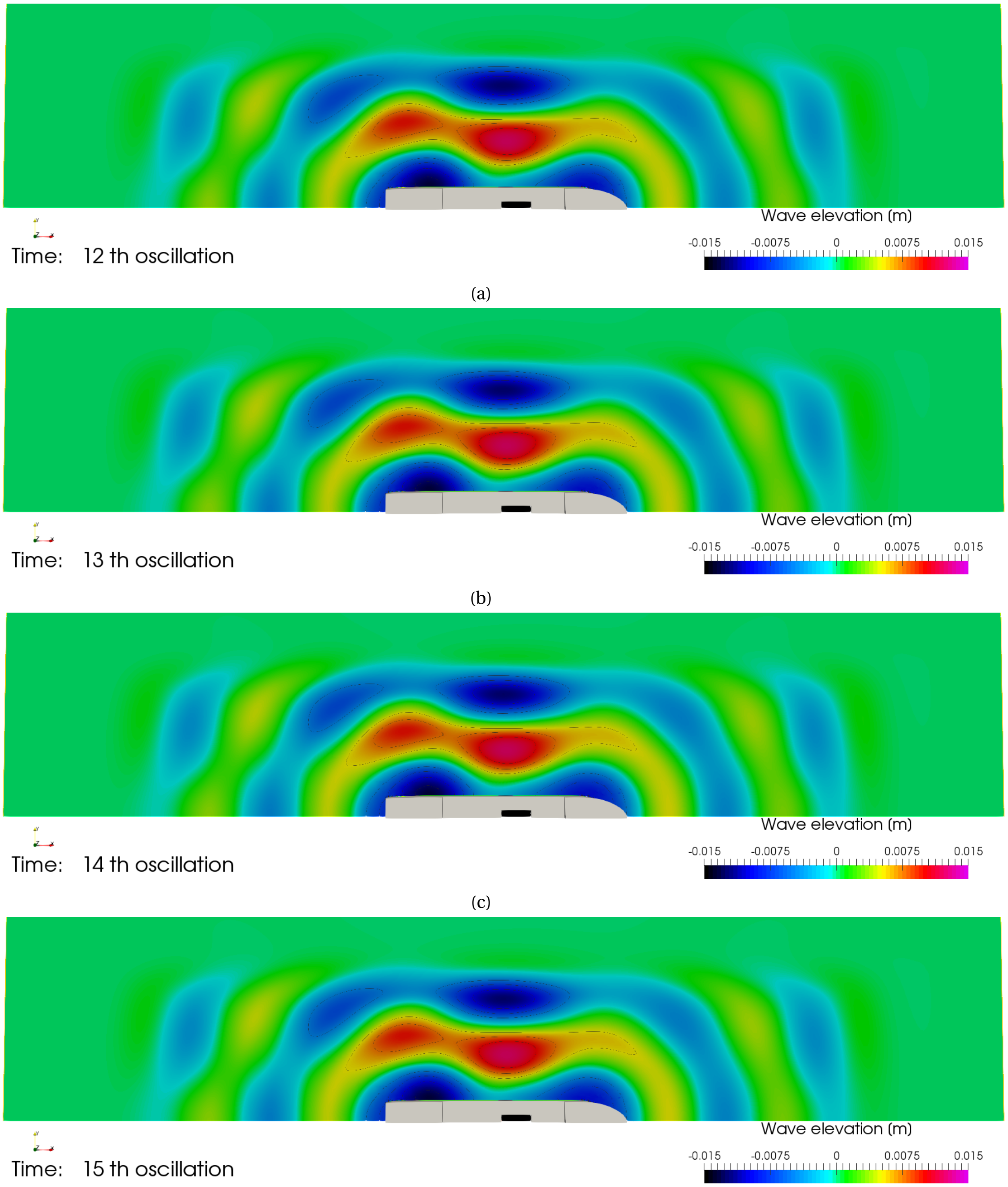

(a)

(b)

(c)

(d)

Figure C.10: Wave elevation case C

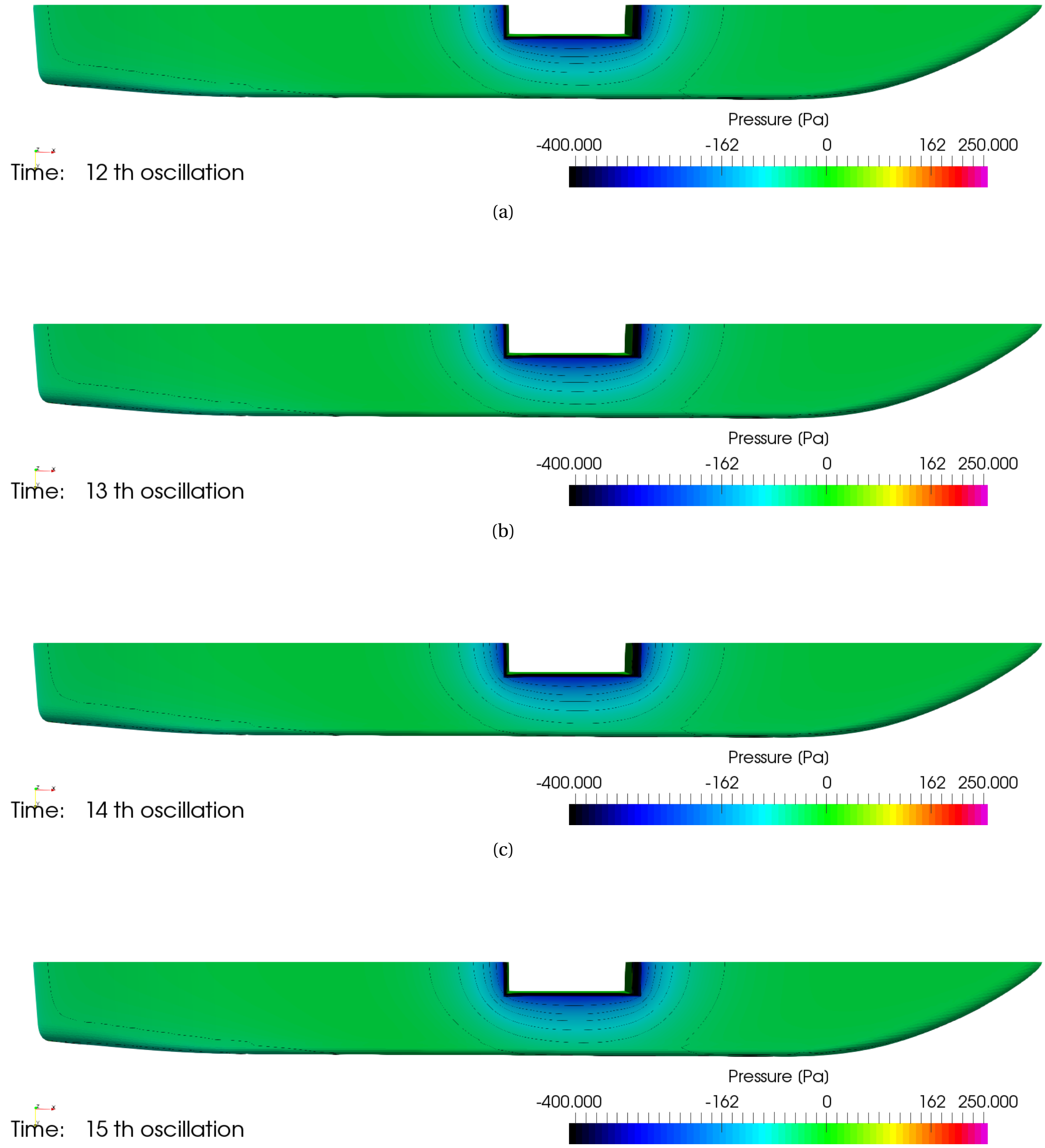

(a)

(b)

(c)

(d)

Figure C.11: Pressure distribution along the bottom for case C

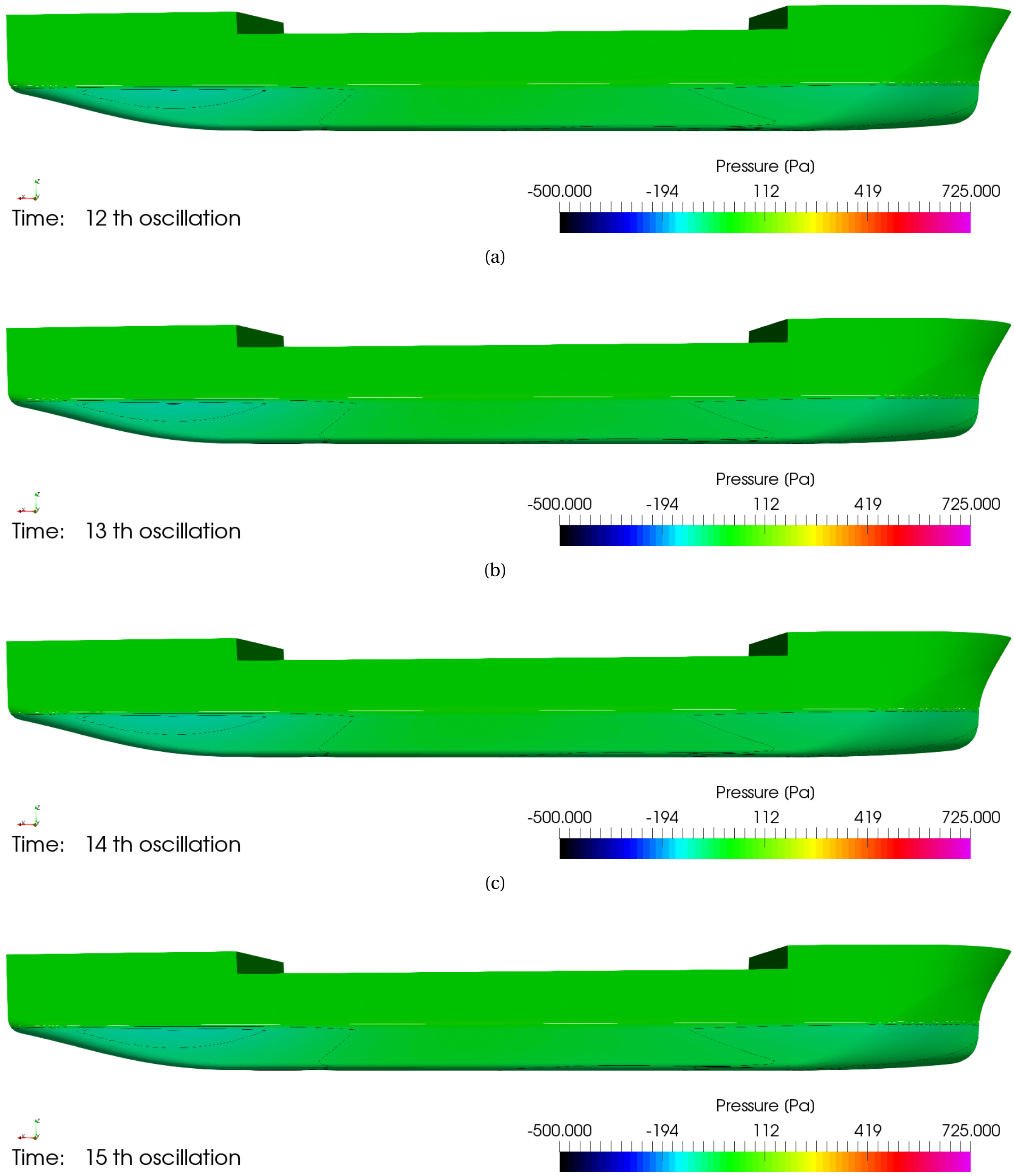

(a)

(b)

(c)

(d)

Figure C.12: Pressure distribution along the side for case C

D

Appendix Free floating vessel

D.1. Case A

- Grid: coarse (4.2M cells)
- Timestep: T/400
- Convergence level : 10^{-5}
- Domain length: 2.5 λ in front and aft the vessel
- Domain width : 1.5 λ
- Discretization scheme for the momentum equation : QUICK
- Convergence tolerance = 10^{-2}
- Boundary conditions:
    1. Inlet: BC Wall
    2. Side: BC Wall
    3. Outlet: BC Wall

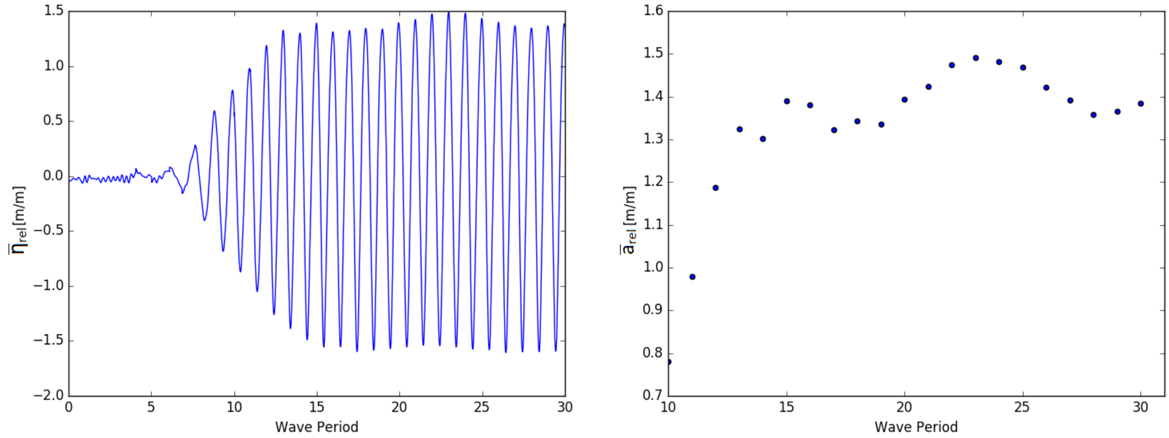

(a) Time trace η_{rel} (b) Wave amplitude

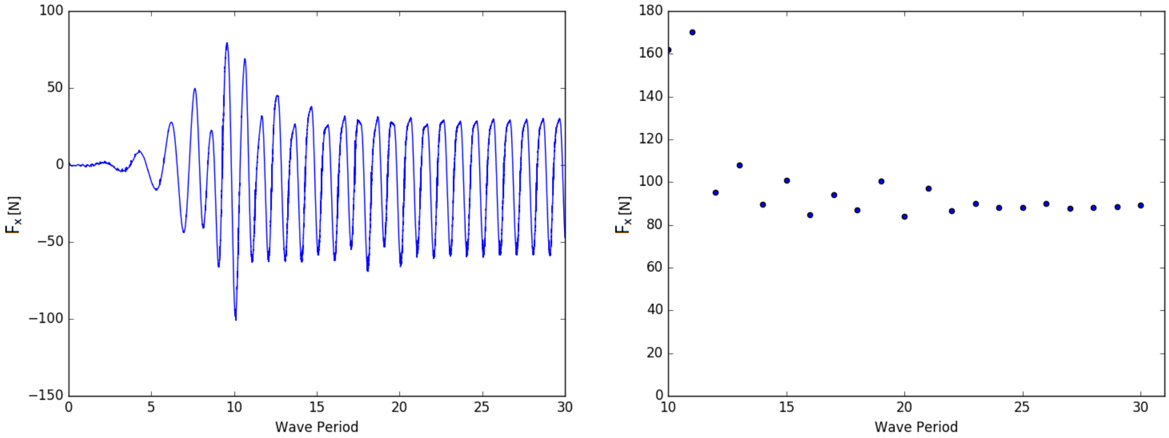

(c) Time trace F_x (d) Scatter amplitude F_x

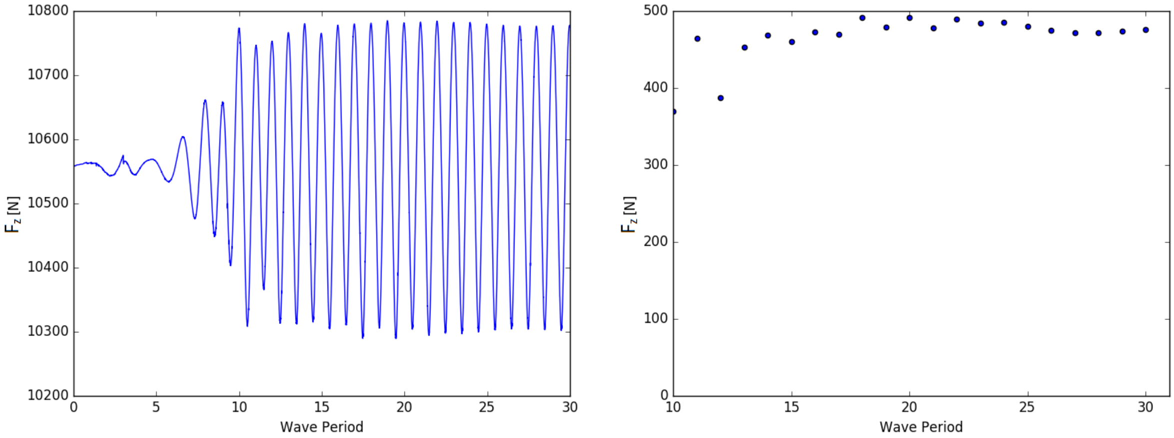

(e) Time trace F_z (f) Scatter amplitude F_z

Figure D.1: Case A free floating

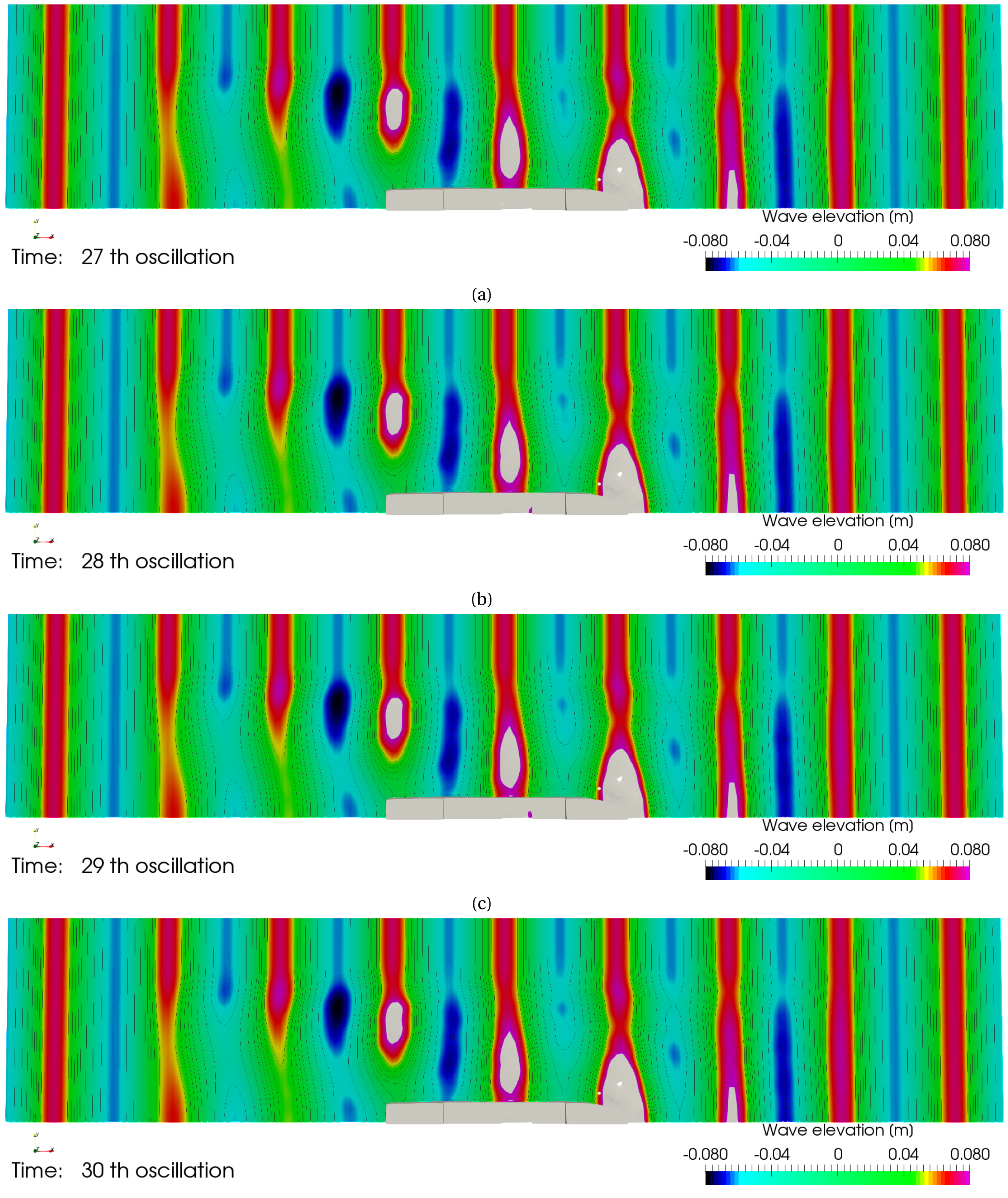

(a)

(b)

(c)

(d)

Figure D.2: Wave elevation case A

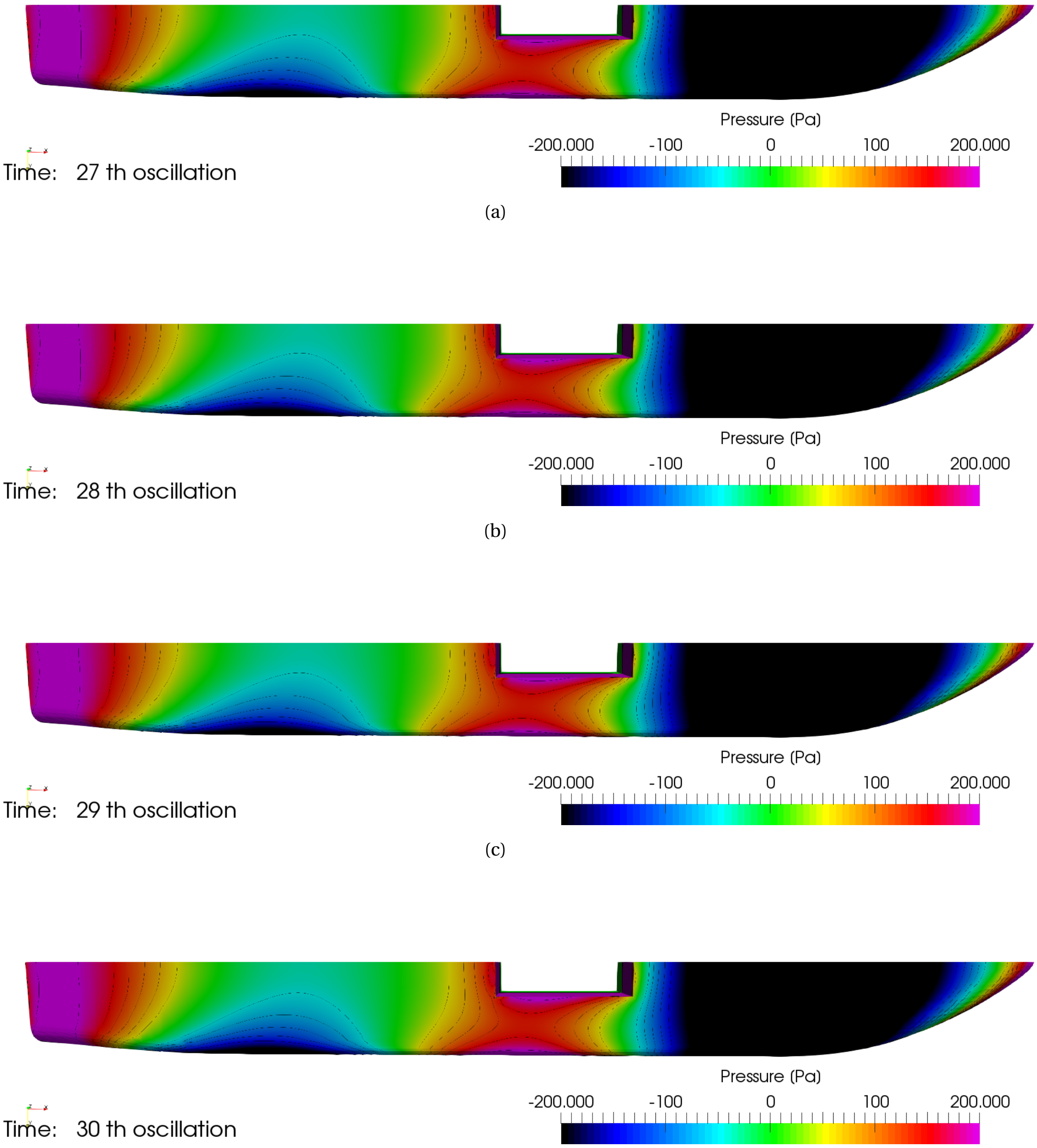

(a)

(b)

(c)

(d)

Figure D.3: Pressure distribution along the bottom for case A

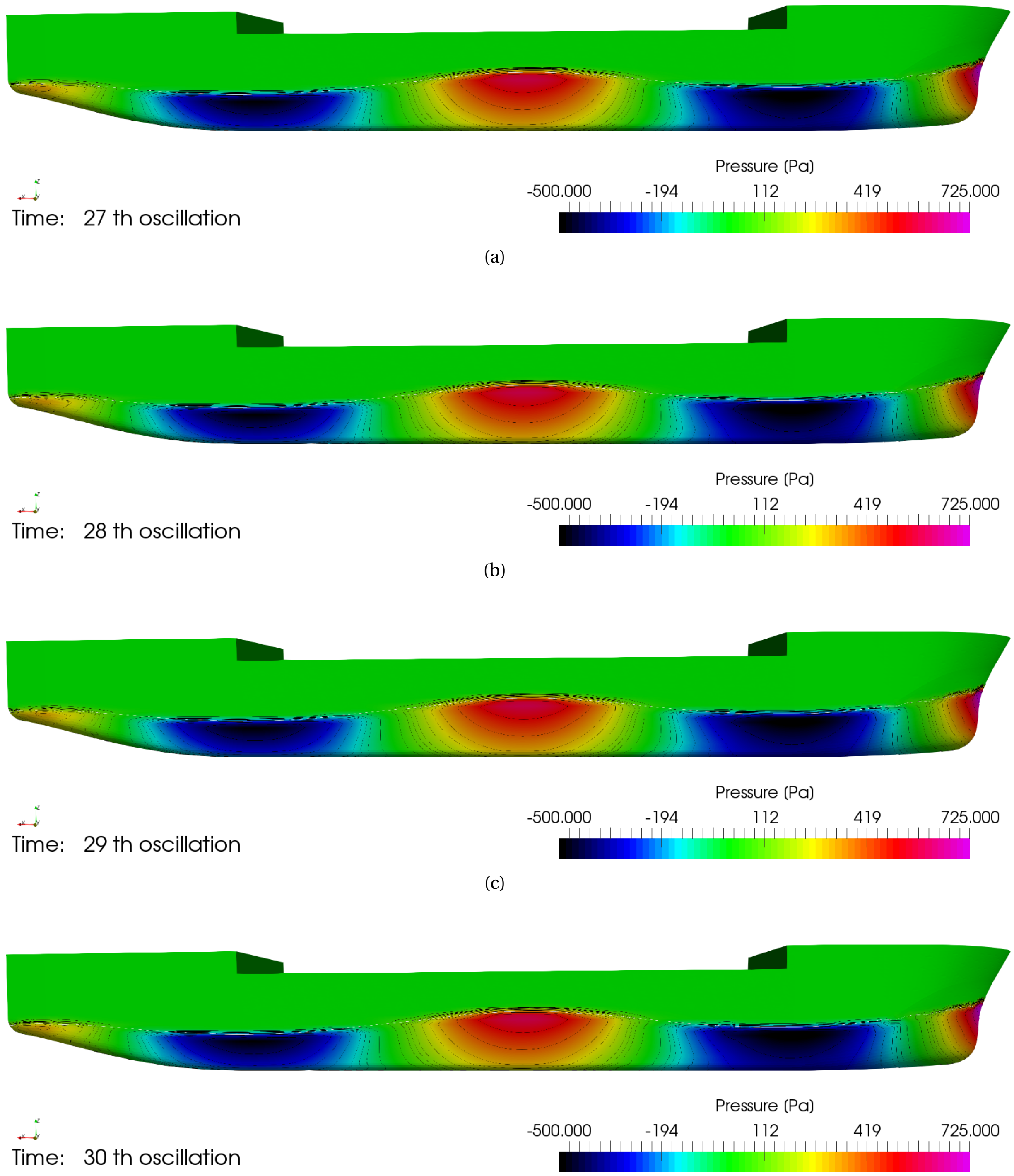

(a)

(b)

(c)

(d)

Figure D.4: Pressure distribution along the side for case A

D.2. Case B

- Grid: coarse (4.2M cells)
- Timestep: T/400
- Convergence level : 10^{-5}
- Domain length: 2.5 λ in front and aft the vessel
- Domain width : 1.5 λ
- Discretization scheme for the momentum equation : LIMITED QUICK
- Convergence tolerance = 10^{-2}
- Boundary conditions:
    1. Inlet: BC Wall
    2. Side: BC Wall
    3. Outlet: BC Wall

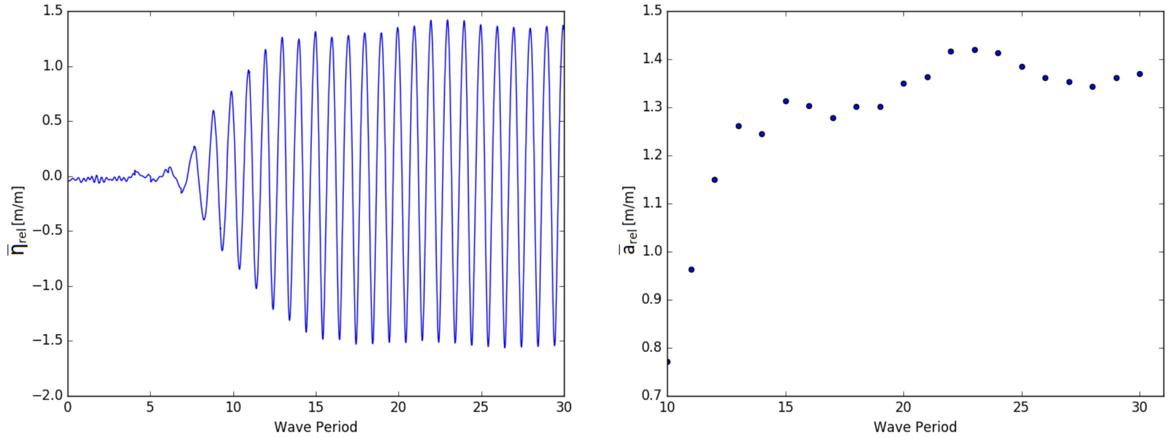

(a) Time trace η_{rel} (b) Wave amplitude

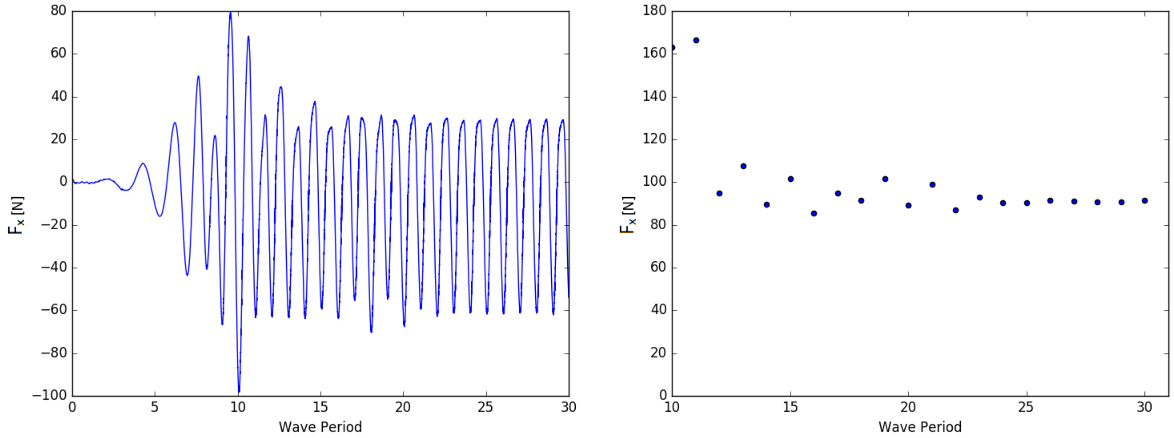

(c) Time trace F_x (d) Scatter amplitude F_x

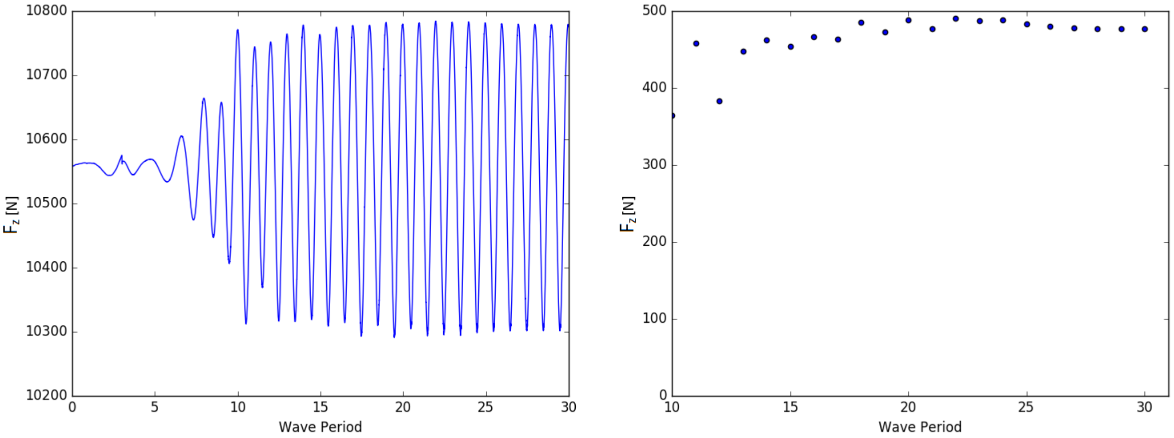

(e) Time trace F_z (f) Scatter amplitude F_z

Figure D.5: Case B free floating

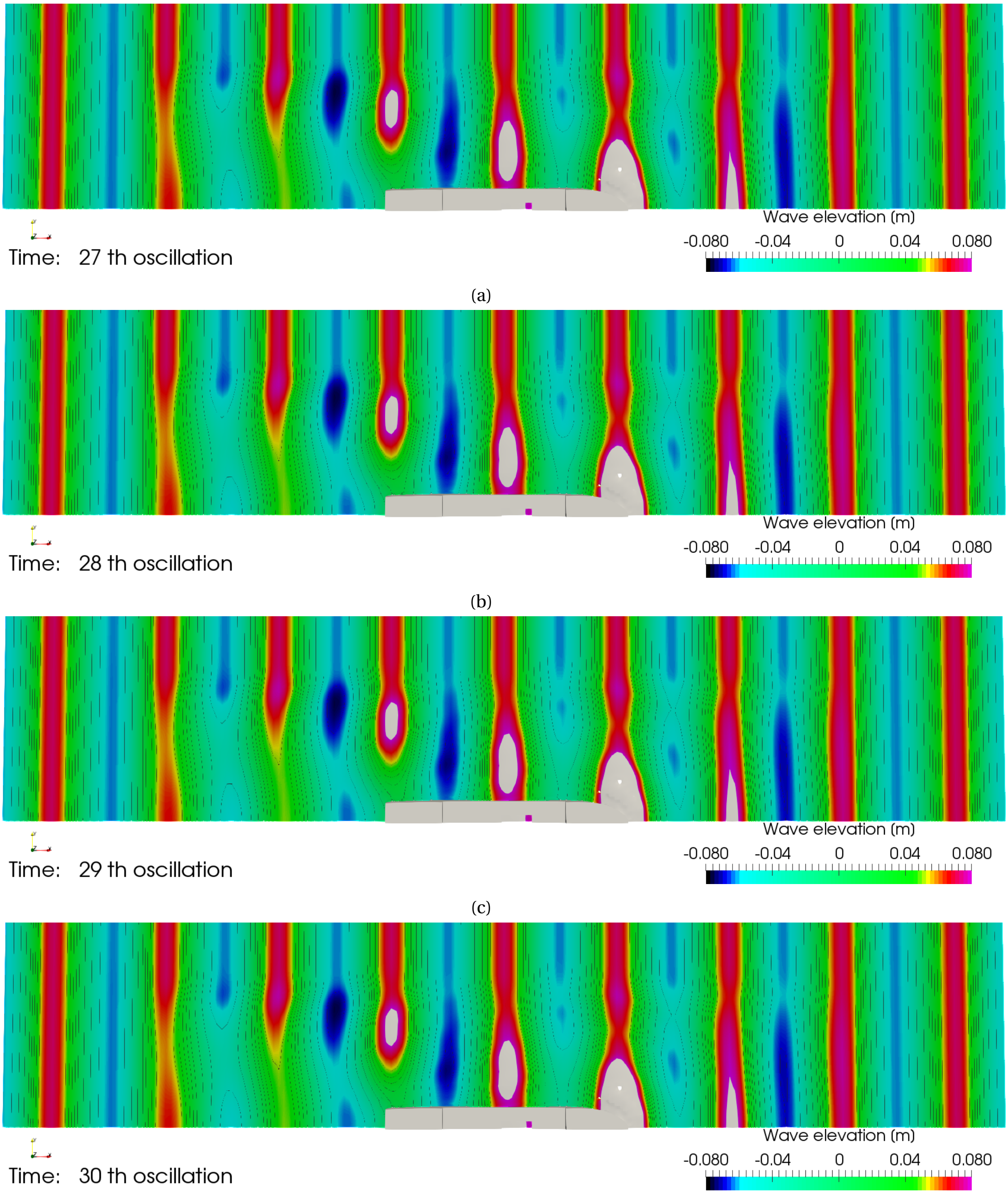

(a)

(b)

(c)

(d)

Figure D.6: Wave elevation case B

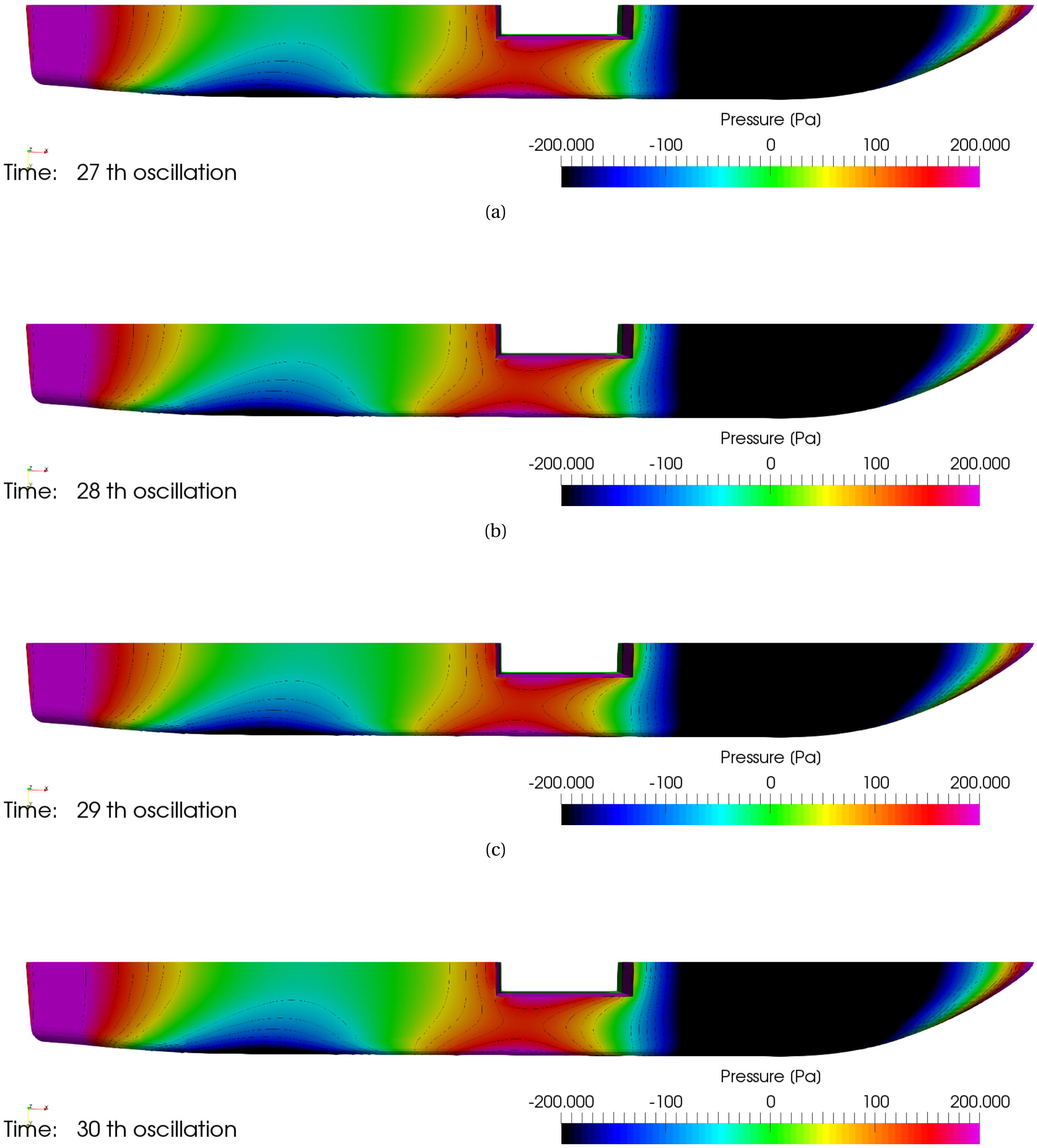

(a)

(b)

(c)

(d)

Figure D.7: Pressure distribution along the bottom for case B

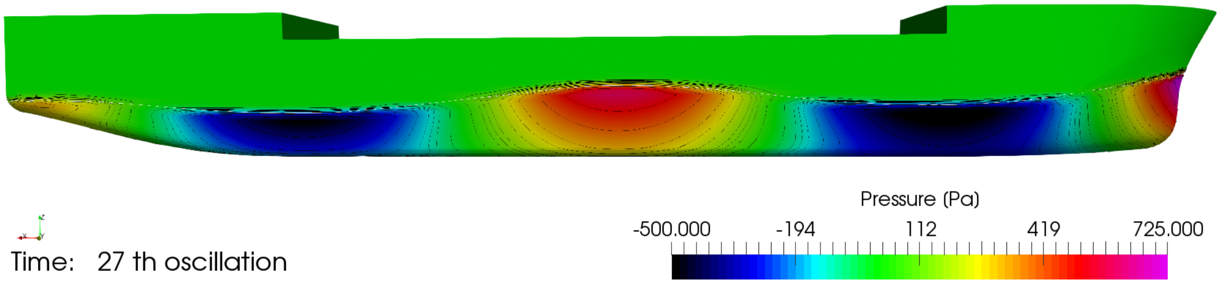

(a)

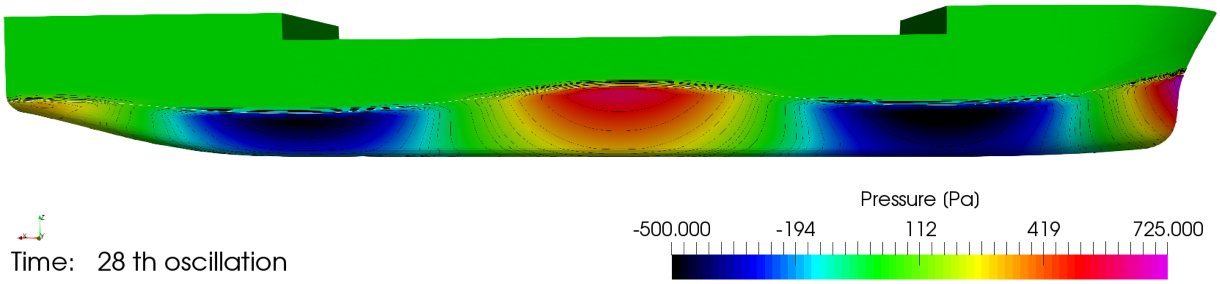

(b)

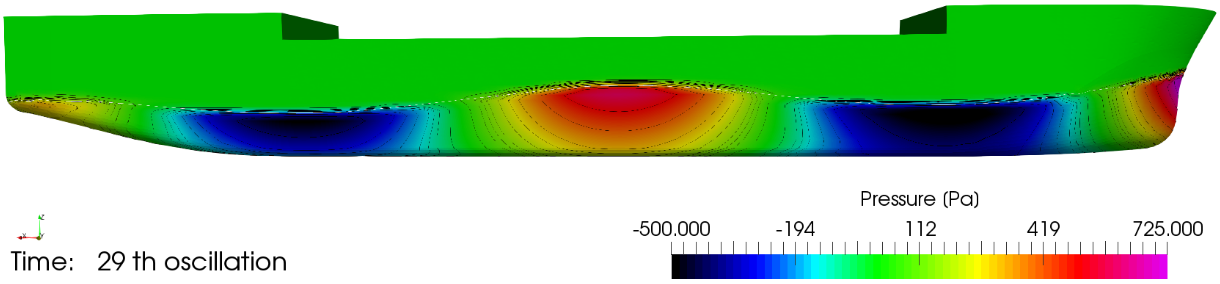

(c)

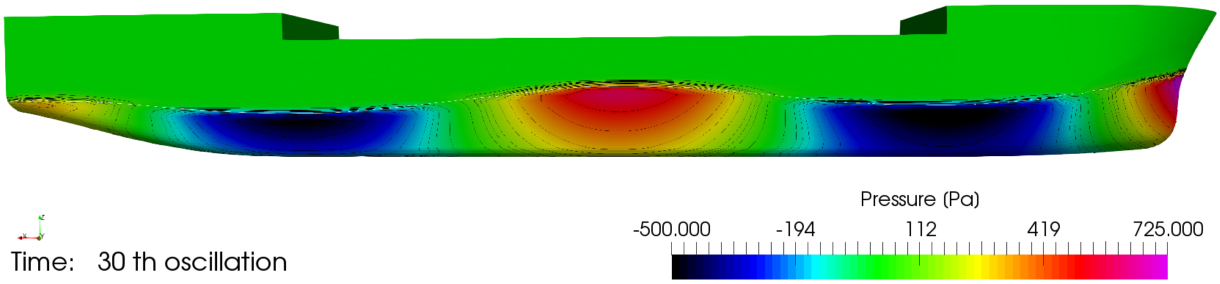

(d)

Figure D.8: Pressure distribution along the side for case B

D.3. Case C

- Grid: coarse (4.2M cells)
- Timestep: T/400
- Convergence level : 10^{-5}
- Domain length: 2.5 λ in front and aft the vessel
- Domain width : 1.5 λ
- Discretization scheme for the momentum equation : LIMITED QUICK
- Convergence tolerance = 10^{-3}
- Boundary conditions:
  1. Inlet: BC Wall
  2. Side: BC Wall
  3. Outlet: BC Wall

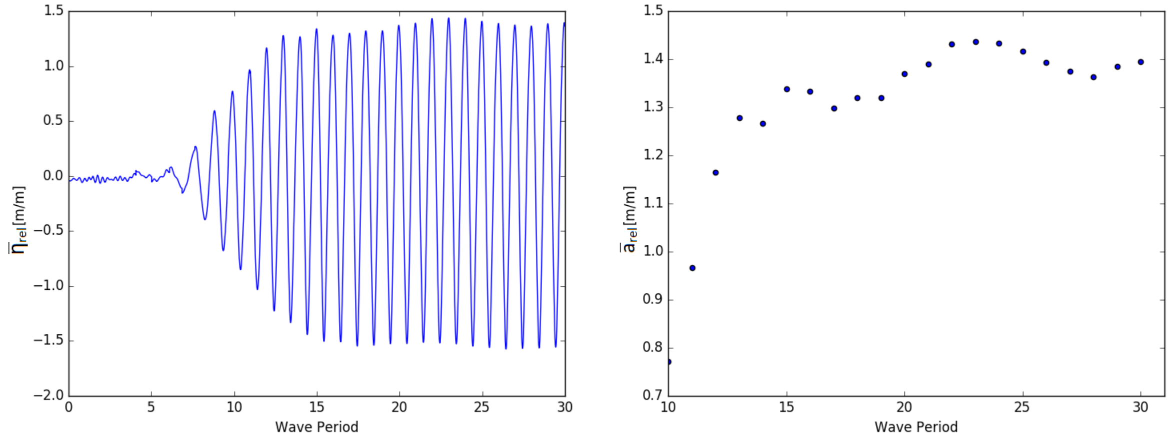

(a) Time trace η_{rel} (b) Wave amplitude

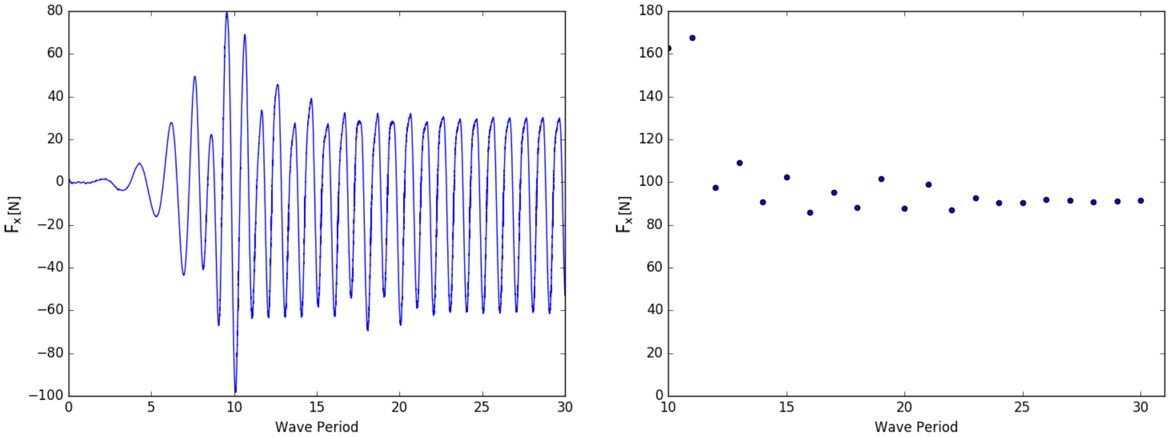

(c) Time trace F_x (d) Scatter amplitude F_x

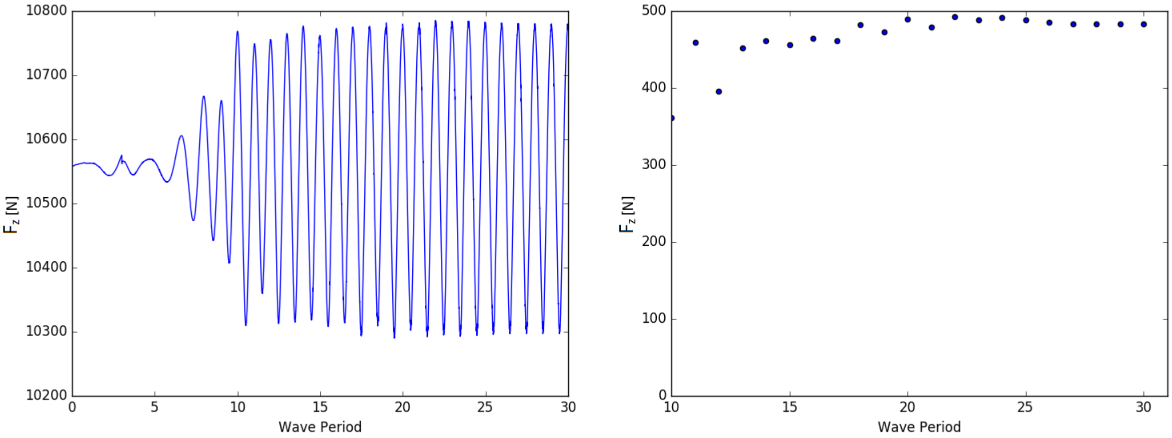

(e) Time trace F_z (f) Scatter amplitude F_z

Figure D.9: Case C free floating

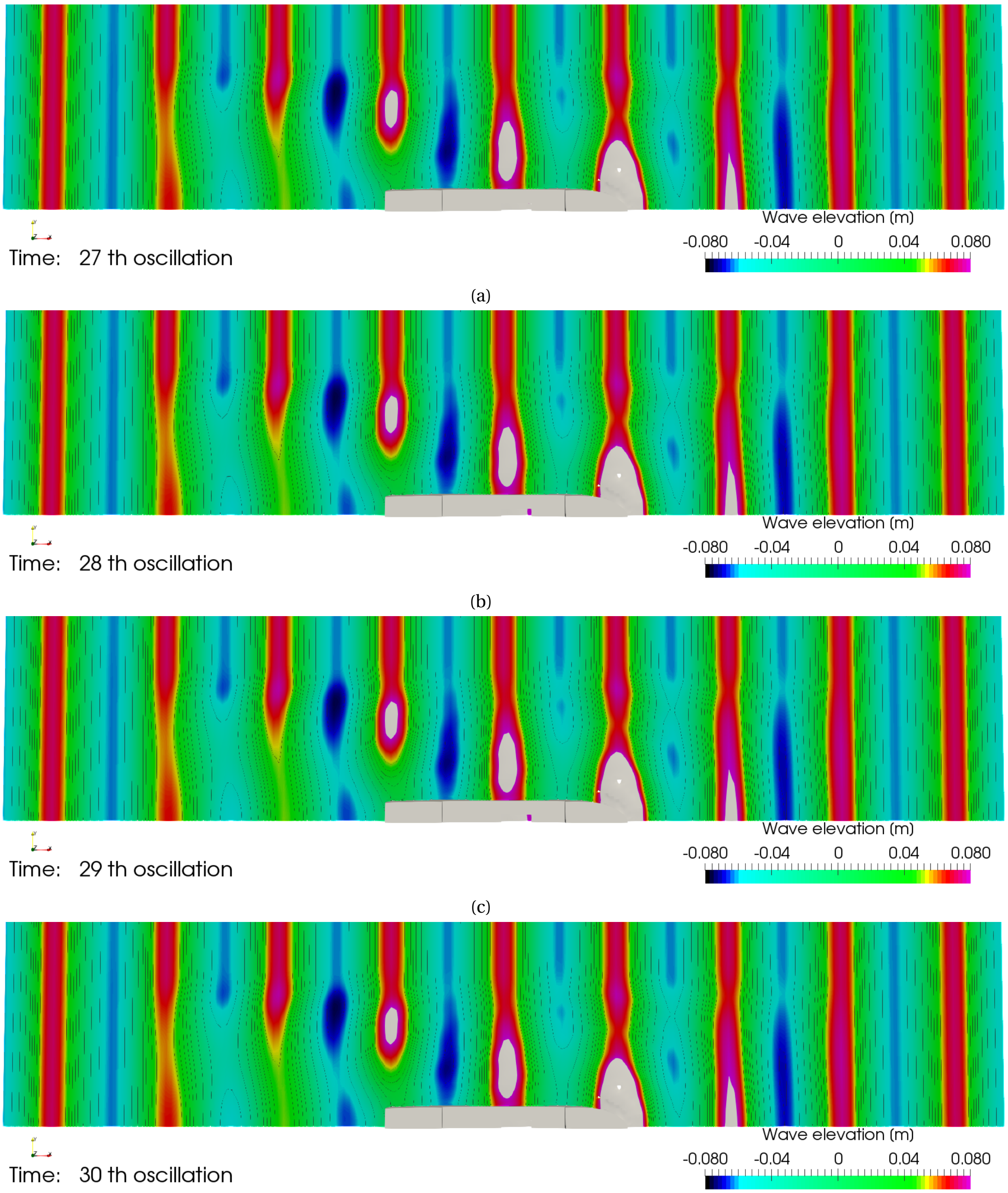

(a)

(b)

(c)

(d)

Figure D.10: Wave elevation case C

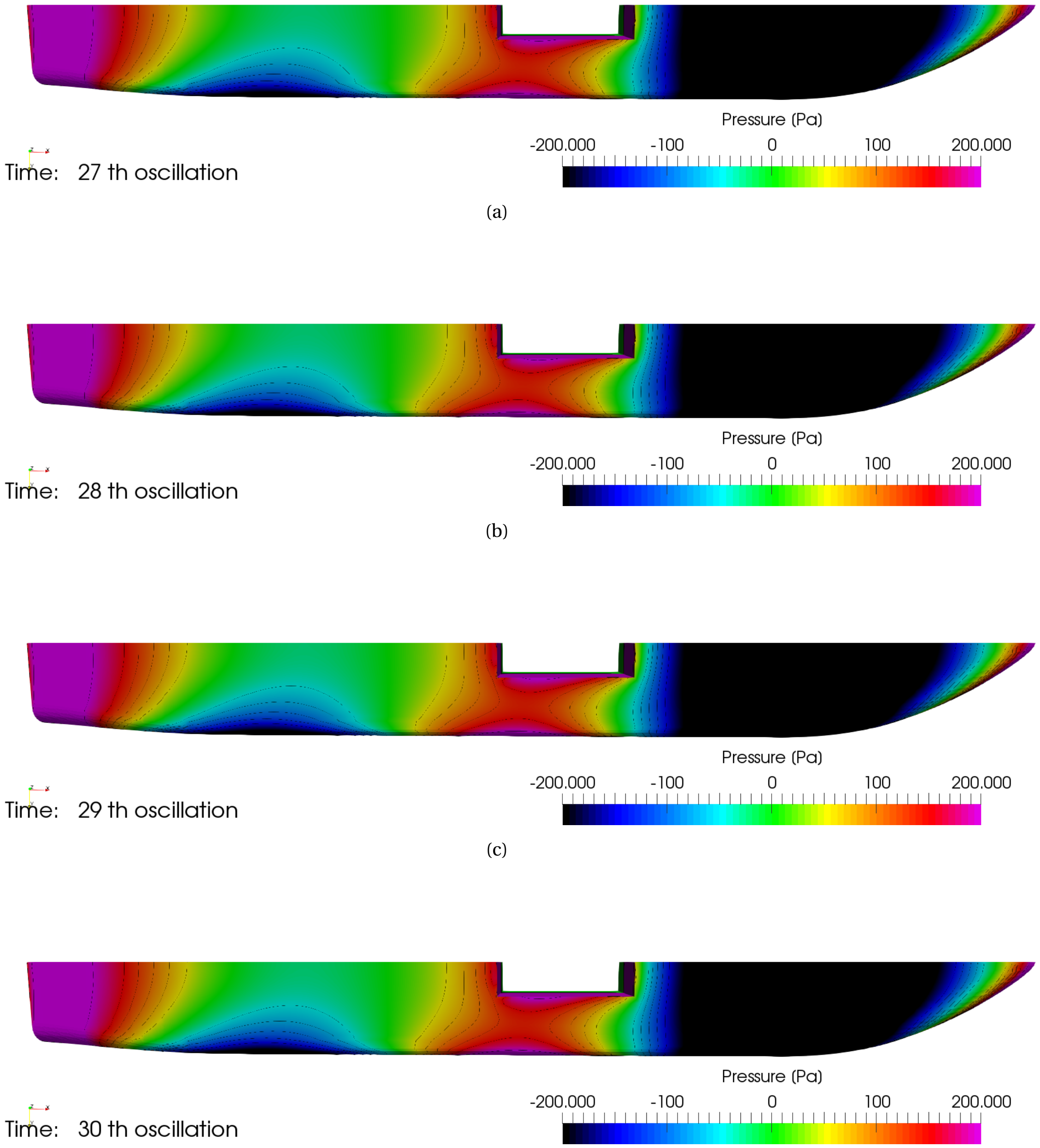

(a)

(b)

(c)

(d)

Figure D.11: Pressure distribution along the bottom for case C

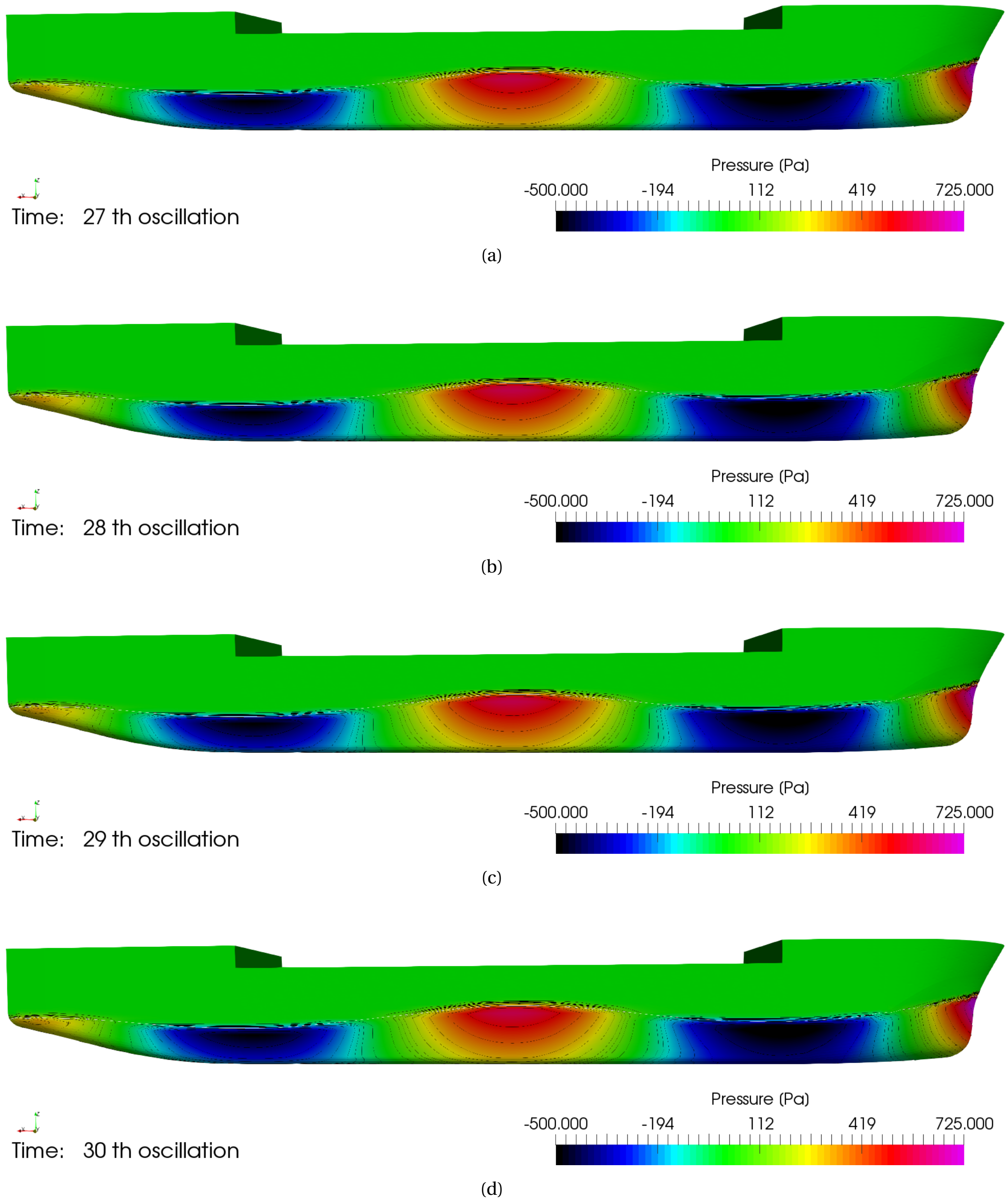

(a)

(b)

(c)

(d)

Figure D.12: Pressure distribution along the side for case C

D.4. Case D

- Grid: coarse (4.2M cells)
- Timestep: T/400
- Convergence level : 10^{-5}
- Domain length: 2.5 λ in front and aft the vessel
- Domain width : 1.5 λ
- Discretization scheme for the momentum equation : LIMITED QUICK
- Convergence tolerance = 10^{-4}
- Boundary conditions:
    1. Inlet: BC Wall
    2. Side: BC Wall
    3. Outlet: BC Wall

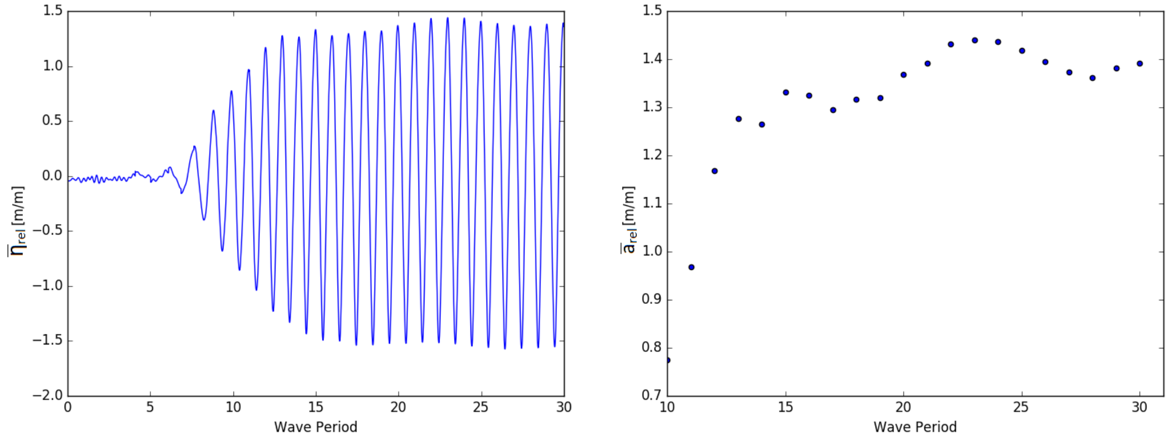

(a) Time trace η_{rel} (b) Wave amplitude

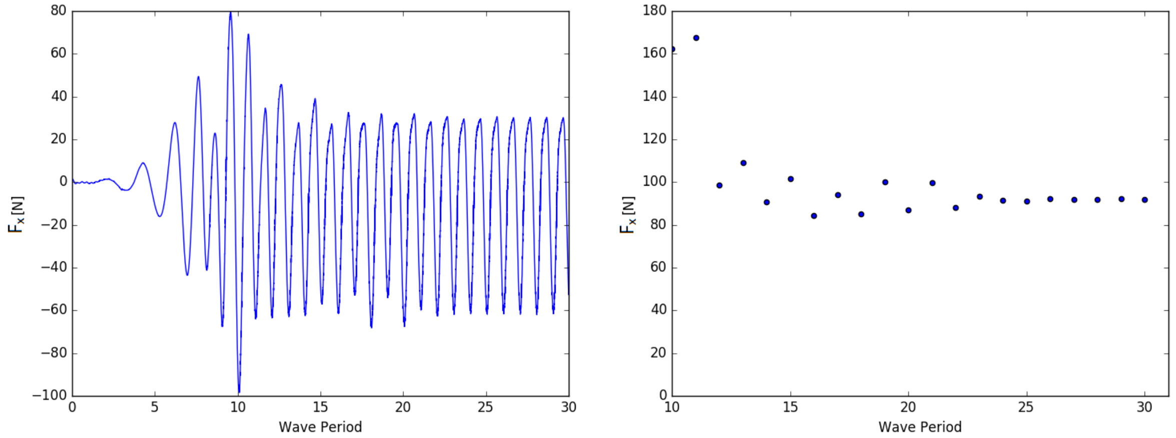

(c) Time trace F_x (d) Scatter amplitude F_x

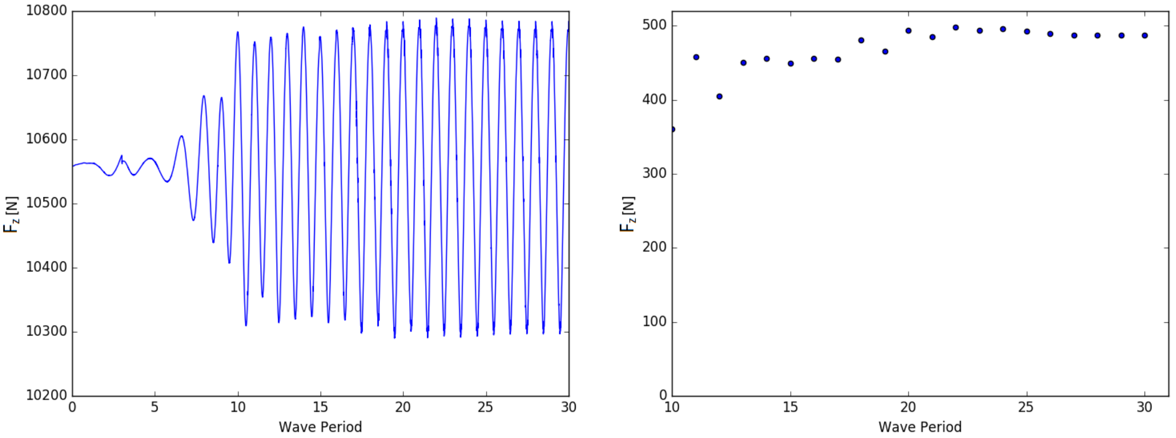

(e) Time trace F_z (f) Scatter amplitude F_z

Figure D.13: Case D free floating

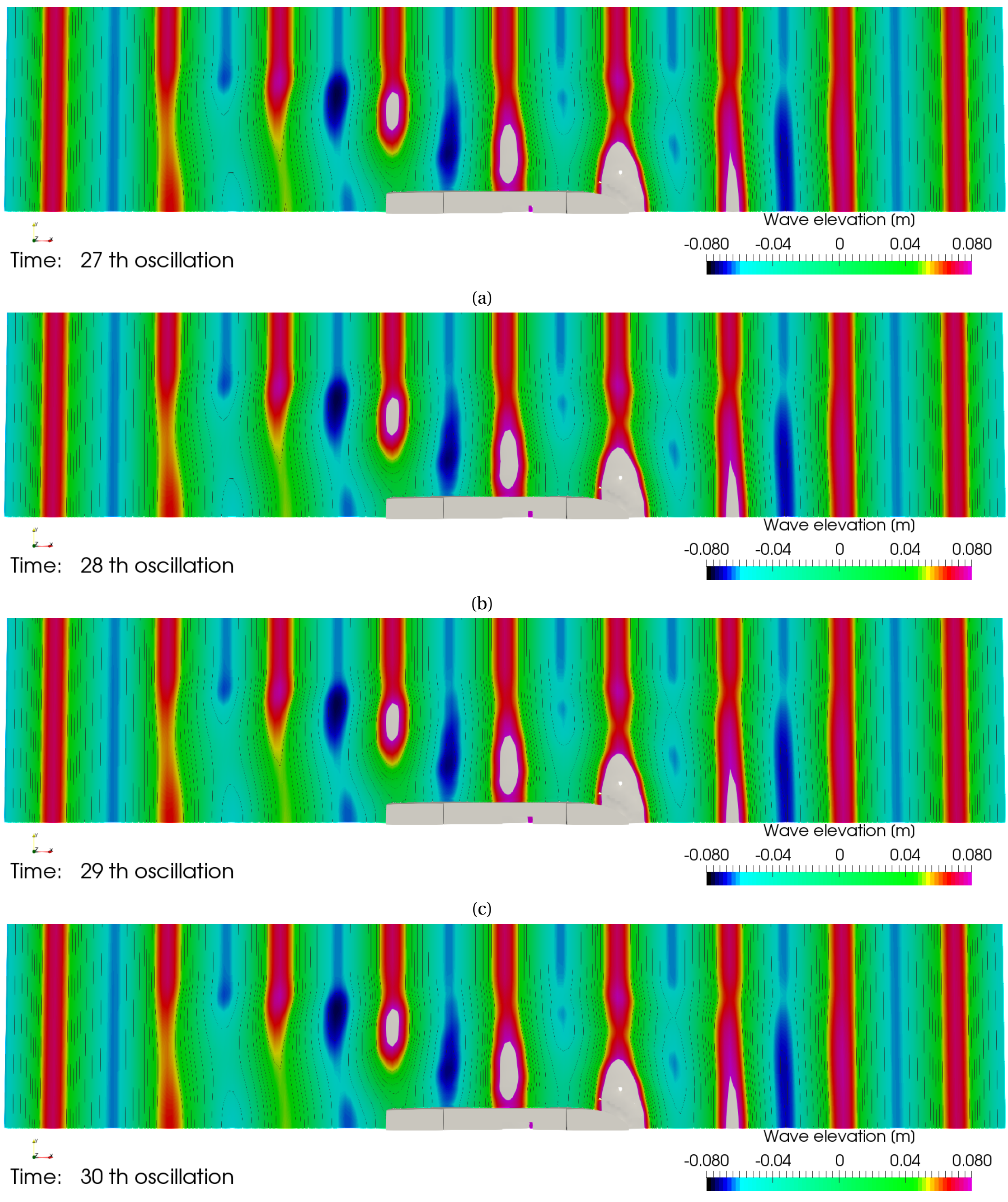

(a)

(b)

(c)

(d)

Figure D.14: Wave elevation case D

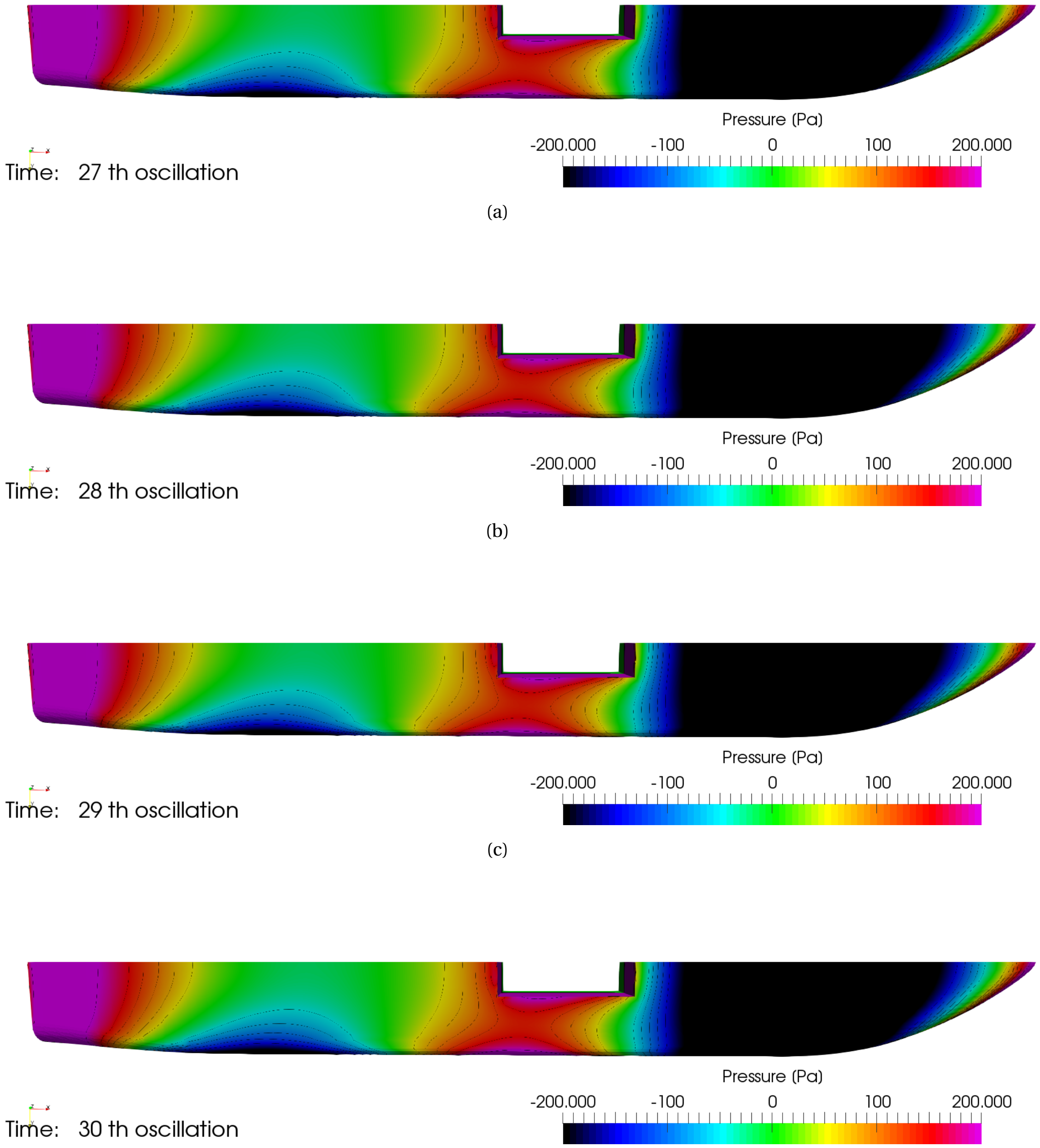

(a)

(b)

(c)

(d)

Figure D.15: Pressure distribution along the bottom for case D

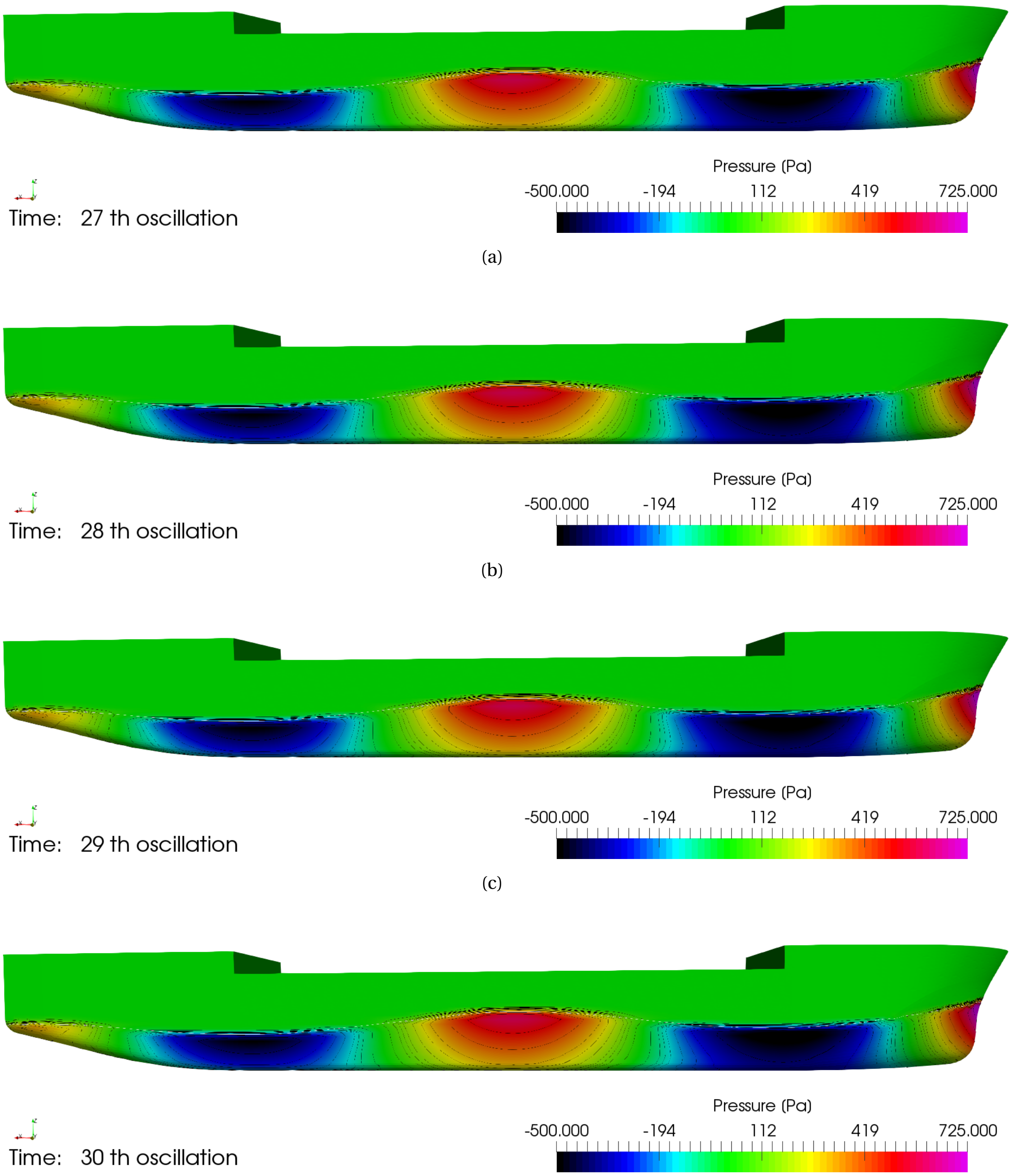

(a)

(b)

(c)

(d)

Figure D.16: Pressure distribution along the side for case D